



深圳大学  
SHENZHEN UNIVERSITY

# 王义平教授团队工作报告

(2012 年 — 2014 年)

报告人：王义平

深圳大学光电工程学院  
深圳市物联网光子器件与传感系统重点实验室

2015 年 04 月 01 日

<http://cofs.szu.edu.cn>

## 目 录

1. 报告摘要 .....	1
2. 团队简介 .....	2
3. 人才培养 .....	3
4. 实验室建设 .....	7
5. 研究方向 .....	9
6. 基金项目 .....	10
7. 教学和社会实践 .....	12
8. 发明专利 .....	13
9. 学术论文 .....	14
10. 期刊论文全文 .....	19



# 王义平教授团队工作报告摘要

王义平博士 2012 年 1 月 1 日入职深圳大学特聘教授。在学校和学院大力支持下，依托光电工程学院组建光纤传感技术研究团队和实验室。工作报告摘要如下：

## ★ 团队简介

团队成员 21 人，其中教师 2 人（特聘教授 1 人和讲师 1 人）、博士后 6 人、博士生 4 人和硕士生 9 人。

## ★ 人才培养

国家杰出青年科学基金 1 人，珠江学者特聘教授 1 人，孔雀计划高层次人才 2 人，研究生获国家奖学金等奖励 11 人次。

## ★ 实验室建设

牵头组建的“[深圳物联网光子器件与传感系统重点实验室](#)”已立项建设，超净间 200 平米，到位仪器设备 1000 余万元，具备飞秒激光微加工系统、光纤光栅制备系统等开展光纤传感实验研究的主要仪器设备。

## ★ 研究方向

实验室主要开展光纤传感技术及应用研究，具体研究方向：(1) 光纤光栅传感技术；(2) 光纤生化传感技术；(3) 光纤干涉传感技术。

## ★ 基金项目

已立项科研项目 18 项（国家级项目 7 项、省部级项目 3 项、市级项目 5 项、中国博士后基金 3 项）

## ★ 教学和社会实践

开设研究生课程 4 门。组织“教育部香港与内地高校师生交流计划”。研究生参加教育部“光纤技术新进展”暑期学校 10 人次，骑行川藏线到拉萨。

## ★ 发明专利

深圳大学唯一发明单位授权实用新型专利 6 项，公布（实审）发明专利 7 项。

## ★ 学术论文

国际期刊论文 27 篇（深圳大学第一署名单位 Nature 集团刊物(Scientific Report) 1 篇、JCR 一区 2 篇、二区 18 篇）；会议论文 37 篇（大会报告 1 篇、特邀报告 16 篇），主办国际会议分会 1 次；研究生参加国际国内学术会议 20 人次，口头报告 5 人次。其中 1 篇发表于 Optics Letters 的论文入选美国光学学会月度最热门下载论文（Top Downloads），另 1 篇发表于 Optics Letters 的论文入被美国光学学会 Virtual Journal for Biomedical Optics 转载报道。

# 光纤传感技术研究团队简介

王义平博士 2012 年 1 月 1 日入职深圳大学特聘教授，在学校和学院大力支持下，依托光电工程学院牵头组建“[光纤传感技术研究团队](#)”，目前团队成员 21 人。

## ★ 教 师：(2 人)

王义平（特聘教授、国家杰青、珠江学者）  
廖常锐（讲师、博士、孔雀计划高层次人才）

## ★ 博士后：(6 人)

王冠军（北京航空航天大学 博士）  
尹国路（北京交通大学 博士）  
孙 兵（江苏大学 博士）  
何 俊（中科院半导体所 博士）  
汪 超（香港理工大学 博士）  
白志勇（南开大学 博士）

## ★ 博士生：(4 人)

赵 静、唐 剑、刘 申、杨凯明

## ★ 硕士生：(9 人)

李正勇、钟晓勇、周江涛、刘颖洁、王侨、徐锡镇、谭展、黄益建、邓蜜

## 光纤传感技术研究团队



## 人才培养

团队成员获国家杰出青年科学基金 1 人、广东省珠江学者特聘教授 1 人、孔雀计划高层次人才 2 人。研究生获国家奖学金和社会奖学金 11 人次。

- ★ 国家杰出青年科学基金 1 人（王义平）
- ★ 广东省珠江学者特聘教授 1 人（王义平）
- ★ 深圳市孔雀计划高层次人才 2 人（王义平、廖常锐）
- ★ 2014 年深圳大学国家奖学金 4 人（周江涛、李正勇、钟晓勇、刘颖洁），**第一届硕士生 4 人全部获国家奖学金。**
- ★ 2014 年深圳大学优秀研究生奖学金 4 人（周江涛、李正勇、钟晓勇、刘颖洁），**第一届硕士生 4 人全部获优秀研究生奖学金。**
- ★ 2014 年深圳大学优秀博士支持计划 1 人（刘申）
- ★ 2014 年深圳大学牛憨笨奖学金 1 人（周江涛）
- ★ 2014 年深圳大学腾讯奖学金 1 人（刘申）



王义平  
特聘教授  
国家杰青  
珠江学者



廖常锐  
讲师  
孔雀计划高层次人才

## 2014 年深圳大学优秀博士支持计划获得者

## 2014 年深圳大学腾讯奖学金获得者



刘申  
2014 级博士生  
第一作者 Nature 集团刊物(Scientific Report) 1 篇  
JCR 二区 1 篇, 授权专利 1 项  
(毕业院校: 重庆邮电大学)



## 2014 年深圳大学国家奖学金获得者

## 2014 年深圳大学优秀研究生奖学金获得者



周江涛  
2012 级硕士生  
第一作者 JCR 一区 1 篇  
二区 2 篇、授权专利 1 项  
(毕业院校：安徽建筑学院)



李正勇  
2012 级硕士生  
第一作者 JCR 一区 1 篇  
二区 2 篇、授权专利 1 项  
(毕业院校：华中科技大学文华学院)



钟晓勇  
2012 级硕士生  
第一作者 JCR 二区 3 篇  
授权专利 1 项  
(毕业院校：广东工业大学)



刘颖洁  
2012 级硕士生  
第一作者 JCR 二区 1 篇  
授权专利 1 项  
(毕业院校：广西梧州学院)

## 2014 年深圳大学牛憨笨奖学金获得者



周江涛  
**2012 级硕士生**  
**第一作者 JCR 一区 1 篇**  
**二区 2 篇、授权专利 1 项**  
(毕业院校：安徽建筑学院)



# 实验室建设

2012年初入职深圳大学后，从零开始组建实验室，目前实验室初具规模：

- ★ 牵头组建的“[深圳市物联网光子器件与传感系统重点实验室](#)”2014年批准立项。
- ★ 千级、万级超净间200余平米，仪器设备1000余万元，已具备开展光纤传感技术研究的主要仪器设备。
- ★ 组建了内容丰富的重点实验室网站：<http://cofs.szu.edu.cn/>

超净实验室



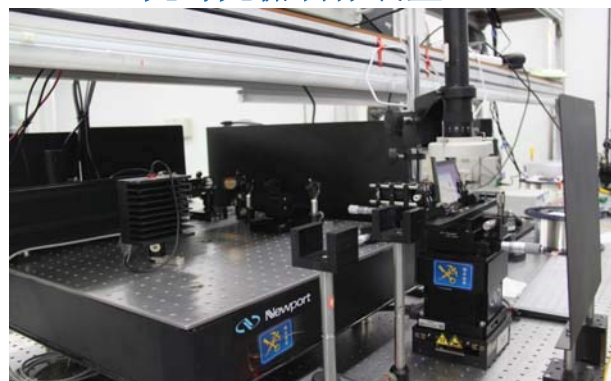
超净实验室



飞秒激光微加工系统



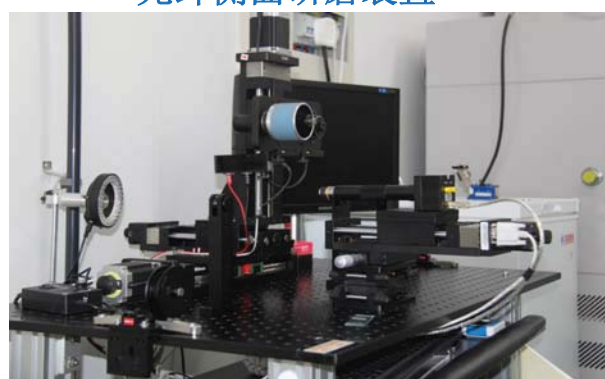
光纤光栅制作装置



微纳光纤制备系统



光纤侧面研磨装置



## 深圳物联网光子器件与传感系统重点实验室

Key Lab of Photonic Devices and Sensing Systems for Internet of Things of Shenzhen



深圳大学  
SHENZHEN UNIVERSITY

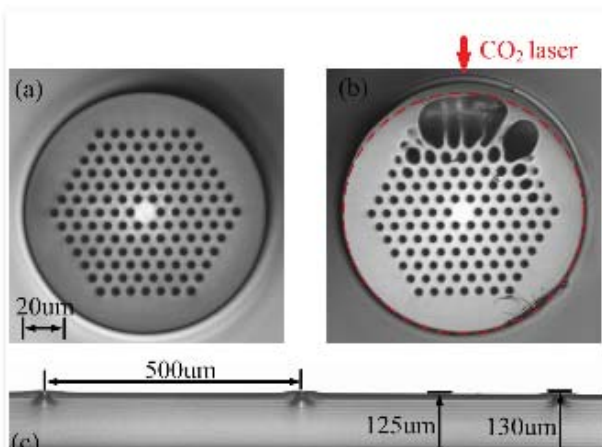
实验室简介 研究方向 团队成员 论文专利 基金项目 仪器设备 团队风貌 招生招聘



2012年王义平教授入职深圳大学光电工程学院，在中国工程院院士牛憨笨教授的大力支持下，依托光学工程博士点和博士后流动站组建光纤传感技术研究团队和实验室。

2014年王义平教授牵头组建的“深圳物联网光子器件与传感系统重点实验室”获深圳市科技创新委员会批准立项建设。实验室现拥有百级超净实验室以及飞秒激光微加工系统、光纤光栅制备系统、微纳光纤拉制系统等1000余万元的仪器设备。实验室现有成员20人，其中教师2人、博士后5人、博士生3人、硕士生10人。

## 研究进展



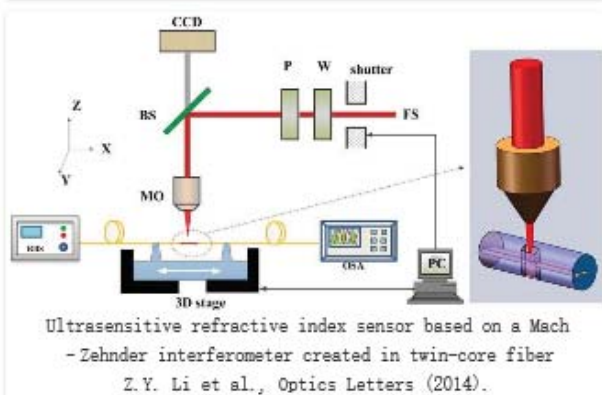
High-sensitivity strain sensor based on inflated long period fiber grating  
X. Y. Zhong et al. Optics Letters, Vol. 39, Issue 18, pp. 5463-5466 (September 2014)

## 年度报告

- 2014 年度报告

## 学术动态

- 2014年11月7号  
硕士生李正勇发表于Optical Letters的工作入选Virtual Journal for Biomedical Optics (VJBO)
- 2014年10月23日  
王义平教授团队在研究生培养中取得突出成绩
- 2014年9月22日 - 9月25日  
全国光纤传感学术会议暨产业化论坛
- 2014年9月15日  
学术报告——偏振外差光纤光栅激光传感技术
- 2014年9月4日  
学术报告——硅基光子信息处理器件与集成
- 2014年9月3日  
学术报告——Photonic Technologies at Aston Universit
- 2014年8月25日 - 8月28日  
PIERS 2014 会议在广州举办



Ultrasensitive refractive index sensor based on a Mach-Zehnder interferometer created in twin-core fiber  
Z. Y. Li et al., Optics Letters (2014).

## 热点链接

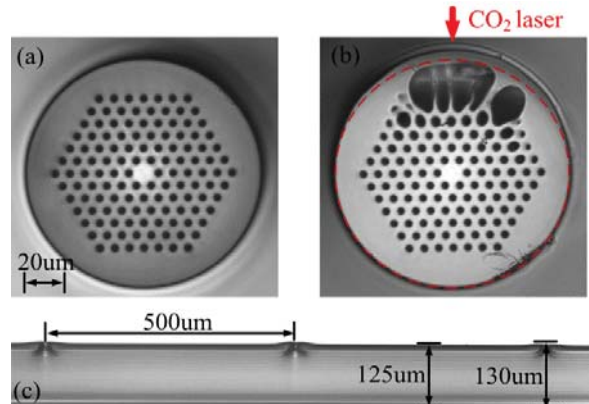
- 深圳大学
- 深圳大学光电工程学院
- 英国南安普顿大学光电研究中心
- 香港理工大学
- 国家自然科学基金委
- 深圳市科技创新委员

# 研究方向

实验室主要开展光纤传感技术及应用研究，重点研究光纤光栅、微纳光纤、光子晶体光纤等新型微纳光子器件的传感机理、制作方法及传感应用，尤其是在生物化学传感领域的应用。包括三个主要研究方向：

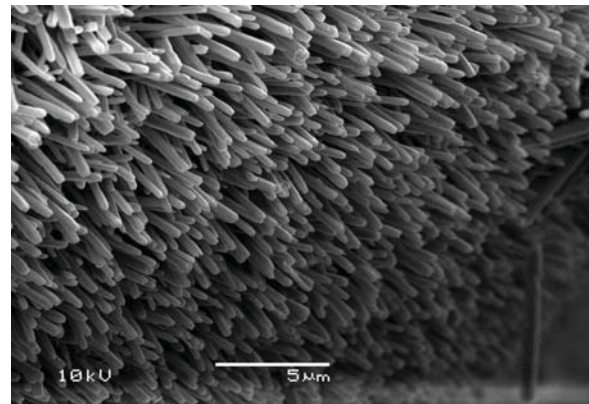
## (1) 光纤光栅传感技术

光纤光栅是一种重要的光纤传感和通信器件。本方向主要研究不同类型光纤光栅的制备方法、耦合机理及应用。搭建了飞秒激光、紫外激光、CO<sub>2</sub>激光、电弧放电制备光纤光栅的装置。利用相位掩模、二维扫描、点对点技术在不同类型光纤（单模光纤、光子晶体光纤、空气芯光子带隙光纤、D型光纤、微纳光纤）上制备光纤布拉格光栅和长周期光纤光栅，并研究其在传感、通信和激光器领域的应用。



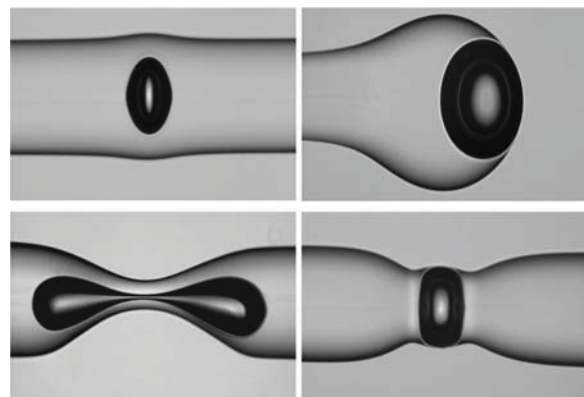
## (2) 光纤生化传感技术

光纤生化传感技术在生物医学、食品安全及化学分析等领域具有重要的应用。本方向主要研究基于金属纳米结构、金属薄膜、ZnO 纳米线等的光纤生化传感芯片以及其在疾病早期诊断、痕量气体检测应用等方面的关键技术。利用化学合成法在光纤表面成功实现了纳米金粒子合成及表征，构建了光纤表面等离激元（LSPR）检测系统。利用光纤侧面抛磨技术实现了粉尘和气体浓度检测。利用两步溶液化学合成法在光纤表面成功制备了 ZnO 纳米线，实现了高灵敏度湿度检测。



## (3) 光纤干涉传感技术

光纤干涉传感技术具有灵敏度高、结构紧凑、抗电磁干扰等优点，在传感领域具有重要应用。本方向主要研究不同类型光纤 Fabry-Perot、Michelson、Mach-Zehnder 干涉仪的制作方法及传感应用。利用光纤错位熔接、光纤微环、光纤端帽、纤芯开槽、双芯光纤等方法研制了不同类型的光纤干涉型应变、温度、折射率传感器。利用电弧放电法制作了基于不同类型气泡（球形、椭圆形、矩形、纺锤形）的光纤干涉仪，实现了高灵敏度气压传感。



## 基金项目

已立项科研项目 **18 项**，其中国家级项目 7 项、省部级项目 3 项、市级项目 5 项、中国博士后基金 3 项。

编号	项目类别	项目名称(编号)	起止时间	负责人
1	国家杰出青年科学基金	光纤传感技术(61425007)	2015-2018	王义平
2	国家自然科学基金面上项目	空气芯光子带隙光纤光栅(61377090)	2014-2017	王义平
3	国家自然科学基金面上项目	光子晶体光纤导光机理可逆转换及应用(11174064)	2012-2015	王义平
4	国家自然科学基金青年项目	基于微纳光纤布拉格光栅的光开关研究(61308027)	2014-2016	廖常锐
5	国家自然科学基金青年项目	基于双芯光纤定向耦合的双参数传感技术(61405128)	2015-2017	尹国路
6	国家自然科学基金青年项目	基于光纤微泡结构的 LSPR 线宽压缩方法研究 (61405127)	2015-2017	王冠军
7	国家自然科学基金青年项目	基于悬挂芯光纤微单元的矢量加速度传感器研究 (61405125)	2015-2017	汪超
8	教育部香港与内地高校师生交流计划项目	光传感方法、技术及应用的多学科合作研究	2015-2015	王义平
9	广东省珠江学者专项支持项目	光子晶体光纤光栅制作及传感通信应用(829-000001)	2014-2016	王义平
10	广东省自然科学基金重大基础研究培育项目	飞秒激光高效并行微加工技术	2014-2017	王义平
11	深圳市重点实验室组建项目	深圳物联网光子器件与传感系统重点实验室(ZDSYS20140430164957664)	2014-2016	王义平
12	南山区重点实验室组建项目	南山区物联网光子传感器件与系统重点实验室(KC2014ZDZJ0008A)	2014-2015	王义平
13	深圳市海外高层次人才孔雀计划项目	液体填充的光子晶体光纤及传感和通信应用(KQCX20120815161444632)	2013-2015	王义平
14	深圳市战略新兴产业发展专项资金项目	空气芯光子带隙光纤光栅的写入技术及应用(JCYJ20130329140017262)	2013-2015	王义平
15	深圳市海外高层次人才孔雀计划项目	超快激光高效制备光纤光栅技术及其在氢气检测中的应用	2014-2016	廖常锐

16	中国博士后科学基金	基于耦合型双芯光纤的多参数同时传感研究 (2014M552227)	2014-2015	尹国路
17	中国博士后科学基金	基于智能手机的 LSPR 生物传感器 (2014M562202)	2014-2015	王冠军
18	中国博士后科学基金	快速电光调谐光子晶体光纤光栅研究 (2014M562201)	2014-2015	孙 兵

## 教学和社会实践

★ 开设研究生课程 4 门：

- 光纤传感技术 (任课教师：王义平、廖常锐)
- 光纤光栅原理及应用 (任课教师：王义平)
- 微纳光纤技术 (任课教师：王义平)
- 光电检测技术 (任课教师：廖常锐)

★ 王义平受邀在 2013 年教育部“光纤技术新进展”暑期学校开设“光纤传感技术”课程（电子科技大学主办）。课题组研究生 10 人次参加该暑期学校。

★ 研究生参加国际国内学术会议 20 人次，口头报告 5 人次。

★ 2013 年团队成员户外拓展训练，增强团队协作精神。

★ 2014 年组织“教育部香港与内地高校师生交流计划项目”，开展“光传感方法、技术及应用的多学科合作研究”，时间 3 个月，香港理工大学师生 12 人参加。

★ 2014 年暑期硕士生杨凯明骑行川藏线从成都到拉萨，挑战自我!!!

香港与内地高校师生交流计划



团队成员骑行川藏线



团队暑期出游



团队户外拓展训练



# 发明专利

授权实用新型专利 6 项，申请公布(实审)发明专利 7 项。

编号	专利名称	发明人	专利国家	专利类别	申请授权	授权或申请日
1	强度调制型光纤迈克尔逊应变传感器及传感器装置(201420082778.7)	深圳大学 王义平, 周江涛, 廖常锐	中国	实用新型	授权	2014,06,25
2	一种光子晶体光纤紧凑型可调谐的带通滤波器(201420153147.X)	深圳大学 王义平, 刘颖洁, 廖常锐	中国	实用新型	授权	2014,06,26
3	可调FP腔的FP干涉仪的制作装置(201420153237.9)	深圳大学 王义平, 廖常锐	中国	实用新型	授权	2014,07,04
4	基于迈克尔逊干涉仪的全光纤折射率计及其系统(201420189564.X)	深圳大学 王义平, 李正勇, 廖常锐	中国	实用新型	授权	2014,07,09
5	基于光子晶体光纤的膨胀型长周期光纤光栅(201420209917.8)	深圳大学 王义平, 钟晓勇, 廖常锐	中国	实用新型	授权	2014,08,07
6	基于光纤FP干涉仪的压力传感器(201420209878.1)	深圳大学 王义平, 廖常锐, 刘申	中国	实用新型	授权	2014,10,15
7	一种相移可调的光纤布拉格光栅器件及其制作方法	廖常锐, 王义平	中国	发明	申请	2013,11,15
8	强度调制型光纤迈克尔逊应变传感器及制作方法(201410065837.4)	深圳大学 王义平, 周江涛, 廖常锐	中国	发明	申请	2014,02,26
9	光子晶体光纤紧凑型可调谐的带通滤波器及其制作方法(201410126998.X)	深圳大学 王义平, 刘颖洁, 廖常锐	中国	发明	申请	2014,02,26
10	可调FP腔的FP干涉仪的制作方法及制作装置(201410127074.1)	深圳大学 王义平, 刘申, 廖常锐	中国	发明	申请	2014,03,31
11	基于迈克尔逊干涉仪的全光纤折射率计、制作方法及系统(201410156179.X)	深圳大学 王义平, 李正勇, 廖常锐	中国	发明	申请	2014,04,18
12	基于光子晶体光纤的膨胀型长周期光纤光栅及其制作方法(201410173103.8)	深圳大学 王义平, 钟晓勇, 廖常锐	中国	发明	申请	2014,04,25
13	基于光纤FP干涉仪的压力传感器及其制作方法(201410173102.3)	深圳大学 王义平, 廖常锐, 刘申	中国	发明	申请	2014,04,25

# 学术论文

发表国际期刊论文 30 篇（深圳大学第一署名单位 Nature 集团刊物(Scientific Report) 1 篇、JCR 一区 2 篇、二区 20 篇）；会议论文 37 篇（大会报告 1 篇、特邀报告 16 篇），主办国际会议分会 1 次；研究生参加国际国内学术会议 20 人次，口头报告 5 人次。其中 1 篇发表于 Optics Letters 的论文入选美国光学学会月度最热门下载论文（Top Downloads），另 1 篇发表于 Optics Letters 的论文入被美国光学学会 Virtual Journal for Biomedical Optics 转载报道。

## ★ 期刊论文：（30 篇，其中 JCR 一区 2 篇、二区 18 篇，\*通信作者）

### 2015 年度

- [1] Shen Liu, Kaiming Yang, **Yiping Wang\***, Junle Qu, Changrui Liao, Jun He, Zhengyong Li, Guolu Yin, Bing Sun, Jiangtao Zhou, Guanjun Wang, Jian Tang, and Jing Zhao, High sensitivity strain sensor based on in-fiber rectangular air bubble, **Scientific Reports** , 5, 7624, 2015 (**JCR 二区, IF=5.078**)
- [2] Xiaoyong Zhong, **Yiping Wang\*** Changrui Liao, Shen Liu, Jian Tang, and Qiao Wang, Temperature-insensitivity gas pressure sensor based on inflated long period fiber grating inscribed in photonic crystal fiber, **Optics Letters** 40(8), 1791-1794, 2015. (**JCR 二区, IF=3.179**)
- [3] Jun He, **Yiping Wang\*** Changrui Liao, Qiaoni Wang, Kaiming Yang, Bing Sun, Guolu Yin, Shen Liu, Jiangtao Zhou, and Jing Zhao, Highly birefringent phase-shifted fiber Bragg gratings inscribed with femtosecond laser, **Optics Letters** 40(9), 2008-2011, 2015. (**JCR 二区, IF=3.179**)
- [4] Bing Sun, Yijian Huang, Shen Liu, Chao Wang, Jun He, Changrui Liao, Guolu Yin, Jing Zhao, Yingjie Liu, Jian Tang, Jiangtao Zhou, and **Yiping Wang**, Asymmetrical in-fiber Mach-Zehnder interferometer for curvature measurement, **Optics Express** 23(11), 14596-14602 2015. (**JCR 二区, IF=3.528**)
- [5] Bing Sun, **Yiping Wang\***, Junle Qu, Changrui Liao, Guolu Yin, Jun He, Jiangtao Zhou, Jian Tang, Shen Liu, Zhengyong Li and Yingjie Liu, Simultaneous measurement of pressure and temperature by employing Fabry-Perot interferometer based on pendant polymer droplet, **Optics Express** 23(3), 1906-1911, 2015. (**JCR 二区, IF=3.528**)
- [6] Zhengyong Li, Changrui Liao, **Yiping Wang\*** Lei Xu, Dongning Wang, Xiaopeng Dong, Shen Liu, Qiao Wang, Kaiming Yang, and Jiangtao Zhou, Highly-sensitive gas pressure sensor using twin core fiber based in-line Mach-Zehnder interferometer, **Optics Express** 23(5), 6673-6678, 2015. (**JCR 二区, IF=3.528**)
- [7] Jiangtao Zhou, **Yiping Wang\***, Changrui Liao, Guolu Yin, Bing Sun, Zhengyong Li, Jun He, Guanjun Wang, Xiaoyong Zhong, and Jing Zhao, Intensity-modulated refractive index sensor based on optical fiber Michelson interferometer, **Sensors and Actuators B-Chemical**, 208, 315-319, 2015. (**JCR 一区, IF=3.840**)
- [8] Guolu Yin, **Yiping Wang\***, Changrui Liao, Bing Sun, Yingjie Liu, Shen Liu, Qiao Wang, Kaiming Yang, Jian Tang, and Xiaoyong Zhong, “Simultaneous refractive Index and Temperature Measurement with LPFG and Liquid-Filled PCF”, **IEEE Photonics Technology Letters**, 27(4), 375-378, 2015. (**JCR 二区, IF=2.176**)
- [9] Jing Zhao, Guolu Yin, Changrui Liao, Shen Liu, Jun He, Bing Sun, Guanjun Wang, Xizheng Xu, and **Yiping Wang\***, Rough side-polished fiber with surface scratches for sensing applications, **IEEE Photonics Journal**, 7(3), 6801107, 2015. (**JCR 二区, IF=2.330**)
- [10] Bing Sun, **Yiping Wang\***, Yingjie Liu, Shen Liu, Changrui Liao, and Ming-Yang Chen, “Compact device employed a hybrid plasmonic waveguide for polarization-selective splitting,” **Optics Communications**, 334, 240-246, 2015(**JCR 三区, IF=1.438**)
- [11] Guanjun Wang, Chao Wang, Jing Zhao, Changrui Liao, Shen Liu, xizhen Xu, Haijian Liang, **Yiping Wang\***, Side-opened suspended core fiber-based surface Plasmon resonance sensor. **IEEE Sensors Journal**, 10267, 2015. (**JCR 三区, IF=1.678**)

## 2014 年度

- [12] Zhengyong Li, **Yiping Wang\***, Changrui Liao, Shen Liu, Jiangtao Zhou, Xiaoyong Zhong, Yingjie Liu, Kaiming Yang, Qiao Wang, and Guolu Yin, "Temperature-insensitive refractive index sensor based on in-fiber Michelson interferometer," Sensors and Actuators B-Chemical, 199,31-35, 2014 (**JCR 一区, IF=3.840**)
- [13] Xiaoyong Zhong, **Yiping Wang\***, Junle Qu\*, Changrui Liao, Shen Liu, Jian Tang, Qiao Wang, Jing Zhao, Kaiming Yang, Zhengyong Li, High-sensitivity strain sensor based on inflated long period fiber grating, Optics Letters, 39(18), 5463-5466,2014 (**JCR 二区, IF=3.179**) (入选美国光学学会 2014 年 9 月最热门下载论文 (Top Downloads))
- [14] Shen Liu, **Yiping Wang\***, Changrui Liao, Zhengyong Li, Qiao Wang, Jiangtao Zhou, Kaiming Yang, Xiaoyong Zhong, Jing Zhao, and Jian Tang, High-sensitivity strain sensor based on in-fiber improved Fabry-Perot interferometer, Optics Letters, 39(7), 2121-2124, 2014 (**JCR 二区, IF=3.179**)
- [15] Yingjie Liu, **Yiping Wang\***, Bing Sun, Changrui Liao, Jun Song, Kaiming Yang, Guanjun Wang, Qiao Wang, Guolu Ying, and Jiangtao Zhou, "Compact tunable multibandpass filters based on liquid-filled photonic crystal fibers," Optics Letters, 39(7), 2148-2151, 2014 (**JCR 二区, IF=3.179**)
- [16] Changrui Liao, Shen Liu, Lei Xu, Chao Wang, **Yiping Wang\***, Zhengyong Li, Qiao Wang, and D. N. Wang, "Sub-micron silica diaphragm based fiber-tip Fabry-Perot interferometer for pressure measurement," Optics Letters, 39(10), 2827-2830, 2014 (**JCR 二区, IF=3.179**)
- [17] Zhengyong Li, Changrui Liao, **Yiping Wang\***, Xiaopeng Dong, Shen Liu, Kaiming Yang, Qiao Wang, and Jiangtao Zhou "Ultrasensitive refractive index sensor based on a Mach-Zehnder interferometer created in twin-core fiber," Optics Letters, 39(17), 4982-4985, 2014 (**JCR 二区, IF=3.179**) (被美国光学学会虚拟期刊 Virtual Journal for Biomedical Optics 转载报道, Volume 9, Issue 11, 2014)
- [18] Changrui Liao, Lei Xu, Chao Wang, D. N. Wang, **Yiping Wang\***, Qiao Wang, Kaiming Yang, Zhengyong Li, Xiaoyong Zhong, Jiangtao Zhou, and Yingjie Liu, "Tunable phase-shifted fiber Bragg grating based on femtosecond laser fabricated in-grating bubble," Optics Letters, 38(21), 4473-4476, 2013 (**JCR 二区, IF=3.179**)
- [19] Jiangtao Zhou, Changrui Liao, **Yiping Wang\***, Guolu Yin, Xiaoyong Zhong, Kaiming Yang, Bing Sun, Guanjun Wang, and Zhengyong Li, "Simultaneous measurement of strain and temperature by employing fiber Mach-Zehnder interferometer," Optics Express, 22(2), 1680-1686, 2014. (**JCR 二区, IF=3.528**)
- [20] Xiaoyong Zhong, **Yiping Wang\***, Changrui Liao, Guolu Yin, Jiangtao Zhou, Guanjun Wang, Bing Sun and Jian Tang, "Long period fiber gratings inscribed with an improved two-dimensional scanning technique", IEEE Photonics Journal, 6(4), 2201508, 2014 (**JCR 二区, IF=2.330**)
- [21] Jiangtao Zhou, **Yiping Wang\***, Changrui Liao, Guolu Yin, Xi Xu, Kaiming Yang, Xiaoyong Zhong, Qiao Wang, and Zhengyong Li, "Intensity-Modulated Strain Sensor Based on Fiber In-Line Mach-Zehnder Interferometer," IEEE Photonic Technology Letter, 26(5), 508-511, 2014. (**JCR 二区, IF=2.176**)
- [22] Guolu Yin, **Yiping Wang\***, Changrui Liao, Jiangtao Zhou, Xiaoyong Zhong, Guanjun Wang, Bing Sun, and Jun He, "Long Period Fiber Gratings Inscribed by Periodically Tapering a Fiber," IEEE Photonic Technology Letters, 26(7), 698-701, 2014 (**JCR 二区, IF=2.176**)
- [23] Chao Wang, Wa Jin, Changrui Liao, Jun Ma, Wei Jin\*, Fan Yang, Hoi Lut Ho, and **Yiping Wang**, "Highly birefringent suspended-core photonic microcells for refractive-index sensing," Applied Physics Letters, 105(6), 061105-1-4, 2014 (**JCR 二区, IF=3.515**)
- [24] Wa Jin, Haifeng Xuan, Chao Wang, Wei Jin\*, and **Yiping Wang**, Robust microfiber photonic microcells for sensor and device applications, Optics Express, 22(23), 28132-28141, 2014. (**JCR 二区, IF=3.528**)
- [25] Fan Yang, Wei Jin\*, Yingchun Cao, Hoi Lut Ho, **Yiping Wang**, Towards high sensitivity gas detection with hollow-core photonic bandgap fibers, Optics Express, 22(20), 24894-24907, 2014.
- [26] Tao Chen, Changrui Liao, D. N. Wang\*, **Yiping Wang**, "Polarization-locked vector solitons in a mode-locked fiber laser using polarization-sensitive few-layer graphene deposited D-shaped fiber saturable absorber," J. of Optical Society of America B 31(6), 1377-1382, 2014 (**JCR 三区, IF=1.806**)
- [27] Tao Chen, Liao Changrui, D. N. Wang\*, **Yiping Wang**, "Passively mode-locked fiber laser by using monolayer chemical vapor deposition of graphene on D-shaped fiber," Applied Optics 53(13), 2828-2832, 2014 (**JCR 三区, IF=1.689**)

## 2013 年度

- [28] Yiping Wang\*, Changrui Liao, Xiaoyong Zhong, Jiangtao Zhou, Yingjie Liu, Zhengyong Li, Guanjun Wang; Kaiming Yang , Long period fiber gratings written in photonic crystal fibers by use of CO<sub>2</sub> laser, Photonic Sensors, 3(3), 193-201, 2013
- [29] Yiping Wang\*, Changrui Liao, Jiangtao Zhou, Yinjie Liu, Zhengyong Li, Xiaoyong Zhong, Fabrications and applications of fiber gratings based on microstructured optical fibers, J. Shenzhen University Science and Engineering, 30, 23-29, 2013

## 2012 年度

- [30] Yiping Wang\*, H. Bartelt, M. Becker, S. Brueckner, J. Bergmann, J. Kobelke, and M. Rothhardt, "Fabrications of Fiber Bragg Gratings Written in Photonic Crystal Fibers," Sensor Letters. 10(7), 1382-1386, 2012. (**JCR 四区, IF=0.517**)

## ★ 会议论文：(37 篇，其中大会报告 1 篇、特邀报告 16 篇)

- [1] Yiping Wang, 主办国际会议“Progress in Electromagnetics Research Symposium (PIERS)”的 Optical Fiber Sensing Devices 分会, Aug. 25-28, 2014, Guangdong, China.
- [2] Yiping Wang\*, Changrui Liao, Shen Liu, “High-sensitive optical sensors based on in-fiber air bubbles,” Session 2P9b, SC3: Ultrasensitive Optical Sensors, Progress In Electromagnetics Research Symposium (PIERS2014), Guangzhou, China, Sep. 2014. (**Invited**)
- [3] Yiping Wang\*, Optical fiber interference devices and sensing applications, China International Optoelectronic Conference (CIOEC), Sep. 2-3, 2013, Shenzhen, China (**Invited**)
- [4] Yiping Wang\*, Changrui Liao, Shen Liu, Zhengyong Li, and Jiangtao Zhou, In-fiber interferometer sensing devices and applications, The 6th Advanced Optical Methods Workshop, Shenzhen, China. Jul. 14-16, 2014. (**Invited**)
- [5] Yiping Wang,\* Changrui Liao, Shen Liu, Zhengyong Li, and Jiangtao Zhou, Optical sensing applications of in-fiber interferometers, The OSA Topical Conference: “AOM 2014–The 4<sup>th</sup> Advances in Optoelectronics and Micro/nano-optics”, Sep. 17-20, 2014, Xi'an, China. (**Invited**)
- [6] Yiping Wang,\* Changrui Liao, Shen Liu, Jiangtao Zhou, and Zhengyong Li, High-sensitive optical sensors based on in-fiber interferometers, Photonics Asia2014, Proc. of SPIE 9279-16, Oct. 9-11, 2014. Beijing China. (**Invited**)
- [7] Yiping Wang\*, “In-fiber microstructure devices and sensing applications,” 2014 年中国光纤传感学术会议暨产业化论坛, 2014 年 9 月 22-25, 大连理工大学, 大连. (**特邀报告**)
- [8] 王义平, 基于飞秒激光微加工和电弧放电的光纤干涉仪传感器, 第三届国际光纤陀螺与光纤传感技术及应用研讨会, 2014 年 5 月 13-15 日, 北京航天航空大学, 北京. (**特邀报告**)
- [9] 王义平, 光纤传感技术, 2014 年全国高校机械工程测试技术研究会学术年会, 2014 年 8 月 22-24 日, 深圳大学, 深圳. (**特邀报告**)
- [10] 王义平, 光纤干涉传感器件及应用, 第九届全国光子学学术会议暨中国光学学会纤维光学与集成光学专委会成立 30 周年大会, 2014 年 11 月 7-9 日, 电子科技大学, 成都. (**特邀报告**)
- [11] Yiping Wang\* , Shen Liu, Changrui Liao, Zhengyong Li, Qiao Wang, Guolu Yin, Jun He, Bing Sun, Jing Zhao, Jian Tang, "Temperature-insensitive strain sensor based on in-line Fabry-Perot interferometer," Proc. SPIE 9157, 23rd International Conference on Optical Fibre Sensors, 915725, Santander, Spain. Jun 2-6, 2014.
- [12] Guolu Yin, Yiping Wang\*, Changrui Liao, Jiangtao Zhou, Xiaoyong Zhong, Shen Liu, Qiao Wang, Zhengyong Li, Bing Sun, Jun He and Guanjun Wang, "Improved arc discharge technique for inscribing compact long period fiber gratings ", Proc. of SPIE 9157, 23rd International Conference on Optical Fibre Sensors, 91577X, Santander, Spain. Jun 2-6, 2014.
- [13] Changrui Liao, Lei Xu, Yiping Wang\*, D. N. Wang, Qiao Wang, Zhengyong Li, Xiaoyong Zhong, Jiangtao Zhou and Yingjie Liu, "Tunable phase-shifted FBG based on an in-grating bubble ", Proc. of SPIE 9157, 23rd International Conference on Optical Fibre Sensors, 915778, Santander, Spain. Jun 2-6,

2014.

- [14] Changrui Liao, Lei Xu, **Yiping Wang\***, Shen Liu, Zhengyong Li, and Qiao Wang, "Silica diaphragm based fiber Fabry-Perot interferometric pressure sensor," 2014 年中国光纤传感学术会议暨产业化论坛, 口头报告, 大连, 2014 年 9 月.
- [15] Zhengyong Li, Changrui Liao, **Yiping Wang\***, Xiaopeng Dong, Shen Liu, Kaiming Yang, Qiao Wang, and Jiangtao Zhou, "Mach-Zehnder interferometer based on twin-core fiber for refractive index sensing," 2014 年中国光纤传感学术会议暨产业化论坛, 张贴报告 (Poster-36), 大连, 2014 年 9 月.
- [16] Shen Liu, **Yiping Wang\***, Changrui Liao, Jun He, Zhengyong Li, and Kaiming Yang, "Rectangle air bubble created in a fiber for strain sensing application," 2014 年中国光纤传感学术会议暨产业化论坛, 张贴报告 (Poster-37), 大连, 2014 年 9 月.
- [17] Bing Sun, **Yiping Wang\***, Changrui Liao, Guolu Yin, Jiangtao Zhou, Jian Tang, and Shen Liu, "Miniature fiber-tip Fabry-Perot sensor for simultaneous measurement of pressure and temperature," 2014 年中国光纤传感学术会议暨产业化论坛, 张贴报告 (Poster-38), 大连, 2014 年 9 月.
- [18] Goulu Yin, **Yiping Wang\***, Changrui Liao, Xiaoyong Zhong, and Jian Tang, "Improved arc discharge technique for inscribing long period fiber gratings in SMF, PCF and PBF," 2014 年中国光纤传感学术会议暨产业化论坛, 张贴报告 (Poster-39), 大连, 2014 年 9 月.
- [19] Jing Zhao, Guolu Yin, **Yiping Wang\***, Junle Qu, Changrui Liao, Shen Liu, Jun He, Guanjun Wang, Xizheng Xu, Jiangtao Zhou, Xiaoyong Zhong, and Zhengyong Li, "Simultaneous measurement of strain and temperature based on side-polished fiber with surface scratches," 2014 年中国光纤传感学术会议暨产业化论坛, 张贴报告 (Poster-40), 大连, 2014 年 9 月.
- [20] Xiaoyong Zhong, **Yiping Wang\***, Changrui Liao, Shen Liu, Jian Tang, Qiao Wang, Jing Zhao, and Kaiming Yang, "Inflated long period fiber grating inscribed in photonic crystal fiber for strain measurement," 2014 年中国光纤传感学术会议暨产业化论坛, 张贴报告 (Poster-41), 大连, 2014 年 9 月.
- [21] Changrui Liao, Lei Xu, **Yiping Wang\***, D.N. Wang, Shen Liu, Zhengyong Li, Xiaoyong Zhong, Jiangtao Zhou, Qiao Wang, Kaiming Yang, "Femtosecond laser micromachined Optical Fiber In-line Interferometers," Session 2A9, SC: Optical Fiber Sensing Devices, Progress In Electromagnetics Research Symposium (PIERS2014), Guangzhou, China, 2014. (**Invited**)
- [22] Yingjie Liu, **Yiping Wang\***, Bing Sun, Changrui Liao, "Compact tunable multibandpass filters based on liquid-filled photonic crystal fibers," Session 2A9, SC: Optical Fiber Sensing Devices, Progress In Electromagnetics Research Symposium (PIERS2014), Guangzhou, China, 2014.
- [23] Zhengyong Li, **Yiping Wang\***, Changrui Liao, "Temperature-insensitive Refractive Index Sensor Based on In-fiber Michelson Interferometer," Session 2A9, SC: Optical Fiber Sensing Devices, Progress In Electromagnetics Research Symposium (PIERS2014), Guangzhou, China, 2014.
- [24] 王义平, 光纤微加工制备微纳光子器件及应用, 广东省光学学会 2013 年学术交流大会, 2013 年 12 月 13~15 日, 中山市. (**大会报告**)
- [25] 王义平, 微结构光纤器件的制备技术和应用, 2013 年中国光学学会学术大会, 2013 年 8 月 15~18 日, 国防科技大学, 长沙市中. (**特邀报告**)
- [26] **Yiping Wang\***, Changrui Liao, Xiaoyong Zhong, Zhengyong Li, Yingjie Liu, Jiangtao Zhou, and Kaiming Yang, "Selective-fluid-filled photonic crystal fibres and applications", Proc. of SPIE Vol. 8914, Article number: UNSP 89140J, 2013, 5th International Symposium on Photoelectronic Detection and Imaging Technology and Applications (ISPD1 2013), June 2013, Beijing, China. (**Invited**)
- [27] **Yiping Wang\***, Hartmut Bartelt, Jens Kobelke, Wolfgang Ecke, Reinhardt Willsch, Changrui Liao, Xiaoyong Zhong, Zhengyong Li, Jiangtao Zhou and Yingjie Liu, "Optical attenuators based on fluid-filled microstructured optical fibers", 2013 Optical Fiber Sensor Conference in China, May 2013, Hefei, China. (**Invited**)
- [28] **Yiping Wang\***, Microstructuredoptical fiber devices and sensing applications, China International Optoelectronic Conference (CIOE), Sep. 4-7, 2013, Shenzhen, China (**Invited**)
- [29] **Yiping Wang\***, Hartmut Bartelt, Jens Kobelke, Wolfgang Ecke, Reinhardt Willsch, Changrui Liao, Xiaoyong Zhong, Zhengyong Li, Jiangtao Zhou, and Yingjie Liu, "Optical attenuators based on fluid-filled photonic crystal fibers", Asia Communications and Photonics Conference (ACP2013),

- [30] Yiping Wang\*, Wei Jin, Dongning Wang, Changrui Liao, Xiaoyong Zhong, Zhengyong Li, Jiangtao Zhou, and Yingjie Liu, "Long period fiber gratings written in photonic crystal fibers by CO<sub>2</sub> laser", Prof. of SPIE Vol. 8924, Article number: 89243C, 2013, 4th Asia-Pacific Optical Sensors Conference (APOS), Oct. 2013, Wuhan, China.
- [31] Jiangtao Zhou, Changrui Liao, Yiping Wang\*, Kaiming Yang, Xiaoyong Zhong, Zhengyong Li, Yingjie Liu, and Guangjun Wang, "Intensity-modulated strain sensor based on fiber Mach-Zehnder interferometer employing core-offset," Prof. of SPIE Vol. 8924, Article number: 89240X, Fourth Asia Pacific Optical Sensors Conference (APOS), Wuhan, China, 2013.
- [32] C. R. Liao, D. N. Wang, M. Wang, M. H. Yang, Yiping Wang\*, "Fiber in-line Michelson interferometer for refractive index sensing," Prof. of SPIE Vol. 8924, Article number: 89240Q, Fourth Asia Pacific Optical Sensors Conference (APOS), Wuhan, China, 2013.
- [33] Guanjun Wang, Yiping Wang\*, Changrui Liao, Jiangtao Zhou, "A novel bio-detecting chip based on the opened fiber surface plasmon enhancement mechanism," Prof. of SPIE Vol. 8924, Article number: 892420, Fourth Asia Pacific Optical Sensors Conference (APOS), Wuhan, China, 2013.
- [34] 周江涛, 王义平\*, 廖常锐, "Temperature-insensitive Strain Sensor based on Fiber in-line Mach-Zehnder Interferometer," 2013 年中国光学年会, OJ1307010469, 口头报告, 2013 年 8 月.
- [35] 钟晓勇, 王义平\*, 廖常锐, "基于光子晶体光纤的 Bragg 光栅写入技术", 2013 年中国光学年会, 口头报告, 2013 年 8 月.
- [36] Yiping Wang\*, Optical fiber gratings written in Microstructured optical fibers, Photonics Global Conference 2012 (PGC2012), 13-16 Dec. 2012, Singapore. (**Invited**)
- [37] Yiping Wang\*, In-Fiber gratings written in photonic crystal fibers, International Conference on Optical Fiber Sensing Technology and Its Application on Smart Grid, 13-15 Oct. 2012, Nanjing, China. (**Invited**)



OPEN

# High-sensitivity strain sensor based on in-fiber rectangular air bubble

SUBJECT AREAS:

FIBRE OPTICS AND  
OPTICAL  
COMMUNICATIONS

IMAGING AND SENSING

Received  
23 September 2014Accepted  
4 December 2014Published  
5 January 2015

Correspondence and requests for materials should be addressed to  
Y.W. (ypwang@szu.edu.cn) or J.Q. (jlqu@szu.edu.cn)

\* These authors contributed equally to this work.

Shen Liu\*, Kaiming Yang\*, Yiping Wang, Junle Qu, Changrui Liao, Jun He, Zhengyong Li, Guolu Yin, Bing Sun, Jiangtao Zhou, Guanjun Wang, Jian Tang & Jing Zhao

Key Laboratory of Optoelectronic Devices and Systems of Ministry of Education and Guangdong Province, College of Optoelectronic Engineering, Shenzhen University, Shenzhen 518060, China.

We demonstrated a unique rectangular air bubble by means of splicing two sections of standard single mode fibers together and tapering the splicing joint. Such an air bubble can be used to develop a promising high-sensitivity strain sensor based on Fabry-Perot interference. The sensitivity of the strain sensor with a cavity length of about 61  $\mu\text{m}$  and a wall thickness of about 1  $\mu\text{m}$  was measured to be up to 43.0 pm/ $\mu\epsilon$  and is the highest strain sensitivity among the in-fiber FPI-based strain sensors with air cavities reported so far. Moreover, our strain sensor has a very low temperature sensitivity of about 2.0 pm/ $^{\circ}\text{C}$ . Thus, the temperature-induced strain measurement error is less than 0.046  $\mu\epsilon/\text{ }^{\circ}\text{C}$ .

**H**ighly sensitive strain measurements by use of optical fiber sensors are very attractive in many applications such as structure health monitoring, aerospace, and nanotechnology<sup>1–3</sup>. Such a measurement can be realized by use of fiber-device-based schemes, e.g. fiber in-line interferometers, fiber Bragg gratings (FBGs), and long period fiber gratings (LPFGs). The measured strain sensitivity was typically less than 7.0 pm/ $\mu\epsilon$  for a fiber Mach-Zehnder interferometer<sup>4,5</sup>, about 2.0 pm/ $\mu\epsilon$  for an FBG<sup>6,7</sup>, and about 10 pm/ $\mu\epsilon$  for an LPFG<sup>8–11</sup>. In addition, the cross-sensitivity between strain and temperature was hardly overcome in these sensor schemes. Recently, Fabry-Perot interferometers (FPIs) based on an in-fiber air cavity were proved to be outstanding in lots of sensing applications, such as strain measurements<sup>12–19</sup>, refractive index (RI) measurements<sup>20,21</sup> and pressure measurements<sup>22,23</sup>, due to the advantages of simple configuration, high sensitivity, compact size, and low temperature cross-sensitivity. However, it is very difficult to directly create an air cavity in the fiber. A few complex methods have been proposed to create in-fiber air cavities by use of silica hollow tube<sup>18</sup> or photonic crystal fibers (PCFs)<sup>14,17,21</sup>, direct micromachining using focused femtosecond laser beam<sup>5,13,20</sup>, and assisted chemical etching<sup>24</sup>. The above-mentioned FPIs usually require special optical fibers, high-cost micro-machining equipment, or/and hazardous acid corrosion treatment. Recently, we reported a novel and simple technique for fabricating air-cavity-based FPIs that can be used to develop a strain sensor with a high sensitivity of up to 6.0 pm/ $\mu\epsilon$ <sup>19</sup>. The air cavity was created by use of a common commercial fusion splicer to splice together two sections of standard single mode fibers (SMFs) with easy pretreatment on the fiber ends.

In this paper, we demonstrated an improved technique to create a unique rectangular air bubble by means of splicing together two sections of SMF tapers. The rectangular air-bubble-based FPI with a cavity length of about 61  $\mu\text{m}$  exhibits a high strain sensitivity of 43.0 pm/ $\mu\epsilon$  around the wavelength of 1550 nm. Moreover, such a strain sensor has a very low temperature sensitivity of about 2.0 pm/ $^{\circ}\text{C}$ , where a lower temperature cross-sensitivity of 0.046  $\mu\epsilon/\text{ }^{\circ}\text{C}$  than that reported in ref. 19 was obtained. So the rectangular air-bubble-based FPI could be used to develop a promising high-sensitivity strain sensor with a low temperature sensitivity.

## Experiments

Fig. 1 illustrates the fabrication process of our proposed rectangular air bubble in a SMF, which involves six steps. In step 1, as shown in Fig. 1(I), two sections of SMFs (Corning SMF-28) with cleaved ends were placed in the left and right fiber holds of a commercial fusion splicer (Fujikura FSM-60S). In step 2, as shown in Fig. 1(II), the two fiber ends were reshaped into hemispherical and smooth ends via electrical arc discharge in order to enlarge the surface area of the fiber ends for coating sufficient liquid on the fiber ends. In step 3, as shown in Fig. 1(III), the two hemispherical fiber ends were immersed into a commercial refractive index matching liquid (Cargille Labs, <http://www.cargille.com>) to coat a liquid film on the end surface. The two sections of SMFs with liquid-coated ends were again placed in the left and right fiber holders of the fusion splicer. In step 4, as shown in Fig. 1(IV), the left and right fiber ends were moved toward each other until an overlap of  $2d_0$  was achieved at the touching region of the

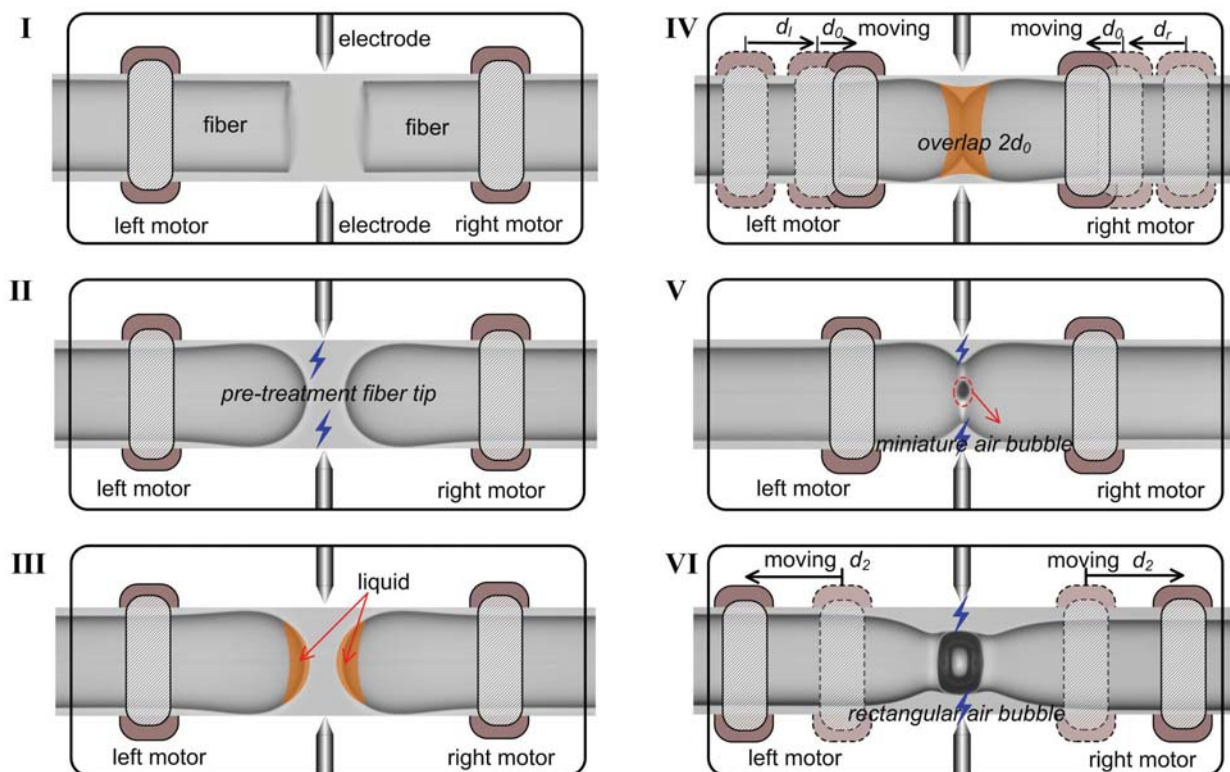


Figure 1 | Schematic diagrams of fabrication process of in-fiber FPI based on an air bubble.

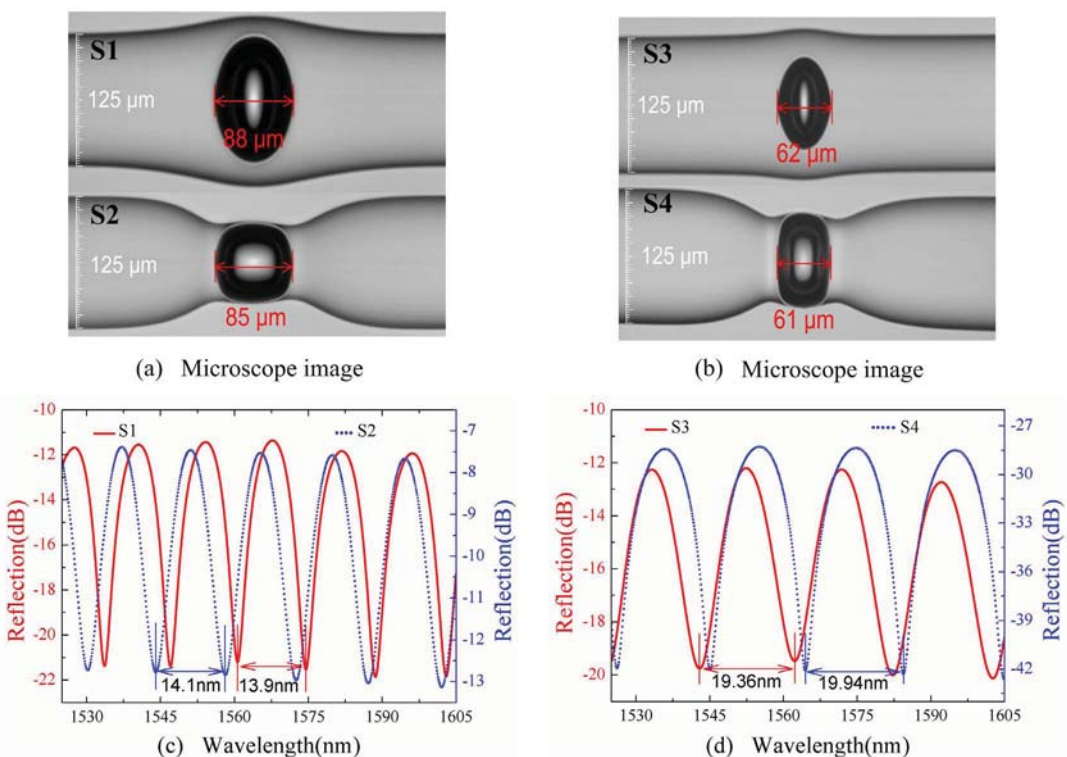
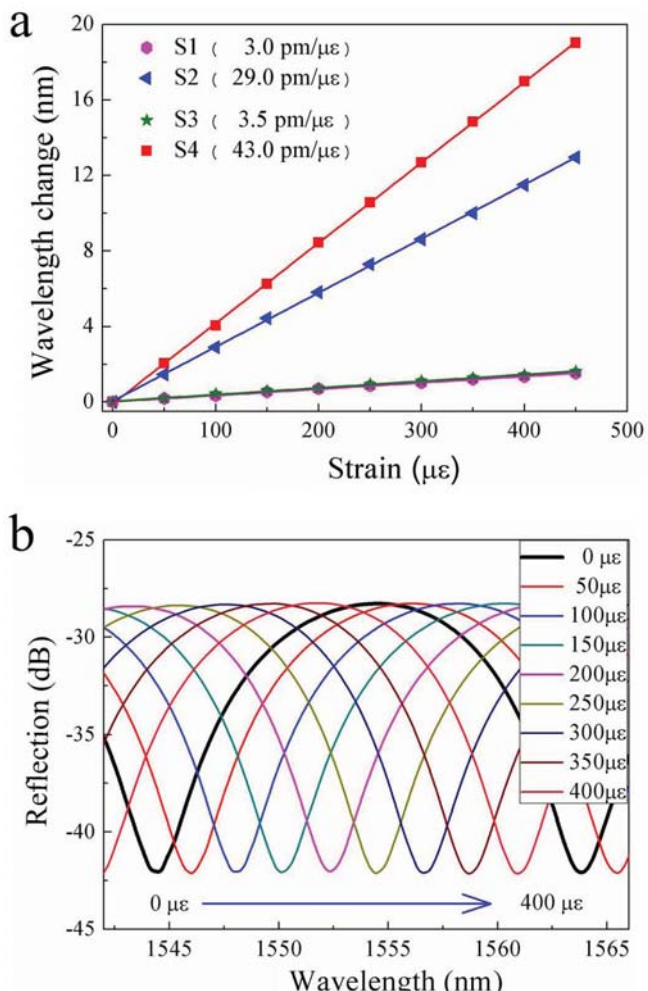


Figure 2 | Four in-fiber air bubble samples. (a) and (b) Microscope images of the created elliptical air bubbles, i.e. S1 and S3, and the created rectangular air bubbles, i.e. S2 and S4, with a cavity length of about 88, 62, 85 and 61  $\mu\text{m}$ , respectively; (c) and (d) The corresponding reflection spectra of the air-cavity-based FPI samples.



**Figure 3 | Strain response of the four air bubble samples.** (a) Wavelength change of the interference fringe around 1550 nm as a function of tensile strain applied to the air-cavity-based FPI samples: (●) S1, (△) S2, (★) S3 and (■) S4, with a cavity length of 88, 85, 62 and 61  $\mu\text{m}$ , respectively; (b) Reflection spectrum evolution of the rectangular air bubble sample, i.e. S4, while the tensile strain increases from 0 to 400  $\mu\epsilon$ .

two fiber ends by means of carefully controlling the movement of the left and right motors of the fusion splicer, where  $d_l$  and  $d_r$  indicate the moved distance of the left and right fiber ends, respectively, before the two fiber ends touched, and  $d_0$  indicates the moved distance of each fiber end after the two fiber ends touched. It should be noted that the value of “ $d_0$ ” here is less than that of “ $d$ ” reported in Ref. 19, which means a smaller axial stress was applied to the fiber ends at the touching region. In step 5, the liquid-coated fiber ends were aligned with each other and then spliced together via electrical arc discharge with a fusion current of 18 mA and a fusion time of 1000 ms. Consequently, as shown in Fig. 1(V), a miniature air bubble with a diameter of about 10  $\mu\text{m}$  was formed in the spliced region with an abrupt taper shape, resulting from the evaporation of the liquid coated on the fiber end faces and the fusion of silica during arc discharge. In step 6, the left and right fiber holders were moved backward to each other with a distance of  $d_2$  in order to apply an axial tensile stress to the air bubble region located in the middle of fused taper, as shown in Fig. 1(VI). And then, an electrical arc discharge with a fusion current of 18 mA and a fusion time of 750 ms was implemented at the middle of air bubble. During the arc discharge, the silica wall of the air bubble melted due to the arc-discharge-induced high temperature and the air in the bubble thermally

expanded, resulting in a rectangular air bubble due to the pre-applied axial tensile stress, as shown in Fig. 1(VI). And the thickness of the silica wall was gradually decreased by means of repeating the step 6. Using the method above, we have successfully fabricated a few in-fiber rectangular air bubble samples. In the whole fabrication process, only a common fusion splicer was employed, and no additional device was required.

To investigate the strain sensitivity difference between the rectangular and elliptical air bubbles, as shown in Fig. 2, two rectangular air bubble sample, i.e. S2 and S4, were created by the technique above, and another two elliptical air bubbles, i.e. S1 and S3, were created by the technique reported previously in ref. 19. Each pair of the rectangular and elliptical air bubbles, e.g. S1 and S2, or S3 and S4, has an approximate cavity length of about 88  $\mu\text{m}$  (85  $\mu\text{m}$ ) or 62  $\mu\text{m}$  (61  $\mu\text{m}$ ) to maintain similar measured parameters. The wall thickness of S1, S2, S3 and S4 was measured to be about 23, 1, 28, and 1  $\mu\text{m}$ , respectively. A broadband light source, a 3-dB fiber coupler, and an optical spectrum analyzer (YOKOGAWA AQ6370C) with a resolution of 0.01 nm were employed to measure the reflection spectra of these two pairs of air bubbles. As shown in Figs. 2(c) and 2(d), clear interference fringes were observed in the reflection spectra of the air bubble samples, S1, S2, S3 and S4. And the corresponding free spectra range (FSR) of the interference fringes around 1550 nm was measured to be 13.9, 14.1, 19.36 and 19.94 nm, respectively. According to the measured FSR above and the equation of  $FSR = \lambda^2/(2nL)$ , the cavity length,  $L$ , of the four samples were calculated to be 85.2, 86.4, 62.0 and 60.2  $\mu\text{m}$ , respectively, which agrees well with the values measured from Figs. 2(a) and 2(b).

## Results and discussion

One end of the air bubble sample was fixed, and another end was attached to a translation stage with a resolution of 10  $\mu\text{m}$ . A tensile strain was applied to the air bubble sample by moving the translation stage away from the fixed one at room temperature. The wavelength shift of the fringe dip around 1550 nm was measured while the tensile strain was increased from 0 to 450  $\mu\epsilon$  with a step of 50  $\mu\epsilon$ . As shown in Fig. 3, the fringe dips of the four samples shifted linearly toward a longer wavelength with the increased tensile strain. The strain sensitivity of S1, S2, S3 and S4 was calculated to be 3.0, 29.0, 3.5 and 43.0  $\text{pm}/\mu\epsilon$ , respectively, by applying a linear fitting of the experimental data. So, the strain sensitivity of the rectangular air bubble samples, i.e. S2 and S4, is almost nine and twelve times higher than that of the elliptical air bubbles, i.e. S1 and S3, respectively, which indicates that the rectangular air bubble can significantly enhance the strain sensitivity of the air-cavity-based FPI.

In order to study the stress distribution and the deformation of the air cavity under an applied tensile strain, simulation models were established by use of a commercial software, i.e. ANSYS, and the measured sizes of the four air bubble samples were illustrated in Figs. 2(a) and 2(b). Fig. 4 illustrate the three- and two dimensional stress contours of the four air bubble samples, i.e. S1, S2, S3, and S4, with a tensile strain of 1  $\mu\epsilon$ , which indicates the calculated stress distribution in different parts of each air bubble sample. While the applied tensile strain increases, as shown in Fig. 5(a), the calculated stress at the ‘A’ point on the outside surface of the two rectangular air bubbles, i.e. S2 and S4, increases linearly with a slope of 23.54 and 46.34 MPa/ $\mu\epsilon$ , respectively, in contrast, that of the two elliptical air bubbles, i.e. S1 and S3, hardly increased with a very low slope of 0.72 and 1.00 MPa/ $\mu\epsilon$ , respectively. So the stress distributed on the silica wall of an in-fiber air bubble sharply increases with the applied tensile strain in case such an air bubble has a rectangular shape and is created in the fused taper. Moreover, while the applied tensile strain increases, as shown in Fig. 5(b), the calculated cavity of the rectangular air bubble samples, i.e. S2 and S4, sharply lengthened with a slope of 1.87, and 3.08 nm/ $\mu\epsilon$ , respectively, in contrast, that of the elliptical air bubble samples, i.e. S1 and S3, slowly lengthened

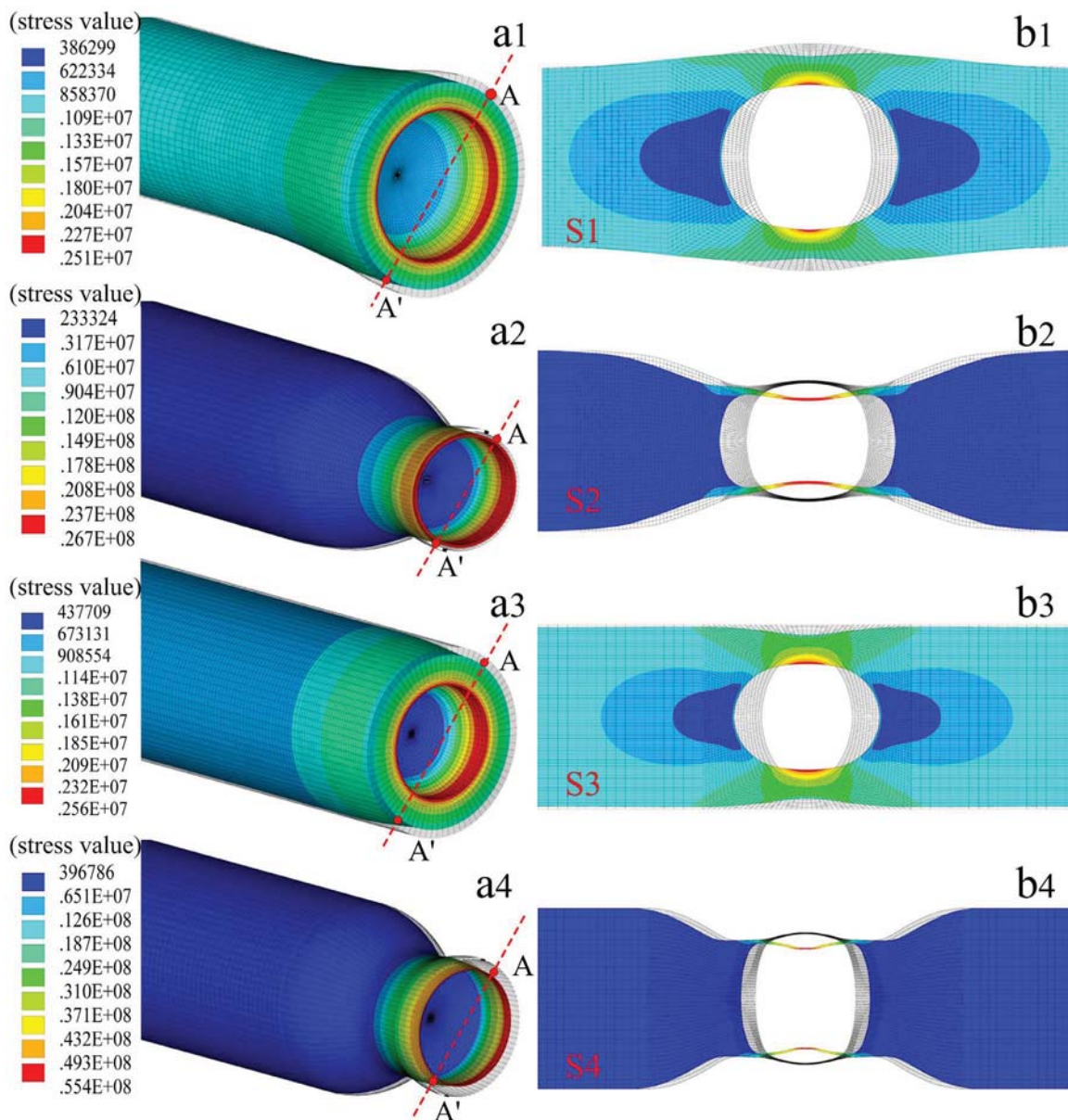


**Figure 4 | Stress distribution of the four air bubble samples, i.e. S1, S2, S3, and S4, under an applied tensile strain of 1  $\mu\epsilon$ .** (a1), (a2), (a3) and (a4) Three-dimensional stress contours and (b1), (b2), (b3), and (b4) Two-dimensional stress contours on the A–A' section plane, where Young's modulus of silica is 73 Gpa, Poisson's ratio is 0.17, silica density is 2700 Kg/m<sup>3</sup>.

with a low slope of 0.20 and 0.25 nm/ $\mu\epsilon$ , respectively. So the calculated cavity length sensitivity, i.e. strain sensitivity, of the rectangular air bubble samples, i.e. S2 and S4, is nine and twelve times higher than that of the elliptical air bubble samples, i.e. S1 and S3, respectively, which agrees well with the measured strain sensitivities, as shown in Fig. 3(a).

It was very difficult to measure the practical perpendicular deformation of the air bubble sample during applying a tensile strain. So we simulated the perpendicular deformation of the rectangular air bubble sample (S4) with a tensile strain. The perpendicular deformation contours on the cross-section of S4 with a tensile strain of 500  $\mu\epsilon$  is shown in Fig. 6 (a), where the dotted and solid line in the inset illustrates the outline of the air bubble wall before and after the tensile strain was applied, respectively. It can be seen from the inset of Fig. 6(a) that a maximum perpendicular deformation of 0.821  $\mu\epsilon$  occurred at the A (A') point of S4. Moreover, while the applied tensile strain increases from 0 to 500  $\mu\epsilon$ , as shown in Fig. 6 (b), the calcu-

lated perpendicular deformation at the A (A') point of S4 increased linearly with a slope of 1.63 nm/ $\mu\epsilon$ .

As shown in Fig. 7 (a), four types of in-fiber air bubble models with a same cavity length of 61  $\mu\text{m}$  was designed to investigate quantitatively the dependency of their strain sensitivity on the wall thickness and the cavity shape, where the tapered sections of Model-I and Model-III are with a same size. We calculated the cavity length change of each air bubble model (I, II, III and IV) with different wall thickness (■) 1  $\mu\text{m}$ , (●) 5  $\mu\text{m}$ , (▲) 10  $\mu\text{m}$ , (▼) 15  $\mu\text{m}$  and (◀) 20  $\mu\text{m}$  while an applied tensile strain increases from 0 to 500  $\mu\epsilon$ . As shown in Fig. 8(a), the cavity length sensitivity of the rectangular air bubble with a tapered section (I) and a wall thickness of 1, 5, 10, 15, and 20  $\mu\text{m}$  is 3.01, 0.91, 0.55, 0.38 and 0.31  $\mu\text{m}/\mu\epsilon$ , respectively. As shown in Fig. 8(b), the cavity length sensitivity of the rectangular air bubble without a tapered section (II) and with a wall thickness of 1, 5, 10, 15, and 20  $\mu\text{m}$  is 1.24, 0.52, 0.35 and 0.26  $\mu\text{m}/\mu\epsilon$ , respectively. As shown in Fig. 8(c), the cavity length sensitivity of the elliptical air

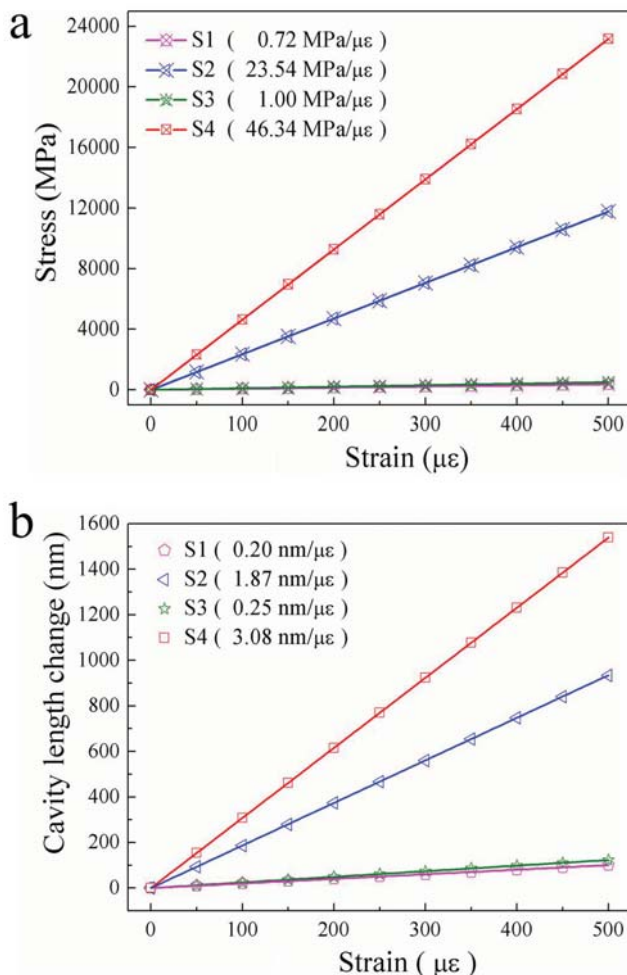


**Figure 5 |** Numerical simulation for the stress concentration and the cavity length change of the four air bubble samples under an applied tensile strain. (a) Calculated stress at the ‘A’ point on the outside surface of each air bubble versus the applied strain, (—○—) S1, (—×—) S2, (—★—) S3, and (—■—) S4; (b) Calculated cavity length change of each air bubble versus the applied strain, (○) S1, (×) S2, (★) S3, and (■) S4.

bubble with a tapered section (III) and a wall thickness of 1, 5, 10, 15, and 20  $\mu\text{m}$  is 2.64, 0.87, 0.52, 0.36 and 0.29  $\mu\text{m}/\mu\epsilon$ , respectively. As shown in Fig. 8(d), the cavity length sensitivity of the elliptical air bubble without a tapered section (IV) and with a wall thickness of 1, 5, 10, 15, and 20  $\mu\text{m}$  is 1.14, 0.48, 0.32, 0.24 and 0.20  $\mu\text{m}/\mu\epsilon$ , respectively.

The cavity length sensitivities of each type of air bubble model above versus different wall thickness are summarized in Fig. 7(b), where the corresponding strain sensitivity (left axis), i.e. the wavelength sensitivity of the interference fringes, was calculated by use of Fabry-Perot interference principle, i.e.  $d\lambda/d\epsilon = (\lambda_m/L)dL/d\epsilon$ , where  $\lambda_m$  is the wavelength of the  $m^{\text{th}}$  order interference dip<sup>20</sup>. As shown in Fig. 7 (b), (1) for each type of air bubbles, the wall thickness is smaller, the strain sensitivity is higher; (2) both rectangular and elliptical air bubbles with a tapered section exhibits a much higher strain sensitivity than those without a tapered section; (3) the rectangular air bubble with or without a tapered section exhibits a litter higher strain sensitivity than the elliptical air bubble with or without a tapered section, respectively. So the strain sensitivity enhancement of the air bubble owes to the reduction of the wall thickness, rather than the shape of the air cavity. In our experiments, it was to reduce the wall thickness of the air cavity and thus enhance its strain sensitivity that

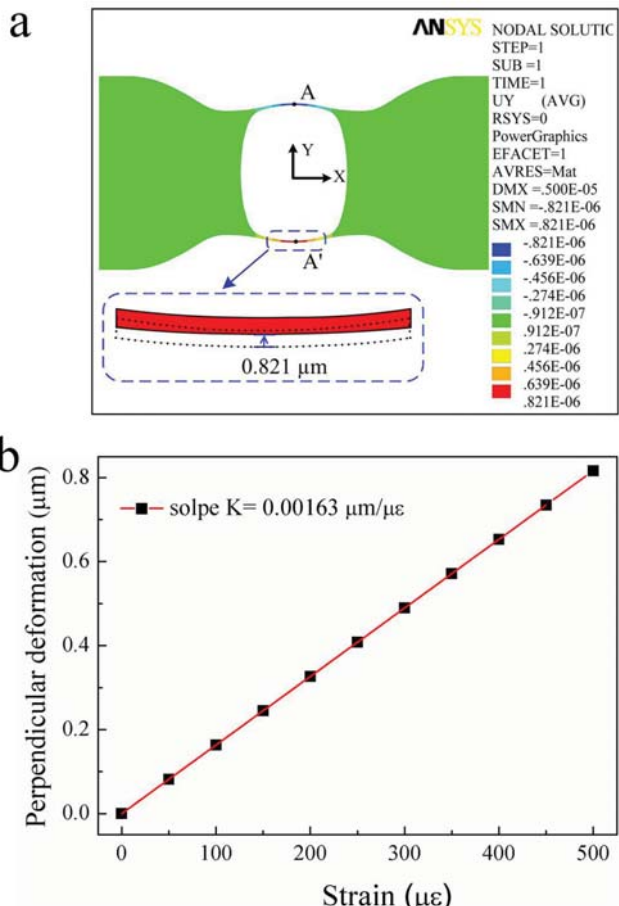


**Figure 6 |** Numerical simulation for the perpendicular deformation of the sample (S4). (a) Simulated perpendicular deformation on the A–A' section plane, illustrated in Fig. 4 (a4), of the sample (S4) with a tensile strain of 500  $\mu\epsilon$ , where the maximum perpendicular deformation is 0.821  $\mu\text{m}$ ; (b) Calculated perpendicular deformation of the sample (S4) versus an applied tensile strain from 0 to 500  $\mu\epsilon$ .

an elliptical air bubble was reshaped into a rectangle air bubble by means of tapering the air cavity section.

A few types of in-fiber FPI-based strain sensors with different air cavities and their sensitivities were presented in Table 1. It can be seen from Table 1 that, to the best of our knowledge, our current strain sensor exhibits the highest sensitivity of 43.0 pm/ $\mu\epsilon$ , which owes that our proposed sensor is based on a rectangular air bubble with a very thin wall thickness of about 1  $\mu\text{m}$  and a tapered section.

Temperature response of the rectangular air bubble sample, i.e. S4, also was investigated by placing it into an electrical oven and gradually raising temperature from 25 to 100°C with a step of 10°C. As shown in Fig. 9, the dip wavelength of the interference fringe in the reflection spectrum of S4 slowly shifted linearly toward a longer wavelength with a low sensitivity of about 2.0 pm/°C. According to the strain and temperature sensitivity of the interference fringe, the temperature-induced strain measurement error is less than 0.046  $\mu\epsilon/\text{°C}$  in case no temperature compensation is done.

## Conclusions

A novel technique was demonstrated to fabricate a unique rectangular air bubble with a very thin wall thickness of about 1  $\mu\text{m}$  and a tapered section in an optical fiber. Such a rectangular air bubble can be used to develop a promising high-sensitivity strain sensor based on Fabry-Perot interference. The sensitivity of the strain sensor is up to 43.0 pm/ $\mu\epsilon$  and is the highest sensitivity among the in-fiber FPI-

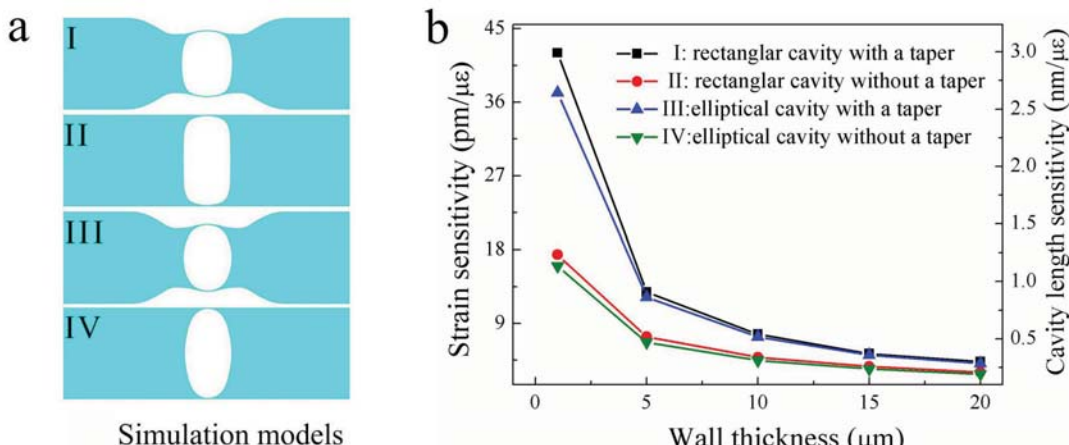


**Figure 7 | Numerical simulation for different types of in-fiber air bubbles.** (a) Four types of air bubble models with a same cavity length of 61 μm, I: a rectangular air bubble with a tapered section, II: a rectangular air bubble without a tapered section, III: an elliptical air bubble with a tapered section, and IV: an elliptical air bubble without a tapered section; (b) Strain sensitivity (Left axis), i.e. the wavelength sensitivity of the interference fringes, and cavity length sensitivity (Right axis) of the air bubbles (I, II, III and IV) with different wall thickness.

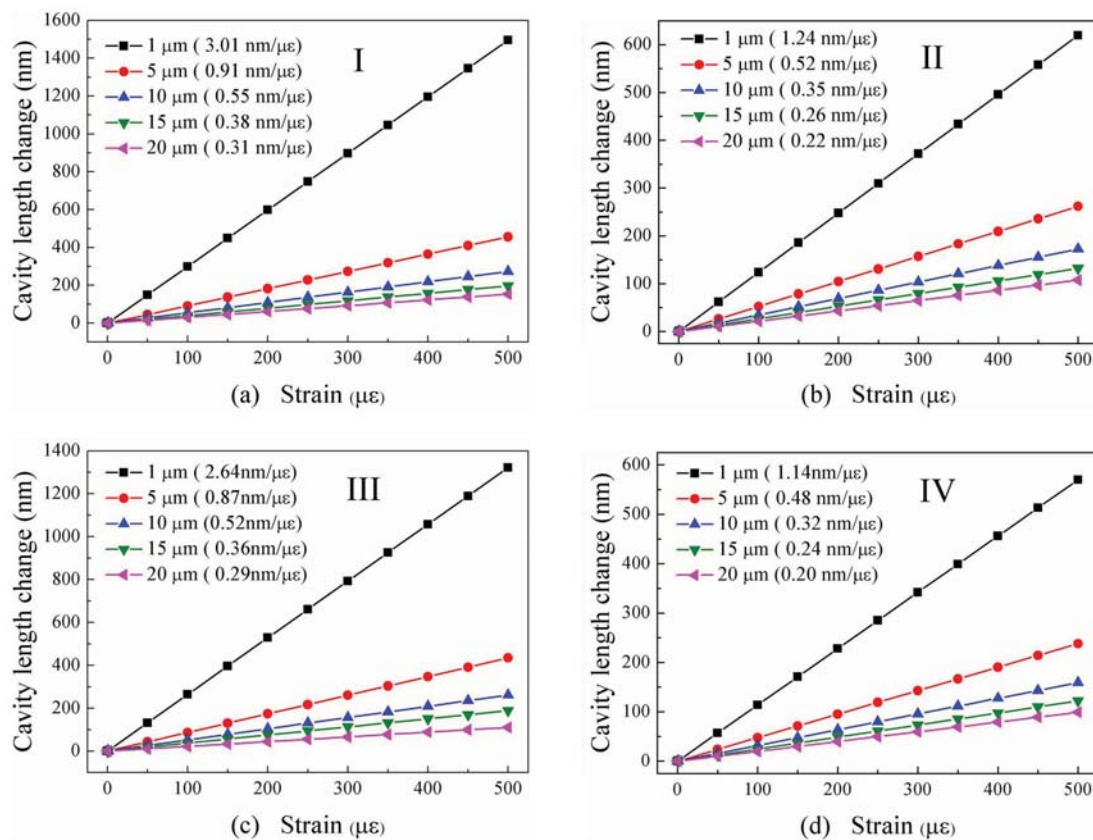


**Figure 8 | Calculated cavity length change of each air bubble model, i.e. (a) I,(b) II, (c) III and (d) IV, with different wall thickness (■) 1 μm, (●) 5 μm, (▲) 10 μm, (▼) 15 μm and (◆) 20 μm while the applied tensile strain increases from 0 to 500 με.**

**Table 1 | A few types of in-fiber FPI-based strain sensors with air cavities**

cavity structure	strain sensitivity	cavity size	reference
elliptical air bubble	6.0 pm/με	46 μm	Ref. 19
hollow-core ring PCF	15.4 pm/με	13 μm	Ref. 17
micro-bubble	4 pm/με	91 μm	Ref. 15
air hole	6 pm/με	80 μm	Ref. 13
spheroidal cavity+PCF	2.7 pm/με	58 μm	Ref. 14
spheroidal cavity	10.3 pm/με	10 μm	Ref. 16
rectangular air bubble	43 pm/με	61 μm	this work

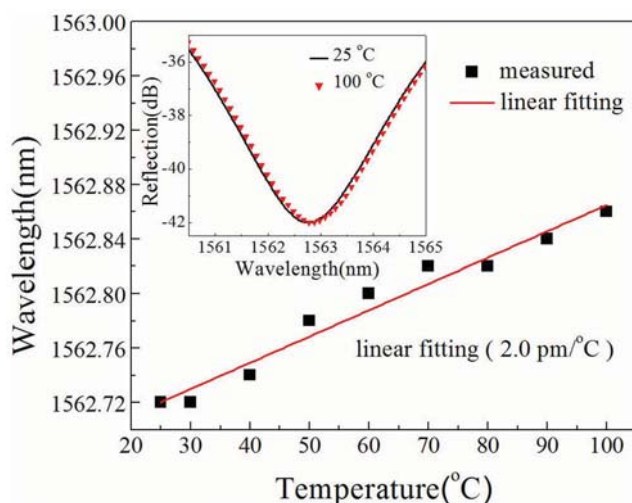


**Figure 9 | Wavelength shift of the interference dip at the wavelength of about 1560 nm of the sample S4 versus ambient temperature.** Inset: Reflection spectra of S4 at 25 and 100°C.

based strain sensors with air cavities reported so far. Moreover, such a strain sensor has a very low temperature sensitivity of about  $2.0 \text{ pm/}^{\circ}\text{C}$ , and therefore the cross-sensitivity between strain and temperature was reduced to a very low value of  $0.046 \mu\text{e/}^{\circ}\text{C}$ .

1. Wang, Y. Review of long period fiber gratings written by CO<sub>2</sub> laser. *J. Appl. Phys.* **108** (2010).
2. Zhu, T. *et al.* In-Line Fiber Optic Interferometric Sensors in Single-Mode Fibers. *Sensors* **12**, 10430–10449 (2012).
3. Islam, M. R. *et al.* Chronology of Fabry-Perot Interferometer Fiber-Optic Sensors and Their Applications: A Review. *Sensors* **14**, 7451–7488 (2014).
4. Hu, L. M. *et al.* Photonic Crystal Fiber Strain Sensor Based on Modified Mach-Zehnder Interferometer. *IEEE Photonics J.* **4**, 114–118 (2012).
5. Liao, C. R., Wang, D. N. & Wang, Y. Microfiber in-line Mach-Zehnder interferometer for strain sensing. *Opt. Lett.* **38**, 757–759 (2013).
6. Rao, Y. *et al.* Temperature-strain discrimination sensor using a WDM chirped in-fibre bragg grating and an extrinsic Fabry-Perot. *Chin. Phys. Lett.* **18**, 644–644 (2001).
7. Chen, C. *et al.* Sensitivity of photonic crystal fiber modes to temperature, strain and external refractive index. *Opt. Express* **16**, 9645–9653 (2008).
8. Wang, Y. P., Chen, J. P. & Rao, Y. J. Torsion characteristics of long-period fiber gratings induced by high-frequency CO<sub>2</sub> laser pulses. *J. Opt. Soc. Am. B-Opt. Phys.* **22**, 1167–1172 (2005).
9. Wang, Y. P. *et al.* A novel tunable gain equalizer based on a long-period fiber grating written by high-frequency CO<sub>2</sub> laser pulses. *IEEE Photonics Technol. Lett.* **15**, 251–253 (2003).
10. Wang, Y. P. *et al.* Highly sensitive long-period fiber-grating strain sensor with low temperature sensitivity. *Opt. Lett.* **31**, 3414–3416 (2006).
11. Liao, C. *et al.* Femtosecond Laser Inscribed Long-Period Gratings in All-Solid Photonic Bandgap Fibers. *IEEE Photonics Technol. Lett.* **22**, 425–427 (2010).
12. Rao, Y. J. *et al.* Simultaneous strain and temperature measurement of advanced 3-D braided composite materials using an improved EFPI/FBG system. *Opt. Lasers Eng.* **38**, 557–566 (2002).

13. Rao, Y. J. *et al.* Micro Fabry-Perot interferometers in silica fibers machined by femtosecond laser. *Opt. Express* **15**, 14123–14128 (2007).
14. Villatoro, J. *et al.* Photonic-crystal-fiber-enabled micro-Fabry-Perot interferometer. *Opt. Lett.* **34**, 2441–2443 (2009).
15. Duan, D. W. *et al.* Microbubble based fiber-optic Fabry-Perot interferometer formed by fusion splicing single-mode fibers for strain measurement. *Appl. Optics* **51**, 1033–1036 (2012).
16. Favero, F. C. *et al.* Spheroidal Fabry-Perot microcavities in optical fibers for high-sensitivity sensing. *Opt. Express* **20**, 7112–7118 (2012).
17. Ferreira, M. S. *et al.* Towards the control of highly sensitive Fabry-Perot strain sensor based on hollow-core ring photonic crystal fiber. *Opt. Express* **20**, 21946–21952 (2012).
18. Ferreira, M. S. *et al.* Spatial optical filter sensor based on hollow-core silica tube. *Opt. Lett.* **37**, 890–892 (2012).
19. Liu, S. *et al.* High-sensitivity strain sensor based on in-fiber improved Fabry-Perot interferometer. *Opt. Lett.* **39**, 2121–2124 (2014).
20. Liao, C. R., Hu, T. Y. & Wang, D. N. Optical fiber Fabry-Perot interferometer cavity fabricated by femtosecond laser micromachining and fusion splicing for refractive index sensing. *Opt. Express* **20**, 22813–22818 (2012).
21. Wang, Y. *et al.* Temperature-insensitive refractive index sensing by use of micro Fabry-Perot cavity based on simplified hollow-core photonic crystal fiber. *Opt. Lett.* **38**, 269–271 (2013).
22. Ma, J. *et al.* High-sensitivity fiber-tip pressure sensor with graphene diaphragm. *Opt. Lett.* **37**, 2493–2495 (2012).
23. Liao, C. *et al.* Sub-micron silica diaphragm-based fiber-tip Fabry-Perot interferometer for pressure measurement. *Opt. Lett.* **39**, 2827–2830 (2014).
24. Cibula, E. & Donlagic, D. In-line short cavity Fabry-Perot strain sensor for quasi distributed measurement utilizing standard OTDR. *Opt. Express* **15**, 8719–8730 (2007).

## Acknowledgments

This work was supported by National Natural Science Foundation of China (grant nos.61425007, 11174064, 61308027, and 61377090), Natural Science Foundation of SZU (grant no. 8010036401), Science & Technology Innovation Commission of Shenzhen/Nanshan (grants nos. KQCX20120815161444632, JCYJ20130329140017262, ZDSYS20140430164957664, KC2014ZDZJ0008A), and Distinguished Professors Funding from Shenzhen University and Guangdong Province Pearl River Scholars.

## Author contributions

S.L. and K.Y. performed experiments and analyzed the data. S.L. and K.Y. wrote the manuscript. S.L. and C.L. contributed to simulation analysis using software, i.e. ANSYS, and C.L. modified the manuscript. Y.W. and J.Q. were responsible for the overall design and oversight of the project. J.H., Z.L., G.Y., B.S., J.T.Z., G.W., J.T. and J.Z. gave scientific suggestions and intellectual input. All authors contributed to discussion and reviewed the manuscript.

## Additional information

**Competing financial interests:** The authors declare no competing financial interests.

**How to cite this article:** Liu, S. *et al.* High-sensitivity strain sensor based on in-fiber rectangular air bubble. *Sci. Rep.* **5**, 7624; DOI:10.1038/srep07624 (2015).

This work is licensed under a Creative Commons Attribution 4.0 International License. The images or other third party material in this article are included in the article's Creative Commons license, unless indicated otherwise in the credit line; if the material is not included under the Creative Commons license, users will need to obtain permission from the license holder in order to reproduce the material. To view a copy of this license, visit <http://creativecommons.org/licenses/by/4.0/>

# Temperature-insensitivity gas pressure sensor based on inflated long period fiber grating inscribed in photonic crystal fiber

Xiaoyong Zhong, Yiping Wang,\* Changrui Liao, Shen Liu, Jian Tang, and Qiao Wang

Key Laboratory of Optoelectronic Devices and Systems of Ministry of Education and Guangdong Province,

College of Optoelectronic Engineering, Shenzhen University, Shenzhen 518060, China

\*Corresponding author: [ypwang@szu.edu.cn](mailto:ypwang@szu.edu.cn)

Received January 16, 2015; revised March 13, 2015; accepted March 20, 2015;  
posted March 24, 2015 (Doc. ID 232588); published 0 MONTH 0000

We demonstrated an inflated long period fiber grating (I-LPFG) inscribed in a pure-silica photonic crystal fiber (PCF) for high-sensitivity gas pressure sensing applications. The I-LPFG was inscribed by use of the pressure-assisted CO<sub>2</sub> laser beam-scanning technique to inflate periodically air holes of a PCF along the fiber axis. Such an I-LPFG with periodic inflations exhibits a very high gas pressure sensitivity of 1.68 nm/MPa, which is one order of magnitude higher than that, i.e., 0.12 nm/Mpa, of the LPFG without periodic inflations. Moreover, the I-LPFG has a very low temperature sensitivity of 3.1 pm/°C due to the pure silica material in the PCF so that the pressure measurement error, resulting from the cross-sensitivity between temperature and gas pressure, is less than 1.8 Kpa/°C in the case of no temperature compensation. So the I-LPFG could be used to develop a promising gas pressure sensor, and the achieved pressure measurement range is up to 10 MPa. © 2015 Optical Society of America

*OCIS codes:* (060.5295) Photonic crystal fibers; (050.2770) Gratings; (060.2340) Fiber optics components; (060.2370) Fiber optics sensors.

<http://dx.doi.org/10.1364/OL.99.099999>

Over the past decade, various kinds of fiber optic gas pressure sensors such as Fabry–Perot interferometers (FPIs) [1–4], fiber Bragg gratings (FBGs) [5–8], and long-period fiber gratings (LPFGs) [9–12] have been extensively investigated and been widely used in the field industrial and environmental monitoring. Among them, LPFG-based gas-pressure sensors are of great interest owing to their easy fabrication, compact size, low cost, robustness, and immunity to electro-magnetic interference. Unfortunately, gas-pressure sensitivity of LPFG was usually very low, e.g., only 5.1 pm/bar in a Corning SMF-28 fiber [13] and 11.2 pm/bar in a photonic crystal fiber (PCF) [14], respectively. In addition, during the applications of LPFG-based gas pressure sensors, one of the main difficulties is the cross-sensitivity between the gas pressure and the temperature. For instance, the gas-pressure sensor based on a LPFG written in a SMF-28 fiber [13] and a boron co-doped optical fiber [15] exhibited a temperature sensitivity of 49.5 pm/°C and 0.72 nm/°C, respectively. Hence, the cross-sensitivity of the LPFG-based sensors limits their applications in the field of practical gas pressure monitoring.

In this report, we demonstrated the inscription of an inflated long-period fiber grating (I-LPFG) in a PCF by means of the pressure-assisted CO<sub>2</sub> laser beam-scanning technique to inflate periodically air holes along the fiber axis. Such an I-LPFG sensor exhibited a high gas-pressure sensitivity of up to 1.68 nm/Mpa, which is one order of magnitude higher than that reported previously in ref. [14]. The novel I-LPFG also exhibited an intensity-modulated gas-pressure sensitivity of 1.36 dB/Mpa. Moreover, a low temperature sensitivity of 3.1 pm/°C was achieved in the I-LPFG-based gas-pressure sensor, which can effectively reduce the cross-sensitivity between gas pressure and temperature.

An experiment setup, as shown in Fig. 1 reported in Ref. [16], was employed to write an inflated long-period

fiber grating (I-LPFG) by use of the pressure-assisted CO<sub>2</sub> laser beam-scanning technique to inflate periodically air holes of a PCF along the fiber axis. The pressure,  $P_s$ , required to avoid collapsing a hole in a PCF is related to the surface tension,  $\gamma$ , of the hole, which can be expressed as [17]:

$$P_s = 2\gamma/d, \quad (1)$$

where  $d$  is the hole diameter. For a given  $d$  and internal gas pressure  $P$ , the hole in a PCF will either inflate or collapse depending on whether  $P$  is higher or lower than  $P_s$  during CO<sub>2</sub> laser irradiation. And the rate of the hole inflation or collapse depends on the temperature of the glass and the magnitude of the pressure  $P$ . For an inflated

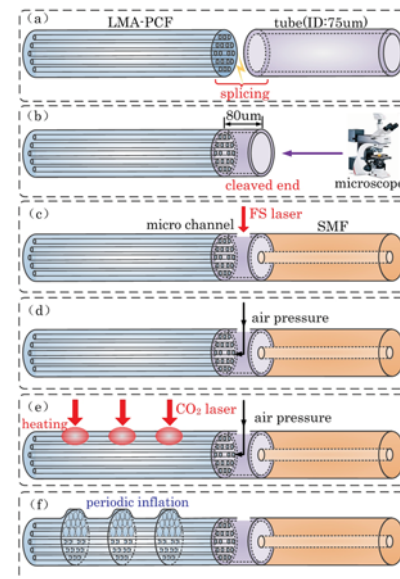


Fig. 1. Schematic diagram for fabricating an I-LPFG sensor.

grating, the main design parameters are the internal gas pressure, CO<sub>2</sub> laser power, and exposure time. In our experiment, the internal gas pressure was about 1.5 MPa, the output power of the CO<sub>2</sub> laser was 0.4 W, and the average exposure time was 200 ms.

Figure 1 illustrates the detailed process for fabricating an I-LPFG-based sensor. First, as shown in Fig. 1(a), an end of a silica tube with an inner/outer diameter of 75/127  $\mu\text{m}$  was spliced with a large-mode-area pure-silica PCF (NKT ESM-12) by use of a commercial fusion splicer (FSM-60) in the manual mode. Note that the discharge current of the splicer must be manually adjusted to avoid collapsing of the air holes at the splicing joint so that air can pass through the silica tube into the holes of the PCF, as described below. Second, as shown in Fig. 1(b), another end of the silica tube was cleaved to shorten its length to be about 80  $\mu\text{m}$  so that we can observe whether the air holes of the PCF end are open or not by use of a microscope. Third, as shown in Fig. 1(c), the cleaved end of the silica tube was spliced with a another single-mode fiber (SMF), thus achieving an air cavity with a length of 80  $\mu\text{m}$ . And then a micro-channel (50\*40  $\mu\text{m}$ ) was drilled through the sidewall of the silica tube by use of a femtosecond laser (a central wavelength of 800 nm, a pulse duration time of 120 fs, and a repetition rate of 1 kHz) so that air pressure can access from the silica tube into the air holes of the PCF. Fourth, as shown in Fig. 1(d), the silica tube with a channel was placed into a gas chamber and sealed by use of strong glue. Then air with a pressure of  $\sim$ 1.5 MPa accessed into the holes of the PCF via the gas chamber by use of a high-pressure air pump. Finally, as shown in Figs. 1(e) and 1(f), the PCF was periodically heated along the fiber axis by use of a focused CO<sub>2</sub> laser beam. As a result, the holes of the PCF inflated periodically along the fiber axis due to high-pressure air and the CO<sub>2</sub>-laser-induced high temperature. Such inflations induce periodically refractive index modulation along the fiber axis, thus inscribing an I-LPFG in the PCF, as shown in Fig. 2. Periodical heating process, i.e., so-call scanning cycle above may be repeated for  $K$  cycles from the first grating period to the last grating period until a desired I-LPFG is achieved, as shown in Fig. 3.

As shown in Fig. 2 (a), air holes of a PCF employed with a diameter of 3.3  $\mu\text{m}$  are arranged in a hexagonal pattern with a pitch of 7.4  $\mu\text{m}$ . The core and cladding diameters of the PCF are 10.4 and 125  $\mu\text{m}$ , respectively. As shown in Figs. 2(b) and 2(c), asymmetric inflations of air holes were clearly created in the PCF along the fiber

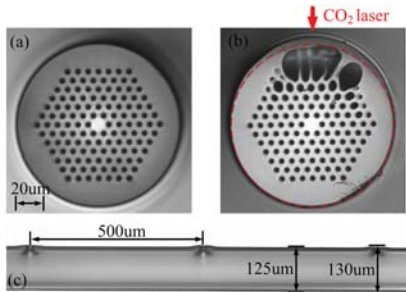


Fig. 2. Microscope image of the cross-section of the PCF (a) before and (b) after CO<sub>2</sub> laser irradiation, (c) side view of the CO<sub>2</sub>-laser-inscribed I-LPFG with periodic inflations.

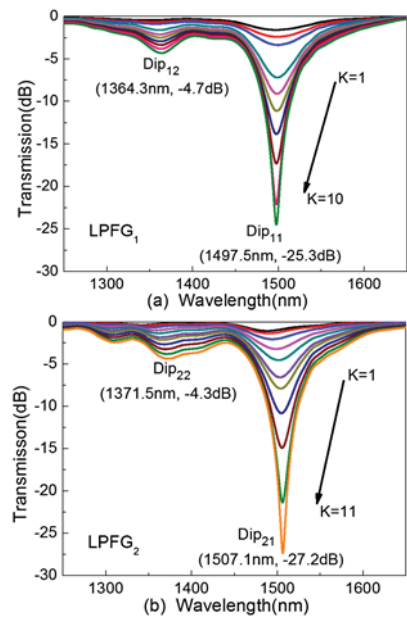


Fig. 3. Transmission spectrum evolution of the CO<sub>2</sub>-laser-inscribed (a) LPFG<sub>1</sub> with periodic inflations and (b) LPFG<sub>2</sub> without periodic inflations while the number of scanning cycles (K) increases.

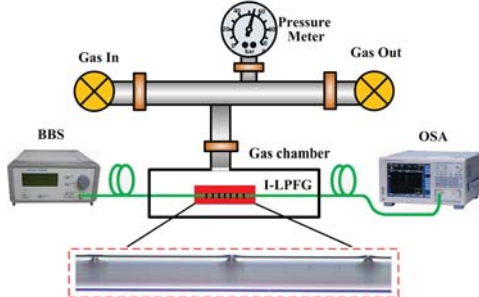
axis, resulting from the single-side irradiation of the focused CO<sub>2</sub> laser beam. Compared with the PCF diameter of 125  $\mu\text{m}$ , the inflated region of the PCF has a diameter of 130  $\mu\text{m}$  along the CO<sub>2</sub> laser irradiation direction. Uneven expansion of the air holes illustrated in Fig. 2(b) may be due to the inhomogeneity of the air holes in the PCF.

As shown in Fig. 3(a), a high-quality I-LPFG sample, i.e., LPFG<sub>1</sub>, with asymmetric periodic inflations, a low insertion loss of  $\sim$ 1 dB, and two attenuation dips (Dip<sub>11</sub> and Dip<sub>12</sub>) were induced after ten scanning cycles of the CO<sub>2</sub> laser beam, where the resonant wavelengths and the attenuation dips of Dip<sub>11</sub> and Dip<sub>12</sub> are  $\lambda_{11} = 1497.5$  nm,  $A_{11} = -25.3$  dB,  $\lambda_{12} = 1364.3$  nm, and  $A_{12} = -4.7$  dB, respectively.

To observe the difference between the gas pressure response of the LPFGs with and without periodic inflations, another LPFG sample, i.e., LPFG<sub>2</sub>, without periodic inflations was inscribed in the same type of PCF by means of the common CO<sub>2</sub> laser irradiation technology [18], in which no high-pressure air was pumped into the air holes of the PCF. During the inscription of LPFG<sub>2</sub>, a lower power of the CO<sub>2</sub> laser was employed to avoid collapsing of the air holes of the PCF [19]. As shown in Fig. 3(b), the insertion loss of  $\sim$ 0.8 dB and two attenuation dips (Dip<sub>21</sub> and Dip<sub>22</sub>) were observed in the transmission spectrum of LPFG<sub>2</sub> after eleven scanning cycles of the CO<sub>2</sub> laser beam, where the resonant wavelengths and the attenuation dips of Dip<sub>21</sub> and Dip<sub>22</sub> are  $\lambda_{21} = 1507.1$  nm,  $A_{21} = -27.2$  dB,  $\lambda_{22} = 1371.5$  nm, and  $A_{22} = -4.3$  dB, respectively. LPFG<sub>1</sub> and LPFG<sub>2</sub> are with the same grating pitch of 500  $\mu\text{m}$  and the same period numbers of 30.

An experimental setup for investigating the responses of the LPFG samples to gas pressure, is illustrated in Fig. 4, where a broadband light source (BBS) and an optical-spectrum analyzer (OSA) with a resolution of

F3:1  
F3:2  
F3:3  
F3:4  
118  
119  
120  
121  
122  
123  
124  
125  
126  
127  
128  
129  
130  
131  
132  
133  
134  
135  
136  
137  
138  
139  
140  
141  
142  
143  
144  
145  
146  
147  
148  
149  
150  
151  
152  
153  
154

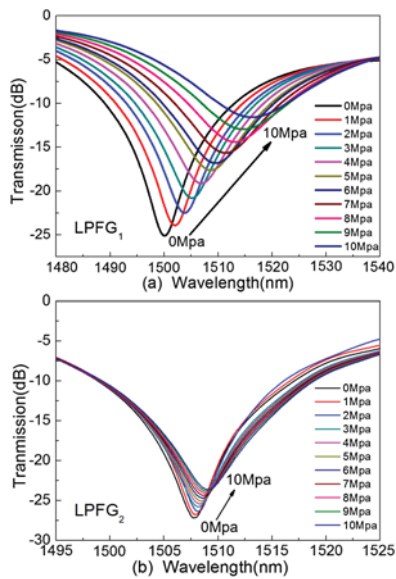


F4:1 Fig. 4. Experimental setup for investigating the response of  
F4:2 the LPFG samples to the gas pressure.

155 0.01 nm were employed to measure the transmission  
156 spectra of the gratings. The LPFG samples, i.e., LPFG<sub>1</sub>  
157 with periodic inflations or LPFG<sub>2</sub>, without periodic inflations  
158 was sealed in a gas chamber by use of a strong glue,  
159 where a commercial air pump was used to realize air  
160 pressure measurement via a high-precision pressure  
161 meter (ConST-162) with a pressure range from up to 40 MPa.  
162

Resonant wavelength of each LPFG sample was measured while the gas pressure in the chamber was increased from 0 to 10 MPa with a step of 1 MPa, remaining for 10 min at each step. With the increase of gas pressure, as shown in Figs. 5 and 6(a), the resonant wavelength of LPFG<sub>1</sub> with periodic inflations, i.e., I-LPFG, shifted rapidly toward a longer wavelength with a higher sensitivity of 1.68 nm/Mpa, whereas, that of LPFG<sub>2</sub> without periodic inflations shifted slowly toward a longer wavelength with a lower sensitivity of 0.12 nm/Mpa. Moreover, with the increase of gas pressure, as shown in Figs. 5 and 6(b), the attenuation dip of LPFG<sub>1</sub> reduced rapidly with a higher sensitivity of 1.36 dB/Mpa, whereas, that of LPFG<sub>2</sub> reduced slowly with a lower sensitivity of 0.25 dB/Mpa.

It is obvious that the gas pressure sensitivity of resonant wavelength of LPFG<sub>1</sub> with periodic inflations is one order of magnitude higher than that of resonant wavelength of LPFG<sub>2</sub> without periodic inflations. In other



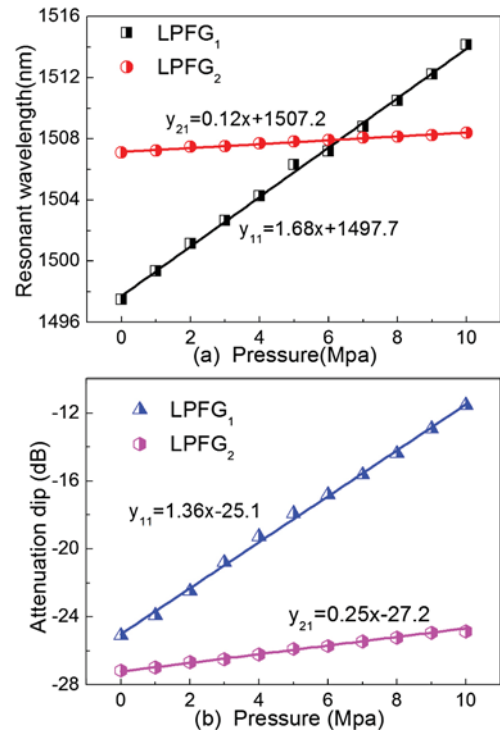
F5:1 Fig. 5. Transmission spectrum evolution of (a) LPFG<sub>1</sub> with  
F5:2 period inflations and (b) LPFG<sub>2</sub> without periodic inflations  
F5:3 while the gas pressure increases from 0 to 10 MPa.

words, the gas pressure sensitivity of the PCF-based LPFG is increased by 14 times by means of inflating periodic air holes of the PCF along the fiber axis. Moreover, the gas pressure sensitivity of our I-LPFG is one order of magnitude higher than that of the taper-induced LPFG in the same type PCF [14]. In terms of an intensity-based measurement, as shown in Fig. 6(b), our I-LPFG sensor exhibits a high pressure sensitivity of 1.36 dB/Mpa, which is much higher than that, i.e., 0.25 dB/Mpa, of LPFG without periodic inflations.

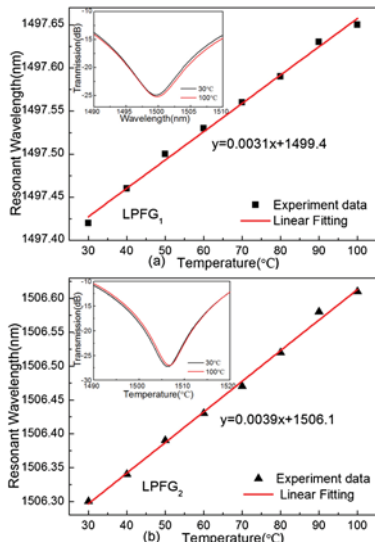
The sensitivity of resonant wavelength,  $\lambda_i$ , of a LPFG to the gas pressure,  $P$ , can be defined as follows [13]:

$$\frac{d\lambda_i}{dP} = \Lambda \frac{d(\delta n_{\text{eff},i})}{dP} + \lambda_i \frac{1}{L} \frac{dL}{dP}, \quad (2)$$

where  $\Lambda$  is the grating pitch,  $L$  is the length of the grating, and  $\delta n_{\text{eff},i}$  is the effective refractive index difference between the core and the cladding. It is very difficult to analyze quantitatively the pressure sensitivity of the I-LPFG because the inflation of air holes is uneven and irregular. Therefore, we only analyzed qualitatively the increased pressure sensitivity of the I-LPFG in comparison to a conventional LPFG. It has been found that the second term on the right side of Eq. (2) does not play an important role because  $dL/dP$  can be neglected in the case of radial pressure. Thus, the resonant wavelength of our I-LPFG sensor is a linear function of the gas pressure, and the gas pressure sensitivity is mainly depend on the fiber materials, i.e., the elasto-optical coefficient of the glass and the pressure-induced physical deformations of the fiber. The resonant wavelength shift of our I-LPFG sensor is a linear function of the gas pressure, which has been



F6:1 Fig. 6. (a) Measured resonant wavelength and (b) attenuation dip of the two LPFG samples, i.e., LPFG<sub>1</sub> and LPFG<sub>2</sub>, versus gas  
F6:2 pressure.  
F6:3



F7:1 Fig. 7. Temperature responses of (a) the I-LPFG sample, i.e.,  
F7:2 LPFG<sub>1</sub> with periodic inflations and (b) the LPFG sample, i.e.,  
F7:3 LPFG<sub>2</sub> without periodic inflations. Inset: transmission spectra  
F7:4 of the LPFG samples at 30°C and 100°C.

verified by our experimental results illustrated in Fig. 6. Moreover, the silica walls within the inflated region of the I-LPFG are thinned due to the inflation of air holes in the PCF. As a result, in the case of a high gas pressure, physical deformations easily occur within the inflated region of the I-LPFG, which changes the effective refractive index difference, i.e.,  $\delta n_{\text{eff},i}$  in Eq. (2), due to the well-known elasto-optical effect and induces a resonant wavelength shift. Thus periodic inflations in the I-LPFG greatly enhance the pressure sensitivity of the grating. So our I-LPFG could be used to develop a promising gas pressure sensor with a high sensitivity of up to 1.68 nm/MPa.

We also investigated the temperature response of the I-LPFG by means of placing LPFG<sub>1</sub> into an electrical oven and raising gradually the temperature from room temperature to 100°C with a step of 10°C. The tested temperature was maintained for 20 min at each temperature rise step. As shown in Fig. 7(a), the resonant wavelength of the I-LPFG with periodic inflations was shifted toward a longer wavelength with a low sensitivity of 3.1 pm/°C. In other words, the I-LPFG based sensor is insensitive to temperature. The reason for this is that the I-LPFG was induced in a pure-silica PCF. For a comparison, we also investigated the temperature response of the LPFG sample, i.e., LPFG<sub>2</sub>, without periodic inflations. As shown in Fig. 7(b), the resonant wavelength of the LPFG<sub>2</sub> was also shifted toward a longer wavelength with a low sensitivity of 3.9 pm/°C. It can be seen from Fig. 7 that the temperature sensitivity of LPFG<sub>1</sub> is similar to that of LPFG<sub>2</sub>. Thus the inflations of air holes in a PCF have little influence on the temperature sensitivity in a low-temperature test. According to the pressure and temperature sensitivities above, proving the I-LPFG is used to measure gas pressure, the pressure measurement error, resulting from the cross-sensitivity between temperature and gas pressure, is less than 1.8 Kpa/°C, which could be neglected in high gas-pressure measurement. Therefore, our I-LPFG pressure sensor could effectively reduce

the cross-sensitivity between gas pressure and temperature.

In conclusion, we have experimentally demonstrated a novel I-LPFG for high-sensitivity gas-pressure measurement. Such an I-LPFG was induced by use of a pressure-assisted CO<sub>2</sub> laser beam-scanning technique to inflate periodically air holes of a PCF. A very high-pressure sensitivity of 1.68 nm/Mpa was achieved, which is increased by 14 times, comparing with that of the LPFG without periodic inflations. Moreover, the I-LPFG exhibited a very low-temperature sensitivity of 3.1 pm/°C so that the pressure measurement error, resulting from the cross-sensitivity between temperature and gas pressure, is less than 1.8 Kpa/°C in the case of no temperature compensation. So the I-LPFG could be used to develop a promising gas-pressure sensor, and the achieved pressure measurement range is up to 10 MPa.

This work was supported by National Natural Science Foundation of China/Guangdong (grant nos. 61425007, 11174064, 61377090 and 61308027), Science & Technology Innovation Commission of Shenzhen/Nanshan (grants nos. KQCX20120815161444632, JCYJ 20130329140017262, ZDSYS20140430164957664, KC2014ZDZJ008A), and Pearl River Scholar Fellowships.

## References

- C. A. Wu, H. Y. Fu, K. K. Qureshi, B. O. Guan, and H. Y. Tam, Opt. Lett. **36**, 412 (2011).
- J. Ma, W. Jin, H. L. Ho, and J. Y. Dai, Opt. Lett. **37**, 2493 (2012).
- Y. N. Zhang, L. Yuan, X. W. Lan, A. Kaur, J. Huang, and H. Xiao, Opt. Lett. **38**, 4609 (2013).
- C. R. Liao, S. Liu, L. Xu, C. Wang, Y. P. Wang, Z. Y. Li, Q. Wang, and D. N. Wang, Opt. Lett. **39**, 2827 (2014).
- T. Chen, R. Z. Chen, C. Jewart, B. T. Zhang, K. Cook, J. Canning, and K. P. Chen, Opt. Lett. **36**, 3542 (2011).
- C. M. Jewart, Q. Q. Wang, J. Canning, D. Grobnić, S. J. Mihailov, and K. P. Chen, Opt. Lett. **35**, 1443 (2010).
- H. J. Sheng, W. F. Liu, K. R. Lin, S. S. Bor, and M. Y. Fu, Opt. Express **16**, 16013 (2008).
- Q. Zhang, N. Liu, T. Fink, H. Li, W. Peng, and M. Han, IEEE Photon. Technol. Lett. **24**, 1519 (2012).
- G. Statkiewicz-Barabach, D. Kowal, M. K. Szczurowski, P. Mergo, and W. Urbanczyk, IEEE Photon. Technol. Lett. **25**, 496 (2013).
- Y. F. Zhang, C. C. Chan, Y. M. Chan, and P. Zu, IEEE SENS. J. **12**, 954 (2012).
- M. Smietana, W. J. Bock, P. Mikulic, and J. H. Chen, J. Lightwave Technol. **30**, 1080 (2012).
- Y. Wang, J. Appl. Phys. **108**, 081101 (2010).
- W. J. Bock, J. Chen, P. Mikulic, and T. Eftimov, IEEE Trans. Instrum. Meas. **56**, 1176 (2007).
- W. J. Bock, J. Chen, P. Mikulic, T. Eftimov, and M. Korwin-Pawlowski, Meas. Sci. Technol. **18**, 3098 (2007).
- M. Smietana, W. J. Bock, J. Chen, and P. Mikulic, Meas. Sci. Technol. **21**, (2010).
- X. Y. Zhong, Y. P. Wang, J. L. Qu, C. R. Liao, S. Liu, J. Tang, Q. Wang, J. Zhao, K. M. Yang, and Z. Y. Li, Opt. Lett. **39**, 5463 (2014).
- W. J. Wadsworth, A. Witkowska, S. G. Leon-Saval, and T. A. Birks, Opt. Express. **13**, 6541 (2005).
- Y. Zhu, P. Shum, H. W. Bay, M. Yan, X. Yu, J. Hu, J. Hao, and C. Lu, Opt. Lett. **30**, 367 (2005).
- Y. P. Wang, L. M. Xiao, D. N. Wang, and W. Jin, Opt. Lett. **31**, 3414 (2006).

# High-sensitivity strain sensor based on in-fiber improved Fabry–Perot interferometer

Shen Liu, Yiping Wang,\* Changrui Liao, Guanjun Wang, Zhengyong Li, Qiao Wang, Jiangtao Zhou, Kaiming Yang, Xiaoyong Zhong, Jing Zhao, and Jian Tang

*Key Laboratory of Optoelectronic Devices and Systems of Ministry of Education and Guangdong Province, Shenzhen University, Shenzhen 518060, China*

\*Corresponding author: [ypwang@szu.edu.cn](mailto:ypwang@szu.edu.cn)

Received January 21, 2014; revised February 27, 2014; accepted February 27, 2014;  
posted March 3, 2014 (Doc. ID 205105); published March 31, 2014

We demonstrated a high-sensitivity strain sensor based on an in-fiber Fabry–Perot interferometer (FPI) with an air cavity, which was created by splicing together two sections of standard single-mode fibers. The sensitivity of this strain sensor was enhanced to  $6.0 \text{ pm}/\mu\text{e}$  by improving the cavity length of the FPI by means of repeating arc discharges for reshaping the air cavity. Moreover, such a strain sensor has a very low temperature sensitivity of  $1.1 \text{ pm}/^\circ\text{C}$ , which reduces the cross sensitivity between tensile strain and temperature. © 2014 Optical Society of America

*OCIS codes:* (120.2230) Fabry-Perot; (060.2370) Fiber optics sensors.  
<http://dx.doi.org/10.1364/OL.39.002121>

Fiber-optic Fabry–Perot interferometers (FPIs) have proved to be useful in the measurements of various physical, chemical, and biological parameters because of the advantage of simple structure, high sensitivity, and compact size [1,2]. Since air cavities created in the fiber have a small thermal expansion coefficient, in-fiber air-cavity-based FPIs have been used to develop temperature-insensitive sensors for measuring refractive index (RI) [3–5], tensile strain [6–13], and pressure [14,15]. Unfortunately, it is difficult or impossible to create directly an air cavity in the fiber, so that complicated pretreatments have to be done to achieve in-fiber air-cavity-based FPIs. For example, air cavities were achieved during splicing two cleaved fiber ends by use of femtosecond laser micromachining [5,6,16] and chemical etching [11,13] to create a microhole on the fiber end in advance. In addition, in-fiber FPIs with an air cavity were demonstrated by employing special optical-fiber structures, such as hollow-core photonic crystal fibers (PCFs) [4,7], solid-core PCFs [8,10], and silica capillaries [14]. However, all these techniques above require complicated pretreatments, expensive PCFs, and/or other special optical fibers.

In this Letter, we demonstrated a promising technique to create an air-cavity-based FPI by means of splicing together two sections of standard single-mode fibers (SMFs), accompanying easy pretreatment on the fiber ends. Such an FPI could be used to develop a high-sensitivity strain sensor with a low cross sensitivity between temperature and tensile stain. And the sensitivity of the strain sensor can be enhanced to  $6.0 \text{ pm}/\mu\text{e}$  by means of reshaping an air cavity created in the fiber.

Figure 1 illustrates the fabrication process of an in-fiber air-cavity-based FPI. First of all, an end of a standard SMF (Corning SMF-28) was immersed into a commercial RI matching liquid (Cargille Labs, <http://www.cargille.com>) to coat a liquid film on the end surface. Such two sections of SMFs with liquid-coated ends were placed in the left and right fiber holders, respectively, of a commercial fusion splicer (Fujikura FSM-60S), as shown in Fig. 1(I). Before being immersed

into the liquid, the fiber end was reshaped into hemispherical and smooth ends by means of electrical arc discharge in order to enlarge the surface of the fiber ends and to coat much liquid on the fiber ends. Second, the left and right fiber ends were moved toward each other until an overlap of  $2d$  was achieved at the touching region of the two fiber ends via the left and right motors of the fusion splicer, as shown in Fig. 1(II), where  $d_l$  and  $d_r$  show the moved distance of the left and right fiber ends, respectively, before the two fiber ends are touched with each other, and  $d$  shows the moved distance of each fiber end after the two fiber ends touch each other. Third, arc discharge was done with default parameters for splicing a standard SMF in the fusion splicer. Consequently, two fiber ends were spliced with each other, and an air bubble was created in the spliced joint, as shown in Figs. 1(III) and 2(a), resulting from the evaporation of the liquid coated on the fiber end facet and quick vaporization and freeze of silica material during arc discharge. Note that (1) the manual operation mode of the fusion splicer (FSM-60S) was used to fabricate the in-fiber air cavity samples; (2) three types of discharge parameters, i.e., ARC1, ARC2, and REARC, are available in the operation menu of the splicer; (3) only the discharge parameter of ARC1 was employed during our pretreating of the fiber ends, fabricating air cavity samples, and reshaping

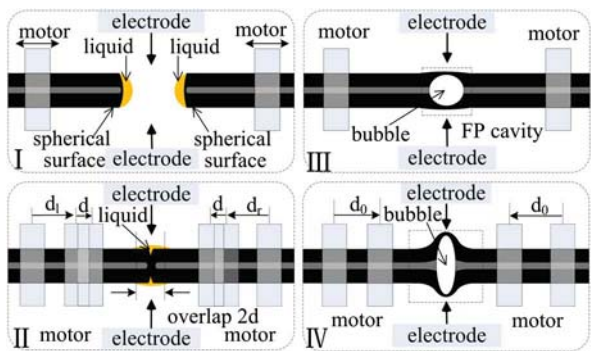


Fig. 1. Schematic diagrams of fabrication process of in-fiber FPI based on an air bubble.

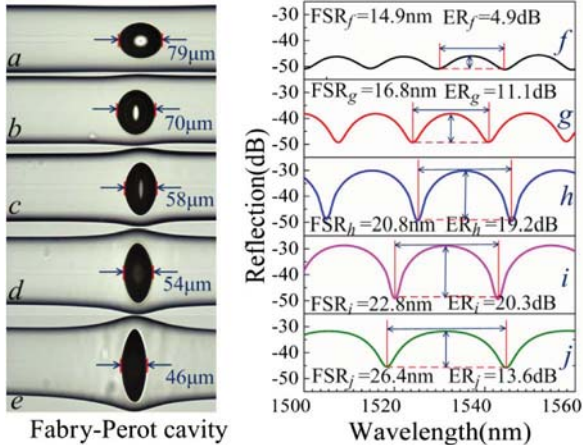


Fig. 2. (a), (b), (c), (d), and (e) Microscope images of the created air bubble with a cavity length of 79, 70, 58, 54, and 46  $\mu\text{m}$ , respectively; (f)–(j) the corresponding reflection spectra of the air-cavity-based FPI. FSR, free spectral range; ER, extinction ratio.

the air cavities. Such an in-fiber air bubble/cavity could be used to develop a promising fiber-optic FPI. As shown in Fig. 2, an interference pattern was observed in the reflection spectrum of the air-cavity-based FPI by use of a 3 dB coupler, a broadband light source (ASE-LIGHGSOURCE), and an optical spectrum analyzer (OSA, YOKOGAWA AQ6370C).

Our experiments show that the diameter of the created air bubble depends strongly on the overlap of  $2d$  and the viscosity of the coated liquid. Providing other fabrication parameters are not changed; the more overlap of  $2d$  is applied to the spliced joint, a larger air bubble can be achieved. Compared with complicated pretreatments, e.g., femtosecond laser micromachining for creating a microhole on the fiber end [5,6], we demonstrated an easy pretreatment, e.g., coating a liquid film on the fiber end, to create an air bubble in the spliced joint. The intensity of the interference fringe in the reflection spectrum can be given by

$$I = I_1 + I_2 + 2\sqrt{I_1 I_2} \cos(\gamma), \quad (1)$$

where  $I_1$  and  $I_2$  are the intensities of light reflected at the two cavity interfaces, respectively, and  $\gamma$  is the phase difference shift between the two reflected lights. Free spectral range of the interference fringes of the air-cavity-based FPI can be given by

$$\text{FSR} = \lambda^2 / (2nL_B), \quad (2)$$

where  $\lambda$  is the wavelength of light,  $n$  is the RI of the medium, i.e., air, trapped inside the bubble, and  $L_B$  is the cavity length of the air bubble created in the spliced joint.

The in-fiber air bubble illustrated in Fig. 2 can be reshaped to enhance the extinction ratio of the interference fringe and change the FSR by means of repeating arc discharges, as discussed below. As shown in Fig. 1(IV), the left and right fiber holders were moved again toward each other by a distance of  $d_0$  in order to apply an axial pressure to the spliced joint, and then arc discharge was

done again. Consequently, the spherical air bubble was reshaped into an elliptical one with a shorter cavity length along the fiber axis. Repeating the process above, we achieved a series of elliptical air bubbles with different cavity lengths of 79, 70, 58, 54, and 46  $\mu\text{m}$  by means of applying different overlap of  $2d_0$  during repeated arc discharges, as shown in Figs. 2(a)–2(e). The corresponding reflection spectra of the air-cavity-based FPIs are illustrated in Figs. 2(f)–2(j), respectively, in which the FSR of the interference fringes is 14.9, 16.8, 20.8, 22.8, and 26.4 nm, respectively, and the extinction ratio is 4.9, 11.1, 19.2, 20.3, and 13.5 dB, respectively. It can be found from Fig. 2 that, with the decrease of the cavity length from 79 to 46  $\mu\text{m}$ , the FSR around 1530 nm is increased from 14.9 to 26.4 nm, and the extinction ratio is enhanced from 4.9 to 20.3 dB and is reduced to 13.5 dB. This is due to the fact that the reshape of the air bubble changes the intensity of light reflected on the air cavity wall. We measured the insertion loss of the air bubble with a cavity length of 79, 70, 58, 54, and 46  $\mu\text{m}$  by means of testing its transmission spectra within the wavelength range from 1450 to 1600 nm. As shown in Fig. 3, the insertion loss reduces with the decrease of the cavity length, and the air bubble with a cavity length of 46  $\mu\text{m}$  has an insertion loss of about 6.5 dB at the wavelength of 1550 nm. According to Eq. (2), we also calculated the FSR around 1530 nm. As shown in Fig. 4, the measured cavity lengths of the air bubble agree well with the calculated results.

We investigated the responses of the air-cavity-based FPI samples with different cavity lengths to the applied tensile strain. First, one end of the air-cavity-based FPI with a cavity length of 79  $\mu\text{m}$ , as illustrated in Fig. 2(a), was fixed, and another end was attached to a translation stage with a resolution of 10  $\mu\text{m}$ . The total length of the stretched fiber, including the SMF and the air bubble, was 400 mm. The wavelength shift of the interference fringe around 1545 nm was measured while the tensile strain was increased from 0 to 1050  $\mu\text{e}$  with a step of 50  $\mu\text{e}$ . Second, the air bubble with a cavity length of 79  $\mu\text{m}$  was reshaped to shorten its cavity length to 70  $\mu\text{m}$  by use of the arc discharge technique illustrated in Figs. 1(IV) and 2(b). And then the response of the air-cavity-based FPI with a cavity length of 70  $\mu\text{m}$  to the applied tensile strain was investigated. The experiment

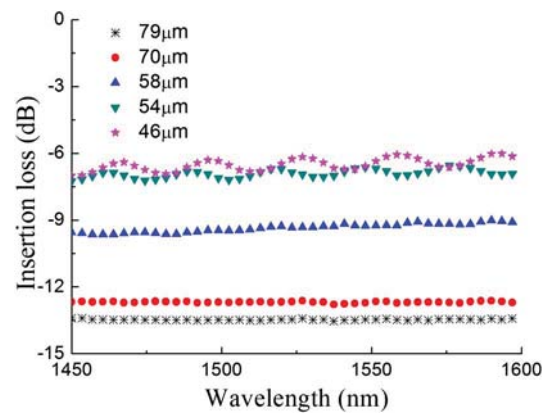


Fig. 3. Insertion loss of the air bubble with a cavity length of 79, 70, 58, 54, and 46  $\mu\text{m}$ .

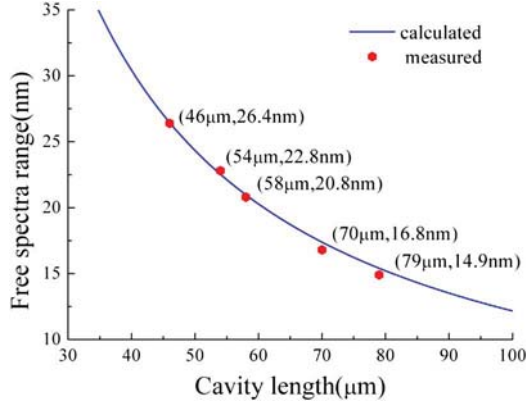


Fig. 4. Measured and calculated FSR of interference fringes of the in-fiber air-cavity-based FPI with different cavity lengths of 46, 54, 58, 70, and 79  $\mu\text{m}$ .

process above was repeated until the response of the air-cavity-based FPI samples with a cavity length of 58, 54, and 46  $\mu\text{m}$ , as illustrated in Figs. 2(c)-2(e), to the applied tensile strain was investigated. As shown in Figs. 5(a) and 5(b), the dip wavelength of the interference fringe of each air-cavity-based FPI sample shifts linearly toward a longer wavelength with the increased tensile strain. And the shorter cavity length the FPI sample has, a higher

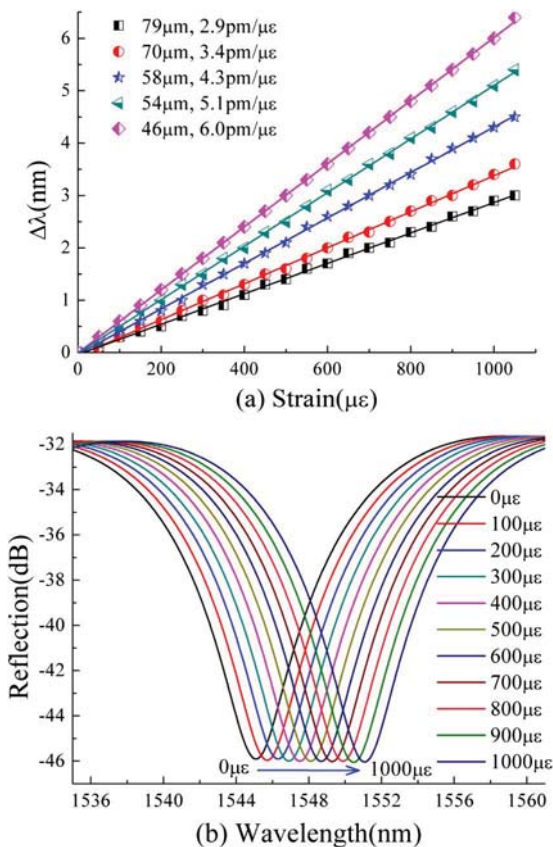


Fig. 5. (a) Wavelength shift of the interference fringe around 1545 nm as a function of tensile strain applied to the air-cavity-based FPI sample with different cavity length of (■) 79  $\mu\text{m}$ , (●) 70  $\mu\text{m}$ , (★) 58  $\mu\text{m}$ , (△) 54  $\mu\text{m}$ , and (◆) 46  $\mu\text{m}$ . (b) Reflection spectrum evolution of the air-cavity-based FPI sample with a cavity length of 46  $\mu\text{m}$  while the tensile strain increases from 0 to 1000  $\mu\epsilon$ .

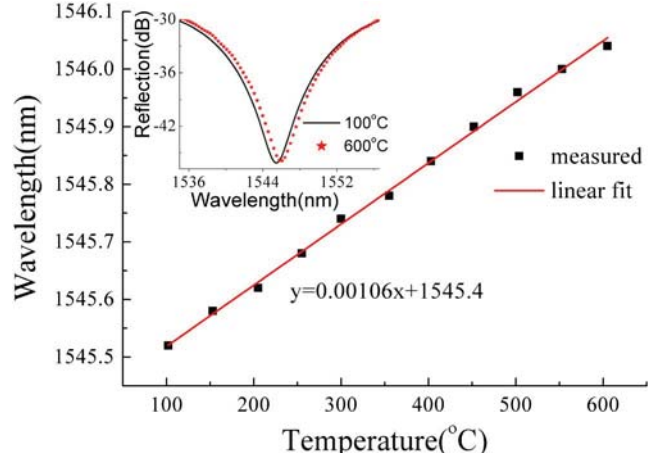


Fig. 6. Temperature response of the dip wavelength in the reflection spectrum of the air-cavity-based FPI sample with a cavity length of 46  $\mu\text{m}$ .

strain sensitivity the wavelength is. Hence the strain sensitivity of the air-cavity-based FPI sensor can be enhanced by means of reshaping the air bubble to shorten the cavity length via arc-discharge technique. For example, the strain sensitivity of the air-cavity-based FPI was enhanced from 2.9 to 6.0  $\text{pm}/\mu\epsilon$  while the cavity length was shortened from 79 to 46  $\mu\text{m}$ , as shown in Fig. 5(a). Providing an optical spectrum analyzer (YOKOGAWA AQ6370C) with a resolution of 0.02 nm is employed, a strain resolution of 3.3  $\mu\epsilon$  can be achieved in the application of our proposed strain sensor based on Fabry-Perot interference.

We also investigated the temperature responses of the air-cavity-based FPI sample with a cavity length of 46  $\mu\text{m}$ . The FPI sample was placed in a tube furnace to raise its temperature from 100°C to 600°C with a step of 50°C. As shown in Fig. 6, the dip wavelength in the reflection spectrum the FPI sample was shifted toward a longer wavelength with a low temperature sensitivity of only 1.1  $\text{pm}/^\circ\text{C}$ . In other words, the interference fringe is insensitive to temperature [17]. According to the strain and temperature sensitivity of the interference fringe, in case no temperature compensation is done, the temperature-induced strain measurement error is less than 0.2  $\mu\epsilon/^\circ\text{C}$ . Therefore, the FPI-based strain sensor effectively reduces the cross sensitivity between strain and temperature.

In summary, we demonstrated a versatile technique for fabricating a micro air bubble in the fiber. The air bubble can be reshaped to change its cavity length by arc-discharge technique. Such an in-fiber air bubble can be used to develop a high-sensitivity strain sensor based on Fabry-Perot interference. The sensitivity of this strain sensor was enhanced to 6.0  $\text{pm}/\mu\epsilon$  by improving the cavity length of the FPI. Moreover, such a strain sensor reduces the cross sensitivity between tensile strain and temperature.

This work was supported by the National Natural Science Foundation of China (grant nos. 11174064, 61308027, and 61377090), the Science & Technology Innovation Commission of Shenzhen (grant nos. KQCX20120815161444632 and JCYJ20130329140017

262), and the Distinguished Professors Funding from Shenzhen University and Guangdong Province Pearl River Scholars.

## References

1. T. Zhu, D. Wu, M. Liu, and D. W. Duan, *Sensors* **12**, 10430 (2012).
2. B. H. Lee, Y. H. Kim, K. S. Park, J. B. Eom, M. J. Kim, B. S. Rho, and H. Y. Choi, *Sensors* **12**, 2467 (2012).
3. Y. Wang, D. Wang, C. Liao, T. Hu, J. Guo, and H. Wei, *Opt. Lett.* **38**, 269 (2013).
4. D. Jáuregui Vázquez, J. M. Estudillo Ayala, R. Rojas Laguna, E. Vargas Rodríguez, J. M. Sierra Hernández, J. C. Hernández García, and R. I. Mata Chávez, *Sensors* **13**, 6355 (2013).
5. C. Liao, T. Hu, and D. Wang, *Opt. Express* **20**, 22813 (2012).
6. C. Liao, D. Wang, and Y. Wang, *Opt. Lett.* **38**, 757 (2013).
7. M. S. Ferreira, J. Bierlich, J. Kobelke, K. Schuster, J. L. Santos, and O. Frazao, *Opt. Express* **20**, 21946 (2012).
8. F. Favero, L. Araujo, G. Bouwmans, V. Finazzi, J. Villatoro, and V. Pruneri, *Opt. Express* **20**, 7112 (2012).
9. D.-W. Duan, Y.-j. Rao, Y.-S. Hou, and T. Zhu, *Appl. Opt.* **51**, 1033 (2012).
10. J. Villatoro, V. Finazzi, G. Coviello, and V. Pruneri, *Opt. Lett.* **34**, 2441 (2009).
11. E. Cibula and D. Donlagic, *Opt. Express* **15**, 8719 (2007).
12. Y. P. Wang, D. Wang, W. Jin, and X. H. Fang, *IEEE J. Quantum Electron.* **42**, 868 (2006).
13. X. Chen, F. Shen, Z. Wang, Z. Huang, and A. Wang, *Appl. Opt.* **45**, 7760 (2006).
14. Y. Wang, D. Wang, C. Wang, and T. Hu, *Opt. Express* **21**, 14084 (2013).
15. J. Ma, J. Ju, L. Jin, and W. Jin, *IEEE Photon. Technol. Lett.* **23**, 1561 (2011).
16. C. Liao, L. Xu, C. Wang, D. N. Wang, Y. Wang, Q. Wang, K. Yang, Z. Li, X. Zhong, J. Zhou, and Y. Liu, *Opt. Lett.* **38**, 4473 (2013).
17. Y. Wang, W. Jin, and D. Wang, *Opt. Lasers Eng.* **47**, 1044 (2009).

# Compact tunable multibandpass filters based on liquid-filled photonic crystal fibers

Yingjie Liu, Yiping Wang,\* Bing Sun, Changrui Liao, Jun Song, Kaiming Yang,  
Guanjun Wang, Qiao Wang, Guolu Yin, and Jianguo Zhou

*Key Laboratory of Optoelectronic Devices and Systems of Ministry of Education and Guangdong Province,  
Shenzhen University, Shenzhen 518060, China*

\*Corresponding author: [ypwang@szu.edu.cn](mailto:ypwang@szu.edu.cn)

Received January 16, 2014; revised March 4, 2014; accepted March 6, 2014;  
posted March 6, 2014 (Doc. ID 204898); published March 31, 2014

We demonstrated a compact tunable multibandpass filter with a short size of about 9 mm and a high wavelength-tuning sensitivity of up to  $-2.194 \text{ nm}/^\circ\text{C}$  by means of filling a liquid with a high refractive index of 1.700 into the air holes of a photonic crystal fiber (PCF). Such a PCF-based filter maintains an almost constant bandwidth and a large extinction ratio of more than 40 dB within the whole wavelength tuning range of more than 100 nm. Moreover, the transmission spectrum of the PCF-based filter is insensitive to the stretch force and the curvature of the fiber. © 2014 Optical Society of America

*OCIS codes:* (060.5295) Photonic crystal fibers; (060.4005) Microstructured fibers; (230.7408) Wavelength filtering devices.

<http://dx.doi.org/10.1364/OL.39.002148>

Tunable fiber filters have been extensively used as key components in fiber-optic communication systems. A few methods have been demonstrated for obtaining tunable fiber filters that employed optical fiber gratings [1–4], combinations of different type of fibers [5], and optical fiber Fabry–Perot interferometers [6–8]. However, the characteristics of long-period fiber gratings are easily affected by external perturbations, such as tensile strain, pressure, and bend. Recently, with the development of photonic crystal fibers (PCFs) [9,10], a few types of tunable filters based on liquid-filled PCFs have been reported via the thermo- and electro-optic effects of the liquids [11–18]. This is due to the fact that an index-guided PCF can be transformed into a bandgap-guided photonic bandgap fiber (PBF) [11,15,16] by means of filling the air holes of the PCF with a liquid. As is well known, it is not easy to obtain a type of liquid with a higher refractive index, so the filling liquids have usually had a lower refractive index of about 1.550 in the previous experiments [11,14,15,19,20]. Consequently, the extinction ratio of the bandgap-based filters is sharply reduced with the rise in temperature due to the negative thermo-optic coefficient of the filling liquid. In addition, provided a liquid with a lower refractive index is employed, a longer PCF has to be filled to increase the extinction ratio of the bandgaps in the liquid-filled PCF, which is a disadvantage in the packaging of the bandgap-based filters and may result in a large liquid-induced absorption loss. Since it is difficult to splice a liquid-filled PCF with a single-mode fiber (SMF), the butt-coupling method is usually used to real-time monitor the optical properties of the PCF-based devices, which is not feasible in practical applications.

In this Letter, we demonstrate a compact tunable bandpass filter based on a liquid-filled PCF. Such a filter has a high extinction ratio of about 40 dB within an extremely broad wavelength range from 800 to 1700 nm. The splicing problem of the liquid-filled PCF is solved. Furthermore, we investigate the response of the PCF-based filter to temperature, strain, and bend.

We employed a large-mode-area pure silica PCF (ESM-12 from NKT, <http://www.nktphotonics.com>) with a core diameter of about 12 μm. Air holes with a diameter of 3.3 μm are arranged in a hexagonal pattern with a pitch of 7.4 μm, as shown in Fig. 1(a). One end of the PCF with a length of 70 mm was spliced to a standard SMF using a commercial arc fusion splicer (Fujikura FSM-60S). The discharge parameters of the splicer were modified to reduce the splice loss and to enhance the strength of the splicing joint [21,22]. Consequently, a low splice loss of about 0.5 dB at a wavelength of 1550 nm was achieved in our experiments, which is due to the optimized discharge parameters and the fact that the PCF employed has a similar mode field diameter (i.e., 10.5 μm at 1550 nm) to that of the standard SMF.

The other end of the PCF was immersed in a liquid (refractive index match liquid from Cargille Labs, <http://www.cargille.com>) with a very high refractive index of 1.700 and a thermo-optic coefficient of  $-4.79 \times 10^{-4}/^\circ\text{C}$ .

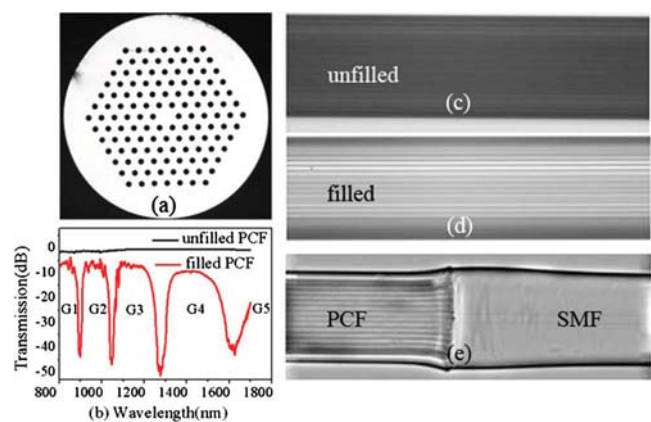


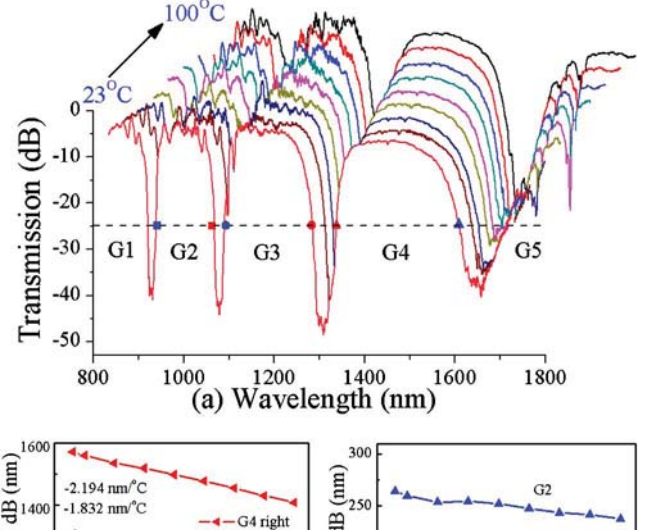
Fig. 1. (a) Cross-sectional image of the PCF employed, (b) transmission spectra of the filled and unfilled PCF, side images of (c) the unfilled PCF and (d) the fully filled PCF, and (e) the fusion joint of the PCF with a single mode fiber. G1, bandgap 1; G2, bandgap 2; G3, bandgap 3; G4, bandgap 4; G5, bandgap 5.

Then the liquid was poured into the air holes of a PCF with well-known capillary action. If the filling time is about 5 min, the liquid-filled PCF has a total length of about 9 mm, as shown in Figs. 1(c) and 1(d). Finally, the open end of the liquid-filled PCF was spliced with another standard SMF. It is more difficult to splice a liquid-filled PCF, rather than an unfilled PCF, with a standard SMF. When the optimized splicing parameters (prefusion power, standard -15 bit; prefusion time, 240 ms; overlap, 10  $\mu\text{m}$ ; fusion power one, standard -10 bit; fusion time one, 200 ms) were employed, the splice loss between the liquid-filled PCF and the SMF was reduced to about 3 dB. The repeated arc discharge technique is usually used to reduce the splicing loss of an unfilled PCF. However, only one arc discharge was done to splice the liquid-filled PCF in our experiment, as shown in Fig. 1(e). The reason for this is that repeated arc discharges could induce gasification of the liquid material, resulting in a bubble in the splicing joint and thus a large splicing loss.

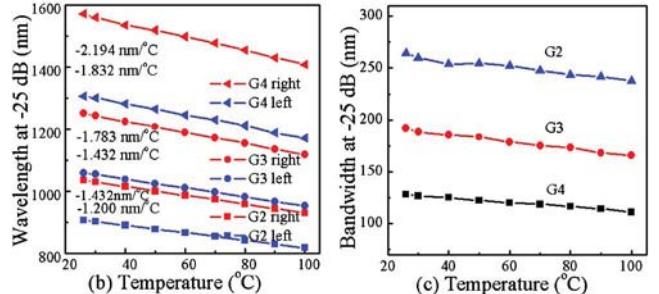
A supercontinuum white-light source (NKT SuperK Compact) and an optical spectrum analyzer (YOKOGAWA AQ6370C) were employed to measure the transmission spectrum of the liquid-filled PCF. As shown in Fig. 1(b), five bandgaps occurred within the wavelength range from 800 to 1700 nm. In other words, the index-guided PCF was transferred into a bandgap-guided PBF, resulting from the higher effective refractive index of the liquid rods in the cladding than that of the pure silica in the core. It can easily be seen in Fig. 1(b) that the extinction ratio of each bandgap is more than 40 dB due to the high refractive index ( $n = 1.700$ ) of the filled liquid. Hence, such a liquid-filled PCF could be used to develop a promising in-fiber bandpass filter with a large extinction ratio of more than 40 dB and a low insertion loss of about 3 dB. And this filter has a compact size, because the length of the liquid-filled PCF is 9 mm.

Our experimental results show that the optical properties, i.e., extinction ratio and wavelength of the bandgaps, of the liquid-filled PCF depend strongly on the type of PCF employed, the length of the filled PCF, and the refractive index of the filled liquid. Provided a liquid with a lower refractive index is employed, a longer PCF has to be filled to increase the extinction ratio of the bandgaps in the liquid-filled PCF. So we selected a liquid with a very high refractive index of 1.700 from Cargille Labs in order to realize a compact filter based on a liquid-filled PCF as described below.

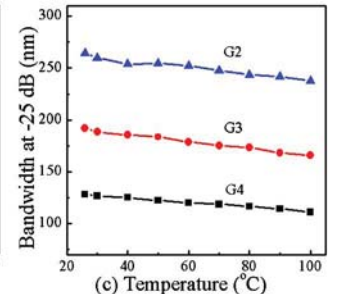
We investigated the temperature response of the liquid-filled PCF, i.e., the filter, by use of a column oven (LCO 102). The liquid-filled PCF was placed in the oven, and then temperature was raised from 30°C to 100°C. As shown in Fig. 2(a), the bandgaps shifted toward a shorter wavelength, a so-called blueshift, with the rise in temperature, resulting from the thermo-optic effect of the filled liquid, but the extinction ratio of each bandgap remained steady at a value of more than 40 dB due to the higher refractive index ( $n = 1.700$ ) of the liquid employed. This is different from the phenomenon reported in [11], in which a liquid with a lower refractive index of 1.480 was employed so that the extinction ratio of the bandgap in the liquid-filled PCF reduced with the rise in temperature.



(a) Wavelength (nm)



(b) Temperature (°C)



(c) Temperature (°C)

Fig. 2. (a) Transmission spectrum evolution of the liquid-filled PCF with the rise in temperature from 30°C to 100°C with steps of 10°C, (b) wavelengths, corresponding to a transmission of -25 dB, at the left and right edges of the three bandgaps, i.e., G2, G3, and G4, and (c) bandwidth of each bandgap versus temperature. Note that the bandwidth in Figs. 2(c), 3(c), and 4(c) is defined as the wavelength difference between the left and right edges of each bandgap at a transmission of -25 dB.

It is very difficult, even impossible, to measure the center wavelength of each bandgap, due to the wide bandpass wavelength range. In order to evaluate quantitatively the temperature-induced shift of the bandgap edges, we illustrated the wavelengths, corresponding to -25 dB, of the left and right edges of each bandgap at different temperatures. During the temperature rise, as shown in Fig. 2(b), the left edges of G2, G3, and G4 linearly shifted toward a shorter wavelength, with high sensitivities of -1.200, -1.432, and -1.832 nm/°C, respectively, and the right edges of G2, G3, and G4 also shifted linearly toward a shorter wavelength, with high sensitivities of -1.432, -1.783, and -2.194 nm/°C, respectively. As shown in Fig. 2(c), the bandwidths of G2 (squares), G3 (circles), and G4 (triangles) hardly changed with the temperature rise. So the proposed filter based on the liquid-filled PCF is wavelength tunable, with a sensitivity of up to 2.194 nm/°C, by means of changing the temperature and has an almost constant bandwidth and a large extinction ratio of more than 40 dB within the whole wavelength tuning range of more than 100 nm.

We investigated the response of the liquid-filled PCF to the bend applied. The liquid-filled PCF was bent using the experimental setup shown in Fig. 3, as reported in [23]. An end of the fiber was fixed, and the other end was moved gradually toward the fixed end. We measured the transmission spectrum evolution of the liquid-filled PCF with the increase in the fiber curvature, as shown

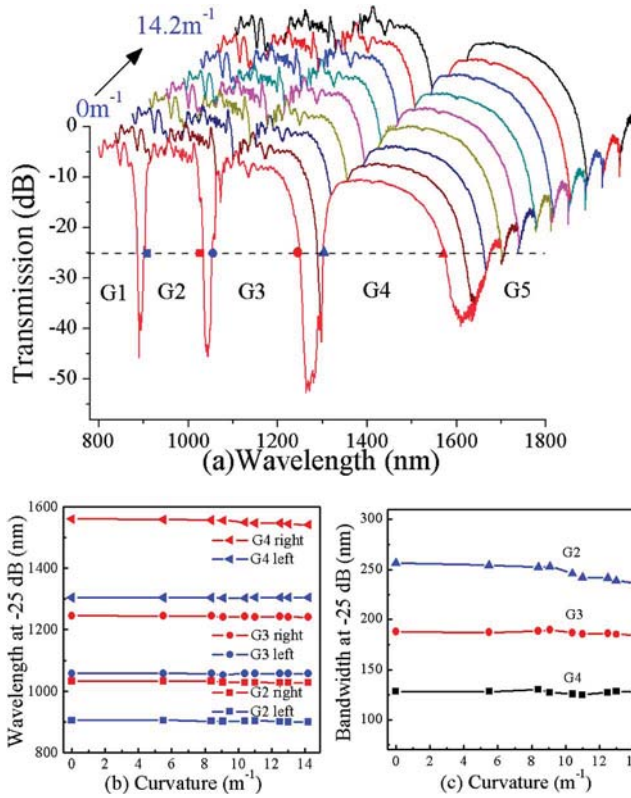


Fig. 3. (a) Transmission spectrum evolution of the liquid-filled PCF with the increase in curvature, (b) wavelengths, corresponding to a transmission of  $-25$  dB, at the left and right edges of the three bandgaps, and (c) the bandwidth of each bandgap versus the curvature.

in Fig. 3(a). The wavelengths, corresponding to the transmission of  $-25$  dB, at the left and right edges of the three bandgaps and the bandwidth of each bandgap are illustrated in Figs. 3(b) and 3(c) in order to evaluate quantitatively the bend-induced shift of the bandgap edges. As shown in Fig. 3, the transmission spectrum of the liquid-filled PCF hardly changed with the increase in the fiber curvature. Also, the bandgap edges and the bandwidths were insensitive to the bend. Hence, the bend of the fiber does not disturb the function of the proposed filter. However, provided a liquid with a low refractive index of 1.480 is used to fill a PCF with a longer length of 200 mm, the transmission spectrum is sensitive to the bend applied, as reported in [24]. So the function of the liquid-filled PCF could depend on the length of the filled PCF and the refractive index of the liquid employed, which will be investigated in our further research.

We investigated the response of the liquid-filled PCF to the tensile strain. An end of the fiber was fixed, and the other end was stretched by use of a translation stage. We measured the transmission spectrum evolution of the liquid-filled PCF with the increase in the tensile strain, as shown in Fig. 4(a). The wavelengths, corresponding to a transmission of  $-25$  dB, at the left and right edges of the three bandgaps and the bandwidth of each bandgap are illustrated in Figs. 4(b) and 4(c) in order to evaluate quantitatively the stretch-induced shift of the bandgap edges. As shown in Fig. 4, the transmission spectrum of the liquid-filled PCF hardly changed with the increase

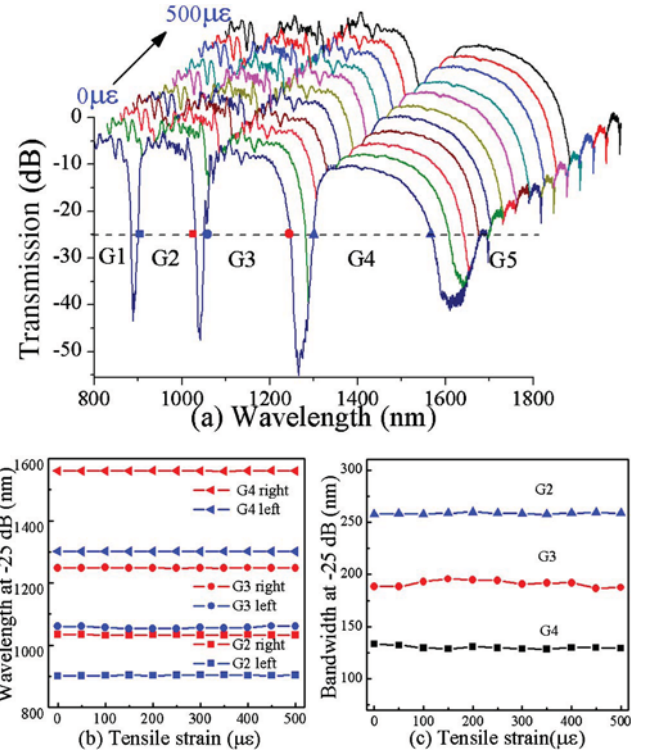


Fig. 4. (a) Transmission spectrum evolution of the liquid-filled PCF with the increase in the tensile strain from 0 to  $500$   $\mu\text{e}$  with steps of  $50$   $\mu\text{e}$ , (b) the wavelengths, corresponding to a transmission of  $-25$  dB, at the left and right edges of the three bandgaps, and (c) the bandwidth of each bandgap versus the tensile strain.

in the tensile strain. Also, the bandgap edges and the bandwidths were insensitive to the stretch force. Hence, the tensile strain of the fiber does not disturb the function of the proposed filter.

We have fabricated five liquid-filled PCF samples with the same parameters and then investigated their response to temperature, bend, and tensile strain. The same experimental results were achieved. In other words, the bandgap of each liquid-filled PCF sample is sensitive to temperature and insensitive to bend and tensile strain, which is the advantage of our bandgap-induced filters. In contrast, the optical properties of the mode-coupling-induced filters, e.g., long-period fiber gratings, are usually sensitive to temperature, bend, and tensile strain [23].

A full-vectorial plane wave method [1] was used to calculate modal maps, i.e., effective index curves, for the modes guided in the liquid-filled PCF at temperatures of  $23^\circ\text{C}$  and  $100^\circ\text{C}$ , as shown in Fig. 5. Thermo-optic effects of both the filling liquid and the pure silica background were taken into consideration in the calculations. To compare with the calculated results, we also measured the transmission spectra of the liquid-filled PCF at the same temperatures. As shown in Fig. 5, the simulation results and the experimental measurements show, in general, good qualitative agreement. Moreover, five bandgaps are observed in both the calculated modal maps and the measured transmission spectra at a temperature of  $23^\circ\text{C}$  within the wavelength range from 800 to 1700 nm. As shown in Fig. 5(b), the bandgap, i.e., G1,

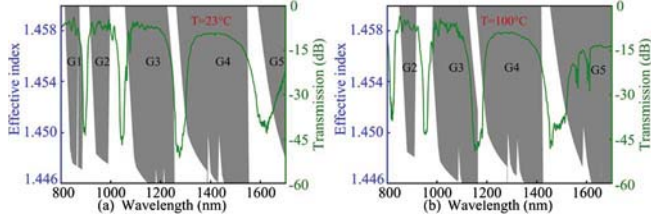


Fig. 5. Calculated bandgap maps and measured transmission spectra of the liquid-filled PCF at a temperature of (a) 23°C and (b) 100°C.

located at the shortest wavelength disappeared and another bandgap, i.e., G5, located at the longest wavelength was gradually observed at a temperature of 100°C, resulting from the blueshift of the bandgaps with the rise in temperature from 23°C to 100°C due to the negative thermo-optic coefficient of the filled liquid.

In summary, the liquid-filled PCF could be used to develop a compact tunable multibandpass filter with a short size of about 9 mm and a high wavelength tuning sensitivity of up to  $-2.194 \text{ nm}^{\circ}\text{C}$ . Such a PCF-based filter maintains an almost constant bandwidth and a large extinction ratio of more than 40 dB within the whole tuning range of the wavelength. Moreover, both the tensile strain and the bend of the fiber do not disturb the function of the PCF-based filter, because the transmission spectrum of the filter is insensitive to the stretch force and the bend. Thus, our proposed filter could find wide application in all-fiber optical communication systems.

This work was supported by the National Natural Science Foundation of China (grants no. 11174064, 61308027, and 61377090), the Science & Technology Innovation Commission of Shenzhen (grants no. KQCX20120815161444632 and JCYJ20130329140017262), and the Distinguished Professors Funding from Shenzhen University and Guangdong Province Pearl River Scholars.

## References

1. K. R. Sohn and K. T. Kim, Opt. Lett. **30**, 2688 (2005).
2. A. M. Vengsarkar, P. J. Lemaire, J. B. Judkins, V. Bhatia, T. Erdogan, and J. E. Sipe, J. Lightwave Technol. **14**, 58 (1996).
3. Y. Wang, W. Jin, J. Ju, H. Xuan, H. L. Ho, L. Xiao, and D. Wang, Opt. Express **16**, 2784 (2008).
4. T. Erdogan, J. Opt. Soc. Am. A **14**, 1760 (1997).
5. B.-W. Liu, M.-L. Hu, X.-H. Fang, Y.-F. Li, L. Chai, J.-Y. Li, W. Chen, and C.-Y. Wang, IEEE Photon. Technol. Lett. **20**, 581 (2008).
6. B. Yu, G. Pickrell, and W. Anbo, IEEE Photon. Technol. Lett. **16**, 2296 (2004).
7. C. Tang and Y. Jiang, Opt. Eng. **48**, 114401 (2009).
8. A. D. Kersey, T. A. Berkoff, and W. W. Morey, Opt. Lett. **18**, 1370 (1993).
9. J. C. Knight, Nature **424**, 847 (2003).
10. P. Russell, Science **299**, 358 (2003).
11. Y. Wang, X. Tan, W. Jin, D. Ying, Y. L. Hoo, and S. Liu, Opt. Lett. **35**, 88 (2010).
12. D. Noordegraaf, L. Scolari, J. Lægsgaard, T. T. Alkeskjold, G. Tartarini, E. Borelli, P. Bassi, J. Li, and S.-T. Wu, Opt. Lett. **33**, 986 (2008).
13. P. Steinurzel, B. J. Eggleton, C. M. de Sterke, and M. J. Steel, Electron. Lett. **41**, 463 (2005).
14. X. Tan, L. Zhang, W. Jiang, Q. Zhang, and J. Zhou, Opt. Eng. **52**, 015010 (2013).
15. Y. Peng, J. Hou, Y. Zhang, Z. Huang, R. Xiao, and Q. Lu, Opt. Lett. **38**, 263 (2013).
16. M. M. Tefelska, S. Ertman, T. Woliński, R. Dąbrowski, and P. Mergo, Photonics Lett. Pol. **5**, 14 (2013).
17. W. Yiping, H. Bartelt, W. Ecke, K. Moerl, H. Lehmann, K. Schroeder, R. Willsch, J. Kobelke, M. Rothhardt, R. Spittel, S. Liye, S. Brueckner, J. Wei, T. Xiaoling, and J. Long, IEEE Photon. Technol. Lett. **22**, 164 (2010).
18. Y. Wang, S. Liu, X. Tan, and W. Jin, J. Lightwave Technol. **28**, 3193 (2010).
19. Y. J. Rao, X. K. Zeng, Y. P. Wang, T. Zhu, Z. L. Ran, L. Zhang, and I. Bennion, in *15th Optical Fiber Sensors Conference Technical Digest* (IEEE, 2002), Vol. 1, pp. 207–210.
20. Y. Yu, X. Li, X. Hong, Y. Deng, K. Song, Y. Geng, H. Wei, and W. Tong, Opt. Express **18**, 15383 (2010).
21. Y. Wang, W. Jin, L. Jin, X. Tan, H. Bartelt, W. Ecke, K. Moerl, K. Schroeder, R. Spittel, R. Willsch, J. Kobelke, M. Rothhardt, L. Shan, and S. Brueckner, Opt. Lett. **34**, 3683 (2009).
22. L. Xiao, M. S. Demokan, W. Jin, Y. Wang, and C.-L. Zhao, J. Lightwave Technol. **25**, 3563 (2007).
23. Y. Wang, H. Bartelt, S. Brueckner, J. Kobelke, M. Rothhardt, K. Mörl, W. Ecke, and R. Willsch, Opt. Express **16**, 7258 (2008).
24. Y. Wang, X. Tan, W. Jin, S. Liu, D. Ying, and Y. L. Hoo, Opt. Express **18**, 12197 (2010).

# High-sensitivity strain sensor based on inflated long period fiber grating

Xiaoyong Zhong,<sup>1</sup> Yiping Wang,<sup>1,2</sup> Junle Qu,<sup>1,3</sup> Changrui Liao,<sup>1</sup> Shen Liu,<sup>1</sup> Jian Tang,<sup>1</sup> Qiao Wang,<sup>1</sup> Jing Zhao,<sup>1</sup> Kaiming Yang,<sup>1</sup> and Zhengyong Li<sup>1</sup>

<sup>1</sup>Key Laboratory of Optoelectronic Devices and Systems of Ministry of Education and Guangdong Province, College of Optoelectronic Engineering, Shenzhen University, Shenzhen 518060, China

<sup>2</sup>e-mail: ypwang@szu.edu.cn

<sup>3</sup>e-mail: jlqu@szu.edu.cn

Received July 11, 2014; revised August 17, 2014; accepted August 18, 2014;  
posted August 19, 2014 (Doc. ID 216723); published September 15, 2014

We demonstrated a high-sensitivity strain sensor based on an inflated long period fiber grating (I-LPFG). The I-LPFG was inscribed, for the first time to the best of our knowledge, by use of the pressure-assisted CO<sub>2</sub> laser beam scanning technique to inflate periodically air holes of a photonic crystal fiber. Such periodic inflations enhanced the sensitivity of the LPFG-based strain sensor to  $-5.62 \text{ pm}/\mu\epsilon$ . After high temperature annealing, the I-LPFG achieved a good repeatability and stability of temperature response with a sensitivity of  $11.92 \text{ pm}/^\circ\text{C}$ . © 2014 Optical Society of America

**OCIS codes:** (060.5295) Photonic crystal fibers; (050.2770) Gratings; (060.2340) Fiber optics components; (060.2370) Fiber optics sensors.

<http://dx.doi.org/10.1364/OL.39.005463>

Long period fiber gratings (LPFGs) inscribed in photonic crystal fibers (PCFs) have been extensively explored for telecommunication and sensor applications [1–3]. Various inscription methods, such as CO<sub>2</sub> laser irradiation [4,5], electric arc discharge [6,7], mechanical pressure [8,9], and femtosecond laser exposure [10,11], have been demonstrated to write LPFGs in different types of PCFs. Among these methods, the CO<sub>2</sub> laser irradiation method is particularly flexible and low cost, because it could be applied to write a LPFG in a pure-silica PCF without photosensitivity [12,13] and a hollow-core photonic bandgap fiber (PBF) [14]. And the writing process usually is computer programmed to produce complicated grating profiles. Unfortunately, the strain sensitivity of the CO<sub>2</sub>-laser-induced LPFGs without physical deformation is usually very low, e.g., only  $-0.45 \text{ pm}/\mu\epsilon$  and  $-0.19 \text{ pm}/\mu\epsilon$  in Corning SMF-28 fiber [15] and in the PCF [12], respectively. Recently a pressure-assisted electrode arc discharge (EAD) technique was first demonstrated to avoid the collapse of air holes during the inscription of a LPFG in a hollow-core PBF [16].

In this Letter, a type of novel inflated long period fiber gratings (I-LPFGs) was inscribed in a solid-core PCF by use of a pressure-assisted CO<sub>2</sub> laser beam scanning technique to inflate periodically air holes along the fiber axis. To the best of our knowledge, the I-LPFG was inscribed successfully in a solid-core PCF for the first time. Such an I-LPFG exhibited a high strain sensitivity of  $-5.62 \text{ pm}/\mu\epsilon$  attributable to periodic inflations of air holes.

We built a CO<sub>2</sub> laser irradiation system for inscribing an I-LPFG in a PCF by means of improving the experimental setup reported in Ref. [17] and integrating a high-pressure air pump. As shown in Fig. 1, such a system consisted of an industrial CO<sub>2</sub> laser with a maximum power of 10 W (SYNRAD 48-1) and a power stability of  $\pm 2\%$ , an electric shutter for turning on/off the laser beam, an infrared lens with a focused length of 63.5 mm, a four-times beam expander for decreasing the diameter of the focused laser spot, and a computer-controlled

two-dimensional ultra-precision translation stage with a minimum incremental motion of 10 nm and a bi-directional repeatability of 80 nm. A PCF (NKT LMA-10) was employed and situated at the focal plane of the CO<sub>2</sub> laser beam and then periodically exposed via the computer-controlled two-dimensional translation stage. A broadband light source (NKT Photonics SuperK) and an optical spectrum analyzer (OSA) (YOKOGAWA AQ6370C) were employed to monitor transmission spectrum evolution of the inscribed LPFG. An air pump with a maximum pressure of 2.5 MPa was employed to provide high-pressure air inside the holes of the PCF, as described below.

First, as shown in Fig. 1(b), an end of a silica tube with an inner/outer diameter of 75/127  $\mu\text{m}$  was spliced with a single-mode fiber (SMF) by use of a commercial fusion

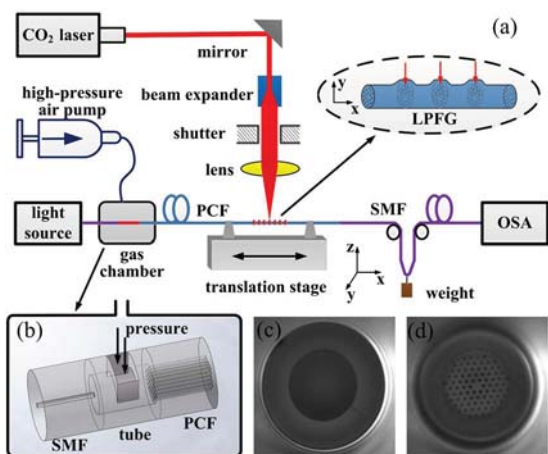


Fig. 1. (a) Experimental setup for I-LPFG inscription with a pressure-assisted CO<sub>2</sub> laser beam scanning technique, (b) schematic diagram of the gas chamber for air passing through the silica tube into air holes of the PCF, (c) and (d) microscope images of the cross sections of the silica tube and the PCF located at the spliced joint.

splice (FSM-60) in the manual mode. Second, another end of the silica tube was cleaved to shorten its length to be  $\sim 100 \mu\text{m}$  and then spliced with a PCF (NKT LMA-10). As shown in Fig. 1(d), although air holes located within the two outer rings were sealed due to arc discharge, the rest of the air holes of the PCF at the spliced joint between the silica tube and the PCF were still open so that air could pass through the silica tube into the holes of the PCF. Third, a microcavity ( $50 \times 40 \mu\text{m}$ ) was fabricated on the sidewall of the silica tube by use of a femtosecond laser pulse (with a central wavelength of 800 nm, a pulse duration time of 120 fs, and a repetition rate of 1 kHz) to create a channel so that air could pass from the gas chamber into the silica tube. Fourth, another end of the PCF was spliced with another SMF and then attached with a small weight of  $\sim 5 \text{ g}$  to keep the fiber straight and to provide a constant prestrain in the fiber, thus enhancing the efficiency of grating inscription [18]. Finally, the silica tube with a channel was placed into a gas chamber, as illustrated in Fig. 1(b).

As shown in Figs. 1 and 2(a), air with a pressure of 1.5 MPa accessed the holes of the PCF via the gas chamber by use of the high-pressure air pump. As shown in Fig. 2(b), the PCF was periodically heated along the fiber axis by the focused CO<sub>2</sub> laser beam. As shown in Fig. 2(c), the holes of the PCF were inflated within the heated region, resulting from high-pressure air and the CO<sub>2</sub>-laser-induced high temperature. Such inflations induce periodically refractive index modulation along the fiber axis, thus inscribing an I-LPFG in the PCF. The periodical heating process above may be repeated for  $K$  cycles from the first grating period to the last grating period until a desired I-LPFG is achieved. As shown in Fig. 3, a high-quality I-LPFG with 30 grating periods and a grating pitch of 480  $\mu\text{m}$  was inscribed in the PCF after the number of scanning cycles ( $K$ ) increased from 1 to 11, where the attenuations at the resonant wavelengths of Dip<sub>1</sub> and Dip<sub>2</sub> are -30.2 dB at 1581.4 nm and -5.5 dB at 1441.1 nm, respectively.

During grating inscription, it is very necessary to real-time monitor the transmission spectrum evolution for achieving a desired LPFG with a required resonant

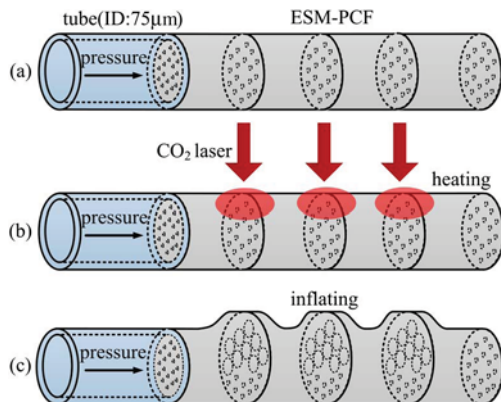


Fig. 2. Schematic diagram of I-LPFG inscription in a PCF with CO<sub>2</sub> laser irradiation. (a) High-pressure air accessed into the holes of the PCF via the gas chamber. (b) The PCF was periodically heated along the fiber axis by the focused CO<sub>2</sub> laser beam. (c) The holes of the PCF were periodically inflated along the fiber axis, and thus inscribing an I-LPFG in the PCF.

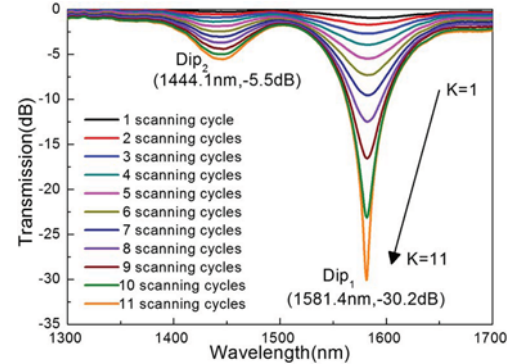


Fig. 3. Transmission spectrum evolution of a CO<sub>2</sub>-laser-inscribed I-LPFG with 30 grating periods and a grating pitch of 480  $\mu\text{m}$  while the number of scanning cycles ( $K$ ) increases from 1 to 11.

wavelength and attenuation dip. In case air was directly pumped into air holes of the PBF end, as reported in [16], it is impossible to real-time monitor the transmission spectrum evolution during grating inscription. So an improved pressure-assisted technique was demonstrated in our experiments, as shown in Fig. 1. That is, the silica tube with a created channel was spliced with the PCF end in order to monitor in real-time the transmission spectrum evolution of the I-LPFG during grating inscription. We inscribed a few I-LPFGs with the same grating pitch and number of grating periods, and the results exhibit an excellent repeatability with a small wavelength error of less than  $\pm 5 \text{ nm}$ , which indicates a good, consistent result for grating inscription.

As shown in Fig. 4(a), air holes of the PCF employed have an average diameter of 1.8  $\mu\text{m}$  and a center-to-center distance of 6.1  $\mu\text{m}$ . The core and cladding diameters of the PCF are 10.4 and 125  $\mu\text{m}$ , respectively. We observed the cross sections of the PCF by use of a microscope before and after CO<sub>2</sub> laser irradiation. As shown in Figs. 4(b) and 4(c), part of the air holes clearly inflated within the fiber side facing the CO<sub>2</sub> laser irradiation, which resulted from the single-side irradiation of the CO<sub>2</sub> laser and the strong CO<sub>2</sub> laser energy absorption of silica glass. Compared with the PCF diameter of 125  $\mu\text{m}$ , the inflated region of the PCF has a diameter of 130  $\mu\text{m}$  along the CO<sub>2</sub> laser irradiation direction.

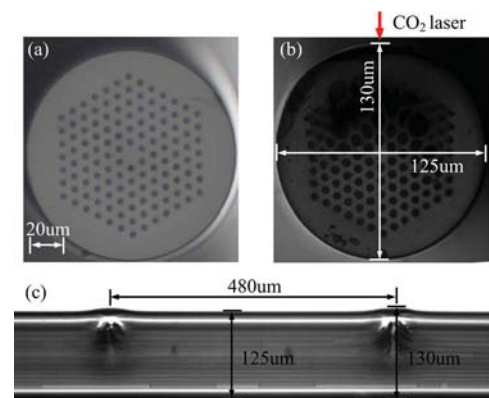


Fig. 4. Microscope image of the cross section of the PCF (a) before and (b) after CO<sub>2</sub> laser irradiation, (c) side view of the CO<sub>2</sub>-laser-inscribed I-LPFG with periodic inflation.

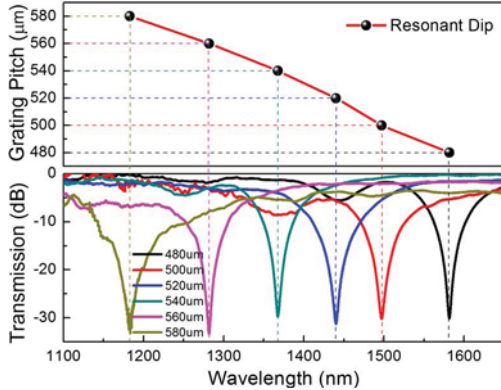


Fig. 5. Variation of I-LPFG resonant wavelengths with grating pitch (upper panel) and their transmission spectra (lower panel). These I-LPFGs are with 30 grating periods and grating pitches of 480, 500, ..., and 580  $\mu\text{m}$ , respectively.

Uneven expansion of the holes illustrated in Fig. 4(b) may be due to the inhomogeneity of the holes in the PCF. So the I-LPFG is an asymmetrical in-fiber grating, thus resulting in a high strain sensitivity [13,19], as described below.

To investigate the phase matching condition as a function of resonant wavelength, six I-LPFGs with the same number of grating periods ( $N = 30$ ) and different pitches of 480, 500, ..., and 580  $\mu\text{m}$  were inscribed in the PCF. We measured their transmission spectra and resonant wavelengths as functions of the grating pitch. As shown in Fig. 5, the resonant wavelength of the I-LPFGs decreases with the increase of grating pitch, which is opposite to the LPFGs in the conventional SMFs, and in agreement with the previously reported results of LPFGs inscribed in solid-core PCFs [11,20] and in air–core photonic bandgap fibers [14].

A polarization controller was integrated between the light source and the inscribed I-LPFG to investigate the influence of the grating birefringence. While the fiber loops of the polarization controller were rotated to change the state of polarization of the input light, as shown in Fig. 6, the attenuation dip of the I-LPFG was split into two dips corresponding to two polarized light resonance, which indicates that the I-LPFG has a high birefringence due to asymmetric inflations resulting from single-side CO<sub>2</sub> laser exposure. Detailed birefringence

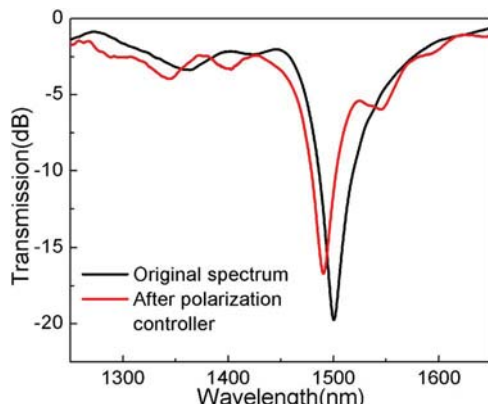


Fig. 6. Transmission spectra of the I-LPFG with (red curve) and without (black curve) using a polarization controller.

response and polarization dependent loss of the I-LPFG will be investigated in our further work.

We investigated the strain responses of the I-LPFG sample with a pitch of 480  $\mu\text{m}$ . The resonant wavelength of the I-LPFG was measured while the tensile strain was increased from 0 to 500  $\mu\text{e}$  with a step of 50  $\mu\text{e}$ . An OSA and a light source were employed to monitor transmission spectrum evolution of the I-LPFG during stretching the grating sample. As shown in Fig. 7(a), the resonant wavelength was shifted linearly toward a shorter wavelength with the increased tensile strain. As shown in Fig. 7(b), the strain sensitivity of the I-LPFG is  $-5.62 \text{ pm}/\mu\text{e}$ , which is one order of magnitude higher than that of the conventional CO<sub>2</sub>-laser-induced LPFGs written in the same type of PCF in which no air holes were periodically inflated [12]. In contrast, the peak transmission attenuation of I-LPFG is hardly changed with an increase of the tensile stain. It is obvious that periodic inflations in our I-LPFGs enhance effectively the strain sensitivity of the grating. The reason for this could be the asymmetry of the I-LPFG and the stretch-induced periodic microbends along the fiber axis [13,19]. Another five I-LPFG samples with different grating pitches illustrated in Fig. 5 were also investigated; and similar strain sensitivity were achieved. Here, only the strain response of the grating sample with a pitch of 480  $\mu\text{m}$  was given in Fig. 7. So our I-LPFGs could be used to develop high-sensitivity strain sensors.

We investigated the annealing behavior of our I-LPFGs to improve the repeatability of their temperature

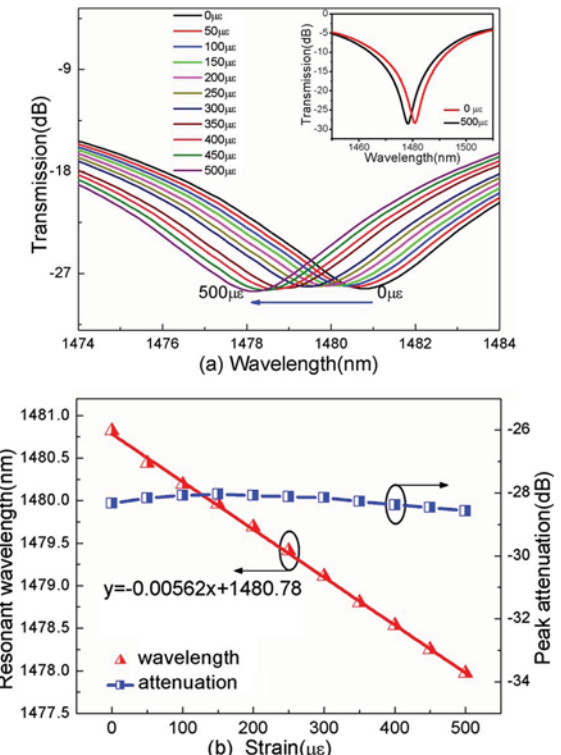


Fig. 7. (a) Transmission spectrum evolution of an I-LPFG sample with a pitch of 480  $\mu\text{m}$  while the tensile strain increases from 0 to 500  $\mu\text{e}$ . Inset illustrates the transmission spectrum evolution within a large wavelength range. (b) Measured resonant wavelength and peak attenuation of the I-LPFG as a function of tensile strain.

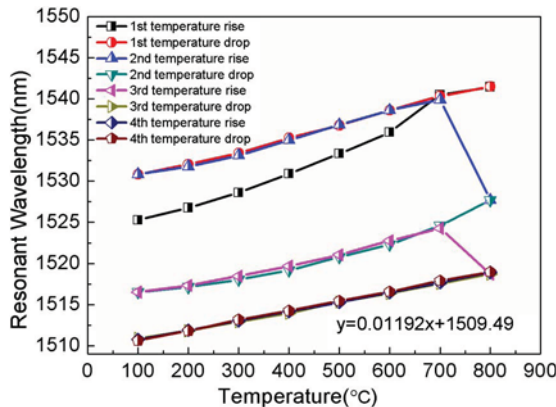


Fig. 8. Measured resonant wavelength of the I-LPFG during temperature rising and dropping.

response. An I-LPFG with a period of  $480\text{ }\mu\text{m}$  was placed in a tube furnace whose temperature can rise from room temperature to  $800^\circ\text{C}$ . An OSA and a light source were employed to monitor transmission spectrum evolution of the I-LPFG during heating and cooling the grating sample. The I-LPFG sample was heated from  $100^\circ\text{C}$  to  $800^\circ\text{C}$  with a step of  $100^\circ\text{C}$ , and then cooled down to  $100^\circ\text{C}$  in the same step. After a desired temperature was achieved each time, the temperature was maintained for 30 min, and then the resonant wavelength of the I-LPFG was recorded. Such a temperature rise-and-drop cycle was repeated four times to anneal the I-LPFG. During temperature rising or dropping, as shown in Fig. 8, the resonant wavelength shifted toward a longer or shorter wavelength, respectively. The resonant wavelength occurred as a sharp shift at the temperature of about  $700^\circ\text{C}$ – $800^\circ\text{C}$  at the first, second, and third temperature rise-and-drop cycles, which may result from the glass densification, frozen-in stresses, or glass volume expending [20,21]. At and after the fourth temperature rise-and-drop cycle, the resonant wavelength linearly shifted with a sensitivity of  $11.92\text{ pm}/^\circ\text{C}$ , and good repeatability was observed during temperature rising and dropping. So the anneal experiment improved effectively the repeatability of the I-LPFG's temperature response. Other I-LPFG samples with different grating pitches were also annealed with the same process above, and similar temperature responses were observed. Similar to the temperature response above and reported in [13,22], the LPFGs inscribed in pure-silica PCFs exhibit a low-temperature sensitivity or insensitivity to temperature due to the pure-silica core, which could reduce or avoid the cross sensitivity between stain and temperature in practical sensing applications.

In summary, we demonstrated a novel method for inscribing an I-LPFG in a PCF by using the pressure-assisted  $\text{CO}_2$  laser beam scanning technique. This technique combined with pressure actuation inside air holes can modify the size and shape of the holes and thus induce refractive index perturbation of the PCF. The PCF's holes filled with high-pressure air were periodically heated and inflated by use of a focus  $\text{CO}_2$  laser

beam, and thus formed an I-LPFG. Periodic inflations of the holes enhanced the strain sensitivity of the I-LPFG to  $-5.62\text{ pm}/\mu\text{e}$ . Hence, such an I-LPFG could be used to develop a promising high-sensitivity strain sensor. Moreover, after high temperature annealing, the I-LPFG demonstrated a good repeatability and stability of temperature response, and a sensitivity of  $11.92\text{ pm}/^\circ\text{C}$  was achieved.

This work was supported by the National Science Foundation of China (Grant Nos. 61308027, 61377090, and 11174064), the Science & Technology Innovation Commission of Shenzhen (Grant Nos. KQCX20120815161444632 and JCYJ20130329140017262), and the Distinguished Professors Funding from Shenzhen University and Guangdong Province Pearl River Scholars.

## References

- Y. Wang, *J. Appl. Phys.* **108**, 081101 (2010).
- L. Rindorf, J. B. Jensen, M. Dufva, L. H. Pedersen, and O. Bang, *Opt. Express* **14**, 8224 (2006).
- Y. P. Wang, L. M. Xiao, D. N. Wang, and W. Jin, *Opt. Lett.* **32**, 1035 (2007).
- G. Kakarantzas, T. Birks, and P. S. J. Russell, *Opt. Lett.* **27**, 1013 (2002).
- Y. P. Wang, Y. J. Rao, Z. L. Ran, T. Zhu, and A. Z. Hu, *IEEE Photon. Technol. Lett.* **15**, 251 (2003).
- G. Humbert, A. Malki, S. Fevrier, P. Roy, and D. Pagnoux, *Electron. Lett.* **39**, 349 (2003).
- H. Y. Choi, K. S. Park, and B. H. Lee, *Opt. Lett.* **33**, 812 (2008).
- J. H. Lim, K. S. Lee, J. C. Kim, and B. H. Lee, *Opt. Lett.* **29**, 331 (2004).
- D. Noordegraaf, L. Scolari, J. L. Søgaard, L. Rindorf, and T. T. Alkeskjold, *Opt. Express* **15**, 7901 (2007).
- C. Florea and K. A. Winick, *J. Lightwave Technol.* **21**, 246 (2003).
- S. Liu, L. Jin, W. Jin, D. Wang, C. Liao, and Y. Wang, *Opt. Express* **18**, 5496 (2010).
- Y. Zhu, P. Shum, H.-W. Bay, M. Yan, X. Yu, J. Hu, J. Hao, and C. Lu, *Opt. Lett.* **30**, 367 (2005).
- Y. P. Wang, L. M. Xiao, D. N. Wang, and W. Jin, *Opt. Lett.* **31**, 3414 (2006).
- Y. Wang, W. Jin, J. Ju, H. Xuan, H. L. Ho, L. Xiao, and D. Wang, *Opt. Express* **16**, 2784 (2008).
- Y. J. Rao, Y. P. Wang, Z. L. Ran, and T. Zhu, *J. Lightwave Technol.* **21**, 1320 (2003).
- A. Iadicicco, S. Campopiano, and A. Cusano, *IEEE Photon. Technol. Lett.* **23**, 1567 (2011).
- X. Y. Zhong, Y. P. Wang, C. R. Liao, G. L. Yin, J. T. Zhou, G. J. Wang, B. Sun, and J. Tang, *IEEE Photon. J.* **6**, 2201508 (2014).
- H. W. Lee and K. S. Chiang, *Opt. Express* **17**, 4533 (2009).
- Y. P. Wang, D. N. Wang, W. Jin, Y. J. Rao, and G. D. Peng, *Appl. Phys. Lett.* **89**, 151105 (2006).
- K. Morishita and Y. Miyake, *J. Lightwave Technol.* **22**, 625 (2004).
- Y. J. Rao, D. W. Duan, Y. E. Fan, T. Ke, and M. Xu, *J. Lightwave Technol.* **28**, 1530 (2010).
- H. Dobb, K. Kalli, and D. J. Webb, *Electron. Lett.* **40**, 657 (2004).

# Sub-micron silica diaphragm-based fiber-tip Fabry–Perot interferometer for pressure measurement

Changrui Liao,<sup>1</sup> Shen Liu,<sup>1</sup> Lei Xu,<sup>2</sup> Chao Wang,<sup>1,3</sup> Yiping Wang,<sup>1,\*</sup> Zhengyong Li,<sup>1</sup> Qiao Wang,<sup>1</sup> and D. N. Wang<sup>3</sup>

<sup>1</sup>Key Laboratory of Optoelectronic Devices and Systems of Ministry of Education and Guangdong Province, College of Optoelectronic Engineering, Shenzhen University, Shenzhen 518060, China

<sup>2</sup>Department of Computing, The Hong Kong Polytechnic University, Hong Kong, China

<sup>3</sup>Department of Electrical Engineering, The Hong Kong Polytechnic University, Hong Kong, China

\*Corresponding author: [ypwang@szu.edu.cn](mailto:ypwang@szu.edu.cn)

Received January 23, 2014; revised April 2, 2014; accepted April 7, 2014;  
posted April 8, 2014 (Doc. ID 205172); published May 2, 2014

We demonstrate a sub-micron silica diaphragm-based fiber-tip Fabry–Perot interferometer for pressure sensing applications. The thinnest silica diaphragm, with a thickness of  $\sim 320$  nm, has been achieved by use of an improved electrical arc discharge technique. Such a sub-micron silica diaphragm breaks the sensitivity limitation imposed by traditional all-silica Fabry–Perot interferometric pressure sensors and, as a result, a high pressure sensitivity of  $\sim 1036$  pm/MPa at 1550 nm and a low temperature cross-sensitivity of  $\sim 960$  Pa/ $^{\circ}$ C are achieved when a silica diaphragm of  $\sim 500$  nm in thickness is used. Moreover, the all-silica spherical structure enhanced the mechanical strength of the micro-cavity sensor, making it suitable for high sensitivity pressure sensing in harsh environments. © 2014 Optical Society of America

OCIS codes: (060.2370) Fiber optics sensors; (310.6845) Thin film devices and applications.

<http://dx.doi.org/10.1364/OL.39.002827>

Fiber optic Fabry–Perot interferometric (FPI) pressure sensors have been extensively investigated and used in various areas of biomedicine, automotive industries, and environmental monitoring. Fiber optic FPI sensors have the advantages of ultra-compact size, high sensitivity, excellent thermal stability, and immunity to electromagnetic interference [1,2]. In an FPI-tip pressure sensor, the elastic diaphragm at the fiber tip is usually utilized as one of the reflecting mirrors and may be composed of silica [3–5], polymer [6], silver [7], graphene [8], or even water film [9]. Among them, all-silica FPI sensors have been proved to be the most robust and thermally stable. However, the high modulus of elasticity of silica requires a very thin diaphragm to achieve a reasonable sensitivity, and it is difficult to fabricate a smooth silica diaphragm with the thickness of less than 1  $\mu$ m using conventional micromachining methods; hence, this limits the applicability of all-silica FPI sensors to low-pressure sensing applications.

In this Letter, we propose and experimentally demonstrate, an improved electrical arc discharge fabrication method to construct an all-silica FPI cavity, based on a sub-micron silica diaphragm. Such an all-silica FPI sensor exhibits a high pressure sensitivity of  $\sim 1036$  pm/MPa at 1550 nm, which is three times larger than the formerly reported result [10,11]. Moreover, a low temperature cross-sensitivity of  $\sim 960$  Pa/ $^{\circ}$ C can also be obtained.

Figure 1 illustrates the fabrication process of the all-silica fiber sensors, which involves four steps. In step 1, as shown in Fig. 1(a), the well-cut ends of two single mode fibers (SMFs) were heated to become spherical surfaces with electrical arc discharge using a commercial fusion splicer (Fujikura-60S). The two fiber ends were then immersed into the refractive index-matching oil (from Cargille) to coat the spherical surface. In step 2, as shown in Figs. 1(b) and 1(c), using the fusion splicer, the oil-coated fiber ends were translated into alignment and spliced together with a fusion current of 18 mA and

fusion time of 1200 ms. An extrusion force was exerted to the touching region before splicing. In Fig. 1(b),  $d_0$  denotes the moved distance of the left and right fiber ends, and  $d$  means the half-overlap of the two fiber ends at the touching region. The half-overlap  $d$  is  $\sim 10$   $\mu$ m here. Since the oil at the touching region was heated suddenly, it rapidly expanded to an air bubble. In step 3, as shown in Figs. 1(d) and 1(e), the fiber segment with the air bubble was tapered to crack by electrical arc discharge and an inner bubble was firmly formed on the fiber end. In Figs. 1(d) and 1(e),  $d_2$  and  $d_3$  are the moved distances of the two fiber ends during the fiber-tapering process. In step 4, as shown in Fig. 1(f), a precise electrical arc discharge, with fusion current of  $\sim 18$  mA and fusion time of  $\sim 1200$  ms, was repeatedly implemented at the top end of the bubble. Note that the discharge number should be less than 10 to avoid breaking the bubble. In this step, the silica wall of the bubble is melted while the air in the bubble is thermally expanded to blow up the bubble

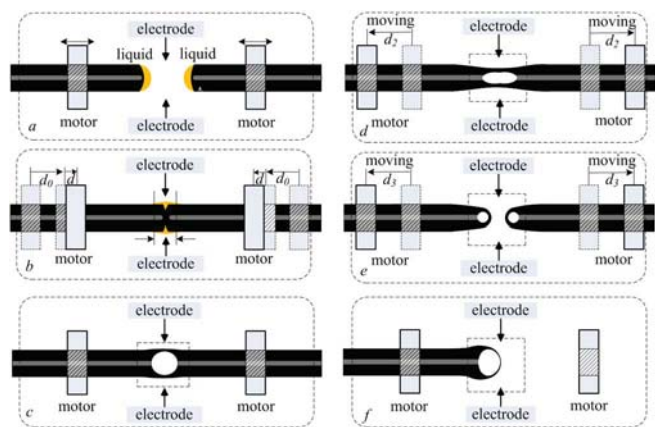


Fig. 1. Schematic diagram of the fabrication process of all-silica fiber-tip FPI sensor using electrical arc discharge assisted with oil coating in advance.

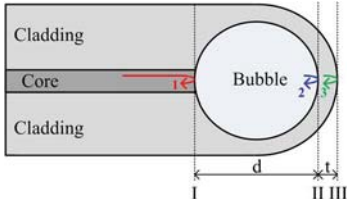


Fig. 2. Schematic diagram of the fiber-tip FPI.

and gradually reduce the thickness of the silica wall. Using this method, we have successfully fabricated an ultra-thin silica wall, with a thickness of hundreds of nanometers, which is actually a sub-micron silica diaphragm. In the whole process, we need only a common fusion splicer; there is no need for additional pressurization or wet chemical etching.

Figure 2 is a schematic diagram of this fiber-tip FPI. Three reflected waves are collected and guided back to the SMF: one is from the bubble bottom, i.e., surface-I, and the other two are from the inner and outer surfaces of the diaphragm, i.e., surface-II and surface-III.

Due to low reflectivity of the silica/air interface (<3.5%), high-order FP interference could be neglected. The light intensity at the sensor output may be expressed as

$$\begin{aligned}
 I = |E|^2 &= \left| E_1 - E_2 \exp\left(\frac{4\pi}{\lambda} n_{\text{air}} d\right) \right. \\
 &\quad \left. + E_3 \exp\left[\frac{4\pi}{\lambda} (n_{\text{silica}} t + n_{\text{air}} d)\right] \right|^2 \\
 &= E_1^2 + E_2^2 + E_3^2 - 2E_1 E_2 \cos\left(\frac{4\pi}{\lambda} n_{\text{air}} d\right) \\
 &\quad - 2E_2 E_3 \cos\left(\frac{4\pi}{\lambda} n_{\text{silica}} t\right) \\
 &\quad + 2E_1 E_3 \cos\left[\frac{4\pi}{\lambda} (n_{\text{silica}} t + n_{\text{air}} d)\right] \\
 &\approx E_1^2 + E_2^2 + E_3^2 - 2(E_1 E_2 - E_1 E_3) \cos\left(\frac{4\pi}{\lambda} n_{\text{air}} d\right) \\
 &\quad - 2E_2 E_3 \cos\left(\frac{4\pi}{\lambda} n_{\text{silica}} t\right) \quad (\text{if } t \rightarrow 0), \tag{1}
 \end{aligned}$$

where  $E_1$ ,  $E_2$ , and  $E_3$  are the amplitudes of the three reflected waves,  $d$  is the length of bubble cavity,  $t$  is the diaphragm thickness,  $\lambda$  is the light wavelength, and  $n_{\text{air}}$  and  $n_{\text{silica}}$  are the refractive indices of air and silica.

Figure 3 shows the optical microscope images and the corresponding reflection spectra of the fiber-tip sensor during the process of thinning the silica diaphragm by the repeating local electrical arc discharge. Since the silica diaphragm is very thin, the modulation of the fringe envelope in Fig. 3 is regarded as the result of the interference between surface-II and surface-III. For FPI, the fringe-envelope spacing can be expressed as  $\lambda^2/2n_{\text{silica}} t$ .

The envelope spacings at different thinning states (states 1–5) in Fig. 3 have been measured to be  $\sim 76$ ,  $\sim 97$ ,  $\sim 139$ ,  $\sim 254$ , and  $\sim 414$  nm, respectively. Thus, the corresponding diaphragm thicknesses can be calculated to be  $\sim 8.4$ ,  $\sim 6.6$ ,  $\sim 4.7$ ,  $\sim 2.2$ , and  $\sim 1.5$   $\mu\text{m}$ , respectively,

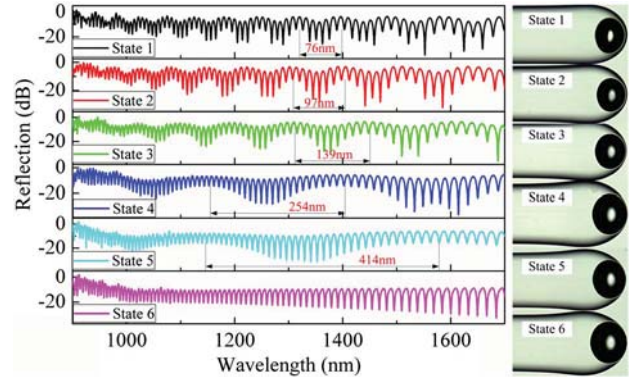


Fig. 3. Reflection spectra and optical microscope images of the fiber-tip FPI pressure sensor at different states of the diaphragm thinning process.

which agree well with the values measured from the optical microscope images.

It is difficult to observe one complete envelope from 900 to 1700 nm for state 6 in Fig. 3. To determine the manufacturing limit of the silica diaphragm thickness, the bubble was cut open using femtosecond laser micro-machining [12]. Figure 4(a) is the scanning electron microscope (SEM) image of the cut plane of the bubble. It can be seen from this figure that the inner surface is very smooth, which helps in increasing its reflectivity. Enlarged partial view of the silica diaphragm is shown in Fig. 4(b), where the diaphragm thickness is measured to be  $\sim 320$  nm. To the best of our knowledge, it is the thinnest silica diaphragm fabricated using an electron arc discharge technique.

The experimental setup to test the proposed fiber-tip pressure sensor is illustrated in Fig. 5, where a broadband light source (BBS) and an optical spectrum analyzer (OSA) with a resolution of 0.01 nm are used, and the reflection spectrum of the sensor is measured by use of a 3-dB fiber coupler. The sensor head is placed into the gas chamber, where a commercial gas pressure generator is incorporated with a high-precision pressure meter (ConST-811) to measure the pressure in the chamber. The pressure chamber is fitted with a feed-through, sealed by strong glue to extend the fiber outside the chamber for real-time measurement.

Three samples with different diaphragm thicknesses have been tested for performance comparison. Figure 6(a) shows the reflection spectrum of the third

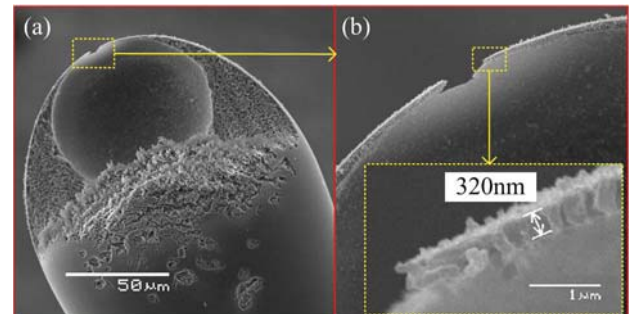


Fig. 4. (a) SEM image of the cut plane of the air bubble. (b) Enlarged partial view of the silica diaphragm at the top end of the bubble.

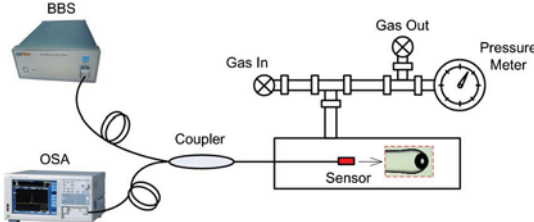


Fig. 5. Experimental setup for gas pressure measurement.

sample, i.e., S3, placed at standard atmospheric pressure and room temperature, where the fringe contrast is  $\sim 25$  dB and the fringe spacing is  $\sim 12.5$  nm at around 1550 nm. In the experiment, the pressure in the chamber was increased from 0 to 2.0 MPa in increments of 0.2 MPa, remaining at each step for 5 min. The reflection spectra at different pressure conditions are illustrated in Fig. 6(b), where it can be seen that, as the pressure increases, the interference dip shifts toward the shorter wavelength, with obviously decreased fringe contrast.

Fringe contrast depends on the relative optical intensity of two interference beams. The reflectivity of surface-I will hardly be changed as the pressure increases, because this surface is well protected in the fiber. Differently, the reflectivity of surface-II is very sensitive to pressure, because the increased pressure will change the flatness of diaphragm. The thinner the diaphragm is, the more significant its deflection. The change in optical intensity reflected from surface-II might result in the variation of fringe contrast. It is believed the best flatness of the diaphragm might be achieved at 0.2 MPa so that we can find an abrupt change at this pressure. To satisfy the requirements of pressure sensitivity and fringe contrast, the diaphragm thickness should be

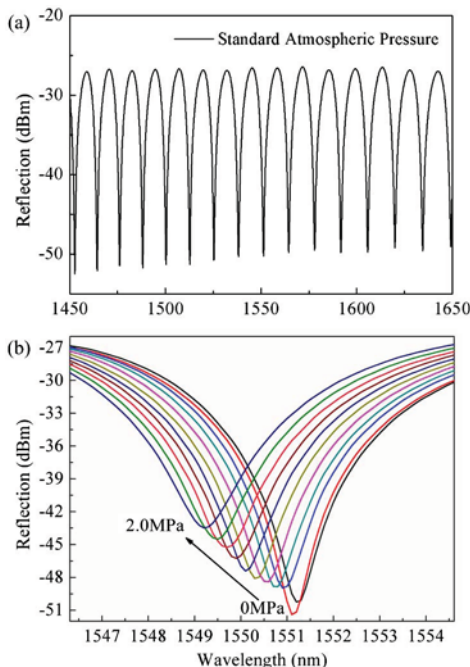


Fig. 6. (a) Reflection spectrum of the third sample, i.e., S3, at standard atmospheric pressure and room temperature. (b) Reflection spectral evolution of the sample S3 with pressure ranging from 0 to 2.0 MPa.

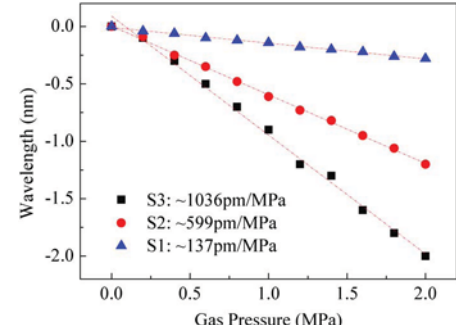


Fig. 7. Wavelength shift of the interference dip at  $\sim 1550$  nm for the three sensor samples with the gas pressure applied.

carefully designed based on the conditions in practical measurement.

The pressure performance of three samples are compared in Fig. 7, where the pressure sensitivities can be calculated to be  $\sim 137$ ,  $\sim 599$ , and  $\sim 1036$  pm/MPa for the samples, i.e., S1, S2, and S3, respectively, by applying a linear fitting of the experimental data. The corresponding diaphragm thicknesses of the three samples are measured as  $\sim 6.7$ ,  $\sim 1.8$ , and  $\sim 0.5$   $\mu\text{m}$ , respectively.

The pressure sensitivity is found to increase as the diaphragm thickness decreases, according to [10]:

$$\frac{\Delta\lambda}{\Delta P} = \frac{(1-\nu)\lambda R^2}{2Edt}, \quad (2)$$

where  $\nu$  is Poisson's ratio,  $\lambda$  is the dip wavelength,  $R$  is the radius of bubble,  $E$  is Young's modulus of silica,  $d$  is the length of bubble cavity, and  $t$  is the diaphragm thickness. The thinnest silica diaphragm in previous reports is 2.2  $\mu\text{m}$ , with the corresponding sensitivity of 315 pm/MPa [10]. Note that the measured sensitivity is not a perfect linear relationship inverse of the diaphragm thickness. In Eq. (2), the bubble is regarded as a thin sphere shell, with a uniform silica wall; in reality, however, the silica wall is not uniform and the central part is much thinner than the surrounding area. The nonuniformity of the wall thickness could result in this nonlinear response.

A simulation model is established in ANSYS to investigate the diaphragm deformation with an increase of pressure. Figure 8(a) shows the simulated deformation of the diaphragm with a thickness of  $\sim 0.5$   $\mu\text{m}$  at 1.0 MPa,

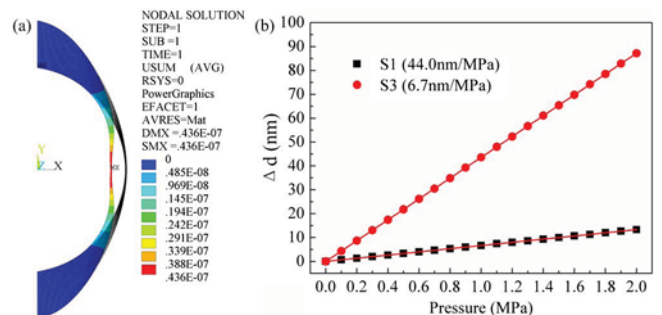


Fig. 8. (a) Simulation model of the diaphragm deformation with increasing pressure. Young's modulus of silica is 73 GPa; Poisson's ratio is 0.17; silica density is  $2700 \text{ kg/m}^3$ . (b) Simulated relationship between the value of the diaphragm deformation and the applied pressure.

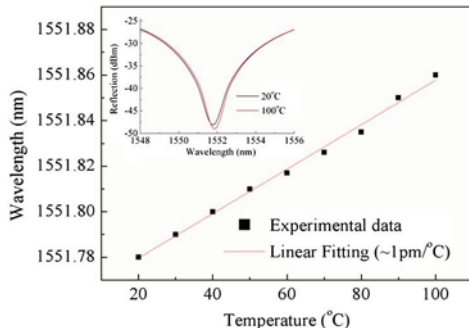


Fig. 9. Linear relationship between the wavelength shift of the interference dip at  $\sim 1550$  nm for sample S3 and ambient temperature. Inset: reflection spectra of sample S3 at  $20^{\circ}\text{C}$  and  $100^{\circ}\text{C}$ .

where the deformation value of different parts is displayed in the note. Using this method, the relationship between the applied pressure and the diaphragm deformation, i.e., the length change of bubble cavity  $\Delta d$ , can be simulated, and the simulation result is shown in Fig. 8(b), where the slopes for the samples S1 and S3 are 6.7 and 44.0 nm/MPa, respectively. The simulated sensitivity of S3 is nearly 7 times larger than that of S1, which agrees well with the experimental result.

Besides reducing the diaphragm thickness, another way to enhance pressure sensitivity is to increase the radius of the bubble. By reducing the diaphragm thickness, the sensor will be compact in size, but its mechanical strength becomes weaker, especially when the diaphragm thickness is less than 1  $\mu\text{m}$ . By increasing the bubble radius, the mechanical strength of sensor is good; however, the increased device size may limit its applications in some precise measurements. The selection of a sensitivity-enhancement method depends on the practical sensing requirements.

The influence of temperature on the fiber sensor has been investigated by placing the device in an electrical oven and gradually increasing the temperature from room temperature to  $100^{\circ}\text{C}$  in increments of  $10^{\circ}\text{C}$  [13–15]. Each tested temperature was maintained for 10 min. The inset of Fig. 9 shows the reflection spectra of the sample S3 at  $20^{\circ}\text{C}$  and  $100^{\circ}\text{C}$ , and a redshift is clearly observed when the temperature is increased. Wavelength shift of the interference dip at  $\sim 1550$  nm with temperature variation is displayed in Fig. 9, where a linear relation is found and the temperature sensitivity obtained is  $\sim 1 \text{ pm}/^{\circ}\text{C}$ . Temperature response of the fiber sensor results from the thermal expansion of the silica bubble. When no temperature compensation is employed in practical measurement, the error resulting from temperature cross-sensitivity is  $\sim 960 \text{ Pa}/^{\circ}\text{C}$ , which could be neglected in the large pressure measurement.

In conclusion, we have experimentally demonstrated a sub-micron silica diaphragm-based fiber-tip FPI for high pressure sensitivity measurement. The ultra-thin silica diaphragm is fabricated using an improved electrical arc discharge technique and the thinnest diaphragm achieved is  $\sim 320$  nm, which might be the thinnest silica diaphragm fabricated by the electron arc discharge method. Pressure response of the fiber FPI sensor has been investigated and the one with a diaphragm thickness of  $\sim 500$  nm exhibits the highest pressure sensitivity of  $\sim 1036 \text{ pm}/\text{MPa}$ . Moreover, such a fiber sensor shows a low temperature cross-sensitivity of  $\sim 960 \text{ Pa}/^{\circ}\text{C}$ . The sub-micron silica diaphragm-based fiber-tip FPI sensors have the advantages of low fabrication cost, high mechanical strength, relatively high pressure sensitivity and low temperature cross-sensitivity, and are promising for high sensitivity pressure sensing in harsh environments.

This work was supported by the National Natural Science Foundation of China (Nos. 11174064, 61308027, 61377090), National Science Foundation of SZU (No. 00036401), Science & Technology Innovation Commission of Shenzhen (Nos. KQCX20120815161444632 and JCYJ20130329140017262), Distinguished Professors Funding from Shenzhen University and Guangdong Province Pearl River Scholars.

## References

- Y. J. Rao, Opt. Fiber Technol. **12**, 227 (2006).
- Y. Wang, D. N. Wang, W. Jin, and X. Fang, IEEE J. Quantum Electron. **42**, 868 (2006).
- D. Donlagic and E. Cibula, Opt. Lett. **30**, 2071 (2005).
- Y. Z. Zhu and A. B. Wang, IEEE Photon. Technol. Lett. **17**, 447 (2005).
- W. H. Wang, N. Wu, Y. Tian, C. Niezrecki, and X. W. Wang, Opt. Express **18**, 9006 (2010).
- H. Bae and M. Yu, Opt. Express **20**, 14573 (2012).
- G. Guo, T. Fink, M. Han, L. Koester, T. Turner, and J. Huang, Opt. Lett. **37**, 1505 (2012).
- J. Ma, W. Jin, H. L. Ho, and J. Y. Dai, Opt. Lett. **37**, 2493 (2012).
- Y. Wang, D. N. Wang, C. Wang, and T. Y. Hu, Opt. Express **21**, 14084 (2013).
- J. Ma, J. Ju, L. Jin, and W. Jin, IEEE Photon. Technol. Lett. **23**, 1561 (2011).
- C. Liao, T. Y. Hu, and D. N. Wang, Opt. Express **20**, 22813 (2012).
- C. Liao, L. Xu, C. Wang, D. N. Wang, Y. Wang, Q. Wang, K. Yang, Z. Li, X. Zhong, J. Zhou, and Y. Liu, Opt. Lett. **38**, 4473 (2013).
- Y. Rao, X. Zeng, Y. Zhu, Y. Wang, T. Zhu, Z. Ran, L. Zhang, and I. Bennion, Chin. Phys. Lett. **18**, 643 (2001).
- Y. Wang, L. Xiao, D. N. Wang, and W. Jin, Opt. Lett. **31**, 3414 (2006).
- C. Liao, D. N. Wang, Y. Li, T. Sun, and K. T. V. Grattan, Appl. Opt. **48**, 3001 (2009).

# Ultrasensitive refractive index sensor based on a Mach-Zehnder interferometer created in twin-core fiber

Zhengyong Li,<sup>1,†</sup> Changrui Liao,<sup>1,†</sup> Yiping Wang,<sup>1,\*</sup> Xiaopeng Dong,<sup>2</sup> Shen Liu,<sup>1</sup> Kaiming Yang,<sup>1</sup> Qiao Wang,<sup>1</sup> and Jiangtao Zhou<sup>1</sup>

<sup>1</sup>Key Laboratory of Optoelectronic Devices and Systems of Ministry of Education and Guangdong Province, College of Optoelectronic Engineering, Shenzhen University, Shenzhen 518060, China

<sup>2</sup>School of Information Science and Engineering, Xiamen University, Xiamen 361005, China

\*Corresponding author: [ypwang@szu.edu.cn](mailto:ypwang@szu.edu.cn)

Received May 29, 2014; revised July 18, 2014; accepted July 21, 2014;  
posted July 21, 2014 (Doc. ID 212897); published August 18, 2014

We proposed and experimentally demonstrated a twin-core fiber (TCF)-based Mach-Zehnder interferometer (MZI) to develop an ultrasensitive refractive index (RI) sensor. This fiber MZI was constructed by splicing a short section of TCF between two sections of single mode fibers. A microchannel was drilled through one core of the TCF by means of femtosecond laser micromachining to create one arm of the proposed interferometer, and the other core worked as the second arm. Such a fiber interferometer exhibits an ultrahigh RI sensitivity of  $-10981 \text{ nm/RIU}$  and a low temperature cross-sensitivity of  $3.96 \times 10^{-6} \text{ RIU/}^{\circ}\text{C}$ . Moreover, the ultra-compact device size and all-fiber configuration make it very suitable for highly sensitive RI sensing at precise location. © 2014 Optical Society of America

OCIS codes: (060.2370) Fiber optics sensors; (140.3390) Laser materials processing; (140.3948) Microcavity devices.  
<http://dx.doi.org/10.1364/OL.39.004982>

Recently, refractive index (RI) sensors based on optical fiber have been extensively investigated and used in various areas of biomedicine, automotive industries, and environmental monitoring. Among them, fiber in-line Mach-Zehnder interferometers (MZIs) are of great interest because of their compact size, high RI sensitivity, immunity to electromagnetic interference, and easy signal detection [1]. So far, many fiber MZI configurations have been realized such as employing long period fiber gratings [2–5], fiber tapers [6,7], offset fusion splicing [8], microfiber-based structures [9,10] and microcavity fabricated by femtosecond (fs) laser micromachining [11,12]. The microcavity-based MZI sensors exhibit much higher RI sensitivities than the other MZI configurations because the optical path difference (OPD) is achieved through light propagation across the fluid-filled cavity, which gives a large effective RI difference.

Fs laser micromachining is an efficient tool for material processing, especially in the fabrication of optical fiber devices, because of its high fabrication efficiency and accurate material processing capability. Several fiber interferometers based on fs-laser induced microcavity have been achieved and used for RI and temperate sensing. Liao *et al.* have reported a highly sensitive RI fiber sensor ( $\sim 9148 \text{ nm/RIU}$ ), which is based on an in-fiber microcavity fabricated by fs laser ablation [13]. However, two arms of the interferometer are not independent of each other so that the measurement accuracy would deteriorate a lot because of the cross talk between the two arms. To overcome this issue, we employ twin-core fiber (TCF) in this work. TCFs are suitable to construct compact fiber in-line interferometers because there are two separate cores being integrated in the same fiber. Several fiber interferometric sensors, which are based on TCFs, have been developed and used for measurement of the RI [14] and curvature [15].

In this Letter we demonstrate an ultra-compact TCF-based MZI, which is fabricated by the means of fs laser micromachining. The fiber interferometer is constructed by splicing a short section of TCF between two SMFs, and the separate cores of the TCF perform as the two interference arms. One arm contains a microchannel, which is created by removing part of one core of the TCF, and the second arm is the other complete core. This TCF-based MZI exhibits an ultrahigh RI sensitivity of  $-10981 \text{ nm/RIU}$  within the RI range between 1.30 and 1.34 and a low cross-sensitivity to a temperature of  $3.96 \times 10^{-6} \text{ RIU/}^{\circ}\text{C}$ . Moreover, the ultra-compact size of the fiber interferometer is able to ensure a precise sensing location.

The schematic diagram of the proposed TCF-based MZI is illustrated in Fig. 1. The light propagating in SMF<sub>1</sub> is divided into two beams in the TCF, which are denoted as  $I_{\text{in}1}$  and  $I_{\text{in}2}$ , respectively.  $I_{\text{in}1}$  remains propagating in core<sub>1</sub> of the TCF while  $I_{\text{in}2}$  travels through the microchannel embedded in core<sub>2</sub>. When the two output beams, i.e.,  $I_{\text{out}1}$  and  $I_{\text{out}2}$  corresponding to  $I_{\text{in}1}$  and  $I_{\text{in}2}$ , recombined in SMF<sub>2</sub>, the interference will take place because of the phase difference between two output beams. The output intensity of TCF-based MZI can be expressed as

$$I = I_{\text{out}1} + I_{\text{out}2} + 2\sqrt{I_{\text{out}1}I_{\text{out}2}} \cos\left(\frac{2\pi L \Delta n}{\lambda} + \varphi_0\right), \quad (1)$$

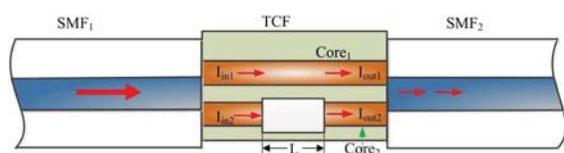


Fig. 1. Schematic diagram of the TCF-based MZI.

where  $\lambda$  is the light wavelength,  $L$  is the length of the microchannel,  $\Delta n = n_{\text{core}} - n_{\text{channel}}$  is the effective RI difference between two interference arms, where  $n_{\text{core}}$  and  $n_{\text{channel}}$  are the effective RI of the core mode and the channel mode, and  $\varphi_0$  is the initial phase of the interference. According to Eq. (1), the interference signal reaches the minimum value when the following condition is satisfied:

$$\frac{2\pi L \Delta n}{\lambda_m} + \varphi_0 = (2m + 1)\pi, \quad (2)$$

where  $m$  is an integer, and  $\lambda_m$  is the wavelength of the  $m$ th order interference dip. The free spectral range (FSR) of such fiber interferometer can be expressed as

$$\text{FSR} = \frac{\lambda^2}{\Delta n L}. \quad (3)$$

The device fabrication involves two steps. First, one end of the TCF was spliced with an SMF (Corning, SMF-28) with a core/cladding diameter of 8/125  $\mu\text{m}$  by using a commercial fusion splicer (Fujikura FSM-60s). The cross-sectional morphology of the TCF supplied by Xiamen University is shown in Fig. 2(a), where the cladding diameter is 125  $\mu\text{m}$  and the major axis and minor axis of the two elliptical cores are measured to be  $\sim 10.9$  and  $\sim 6.5$   $\mu\text{m}$ , respectively. During the splicing, the red laser beam was launched into the SMF<sub>1</sub> and the light intensity of two TCF cores was compared by using an optical microscope. The offset distance between SMF<sub>1</sub> and TCF was carefully adjusted to make sure the light intensity in the two cores becomes roughly equal. Figures 2(b) and 2(c) show the unequal and equal splitting ratios when different offsets are employed. In the experiment the TCF with a length of  $\sim 200$   $\mu\text{m}$  was used and the other end of the TCF was spliced with another SMF<sub>2</sub> with an optimized offset value to obtain the maximum intensity output.

Second, a microchannel was drilled in the TCF by means of fs laser micromachining. The schematic diagram of fs laser micromachining system is shown in

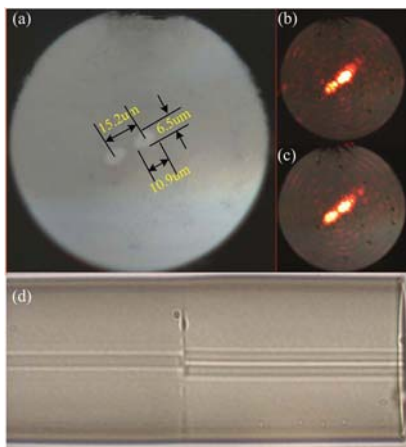


Fig. 2. (a) Optical microscope image of the cross-sectional morphology of the TCF; (b) unequal intensity distribution on the end face of TCF; (c) equal intensity distribution on the end face of TCF; (d) splicing point between SMF and TCF.

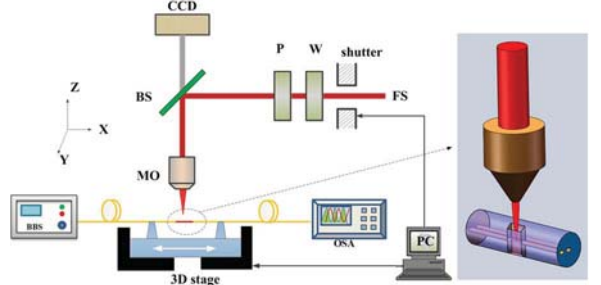


Fig. 3. Schematic diagram of the fs laser micromachining system, which is employed to fabricate in-fiber structure.

Fig. 3. The fs laser (Spectra-Physics, Solstice) with the wavelength of 800 nm, the pulse duration of 120 fs, and the repetition rate of 1 kHz was employed. A laser beam was focused onto the fiber by an objective lens with an NA value of 0.25. The laser power was adjustable in the range between 0 and 4 mJ by rotating a half-wave plate followed by a polarizer, and the average on-target laser power was maintained at  $\sim 20$  mW. A broadband light source (BBS) and an optical spectrum analyzer (OSA) were connected to the fiber to measure its transmission spectrum in real time.

The fiber was fixed on a PC-controlled three-axis (XYZ) translation stage with a resolution of 10 nm, in parallel with the Y axis. The laser beam was initially focused into the center of the core<sub>2</sub> of TCF and then shifted by 15  $\mu\text{m}$  away from the Y axis. The microchannel was directly drilled by fs laser ablation, scanning in parallel with Y axis at a speed of 5  $\mu\text{m}/\text{s}$  with the scanning distance of 40  $\mu\text{m}$  along the fiber axis and then returned to the starting point, which is definite to be one scanning cycle. After each scanning cycle, the focal point of the laser beam was moved toward the core along the Y axis with a step of 3  $\mu\text{m}$  before the next cycle started. When the interference spectrum emerged, the step was reduced to 1  $\mu\text{m}$  until the expected transmission spectrum was obtained. Finally, the microchannel was cleaned by using alcohol after laser fabrication. The optical microscope images of the microchannel in two perpendicular directions were shown in Fig. 4. To learn the real size of the microchannel at the fiber core, the sample was first immersed into the oil with a similar RI to silica in order to improve the image quality and then the microscope focus was moved from the fiber top surface to the core. The rough size of the microchannel at the core can be observed in Fig. 4(a). To learn the accurate size of the microchannel, we need to cut off the microchannel to observe the cross-sectional morphology as shown in

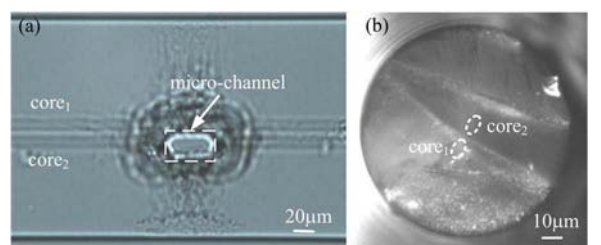


Fig. 4. Optical microscope images of the microchannel from (a) the top view and (b) the side view.

Fig. 4(b). The relatively large surface roughness implies that the employed laser power was somewhat high. Better surface quality may be achieved by optimizing the processing parameters, including laser power and scanning speed [12].

The transmission spectrum in the air of the MZI with a microchannel of 43  $\mu\text{m}$  in length is denoted by the black line in Fig. 5(b), where an insertion loss of  $\sim 10$  dB and a fringe visibility of  $\sim 17$  dB are achieved. There might be three factors causing the large insertion loss: (1) the laser induced rough surface; (2) the loss from the unguided mode propagating through the microchannel; and (3) the loss from fusion splicing. By optimizing the parameters in fusion splicing and laser micromachining, the insertion loss may be decreased to a large degree. Moreover, the insertion loss of this device will also decrease when it is immersed into the liquid because the reduced RI difference at the surface of the microchannel suppresses the scattering loss.

Polarization dependent loss (PDL) of the above sample in C-band was measured by an All Optical Parameter Analyzer (from Agilent) and the result is displayed in Fig. 5(b), where the maximum PDL is  $\sim 1$  dB. Thus, we can say this type of fiber interferometer shows a low polarization dependency.

Equation (3) indicates that there is an inversely proportional relationship between the FSR and the length of the microchannel so that the FSR value could be optimized by adjusting the length of the microchannel at a given operation wavelength. To experimentally study the relationship between the FSR and the microchannel

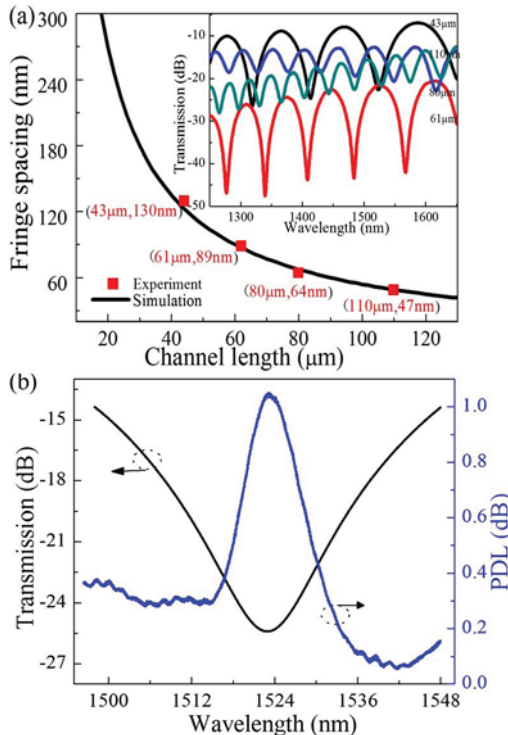


Fig. 5. (a) Fringe spacing as a function of the microchannel length at 1550 nm. Inset: transmission spectra of the TCF-based MZIs with microchannel lengths of 43, 61, 80, and 110  $\mu\text{m}$ ; (b) transmission spectrum and PDL of the TCF-based MZI with the microchannel length of 43  $\mu\text{m}$  in the air.

length, four TCF-based MZIs with different microchannel lengths, i.e., 43, 61, 80, and 110  $\mu\text{m}$ , have been fabricated and measured in air ( $n_{\text{channel}} = 1.00$ ), the corresponding transmission spectra are displayed in Fig. 5(b). Assuming  $n_{\text{core}} = 1.445$  (at 1550 nm), the relationship between the FSR and the microchannel length can be calculated as the black line displayed in Fig. 5(a) and the measured FSR of the four samples at 1550 nm is denoted by the red squares. There is a small deviation between the experimental data and the calculated one that might be explained by the measurement error of the microchannel length in experiment.

The RI response of the TCF-based MZI has been investigated by immersing it into a series of RI liquids (Cargille Labs, <http://www.cargille.com>) in a RI range from 1.300 to 1.340 with an interval of 0.005 at room temperature. The transmission spectrum was recorded by using an OSA with a resolution of 0.02 nm. Each time the sensor was taken out from the tested liquid, it should be carefully cleaned by alcohol to completely remove the residual liquid. When the spectrum returns to the initial state in air, a new round test can be carried out.

Figure 6(a) shows the transmission spectra of the TCF-based MZI with the microchannel length of 43  $\mu\text{m}$  in different RI liquids and it can be found that the fringe dip experienced a significant blue shift with an increase of the liquid RI. The wavelength of the fringe dip and insertion loss varying with the liquid RI is illustrated in Fig. 6(b), where the insertion loss hardly changed with RI but a good linear wavelength response with an ultrahigh sensitivity of  $-10981 \text{ nm/RIU}$  was obtained. Different from other fiber in-line MZIs reported previously, the TCF-based MZI results from the interference between the guided mode in core<sub>1</sub> and the unguided mode traveling through the microchannel in core<sub>2</sub>. The effective RI difference between two interferometer

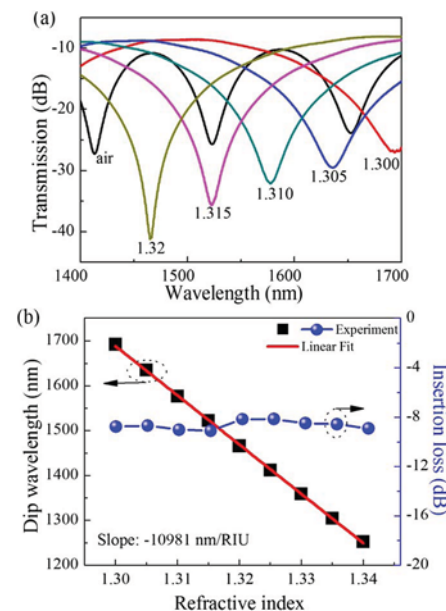


Fig. 6. (a) Transmission spectral evolution within the wavelength range from 1400 to 1700 nm when the surrounding RI changes from 1.0 (in air) to 1.32; (b) Dip wavelength and insertion loss vary with RI.

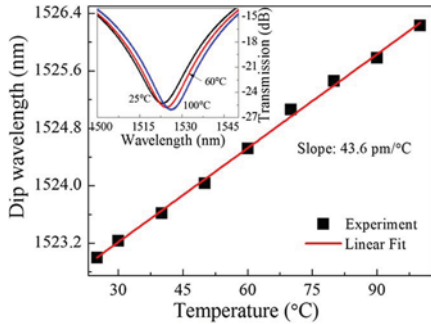


Fig. 7. Wavelength shift of the fringe dip with the temperature varying from 25°C to 100°C. Inset: the evolution of the transmission spectrum with temperature variation.

arms is large ( $\Delta n > 0.1$ ), which guarantees an ultrahigh RI sensitivity.

Assuming that the microchannel length is a constant, the RI sensitivity can be derived from Eq. (2) as  $d\lambda/d(\Delta n) = \lambda/\Delta n$ . This illustrates that the RI response of the TCF-based MZI only depends on the operation wavelength and the RI difference between the core and the medium in microchannel but has nothing to do with the microcavity length. The RI sensitivity is calculated to be  $\sim 10690$  nm/RIU at 1550 nm for  $\Delta n = 1.445 - 1.30 = 0.145$ , which is very close to the experimental result.

Some similar schemes include the MZI fabricated by side-ablating a U-shape microcavity in an SMF [16] and the one fabricated by drilling a hole through an SMF but an RI cross-talk ( $\delta$ ) cannot be avoided in RI test. The RI difference between two interference arms has a modified expression as  $\Delta n' = n_{\text{core}} + \delta - n_{\text{cavity}}$ , which will reduce its RI sensitivity. Differently, the TCF-based MZI proposed here employs two independent arms to overcome the cross-talk to further increase the RI sensitivity. Besides, the large RI difference of the two arms makes the TCF-based MZI more compact.

It is known that the best visibility can be obtained when the light intensity of the two interference beams is equal. For the TCF-based MZI, the first splicing point between SMF<sub>1</sub> and TCF equally splits the input light ( $I_{\text{in}1} \approx I_{\text{in}2}$ ). The employed TCF is very short in length so that the light coupling between the two cores could be neglected, that is to say, the input light in the two cores of the TCF is able to propagate independently. In the core<sub>2</sub>, the microchannel has introduced a large insertion loss for the output beam ( $I_{\text{out}2}$ ) and hence a poor visibility is obtained. However, when the microchannel is filled with liquid, the decreased RI difference reduces both the propagation loss of the unguided mode and the surface scattering loss. Thus,  $I_{\text{out}2}$  is increased to approach  $I_{\text{out}1}$  to improve the fringe visibility.

The influence of temperature on the fiber sensor has been investigated by placing it into an electrical oven and gradually increasing the temperature from room temperature to 100°C. The inset of Fig. 7 shows the transmission spectra of the fiber sensor at 25°C, 60°C, and 100°C and a red shift is clearly observed when the temperature is increased. A wavelength shift of the interference dip at  $\sim 1525$  nm with temperature variation is displayed in Fig. 7, where a linear relation is found and

the temperature sensitivity obtained is at  $\sim 43.6$  pm/°C. When the medium in microchannel is air,  $n_{\text{channel}}$  is a constant ( $n_{\text{channel}} = 1$ ) for different temperatures. The temperature sensitivity of the TCF-based MZI is mainly determined by the thermo-optical coefficient of the core. When no temperature compensation is employed in practical measurement, the error resulting from temperature cross-sensitivity is  $3.96 \times 10^{-6}$  RIU/°C.

In conclusion, we have experimentally demonstrated an ultra-compact TCF-based MZI for RI measurement with extremely high sensitivity and precise sensing location. The two cores of the TCF performed as two interference arms and a microchannel was drilled through one core by means of an fs laser micromachining and the microchannel worked as the sensing region. Such a TCF-based MZI exhibits an ultrahigh RI sensitivity of  $-10981$  nm/RIU in the RI range from 1.30 to 1.34 and a low temperature cross-sensitivity of  $3.96 \times 10^{-6}$  RIU/°C. It is suitable to the applications in the fields of chemical/biomedical sensing and environmental monitoring.

This work was supported by the National Natural Science Foundation of China (grants no. 11174064, 61308027, and 61377090), Natural Science Foundation of SZU (no. 801-00036401), Science & Technology Innovation Commission of Shenzhen (grants no. KQCX20120815161444632 and JCYJ20130329140017262), and Distinguished Professors' Funding from Shenzhen University and Guangdong Province Pearl River Scholars.

<sup>†</sup>These authors contributed equally to this work.

## References

- Z. Li, Y. Wang, C. Liao, S. Liu, J. Zhou, X. Zhong, Y. Liu, K. Yang, Q. Wang, and G. Yin, *Sens. Actuators B* **199**, 31 (2014).
- S. W. James, I. Ishaq, G. J. Ashwell, and R. P. Tatam, *Opt. Lett.* **30**, 2197 (2005).
- Y. P. Wang, Y. J. Rao, Z. L. Ran, T. Zhu, and X. K. Zeng, *Opt. Lasers Eng.* **41**, 233 (2004).
- Y. Wang, *J. Appl. Phys.* **108**, 081101 (2010).
- Y. Wang, J. Chen, and Y. Rao, *J. Opt. Soc. Am. B* **22**, 1167 (2005).
- B. Li, L. Jiang, S. Wang, J. Yang, M. Wang, and Q. Chen, *Opt. Laser Technol.* **44**, 640 (2012).
- J. Yang, L. Jiang, S. Wang, B. Li, M. Wang, H. Xiao, Y. Lu, and H. Tsai, *Appl. Opt.* **50**, 5503 (2011).
- J. Zhou, C. Liao, Y. Wang, G. Yin, X. Zhong, K. Yang, B. Sun, G. Wang, and Z. Li, *Opt. Express* **22**, 1680 (2014).
- T. Y. Hu and D. N. Wang, *Opt. Lett.* **38**, 3036 (2013).
- C. R. Liao, D. N. Wang, and Y. Wang, *Opt. Lett.* **38**, 757 (2013).
- Y. Jung, S. Lee, B. H. Lee, and K. Oh, *Opt. Lett.* **33**, 2934 (2008).
- Y. Wang, M. Yang, D. N. Wang, S. Liu, and P. Lu, *J. Opt. Soc. Am. B* **27**, 370 (2010).
- C. R. Liao, W. Ying, D. N. Wang, and M. W. Yang, *IEEE Photon. Technol. Lett.* **22**, 1686 (2010).
- G. Yin, S. Lou, and H. Zou, *Opt. Laser Technol.* **45**, 294 (2013).
- G. Yin, S. Lou, W. Lu, and X. Wang, *Appl. Phys. B* **115**, 6 (2014).
- L. Zhao, L. Jiang, S. Wang, H. Xiao, Y. Lu, and H.-L. Tsai, *Sensors* **11**, 54 (2011).

# Tunable phase-shifted fiber Bragg grating based on femtosecond laser fabricated in-grating bubble

Changrui Liao,<sup>1,3</sup> Lei Xu,<sup>2</sup> Chao Wang,<sup>3</sup> D. N. Wang,<sup>3</sup> Yiping Wang,<sup>1,\*</sup> Qiao Wang,<sup>1</sup> Kaiming Yang,<sup>1</sup> Zhengyong Li,<sup>1</sup> Xiaoyong Zhong,<sup>1</sup> Jiangtao Zhou,<sup>1</sup> and Yingjie Liu<sup>1</sup>

<sup>1</sup>Key Laboratory of Optoelectronic Devices and Systems of Ministry of Education/Guangdong Province, Shenzhen University, Shenzhen 518060, China

<sup>2</sup>School of Software Engineering, Shenzhen Institute of Information Technology, Shenzhen, Guangdong 518029, China

<sup>3</sup>Department of Electrical Engineering, The Hong Kong Polytechnic University, Hung Hom, Kowloon, Hong Kong, China

\*Corresponding author: [ypwang@szu.edu.cn](mailto:ypwang@szu.edu.cn)

Received October 3, 2013; revised October 11, 2013; accepted October 13, 2013; posted October 15, 2013 (Doc. ID 198872); published October 31, 2013

We present a type of phase-shifted fiber Bragg gratings based on an in-grating bubble fabricated by femtosecond (fs) laser ablation together with a fusion-splicing technique. A microchannel vertically crossing the bubble is drilled by fs laser to allow liquid to flow in or out. By filling different refractive index (RI) liquid into the bubble, the phase-shift peak is found to experience a linear red shift with the increase of RI, while little contribution to the change of phase shift comes from the temperature and axial strain. Therefore, such a PS-FBG could be used to develop a promising tunable optical filter and sensor. © 2013 Optical Society of America

OCIS codes: (060.2970) Fiber optics sensors; (060.3735) Fiber Bragg gratings; (140.7090) Ultrafast lasers.

<http://dx.doi.org/10.1364/OL.38.004473>

As one type of the most successful bandpass filters, phase-shifted fiber Bragg grating (PS-FBG) has a wide range of applications in distributed feedback (DFB) lasers [1], switching elements in dense wavelength-division-multiplexing (DWDM) optical communication systems [2], and sensors for strain and liquid refractive index (RI) [3–6].

Many techniques have been reported for PS-FBG fabrication. The commonly used one is to employ a phase-shifted phase mask in the single exposure process [7]. Such a method possesses good repeatability but poor flexibility because the grating wavelength is determined by the period of the phase mask, and various phase masks are required for different grating wavelengths. In the transverse holographic double exposure process (Moiré method) method [8], two spatially colocated FBGs with slightly different Bragg wavelengths are inscribed in a sequential exposure process, achieved by tuning the laser wavelength, shifting the fiber that is perpendicular to the fiber axis, or applying strain to the fiber before inscribing the second FBG. The Moiré method requires a precise control to guarantee the correct phase shift and hence is of high cost. An alternative is to use the moving fiber-scanning beam approach in which the fiber is mounted on a personal computer (PC)-controlled PZT stage that can be slowly moved relative to the phase mask, allowing a phase shift to be incorporated into the grating [9]. The difficulty existing in the method is to accurately control the relative shift between the fiber and the phase mask. Postprocessing techniques using ultraviolet (UV) laser [10] or CO<sub>2</sub> laser [11] have also been reported for PS-FBG fabrication. By use of focused laser beam to illuminate the fiber grating region, a local RI is induced, thus creating a phase shift in the grating. However, UV postprocessing requires extra exposed time (typically up to hours) while CO<sub>2</sub> laser postprocessing may be difficult to implement for short FBGs due to its large spot size. Although PS-FBG can also be fabricated by external perturbations techniques such

as applying heating [12,13] or local pressure [14], the temporary phase shift will be removed from the grating in the absence of external disturbance.

In this Letter, we proposed a new technique to fabricate tunable PS-FBG by combining femtosecond (fs) laser micromachining together with fusion splicing. In such a device, the phase shift is introduced by an in-grating bubble, which is fabricated by three steps. First, drilling a microhole at the end facet of the fiber with part of FBG and then followed by fusion splicing with another fiber tip with the remaining FBG to form an in-fiber hollow sphere. Finally, a microchannel is inscribed by fs laser to vertically cross the hollow sphere to allow liquid to flow in or out. The response of the device to RI, temperature, and axial strain has been experimentally investigated. With the increase of ambient temperature or axial strain, the transmission spectrum of the device experiences a linear red shift; however, there is little change in the value of the phase shift. The phase-shifted peak of the grating can be tuned by filling different RI liquids inside the bubble and a RI sensitivity of ~9.9 nm/RIU (refractive index unit) can be obtained. Such a device could be used to develop an ultracompact tunable bandpass filter by changing the RI liquid inside the bubble. By filling some functional liquids into the in-grating bubble such as liquid crystal, magnetic liquid, and biological reagent, such a device may find more applications in electro-controlled optical filter and various types of sensors.

Figure 1(a) shows the schematic diagram of the designed PS-FBG, which consists of a through bubble positioned on the center of the FBG. The fabrication procedure involved three steps: first, a 5 mm long FBG with a resonance wavelength of 1578 nm was written in SMF (Corning SMF-28e) by means of 193 nm ArF laser irradiation through a phase mask. Figure 2(a) shows the spectral properties of the obtained FBG, and there is a large transmission loss of ~20 dB at the Bragg resonance wavelength and a negligible insertion loss. Second, the FBG was cut into two sections at the middle of the

grating using fiber cleaver. Then, one microhole with a diameter of  $\sim 3 \mu\text{m}$  was drilled at the center of the cleaved fiber-end facet by use of a Ti: sapphire fs laser system. In the fabrication process, the fs laser pulses ( $\lambda = 800 \text{ nm}$ ) with the duration of 120 fs and the repetition rate of 1 kHz were focused onto the fiber-end facet by a  $20\times$  objective lens with a NA value of 0.5 and a working distance of 2 mm. The group-velocity dispersion of the optical system was minimized by adjusting the amplifier of the laser system. The pulse energy was adjustable by rotating the half-wave plate incorporated with the polarizer and the on-target laser power was maintained at  $\sim 1 \text{ mW}$  with irradiation time of  $\sim 1 \text{ s}$ . The fiber tip with the microhole was spliced together with the other tip containing the rest of the FBG section by use of a fusion splicer (Ericsson FSU-975) with a fusing current of 16.3 mA and a fusing duration of 2.0 s. Since air in the microhole was suddenly heated, it rapidly expanded to a large hollow sphere with a smooth inner surface. The sphere diameter is measured to be  $\sim 50 \mu\text{m}$ . Third, a pair of microchannels was successively fabricated by fs laser drilling from both upper and lower fiber surface vertically to the bubble center to allow external liquid to flow in or out. Details of this fabrication process have been introduced in our previous paper [15,16]. The optical microscope image of the obtained PS-FBG is displayed in Fig. 1(b).

Figure 2(b) shows the spectra of the obtained PS-FBG in air. It can be seen from Fig. 2(b) that the micromachined in-grating microstructure induced an overall insertion loss of  $\sim 3.5 \text{ dB}$  and a sharp phase-shift peak around the center of FBG stop band at 1578.8 nm with FWHM of 30 pm. While the bandwidth of the transmission stop band of the FBG is

$\sim 188 \text{ pm}$ , it gives a finesse of 6.3 for this device. The finesse is comparable to that of PS-FBGs, fabricated by Moiré method [8] and can be further enhanced by raising the reflectivity of the FBGs.

Theoretically, the wavelength of the phase-shift peak depends on location and value of the introduced phase shift. In our configuration, the phase shift is introduced by producing a hollow sphere positioned at the RI modulation region of the grating. The amount of the phase shift depends on both the size of the bubble and the RI liquid inside the bubble. In light of this, the phase-shift peak can be easily adjusted by changing the RI liquid inside the bubble. In the experiment, the fabricated PS-FBG was immersed in series into different RI liquids (Cargille Laboratories, Inc.) to measure its response. After each measurement, the device was rinsed with propyl alcohol carefully until the original spectrum in air was restored so that no residual liquid was left. The transmission spectra were monitored in real time with an optical spectrum analyzer (OSA) with a resolution of 0.01 nm. Figure 3(a) shows the transmission spectra of the device in different RI liquids of 1.412, 1.414, 1.418, and 1.422, respectively. It can be clearly seen from Figs. 3(a) and 2(b) that as the RI liquid is inside the bubble, the transmission loss decreases by  $\sim 3.3 \text{ dB}$ . The reason of this is that the reflectivity of the bubble inner surface is reduced due to the infiltration of the high RI liquid into the cavity. With the increase of RI, the phase-shift peak exhibits an obvious red shift and if the induced phase change exceeds  $2\pi$ , a new peak will be regenerated from the shorter wavelength side, as shown in Fig. 3(b), where a new cycle occurs when the RI changes from 1.408 to 1.412. The strength of the phase-shift peak also changes during

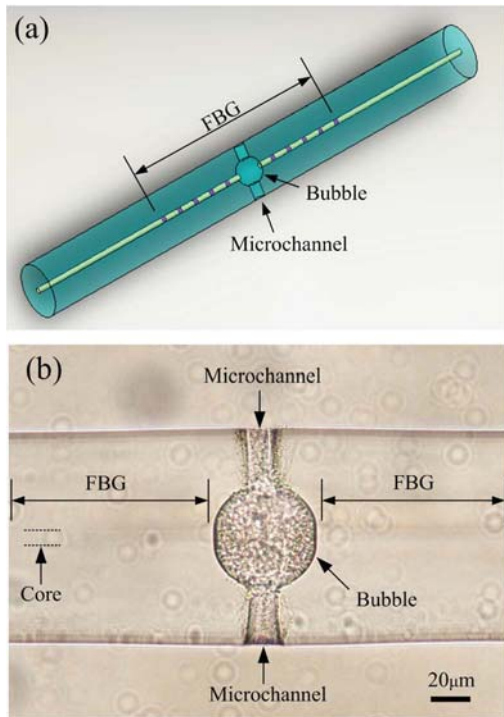


Fig. 1. (a) Schematic diagram of the designed PS-FBG in single mode fiber. (b) Optical microscope image of the PS-FBG fabricated by fs laser ablation together with fusion splicing technique.

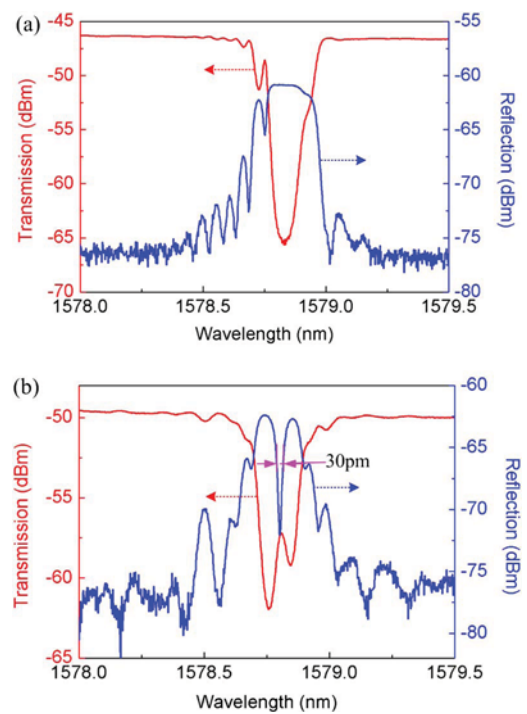


Fig. 2. (a) Transmission (red line) and reflection (blue line) spectra of the FBG fabricated by 193 nm ArF laser through a phase mask. (b) Transmission (red line) and reflection (blue line) spectra of the fabricated PS-FBG.

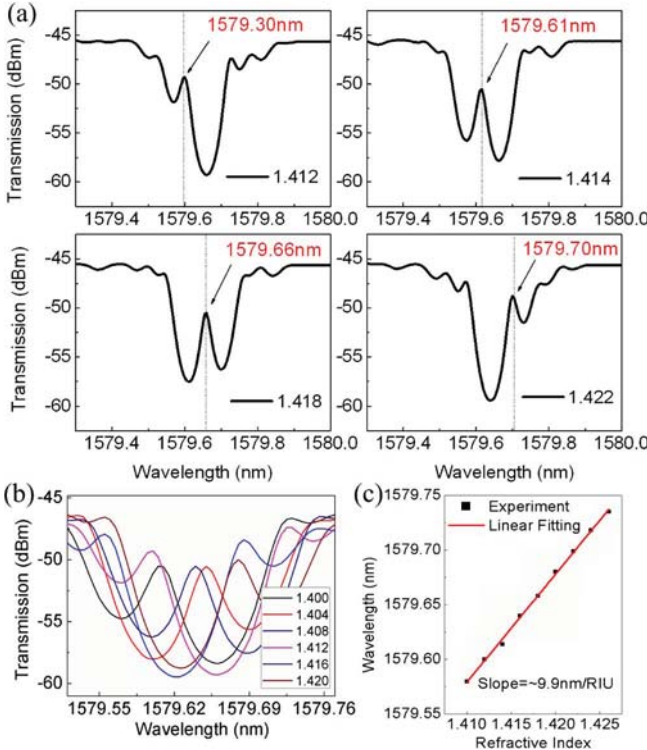


Fig. 3. (a) Spectral evolution of the microchannel PS-FBG subject to different RI liquids. (b) Cyclic feature of the PS-FBG filled with different RI liquids. (c) Linear relationship between the wavelength of the phase-shift peak and RI of the liquid, with a slope of  $\sim 9.9$  nm/RIU.

its shifting process and the peak becomes the strongest when it approaches to the center of the Bragg reflection band. Figure 3(c) shows the linear relationship between the phase-shift peak wavelength and the RI, where an RI sensitivity of  $\sim 9.9$  nm/RIU is obtained.

The influence of temperature on the PS-FBG has been investigated by placing the device into an electrical oven and gradually increasing the temperature from room temperature to  $100^{\circ}\text{C}$ . Figure 4(a) shows the transmission spectra of the PS-FBG at different temperatures, and a red shift is clearly observed when the temperature is increased. The wavelengths at three extreme points in the transmission spectrum, i.e., A, B and C, were tracked and their relation with temperature are given in Fig. 4(b), where a linear relation is found, with temperature coefficients of  $\sim 10.21 \text{ pm}/^{\circ}\text{C}$  for "C,"  $\sim 10.19 \text{ pm}/^{\circ}\text{C}$  for "B," and  $\sim 10.20 \text{ pm}/^{\circ}\text{C}$  for "A." That is to say, the rise of temperature hardly changes the amount of the introduced phase shift since the thermal expansion effect of the hollow sphere is negligible. The spectral temperature sensitivity of the PS-FBG is close to that of the uniform FBG, which is mainly resulting from the effective RI change of core mode by heating the fiber.

The effect of strain variation on the PS-FBG has also been investigated by stretching it along the fiber axis. Figure 5(a) shows the spectral evolution of the device with the increase of strain from 0 to  $1000 \mu\text{e}$  by a step of  $100 \mu\text{e}$ . It can be seen from this figure that the whole spectrum experiences a red shift with the increase of strain. Figure 5(b) shows the wavelengths at three extreme points when different strains were applied, and

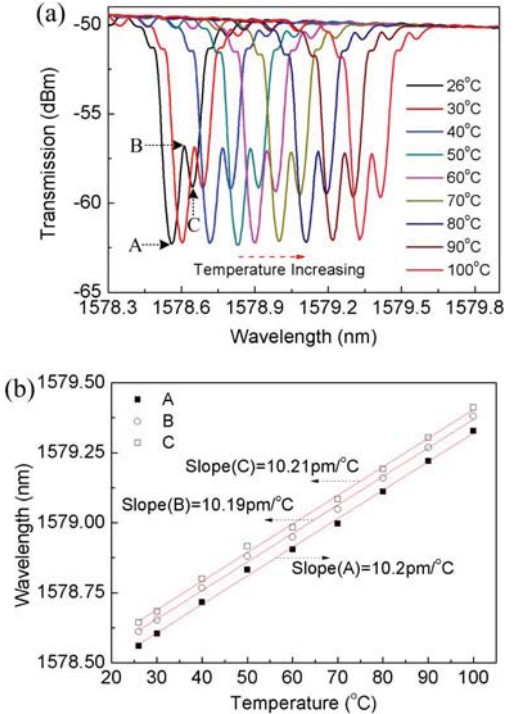


Fig. 4. (a) Transmission spectra the micromachined PS-FBG at different temperatures. (b) Linear relationship between the wavelength of extreme point of the transmission spectrum and the ambient temperature.

a linear relation can be found, with strain coefficients of  $\sim 0.481 \text{ pm}/\mu\text{e}$  for "C,"  $\sim 0.480 \text{ pm}/\mu\text{e}$  for "B," and  $\sim 0.485 \text{ pm}/\mu\text{e}$  for "A." The small difference of the strain coefficient among three extreme points means that the phase shift of grating is hardly changed by strain, similar to that induced by temperature. We believe the strain-induced spectral movement is mainly due to the elasto-optical effect of silica fiber.

However, compared with the uniform FBG without a phase shift (with a strain sensitivity of  $\sim 1.2 \text{ pm}/\mu\text{e}$  at  $\sim 1550 \text{ nm}$  [17,18]), the PS-FBG demonstrates a much lower strain coefficient. This can be explained by the fact that when a stress is applied to the entire fiber, there will be an unequal load of strain along each section of the fiber, depending on the local mechanical resistance [19]. The stress loads applied to the bubble section and to the grating section are equal:

$$\varepsilon_B E A_B = \varepsilon_G E A_G, \quad (1)$$

represent the applied strains on the bubble and the grating section, and  $A_B$  and  $A_G$  refer to the cross-sectional areas of silica part within the bubble and the grating sections, respectively. Thus, the strains applied to these two regions just depend on the ratio of cross-sectional areas,  $\varepsilon_G/\varepsilon_B = A_B/A_G$ , and  $A_B < A_G$ . This means the fiber section with bubble bears more strain loads than the grating section; hence the strain sensitivity of the PS-FBG is depressed to some extent.

We found the spectral envelope of the PS-FBG remains unchanged in the RI test but exhibits a linear red shift with the increase of temperature or axial strain. Thus,

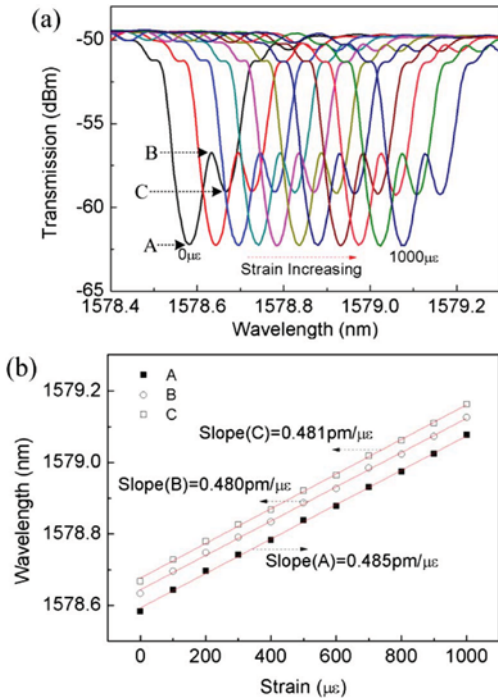


Fig. 5. (a) Spectral evolution of the micromachined PS-FBG subject to different axial strains. (b) Linear relationship between the wavelengths of three extreme points of the transmission spectrum and the applied axial strain.

it is possible to eliminate the cross sensitivity of temperature and axial strain by measuring the envelope movement, and the location of the envelope can be set by the central wavelength of FWHM of the envelope.

In this Letter, we have experimentally demonstrated a tunable PS-FBG based on an in-grating bubble incorporated with a through microchannel. The in-grating bubble is fabricated using fs laser ablation assisted by fusion splicing method in a fiber with FBG. The microchannel is drilled by fs laser to allow liquid to flow in or out. The RI response of this PS-FBG has been investigated and the phase-shift peak shows a linear RI response with a sensitivity of  $\sim 9.9$  nm/RIU, while the spectral envelope of the FBG remaining unchanged. Based on this property, the phase-shift value of the grating can be easily tuned by changing the RI liquid inside the bubble. With the increase of temperature or axial strain, the spectral envelope of the PS-FBG experiences a red shift with a temperature sensitivity of  $\sim 10.2$  pm/ $^{\circ}$ C or a strain sensitivity of  $\sim 0.48$  pm/ $\mu$ e, while the phase-shift value is hardly changed. Overall, the revealed linear RI response

with little cross-sensitivity from temperature and axial strain of the in-grating-bubble PS-FBGs are of great advantage over conventional configurations. The device may find new applications in electro-controlled optical filter and various types of sensors, when filling into the bubble with functional liquid such as liquid crystal, magnetic liquid or biological reagent.

This work was supported by the National Science Foundation of China (Grant Nos. 61308027, 61377090, and 11174064), the Science &Technology Innovation Commission of Shenzhen (Grant Nos. KQCX20120815161444632 and JCYJ20130329140017262), and the Distinguished Professors Funding from Shenzhen University and Guangdong Province Pearl River Scholars.

## References

1. J. T. Kringlebotn, J. L. Archambault, L. Reekie, and D. N. Payne, Opt. Lett. **19**, 2101 (1994).
2. X. H. Zou, M. Li, W. Pan, L. S. Yan, J. Azana, and J. P. Yao, Opt. Lett. **38**, 3096 (2013).
3. D. Gatti, G. Galzerano, D. Janner, S. Longhi, and P. Laporta, Opt. Express **16**, 1945 (2008).
4. K. M. Zhou, Z. J. Yan, L. Zhang, and I. Bennion, Opt. Express **19**, 11769 (2011).
5. Y. P. Wang, H. Bartelt, W. Ecke, R. Willsch, J. Kobelke, M. Kautz, S. Brueckner, and M. Rothhardt, Opt. Commun. **282**, 1129 (2009).
6. Y. J. Rao, X. Zeng, Y. Zhu, Y. P. Wang, T. Zhu, Z. L. Ran, L. Zhang, and I. Bennion, Chin. Phys. Lett. **18**, 643 (2001).
7. R. Kashyap, P. F. McKee, and D. Armes, Electron. Lett. **30**, 1977 (1994).
8. L. Zhao, L. Li, A. Luo, J. Z. Xia, R. H. Qu, and Z. Fang, Optik **113**, 464 (2002).
9. W. H. Loh and R. I. Laming, Electron. Lett. **31**, 1440 (1995).
10. J. Canning and M. G. Sceats, Electron. Lett. **30**, 1344 (1994).
11. L. Xia, P. Shum, and C. Lu, Opt. Express **13**, 5878 (2005).
12. S. Gupta, T. Mizunami, and T. Shimomura, J. Lightwave Technol. **15**, 1925 (1997).
13. C. R. Liao, Y. H. Li, D. N. Wang, T. Sun, and K. T. V. Grattan, IEEE Sens. J. **10**, 1675 (2010).
14. C. J. S. Matos, P. Torres, L. C. G. Valente, W. Margulis, and R. Stubbe, J. Lightwave Technol. **19**, 1206 (2001).
15. C. R. Liao, T. Y. Hu, and D. N. Wang, Opt. Express **20**, 22813 (2012).
16. C. R. Liao, D. N. Wang, and Y. Wang, Opt. Lett. **38**, 757 (2013).
17. Y. J. Rao, Y. P. Wang, Z. L. Ran, T. Zhu, and B. M. Yu, Proc. SPIE **4581**, 327 (2001).
18. Y. P. Wang, H. Bartelt, M. Becker, S. Brueckner, J. Bergmann, J. Kobelke, and M. Rothhardt, Appl. Opt. **48**, 1963 (2009).
19. O. Frazão, S. F. O. Silva, A. Guerreiro, J. L. Santos, L. A. Ferreira, and F. M. Araújo, Appl. Opt. **46**, 8578 (2007).

# Highly-sensitive gas pressure sensor using twin-core fiber based in-line Mach-Zehnder interferometer

Zhengyong Li,<sup>1</sup> Changrui Liao,<sup>1</sup> Yiping Wang,<sup>1,\*</sup> Lei Xu,<sup>2</sup> Dongning Wang,<sup>3</sup> Xiaopeng Dong,<sup>4</sup> Shen Liu,<sup>1</sup> Qiao Wang,<sup>1</sup> Kaiming Yang,<sup>1</sup> and Jiangtao Zhou<sup>1</sup>

<sup>1</sup>Key Laboratory of Optoelectronic Devices and Systems of Ministry of Education and Guangdong Province, College of Optoelectronic Engineering, Shenzhen University, Shenzhen 518060, China

<sup>2</sup>Department of Computing, The HongKong Polytechnic University, HongKong, China

<sup>3</sup>Department of Electrical Engineering, The Hong Kong Polytechnic University, Hong Kong, China

<sup>4</sup>School of Information Science and Engineering, Xiamen University, Xiamen 361005, China

\*ypwang@szu.edu.cn

**Abstract:** A Mach-Zehnder interferometer based on a twin-core fiber was proposed and experimentally demonstrated for gas pressure measurements. The in-line Mach-Zehnder interferometer was fabricated by splicing a short section of twin-core fiber between two single mode fibers. A micro-channel was created to form an interferometer arm by use of a femtosecond laser to drill through one core of the twin-core fiber. The other core of the fiber was remained as the reference arm. Such a Mach-Zehnder interferometer exhibited a high gas pressure sensitivity of  $-9.6 \text{ nm/MPa}$  and a low temperature cross-sensitivity of  $4.4 \text{ KPa/}^{\circ}\text{C}$ . Moreover, ultra-compact device size and all-fiber configuration make it very suitable for highly-sensitive gas pressure sensing in harsh environments.

©2015 Optical Society of America

**OCIS codes:** (060.2370) Fiber optics sensors; (280.5475) Pressure measurement; (140.3948) Microcavity devices; (320.2250) Femtosecond phenomena.

## References and links

1. Z. Li, Y. Wang, C. Liao, S. Liu, J. Zhou, X. Zhong, Y. Liu, K. Yang, Q. Wang, and G. Yin, "Temperature-insensitive refractive index sensor based on in-fiber Michelson interferometer," *Sens. Actuators B Chem.* **199**(0), 31–35 (2014).
2. G. L. Yin, S. Q. Lou, W. L. Lu, and X. Wang, "A high-sensitive fiber curvature sensor using twin core fiber-based filter," *Appl. Phys. B* **115**(1), 99–104 (2014).
3. Y. P. Wang, J. P. Chen, and Y. J. Rao, "Torsion characteristics of long-period gratings induced by high-frequency CO<sub>2</sub> laser pulses," *J. Opt. Soc. Am. B* **22**(6), 1167–1172 (2005).
4. Y. Wang, "Review of long period fiber gratings written by CO<sub>2</sub> laser," *J. Appl. Phys.* **108**(8), 081101 (2010).
5. C. R. Liao, D. N. Wang, M. Wang, and M. H. Yang, "Fiber in-line Michelson Interferometer Tip Sensor Fabricated by Femtosecond Laser," *IEEE Photon. Technol. Lett.* **24**(22), 2060–2063 (2012).
6. C. R. Liao, Y. Li, D. N. Wang, T. Sun, and K. T. V. Grattan, "Morphology and thermal stability of fiber Bragg gratings for sensor applications written in H<sub>2</sub>-free and H<sub>2</sub>-loaded fibers by Femtosecond laser," *IEEE Sens. J.* **10**(11), 1675–1681 (2010).
7. Z. Qi, L. Nan, T. Fink, L. Hong, P. Wei, and H. Ming, "Fiber-optic pressure sensor based on  $\pi$ -phase-shifted fiber Bragg grating on side-hole fiber," *IEEE Photon. Technol. Lett.* **24**(17), 1519–1522 (2012).
8. G. Hu and D. Chen, "Side-hole dual-core photonic crystal fiber for hydrostatic pressure sensing," *J. Lightwave Technol.* **30**(14), 2382–2387 (2012).
9. T. Martynkien, P. Mergo, and W. Urbanczyk, "Sensitivity of birefringent microstructured polymer optical fiber to hydrostatic pressure," *J. Lightwave Technol.* **25**(16), 1562–1565 (2013).
10. J. Long, G. Bai-Ou, and W. Hufeng, "Sensitivity characteristics of Fabry-Perot pressure sensors based on hollow-core microstructured fibers," *J. Lightwave Technol.* **31**(15), 2526–2532 (2013).
11. M. Jun, J. Jian, J. Long, and J. Wei, "A compact fiber-tip micro-cavity sensor for high-pressure measurement," *IEEE Photon. Technol. Lett.* **23**(21), 1561–1563 (2011).
12. C. Liao, S. Liu, L. Xu, C. Wang, Y. Wang, Z. Li, Q. Wang, and D. N. Wang, "Sub-micron silica diaphragm-based fiber-tip Fabry-Perot interferometer for pressure measurement," *Opt. Lett.* **39**(10), 2827–2830 (2014).
13. J. Ma, W. Jin, H. L. Ho, and J. Y. Dai, "High-sensitivity fiber-tip pressure sensor with graphene diaphragm,"

- Opt. Lett. **37**(13), 2493–2495 (2012).
14. F. Xu, D. Ren, X. Shi, C. Li, W. Lu, L. Lu, L. Lu, and B. Yu, “High-sensitivity Fabry-Perot interferometric pressure sensor based on a nanothick silver diaphragm,” Opt. Lett. **37**(2), 133–135 (2012).
  15. J. C. Xu, X. W. Wang, K. L. Cooper, and A. B. Wang, “Miniature all-silica fiber optic pressure and acoustic sensors,” Opt. Lett. **30**(24), 3269–3271 (2005).
  16. Y. Wang, M. Yang, D. N. Wang, S. Liu, and P. Lu, “Fiber in-line Mach-Zehnder interferometer fabricated by femtosecond laser micromachining for refractive index measurement with high sensitivity,” J. Opt. Soc. Am. B **27**(3), 370–374 (2010).
  17. D. Duan, Y. Rao, and T. Zhu, “High sensitivity gas refractometer based on all-fiber open-cavity Fabry-Perot interferometer formed by large lateral offset splicing,” J. Opt. Soc. Am. B **29**(5), 912–915 (2012).
  18. M. Deng, C. P. Tang, T. Zhu, Y. J. Rao, L. C. Xu, and M. Han, “Refractive index measurement using photonic crystal fiber-based Fabry-Perot interferometer,” Appl. Opt. **49**(9), 1593–1598 (2010).
- 

## 1. Introduction

Fiber optic sensors have been demonstrated to extremely attractive for various areas of biomedicine, automotive industries and environmental monitoring [1–6]. Among them, optical fiber pressure sensors are of great interests owing to their great multiplexing capability, compact size, immunity to electromagnetic interference and easy signal detection. So far, various optical fiber configurations for pressure measurement have been reported, i.e.  $\pi$ -phase-shift fiber Bragg grating fabricated on side-hole fiber [7], side-hole dual-core photonic crystal fiber [8], and PMMA birefringent fiber [9]. Fabry-Pérot interferometers (FPIs) have played an extra-ordinary role in pressure sensing due to their compact size and easy fabrication [10–15]. Hollow-core fiber based FPI exhibits an pressure sensitivity of  $-23.4 \text{ pm/MPa}$  [10]. Fiber-tip micro-bubble based FPI shows a pressure sensitivity of  $315 \text{ pm/MPa}$  [11]. Liao et al. optimized the fabrication process and enhanced the pressure sensitivity up to  $1036 \text{ pm/MPa}$  [12]. All silica structure of the above FPIS limits the pressure performance and in order to further improve the pressure sensitivity, new FPIS based on graphene diaphragm [13] and silver diaphragm [14] have been realized and exhibited an ultrahigh pressure sensitivity of  $39.4 \text{ nm/kPa}$  and  $70.5 \text{ nm/kPa}$ , respectively. Unfortunately, the mechanical strength of these FPIS is poor because the thin diaphragm attached at the fiber end is easily cracked that will limit its application in high pressure environment.

In this letter, we present a highly-sensitive pressure sensor based on a fiber in-line MZI, which is fabricated by using femtosecond laser (FS) micromachining and fusion splicing technique. This fiber interferometer is constructed by splicing a short section of twin-core fiber (TCF) between two single mode fibers (SMFs) and the separate cores of the TCF perform as the two interference arms. One arm contains a micro-channel, which is created by removing part of one core of the TCF, and the second arm is the other complete core. Different from previously reported fiber pressure sensors, gas density change in the micro-channel induced by the increased pressure causes the spectral response. The TCF-based MZI exhibits a high pressure sensitivity of  $-9.6 \text{ nm/MPa}$  within the pressure range between 0 and 2 MPa and a small cross-sensitivity to temperature of  $4.4 \text{ KPa/}^{\circ}\text{C}$ . Moreover, the ultra-compact size of the fiber interferometer is able to ensure a precise sensing location.

## 2. Operating principle and fabrication

Figure 1 is shown the schematic diagram of the proposed TCF-based MZI. A short section of TCF is spliced between two sections of SMFs and a micro-channel is created in the core<sub>2</sub> of the TCF by using FS laser micromachining. The light propagating in SMF<sub>1</sub> is equally splitted into two beams in the TCF, which is denoted as I<sub>in1</sub> and I<sub>in2</sub>, respectively. The length of TCF is very short so that the mode coupling effect between the two cores can be neglected, that is to say, the light of two cores is able to propagate independently. Beam (I<sub>in1</sub>) remains to propagate in the core<sub>1</sub> while beam (I<sub>in2</sub>) travels through the micro-channel, where an optical path difference (OPD) is obtained. When the two output beams, i.e. I<sub>out1</sub> and I<sub>out2</sub> corresponding to I<sub>in1</sub> and I<sub>in2</sub>, recombined in SMF<sub>2</sub>, the notable interference spectrum is

achieved because of the phase difference between the two output beams. The output intensity of TCF-based MZI can be expressed as,

$$I = I_{out1} + I_{out2} + 2\sqrt{I_{out1}I_{out2}} \cos\left(\frac{2\pi L \Delta n}{\lambda} + \phi_0\right), \quad (1)$$

where  $\lambda$  is the light wavelength,  $L$  is the length of the micro-channel,  $\Delta n = n_{core} - n_{channel}$  is the effective RI difference between the two interference arms, where  $n_{core}$  and  $n_{channel}$  are the effective RI of the core mode and the channel mode, and  $\phi_0$  is the initial phase of the interference. According to Eq. (1), the interference signal reaches the minimum value when the following condition is satisfied,

$$\frac{2\pi L \Delta n}{\lambda_m} + \phi_0 = (2m+1)\pi, \quad (2)$$

where  $m$  is an integer,  $\lambda_m$  is the wavelength of the  $m^{\text{th}}$  order interference dip.

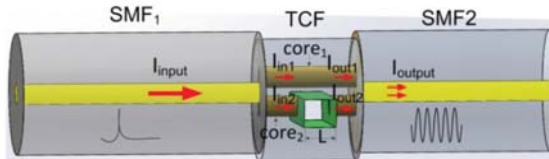


Fig. 1. Schematic diagram of the TCF based MZI.

The fabrication process of the proposed TCF-based MZI involves of two steps. The first step: one end of the TCF was spliced with an SMF (Corning, SMF-28) with the core/cladding diameters of 8/125  $\mu\text{m}$  by using a commercial fusion splicer (Fujikura FSM-60s). The cross-sectional morphology of the TCF that is supplied by Xiamen University is shown in Fig. 2(c), where the cladding diameter is 125  $\mu\text{m}$  and the major/mirror axes of the two elliptical cores are measured to be  $\sim 10.9$  and  $\sim 6.5 \mu\text{m}$ , respectively. The splicing process is demonstrated in Fig. 2, where a red laser beam was launched into the SMF<sub>1</sub> and the light intensity of the two TCF cores was observed by using an optical microscope. The offset distance between the SMF and the TCF was carefully adjusted to let the light intensity in the two cores become roughly equal. Figures 2(a) and 2(b) shows the unequal and equal splitting ratios when different offsets are employed. In the experiment the TCF with a length of  $\sim 200 \mu\text{m}$  was used and the other end of TCF was spliced with another SMF with an optimized offset value to obtain the maximum intensity output. Splicing errors, i.e. fiber offset distance in splicing, will result in the decay of the fringe visibility that is harmful to sensing applications and a very short piece of TCF ( $\sim 200 \mu\text{m}$ ) was employed in this MZI to avoid the light coupling between the two cores and decrease the total insertion loss of this device.

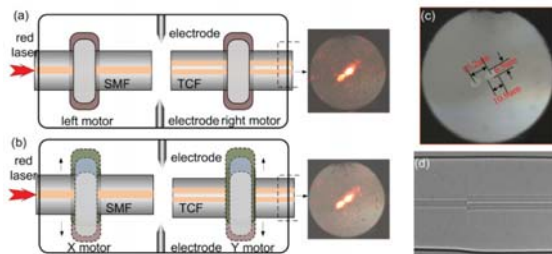


Fig. 2. Schematic diagram of the splicing process assisted with a red beam irradiation, (a) before fusion splicing; (b) adjusting X and Y motors to make the light intensity of the two cores become equal with each other; (c) microscope image of the cross section of TCF; and (d) microscope image of the spliced joint.

The second step: a micro-channel was drilled through the first core, i.e. core<sub>1</sub>, of the TCF by employing a FS laser (Spectra-Physics Solstice, 120 fs, 800 nm, 1 KHz, 4 mJ), as described below. The laser beam was focused by use of an objective lens with an NA value of 0.25. The laser power was adjustable in the range between 0 and 4mJ by rotating a half-wave plate followed by a polarizer, and the average on-target laser power was maintained at ~20mW. The TCF was mounted on a computer-controlled X-Y-Z translation stage (Newport)with a resolution of 10 nm. The fabrication of the micro-channel was similar to the process described in Ref [16]. Firstly, FS laser beam was focused on the center of the fiber core and shifted by 15  $\mu\text{m}$  away from fiber axis. This position was set to be the jumping-off point. Secondly, the focused FS laser beam was scanned with a distance of 45 $\mu\text{m}$  along the fiber axis at a speed of 5  $\mu\text{m}/\text{s}$ , and then was returned to the jumping-off point. Such a process is called one scanning cycle. Thirdly, the laser beam was moved toward the core with a step of 5 $\mu\text{m}$  in order to start next scanning cycle. The laser was switched off as soon as an expected transmission spectrum was observed. Thus a micro-channel was created in the TCF, as shown in Figs. 3(a) and 3(b). Finally, the achieved micro-channel was cleaned by using alcohol to remove silica scraps. The size and geometry of the micro-channel is very important for the spectral property of our fiber MZI, i.e. insertion loss, fringe spectrum range and fringe visibility. Thanks to the ultra-small focal point of the FS laser beam and the nano-positioning stages employed, the size and geometry of the micro-channel can be well guaranteed in our experiment.

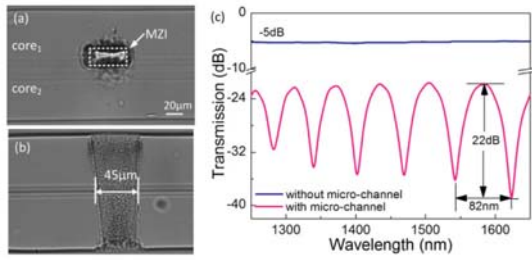


Fig. 3. (a) Top-view and (b) side-view microscope images of the created micro-channel; (c) transmission spectra of the TCF with and without a micro-channel in air.

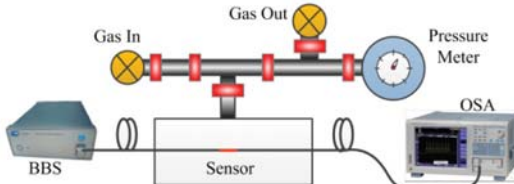


Fig. 4. Experimental setup for gas pressure measurements.

The transmission spectrum was measured in real time by using a broadband light source (BBS, Fiberlaker) ranging from 1250 to 1670 nm and an optical spectrum analyzer (OSA, Yokogama, AQ6370C). Figure 3(c) shows the transmission spectra of the device before and after the micro-channel was drilled in the TCF in air. Before drilling of the micro-channel, the initial insertion loss is ~5 dB, which mainly comes from the splicing loss between the SMF and TCF. The flat spectrum indicates that there is no OPD induced by the TCF being spliced between two SMFs. After drilling the micro-channel with a length of 50  $\mu\text{m}$ , the insertion loss is increased to ~21dB and the fringe visibility of ~22 dB and the fringe spectral range (FSR) of ~82 nm are obtained. One core of TCF was removed so that the effective RI of this arm is reduced to 1.0 (air) but another arm is unchanged (silica). Thus, a significant OPD can be achieved. The fringe visibility depends on the intensity of  $I_{\text{out}1}$  and  $I_{\text{out}2}$ . The first splicing joint

between SMF<sub>1</sub> and TCF equally splits the input light ( $I_{in1} \approx I_{in2}$ ). The appearance of the micro-channel brings a large insertion loss to  $I_{in2}$ , which changes the balance between  $I_{out1}$  and  $I_{out2}$ . So a poor fringe visibility is obtained.

### 3. Gas pressure and temperature experiments

The gas pressure response of the TCF-based MZI is tested and the experimental setup is shown in Fig. 4, where a BBS and an OSA with a resolution of 0.05 nm are employed to measure the transmission spectrum. The device is placed into the gas chamber, where a commercial gas pressure generator with a stability of  $\pm 0.2$  KPa is equipped with a high-precision digital pressure meter (ConST-811) to measure the pressure in the chamber. The chamber is fitted with a feed-through and sealed by strong glue to extend the fiber pigtail outside the chamber for real-time measurement. The pressure in the chamber is increased from 0 to 2 MPa with an interval of 0.2 MPa at room temperature, remaining at each step for 5 min.

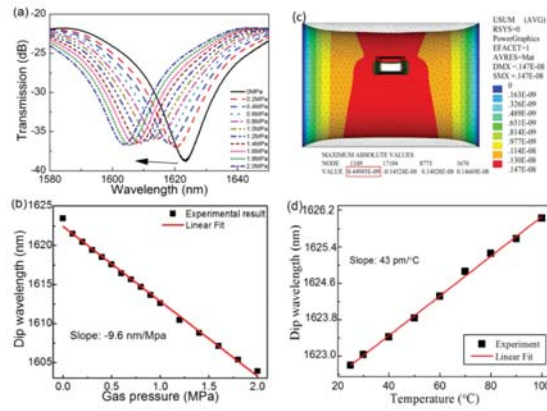


Fig. 5. (a) Transmission spectral evolution within the wavelength range from 1580 to 1650nm when the gas pressure increases from 0 to 2 MPa; (b) dip wavelength versus gas pressure; (c) Simulation model of the micro-channel deformation; (d) dip wavelength versus temperature.

Figure 5(a) shows the transmission spectra of the TCF-based MZI in different air pressure conditions and it can be found that the fringe dip shifts toward shorter wavelength with the applied pressure. The relationship between the wavelength of the fringe dip and the pressure is illustrated in Fig. 5(b), where a good linear response with an ultra-high pressure sensitivity of  $-9.6$  nm/MPa is obtained. When the OSA was working with a resolution of 0.05 nm, the minimum detectable pressure change can be calculated to be  $\sim 5.2$  KPa.

Firstly, it is important to discuss the deformation of the micro-channel with the increased gas pressure. A longitudinal strain ( $\epsilon$ ) translated from the lateral pressure  $P$  through Poisson's ratio is [17]

$$\epsilon = \frac{\Delta L}{L} = \frac{(1-2\delta)}{E} P, \quad (3)$$

where  $E$  is the Young's modulus,  $\delta$  is the Poisson's ratio,  $L$  is the micro-channel length, and  $P$  is the applied gas pressure. Assuming  $E = 73$  GPa,  $\delta = 0.17$ ,  $L = 50$   $\mu\text{m}$ , and  $P = 1$  MPa, the value of  $\epsilon$  and the length change of micro-channel  $\Delta L$  are calculated to be  $9.04 \times 10^{-6}$  and 0.452 nm, respectively. Simulation model is also established in ANSYS with the same parameters setting as above. The simulation result under the applied pressure of 1 MPa is displayed in Fig. 5(c) and it can be seen from this figure that the length of the micro-channel is increased by 0.449 nm, which agrees well with the calculated result. From Eqs. (2) and (3), the relationship between the longitudinal strain of the interferometer cavity and the induced

dip wavelength shift can be expressed as  $\varepsilon = \Delta L/L = \Delta\lambda/\lambda$ . The applied gas pressure of 1 MPa will result in a very small dip movement of 14 pm, which could be ignored.

Assuming that the length of micro-channel is a constant, the pressure sensitivity can be derived from Eq. (2) as

$$\frac{d\lambda}{dP} = \frac{\lambda}{\Delta n} \frac{d(\Delta n)}{dP}, \quad (4)$$

where  $d(\Delta n)/dP$  illustrates the RI change of air in micro-channel varying with pressure. At room temperature (15~25 °C), the RI of air is a function of the pressure and temperature [18]:

$$n = 1 + \frac{2.8793 \times 10^{-9} \times P}{1 + 0.003671 \times t}, \quad (5)$$

where  $n$ ,  $P$ ,  $t$  are the RI of air, the pressure (Pa), and the temperature (°C). If the temperature remains unchanged, there is a linear relationship between the air RI and the pressure.  $d(\Delta n)/dP$  can be calculated to be  $2.63 \times 10^{-3}$  when the temperature is 25 °C and the pressure is increased to 2 MPa. From Eq. (4) the pressure sensitivity of the TCF-based MZI can be calculated to be  $\sim 9.52$  nm/MPa at 1610 nm for  $\Delta n = 1.445 - 1.0 = 0.445$ , which is very close to the experimental result. Therefore, the RI variation of the air in the micro-channel induced by the increased pressure plays a leading role on its pressure response. Comparing with the previously reported fiber pressure sensors, such as  $\pi$ -phase-shifted FBG (6.9 pm/Mpa) [7], side-hole dual-core photonic crystal fiber (32 pm/Mpa) [8], fiber tip micro-cavity (315 pm/Mpa) [11], our TCF-based MZI shows a much higher sensitivity of -9.6 nm/Mpa and more compact structure.

Temperature response of the fiber sensor was also investigated, where the TCF-based MZI is placed into an electrical oven and gradually increasing the temperature from room temperature to 100 °C with a step of 10°C. A red shift is clearly observed when the temperature is increased. Wavelength shift of the interference dip at ~1623 nm with temperature variation is displayed in Fig. 5(d), where a good linear response with a temperature sensitivity of 43 pm/°C was obtained. The temperature response of the TCF-based MZI is mainly determined by the thermo-optical effect of the fiber core. In case no temperature compensation is employed in practical measurements, the gas pressure measurement error resulting from temperature is 4.4 KPa/°C, which is lower than the minimum detectable gas pressure change (5.2 KPa) of this MZI sensor. Hence the pressure-temperature crosstalk can be ignored.

#### 4. Conclusions

In summary, we reported a micro-channel based TCF in-line MZI for gas pressure measurement. This device is fabricated by combining fusion splicing with fs laser micromachining technique. The two cores of the TCF perform as two interference arms and a micro-channel was drilled through one core by means of FS laser micromachining and the micro-channel worked as the precise sensing region. The proposed TCF-based MZI exhibits an ultra-high gas pressure sensitivity of -9.6 nm/MPa from 0 to 2 Mpa and a low temperature cross-sensitivity of 4.4 KPa/°C. It is suitable for gas pressure detection, biomedical sensing, environmental monitoring and other industrial applications.

#### Acknowledgments

This work was supported by National Natural Science Foundation of China/Guangdong (grant nos. 61425007, 11174064, 61377090, and 61308027), Science & Technology Innovation Commission of Shenzhen/Nanshan (grants nos. KQCX20120815161444632, JCYJ20130329140017262, ZDSYS20140430164957664, KC2014ZDZJ0008A), and Pearl River Scholar Fellowships.

# Simultaneous measurement of strain and temperature by employing fiber Mach-Zehnder interferometer

Jiangtao Zhou, Changrui Liao, Yiping Wang,<sup>\*</sup> Guolu Yin, Xiaoyong Zhong, Kaiming Yang, Bing Sun, Guanjun Wang, and Zhengyong Li

Key Laboratory of Optoelectronic Devices and Systems of Ministry of Education and Guangdong Province, Shenzhen University, Shenzhen 518060, China  
[ypwang@szu.edu.cn](mailto:ypwang@szu.edu.cn)

**Abstract:** We demonstrated a novel fiber in-line Mach-Zehnder interferometer (MZI) with a large fringe visibility of up to 17 dB, which was fabricated by misaligned splicing a short section of thin core fiber between two sections of standard single-mode fiber. Such a MZI could be used to realize simultaneous measurement of tensile strain and temperature. Tensile strain was measured with an ultrahigh sensitivity of  $-0.023 \text{ dB}/\mu\epsilon$  via the intensity modulation of interference fringes, and temperature was measured with a high sensitivity of  $51 \text{ pm}^\circ/\text{C}$  via the wavelength modulation of interference fringe. That is, the MZI-based sensor overcomes the cross-sensitivity problem between tensile strain and temperature by means of different demodulation methods. Moreover, this proposed sensor exhibits the advantages of low-cost, extremely simple structure, compact size (only about 10 mm), and good repeatability.

©2014 Optical Society of America

**OCIS codes:** (060.2370) Fiber optics sensors; (060.2340) Fiber optics components; (120.3180) Interferometry.

## References and links

- Y. Ji, Y. Chung, D. Sprinzak, M. Heiblum, D. Mahalu, and H. Shtrikman, "An electronic Mach-Zehnder interferometer," *Nature* **422**(6930), 415–418 (2003).
- Y. P. Wang, J. P. Chen, X. W. Li, J. X. Hong, X. H. Zhang, J. H. Zhou, and A. L. Ye, "Measuring electro-optic coefficients of poled polymers using fiber-optic Mach-Zehnder Interferometer," *Appl. Phys. Lett.* **85**(21), 5102–5103 (2004).
- L. V. Nguyen, D. Hwang, S. Moon, D. S. Moon, and Y. Chung, "High temperature fiber sensor with high sensitivity based on core diameter mismatch," *Opt. Express* **16**(15), 11369–11375 (2008).
- Z. Ou, Y. Yu, P. Yan, J. Wang, Q. Huang, X. Chen, C. Du, and H. Wei, "Ambient refractive index-independent bending vector sensor based on seven-core photonic crystal fiber using lateral offset splicing," *Opt. Express* **21**(20), 23812–23821 (2013).
- Y. P. Wang, "Review of long period fiber gratings written by CO<sub>2</sub> laser," *J. Appl. Phys.* **108**(8), 081101 (2010).
- Y. P. Wang, Y. J. Rao, Z. L. Ran, T. Zhu, and X. K. Zeng, "Bend-insensitive long-period fiber grating sensors," *Opt. Lasers Eng.* **41**(1), 233–239 (2004).
- Y. H. Li and L. M. Tong, "Mach-Zehnder interferometers assembled with optical microfibers or nanofibers," *Opt. Lett.* **33**(4), 303–305 (2008).
- C. R. Liao, D. N. Wang, and Y. Wang, "Microfiber in-line Mach-Zehnder interferometer for strain sensing," *Opt. Lett.* **38**(5), 757–759 (2013).
- W. Zhou, W. C. Wong, C. C. Chan, L. Y. Shao, and X. Y. Dong, "Highly sensitive fiber loop ringdown strain sensor using photonic crystal fiber interferometer," *Appl. Opt.* **50**(19), 3087–3092 (2011).
- B. Dong, D.-P. Zhou, and L. Wei, "Temperature insensitive all-fiber compact polarization-maintaining photonic crystal fiber based interferometer and its applications in fiber sensors," *J. Lightwave Technol.* **28**(7), 1011–1015 (2010).
- Y.-G. Han, "Temperature-insensitive strain measurement using a birefringent interferometer based on a polarization-maintaining photonic crystal fiber," *Appl. Phys. B* **95**(2), 383–387 (2009).
- L. Jiang, J. Yang, S. Wang, B. Li, and M. Wang, "Fiber Mach-Zehnder interferometer based on microcavities for high-temperature sensing with high sensitivity," *Opt. Lett.* **36**(19), 3753–3755 (2011).
- A. B. Socorro, I. Del Villar, J. M. Corres, F. J. Arregui, and I. R. Matias, "Mode transition in complex refractive index coated single-mode-multimode-single-mode structure," *Opt. Express* **21**(10), 12668–12682 (2013).

14. H. T. Wang, S. L. Pu, N. Wang, S. H. Dong, and J. Huang, "Magnetic field sensing based on singlemode-multimode-singlemode fiber structures using magnetic fluids as cladding," *Opt. Lett.* **38**(19), 3765–3768 (2013).
15. P. Lu and Q. Chen, "Asymmetrical Fiber Mach-Zehnder Interferometer for Simultaneous Measurement of Axial Strain and Temperature," *IEEE Photonics J.* **2**(6), 942–953 (2010).
16. Z. Tian, S.-H. Yam, and H.-P. Loock, "Single-mode fiber refractive index sensor based on core-offset attenuators," *IEEE Photon. Technol. Lett.* **20**(16), 1387–1389 (2008).
17. P. Lu, L. Men, K. Sooley, and Q. Chen, "Tapered fiber Mach-Zehnder interferometer for simultaneous measurement of refractive index and temperature," *Appl. Phys. Lett.* **94**(13), 131110 (2009).
18. D. Wu, T. Zhu, K. S. Chiang, and M. Deng, "All Single-Mode Fiber Mach-Zehnder Interferometer Based on Two Peanut-Shape Structures," *J. Lightwave Technol.* **30**(5), 805–810 (2012).
19. Y. J. Rao, X. K. Zeng, Y. P. Wang, T. Zhu, Z. L. Ran, L. Zhang, and I. Benning, "Temperature-strain discrimination using a wavelength-division-multiplexed chirped in-fiber-Bragg-Grating/extrinsic Fabry-Perot sensor system," *Chin. Phys. Lett.* **18**(5), 643–645 (2001).
20. D.-P. Zhou, L. Wei, W.-K. Liu, Y. Liu, and J. W. Lit, "Simultaneous measurement for strain and temperature using fiber Bragg gratings and multimode fibers," *Appl. Opt.* **47**(10), 1668–1672 (2008).
21. Y. J. Rao, S. F. Yuan, X. K. Zeng, D. K. Lian, Y. Zhu, Y. P. Wang, S. L. Huang, T. Y. Liu, G. F. Fernando, L. Zhang, and I. Bennion, "Simultaneous strain and temperature measurement of advanced 3-D braided composite materials using an improved EFPI/FBG system," *Opt. Lasers Eng.* **38**(6), 557–566 (2002).
22. W. Qian, C.-L. Zhao, X. Dong, and W. Jin, "Intensity measurement based temperature-independent strain sensor using a highly birefringent photonic crystal fiber loop mirror," *Opt. Commun.* **283**(24), 5250–5254 (2010).
23. M.-S. Yoon, S. Park, and Y.-G. Han, "Simultaneous measurement of strain and temperature by using a micro-tapered fiber grating," *J. Lightwave Technol.* **30**(8), 1156–1160 (2012).
24. C. R. Liao, Y. Wang, D. N. Wang, and M. W. Yang, "Fiber In-Line Michelson Interferometer Tip Sensor Fabricated by Femtosecond Laser," *IEEE Photon. Technol. Lett.* **24**(22), 2060–2063 (2012).

## 1. Introduction

Optical fiber sensors based on Mach-Zehnder interferometers (MZI) have attracted great research interests and been widely used to monitor the health of smart engineering structures due to their unique advantages of compact size, low cost, high sensitivity, and immunity to electromagnetic interference [1–4]. So far, a few types of fiber MZI configurations have been demonstrated via long period fiber gratings (LPFGs) [5,6], microfiber-based structures [7,8], photonic crystal fibers (PCFs) [9–11], and air-hole formed by femtosecond laser [12]. Besides these structure of costly fiber and complex technology, some low-cost MZI based on single-mode fiber were presented such as single-mode-multimode-single-mode (SMS) fiber structure [13, 14], mode field mismatch fusion [15], two core offset structure [16], fiber waist-deformed fiber taper [17], peanut-shape structure [18]. These configurations exhibit good performance in the applications of sensing temperature, strain and surrounding refractive index. However, the cross sensitivity between strain, RI and temperature is one of the most serious problem, resulting in poor measurement precision, of these MZI-based sensors [19–21].

In this paper, we demonstrated a novel fiber in-line MZI which was fabricated by splicing a section of thin core fiber (TCF) between two sections of standard single-mode fibers (SMFs) with one misaligned spliced joint. Such a MZI can be used to develop a promising smart sensor for realizing simultaneous measurement of strain and temperature and overcoming their cross-sensitivity problem. This MZI-based sensor exhibits show an ultrahigh strain sensitivity of  $-0.023 \text{ dB}/\mu\epsilon$  (one order higher than that, e.g.  $-0.0032 \text{ dB}/\mu\epsilon$ , reported in references [22, 23]) and a high temperature sensitivity of up to  $51 \text{ pm}/^\circ\text{C}$ .

## 2. Basic principle of the MZI

Figure 1 illustrates a 3-D schematic diagram of the proposed fiber in-line MZI structure, in which a section of TCF is spliced between two sections of standard SMFs, i.e. so-called the lead-in SMF and the lead-out SMF. A core offset is created at the spliced joint between the lead-in SMF and the TCF. At the spliced joint with a core offset, light propagating in the lead-in SMF core is divided into two parts: a fraction of light will propagate into the core of the TCF as a core mode and majority of light will propagate into the cladding of the TCF as a cladding mode. After propagating through the TCF, the two parts of light will meet and recombine in the lead-out SMF, resulting in an interference pattern depending on the difference between the distances they travel.

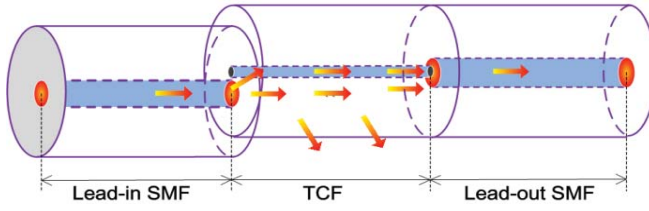


Fig. 1. Schematic diagram of the proposed fiber in-line MZI and the propagating light distribution in this structure.

Assuming that the amplitude of electrical field launched into the lead-in SMF is  $E_0$ , the output intensity of the MZI could be expressed as [24]:

$$I_{out} = (E_0 \gamma \beta)^2 + [E_0(1-\gamma)]^2 + 2E_0 \gamma (1-\gamma) \beta \cos \varphi \quad (1)$$

where  $\gamma$  is the ratio of light emitted into the core and the cladding of the TCF at the lead-in spliced joint,  $\beta$  is the propagation loss of the cladding modes because of the propagating condition of the TCF cladding, and  $\varphi$  is the phase difference between the two modes. The visibility of fringe pattern can be given as:

$$V = 2\beta(\beta^2 \frac{\gamma}{1-\gamma} + \frac{1-\gamma}{\gamma})^{-1} \quad (2)$$

It can be easily found from Eq. (2) that the fringe visibility is critically determined by the splitting ratio  $\gamma$ , which can be carefully adjusted by changing the value of the core offset at the left spliced joint.

The accumulated phase difference  $\varphi$  between the two modes can be approximated as:

$$\varphi = \frac{2\pi \cdot \Delta n_{eff} \cdot L}{\lambda} \quad (3)$$

where  $\Delta n_{eff}$  is effective refractive index difference between the core mode and the cladding mode in the TCF,  $L$  is the length of the TCF and  $\lambda$  is the wavelength of light in vacuum. When the phase term satisfies the condition:  $\varphi = (2k+1)\pi$ , where  $k$  is the order of the modes, an intensity dip appears at the wavelength:

$$\lambda_{dip} = \frac{2\Delta n_{eff} \cdot L}{2m+1} \quad (4)$$

Equations (1) and (4) indicate that the length increase of the TCF will only shift linearly the wavelength of fringe dips but not impact the fringe visibility. And the shift of fringe dips can be impacted by the MZI length and the effective refractive index difference between the core and the cladding. Thus the strain-induced shift of fringe dips can be expressed as [15]:

$$\delta\lambda_{dip,\epsilon} = \frac{2(\Delta n_{eff,\epsilon} - \delta n_{eff,\epsilon})(L + \delta L)}{2m+1} - \frac{2\Delta n_{eff,\epsilon} \cdot L}{2m+1} \approx 2 \frac{\Delta n_{eff,\epsilon} \cdot \delta L - \delta n_{eff,\epsilon} \cdot L}{2m+1} \quad (5)$$

where  $\Delta n_{eff,\epsilon}$  is effective refractive index difference between the core mode and the cladding mode at the tensile strain of  $\epsilon$ ,  $\delta n_{eff,\epsilon}$  is the strain-induced change of  $\Delta n_{eff,\epsilon}$  and  $\delta L$  is the strain-induced change of the TCF length.

And the temperature-induced shift of fringe dips can be expressed as [17]:

$$\delta\lambda_{dip,T} = \frac{2(\Delta n_{eff,T} + \delta n_{eff,T})L}{2m+1} - \frac{2\Delta n_{eff,T} \cdot L}{2m+1} = \frac{2\delta n_{eff,T} \cdot L}{2m+1} \quad (6)$$

where  $\Delta n_{\text{eff},T}$  is effective refractive index difference between the core and the cladding modes at the temperature of T,  $\delta n_{\text{eff},T}$  is the temperature-induced change of  $\Delta n_{\text{eff},T}$ .

### 3. Fabrication and experiments of MZI

#### 3.1 Fabrication of MZI

As we can see in Fig. 2, a standard SMF (Corning SMF-28) with a core diameter of about 8  $\mu\text{m}$  and a TCF (Nufern UHNA-3) with a core diameter about 4  $\mu\text{m}$  were employed in our experiments. As shown in Fig. 2(a), a section of TCF was spliced between two sections of SMFs. And a core offset was created at the spliced joint between the lead-in SMF and the TCF. Figures 2(b) and 2(c) show microscope images of the two spliced joints with/without a core offset, respectively.

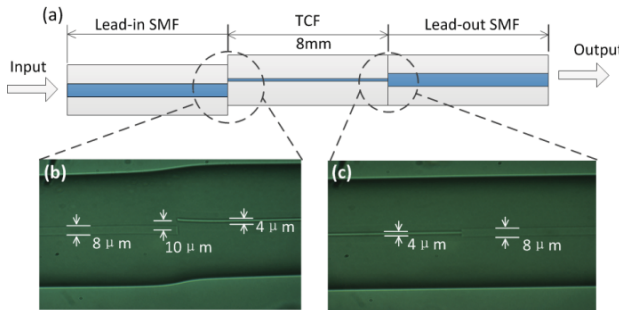


Fig. 2. (a) Fiber in-line MZI structure; Optical microscope image of (b) the lead-in spliced joints with a core offset and (c) the lead-out spliced joints without a core offset.

Fabrication process of the MZI structure is described as follow. Firstly, a section of TCF (Nufern UHNA-3) with a length of 8 mm was spliced with a standard SMF (Corning SMF-28), i.e. the lead-out SMF, without a core offset by use of a commercial splicer (Fujikura FSM-60s), as illustrated in Fig. 2(c). Secondly, another end of the TCF and the end of another standard SMF (Corning SMF-28), i.e. the lead-in SMF, were fixed via the left and right fiber holders, respectively, in the splicer. Meanwhile, a broadband light source and an optical spectrum analyzer were connected with the lead-in and lead-out SMFs, respectively, to monitor interference spectrum. The core offset between the lead-in SMF and the TCF was carefully adjusted via the hand mode of the splicer until good fringe visibility was observed.

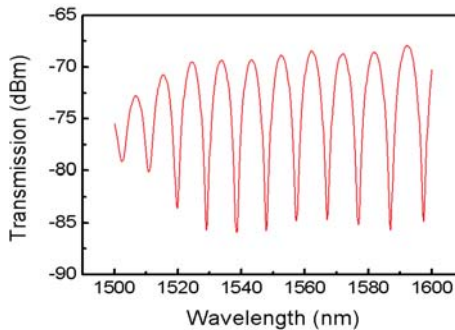


Fig. 3. Interference fringe pattern of the achieved MZI with a core offset of about 10  $\mu\text{m}$ .

Consequently, a lead-in spliced joint with a core offset of about 10  $\mu\text{m}$  was created, as illustrated in Fig. 2(b), where the core of TCF was curved upward slightly caused by more splice overlap induced. So an in-fiber MZI with a core offset was successfully achieved and a good fringe pattern with a visibility of up to 17dB near the wavelength of 1550 nm was observed, as shown in Fig. 3.

### 3.2 Strain response

To investigate the response of the MZI structure to tensile strain, the lead-in SMF of the structure was fixed, and the lead-out SMF was stretched along the fiber axis to induce a tensile strain from 0 to 1500  $\mu\text{e}$  by use of a translation stage with a resolution of 10  $\mu\text{m}$ . The length of the stretched fibers, including the lead-in and lead-out SMFs and the TCF, is 200 mm. Typical interference fringe patterns of the MZI with different tensile strains are illustrated in Fig. 4(a), where the tensile strain increases from 0 to 500  $\mu\text{e}$  with a step of 50  $\mu\text{e}$  and from 500 to 1500  $\mu\text{e}$  with a step of 200  $\mu\text{e}$ .

As shown in Fig. 4(a), the dip wavelength hardly changed with an increased tensile strain from 0 to 500  $\mu\text{e}$ , but the fringe visibility was enhanced. In contrast, while the tensile strain was increased beyond 500  $\mu\text{e}$ , the fringe visibility hardly changed but the interference fringe exhibited a blue shift.

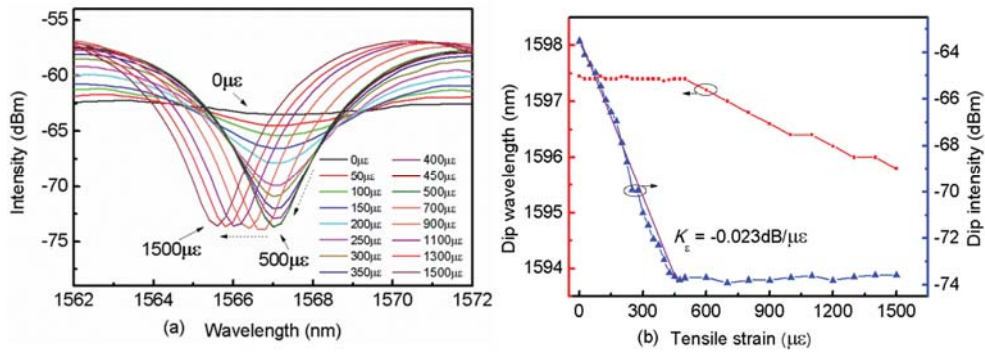


Fig. 4. (a) Interference fringe patterns of the MZI with different strain; (b) Dip wavelength and intensity versus tensile strain.

As shown in Fig. 4(b), the minimum intensity of interference fringe, i.e. dip intensity, linearly decreased with an ultrahigh sensitivity of  $-0.023 \text{ dB}/\mu\text{e}$  while the applied tensile strain was increased from 0 to 500  $\mu\text{e}$ , but the dip wavelength hardly changed. To the best of our knowledge, this strain sensitivity is about one order of magnitude higher than that reported in references [22, 23], in which a highly birefringent photonic crystal fiber loop mirror was employed to achieve a strain sensor with a sensitivity of  $-0.0032 \text{ dB}/\mu\text{e}$ . In contrast, the dip wavelength linearly shifted toward a shorter wavelength with an increased tensile strain of beyond 500  $\mu\text{e}$ , but the change of the dip intensity was negligible. Furthermore, the above strain experiment of the MZI sample were done five times, and good repeatability was achieved owe to the simple and compact MZI structure, the strong strength of the lead-in spliced joint, and the power stability of the broadband light source employed.

In case the tensile strain was less than 500  $\mu\text{e}$ , the applied tensile strain induced a significant physical deformation, i.e. the change of the core offset between the lead-in SMF and the TCF and the slightly curved core of TCF at the misalignment-spliced region, which changed the ratio,  $\gamma$ , of light emitted into the core and the cladding of the TCF. According to Eq. (1), the fringe visibility was effectively modulated with a strain sensitivity of  $-0.023 \text{ dB}/\mu\text{e}$ , as a result. In case the tensile strain was increased over a threshold of 500  $\mu\text{e}$ , further physical deformation induced by the increased tensile strain at the misalignment-spliced joint is very weak due to the limit of the core offset so that the splitting ratio of light was hardly affected. And the increased tensile strain mainly resulted in an extension of the MZI cavity length. Hence, the dip intensity was insensitive to the applied strain of more than 500, whereas the dip wavelength shifted toward a shorter wavelength, as shown in Fig. 4(b). The threshold of the tensile strain depends strongly on the fabrication parameters such as the type of the fiber employed, the core offset, the fiber overlap at the splicing joint, and arc discharge parameters. Our experiments shows that, providing the fabrication parameters are not

changed, a few MZI samples has a similar strain threshold of about  $500\mu\text{e}$ . In other words, a repeatable results could be achieved for different MZI samples created by use of the same fabrication parameters. According to Eq. (5), the reason of above is that, the increase of the MZI cavity length,  $\Delta n_{\text{eff},e} \cdot \delta L$ , has a weaker impact on the dip wavelength than the decrease of the effective refractive index difference,  $-\delta n_{\text{eff},e} \cdot L$ , so that the dip wavelength ‘blue’ shifts while the tensile strain increases over  $500\mu\text{e}$  [15].

### 3.3 Temperature response

Temperature response of the MZI was also investigated by means of placing it into a tube furnace with a temperature range from room temperature to  $100^\circ\text{C}$  (with a stability of  $\pm 0.2^\circ\text{C}$ ). If the extinction ratio of the measured interference dip is not enough large, the measurement precision of the dip wavelength is very poor. So another interference dip with a large extinction ratio at the wavelength of  $1538.36\text{ nm}$  was measured to investigate the temperature response of the dip wavelength. Temperature in the furnace rose gradually from  $30$  to  $100^\circ\text{C}$  with a step of  $10^\circ\text{C}$ , and then maintained about  $30$  min during each temperature rise.

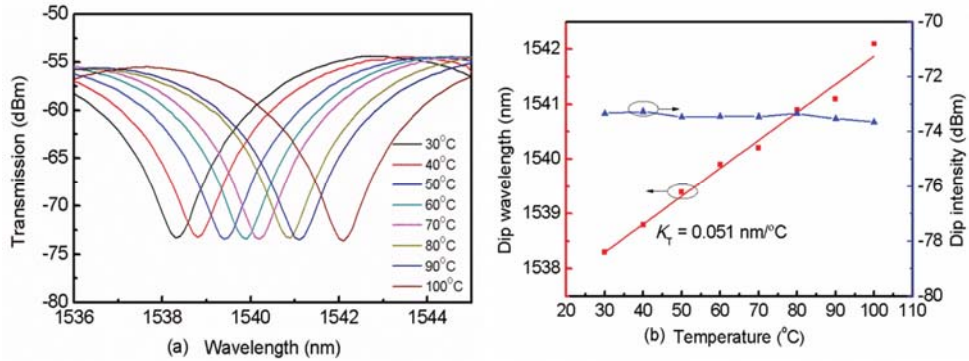


Fig. 5. (a) Interference fringe of the MZI with different temperature; (b) Dip wavelength and dip intensity versus temperature.

As shown in Fig. 5(a), interference fringes of the MZI shifted toward a longer wavelength with temperature rise. It can be easily found from Fig. 5(b) that the dip wavelength of the MZI ‘red’ shifted linearly with a sensitivity of  $51\text{ pm/}^\circ\text{C}$ , but the dip intensity hardly changed. Temperature-induced ‘red’ shift of the dip wavelength could be explained below. Since thermo-optic coefficient of the Ge-doped silica core is higher than that of the cladding consisting of fused silica [17], effective refractive index difference between the core and the cladding modes will increase with temperature rise. Consequently, according to Eq. (6), the dip wavelength shifts toward a longer wavelength due to the temperature-induced of  $\delta n_{\text{eff},T}$  while environmental temperature rises.

## 4. Discussions

Owing to the induced core offset between the lead-in SMF and the TCF and the slightly curved core of TCF at the misalignment-spliced region, the increase of tensile strain would change the splitting ratio, which result in the change of fringe visibility. And owing to the induced core offset, the cladding mode propagating in the cladding of TCF would be change by temperature, which result in wavelength shift of fringe dip.

According to Figs. 4(b) and 5(b), the dip intensity of the MZI decreases linearly with the increase of tensile strain within  $500\mu\text{e}$  and is insensitive to temperature rise. In contrast, the dip wavelength of the MZI shifts linearly toward a longer wavelength with temperature rise and is insensitive to a tensile strain of less than  $500\mu\text{e}$ . Hence, the MZI can be used to

develop a promising sensor that can measure simultaneously tensile strain and temperature, which is an excellent advantage of overcoming the cross-sensitivity problem between tensile strain and temperature in practical sensing applications of smart engineering structures. In other words, tensile strain can be measured via intensity modulation of interference fringe with a high sensitivity of  $-0.023 \text{ dB}/\mu\epsilon$  and a measurement range of up to  $500 \mu\epsilon$ . And temperature can be measured via wavelength modulation of interference fringe with a very high sensitivity of  $51 \text{ pm}/^\circ\text{C}$ . Therefore, our MZI-based sensor can realize simultaneous measurement of tensile strain and temperature.

It can be found from Figs. 4(b) and 5(b) that the fluctuation of the dip wavelength is less than  $0.04 \text{ nm}$  while tensile strain is less than  $500 \mu\epsilon$  and the fluctuation of the dip intensity is less than  $0.028 \text{ dBm}$  during temperature rise. As a result, the strain-caused error of the dip wavelength and the temperature-caused error of the dip intensity are less than  $0.8^\circ\text{C}$  and less than  $1.2 \mu\epsilon$ , respectively, during simultaneous measurement of tensile strain and temperature, which can meet the sensing applications in smart engineering structures.

## 5. Conclusion

In conclusion, a novel fiber in-line MZI with a misalignment-spliced joint was demonstrated to develop a promising sensor that can realize simultaneous measurement of tensile strain and temperature. The strain and temperature sensitivities of the proposed sensor are  $-0.023 \text{ dB}/\mu\epsilon$  and  $51 \text{ pm}/^\circ\text{C}$ , respectively. Such a sensor overcomes the cross-sensitivity problem between tensile strain and temperature. Furthermore, our MZI-based sensor exhibits the merits of compact size (only about  $8 \text{ mm}$ ), high sensitivities, intensity-modulated for strain, good repeatability and mechanical reliability so that it is a good candidate of next-generation sensors in smart engineering structures.

## Acknowledgments

This work was supported by the National Science Foundation of China (grants no. 11174064, 61308027, and 61377090), the Science & Technology Innovation Commission of Shenzhen (grants no. KQCX20120815161444632, and JCYJ20130329140017262), and the Distinguished Professors Funding from Shenzhen University and Guangdong Province Pearl River Scholars.



## Temperature-insensitive refractive index sensor based on in-fiber Michelson interferometer

Zhengyong Li, Yiping Wang\*, Changrui Liao, Shen Liu, Jiangtao Zhou, Xiaoyong Zhong, Yingjie Liu, Kaiming Yang, Qiao Wang, Guolu Yin

*Key Laboratory of Optoelectronic Devices and Systems of Ministry of Education and Guangdong Province, Shenzhen University, Shenzhen 518060, China*



### ARTICLE INFO

#### Article history:

Received 7 February 2014

Received in revised form 11 March 2014

Accepted 16 March 2014

Available online 1 April 2014

#### Keywords:

Optical fiber sensor

Michelson interferometer

Refractive index

Temperature

### ABSTRACT

A novel intensity-modulated refractive index sensor based on an in-fiber Michelson interferometer is demonstrated by splicing a section of thin core fiber between two standard single mode fibers. Such a refractive index sensor exhibits an ultrahigh sensitivity of  $-208.24$  and  $125.44 \text{ dB/RIU}$  at the refractive index of 1.440 and 1.500, respectively. The refractive index sensor is insensitive to temperature and thus solves the cross-sensitivity problem between temperature and surrounding refractive index. Moreover, the promising RI sensor has the advantages of short size (less than 2 mm) and easy fabrication.

© 2014 Elsevier B.V. All rights reserved.

## 1. Introduction

In recent years, fiber optic refractive index (RI) sensors in the field of chemical and biomedical applications has attracted significant attentions of researchers due to the advantages of their small size, high sensitivity, short response time, anti electromagnetic interference, and corrosion resistance. One has developed various in-fiber RI sensors based on typical in-fiber devices such as fiber Bragg gratings (FBGs) [1], long period fiber gratings (LPFGs) [2–4], Mach-Zehnder interferometers (MZIs) [5], surface plasmon resonance (SPR) [6], Fabry–Perot interferometers (FPIs) [7,8], Michelson interferometers (MIs) [9–13], and photonic crystal fibers (PCFs) [14]. However, complicated fabrication techniques, such as femtosecond laser micromachining [10], repeated arc discharges [12], fiber taping [13], and chemical etching [9], have employed to achieve refractive index sensors above. For example, a fiber in-line Michelson interferometer tip sensor based on open micro-cavity was fabricated by femtosecond laser micromachining [10]. A miniature core-offset RI sensor was created by means of repeated arc discharges, resulting in melting a fiber end into a rounded tip to excite high order cladding modes [12]. A refractive index sensor based on a Michelson interferometer was demonstrated by tapering abruptly a single mode fiber (SMF) and coating gold on the fiber

end fact [13]. In addition, the wavelength-modulated refractive index sensor usually is sensitive to temperature [9,15,16] so that the cross-sensitivity problem between temperature and surrounding refractive index has to be solved in practical sensing applications [17–20].

In this paper, a novel intensity-modulated refractive index sensor based on in-fiber Michelson interferometer was demonstrated by splicing a section of thin core fiber between two standard SMFs. Such a RI sensor is insensitive to temperature and thus solves the cross-sensitivity problem between temperature and surrounding refractive index. The MI-based RI sensor exhibits an ultrahigh sensitivity of  $-208.24$  and  $125.44 \text{ dB/RIU}$  at the refractive index of 1.440 and 1.500, respectively.

## 2. Device fabrication

Microscope image and schematic diagram of our proposed refractive index sensor based on a Michelson interferometer are shown in Fig. 1. One end of a standard SMF (Corning, SMF-28), i.e. SMF1, with a core/cladding diameter of  $8.2 \mu\text{m}/125 \mu\text{m}$  was connected to a broadband light source with a wavelength range from 1250 to 1650 nm (Fiber Lake ASE-LIGHT SOURCE) and an optical spectrum analyzer (OSA, YOKOGAWA AQ6370C) with a resolution of 2 nm via a 3 dB coupler in order to observe the reflection spectrum in real time during the fabrication of the MI-based sensor sample. After the right end of SMF1 was cleaved by use of a cutting knife (Fujikura DT-30), the observed reflection spectrum

\* Corresponding author. Tel.: +86 13510186456.

E-mail addresses: [ypwang@szu.edu.cn](mailto:ypwang@szu.edu.cn), [ypwang@china.com](mailto:ypwang@china.com) (Y. Wang).

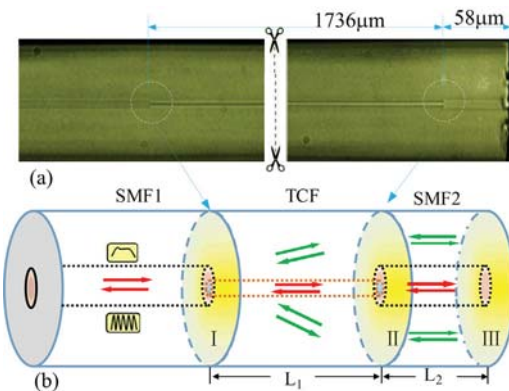


**Fig. 1.** (a) Microscope image and (b) schematic diagram of the created Michelson interferometer sample. Note that the image is cut off to illustrate the spliced joints of the sample.

was illustrated in Fig. 2(a). Secondly, the cleaved right end of SMF1 was spliced with a thin core fiber (Nufern, UHNA3), i.e. TCF, with a core/cladding diameter of  $4 \mu\text{m}/125 \mu\text{m}$  by use of a commercial fusion splicer (Fujikura FSM-60s). Before and after the right end of the TCF was cleaved, the observed reflection spectra were illustrated in Fig. 2(b) and 2(c), respectively. Interference fringes shown in Fig. 2(c) result from the Fabry–Perot interference between the two end facets of the TCF. Thirdly, another standard SMF (Corning, SMF-28), i.e. SMF2, was spliced with the cleaved right end of the TCF. Before and after the right end of SMF2 was cleaved, the observed reflection spectra were illustrated in Fig. 2(d) and 2(e), respectively. Interference fringes shown in Fig. 2(e) result from the

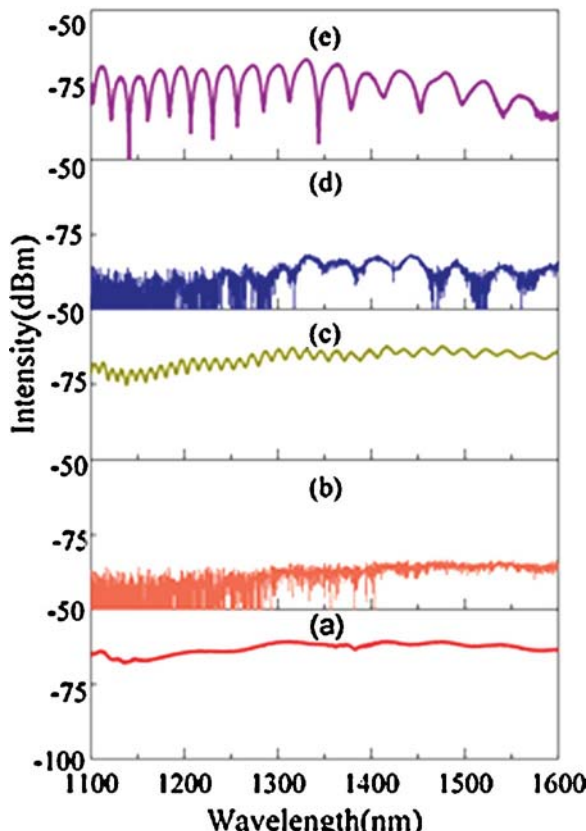


**Fig. 2.** Reflection spectra of (a) after the right end of SMF1, (b) before and (c) after the right end of the TCF was cleaved, (d) before and (e) after the right end of SMF2 was cleaved.

Michelson interference between the reflected core and cladding modes at the cleaved right end of SMF2, as discussed below.

Since SMF1 has a larger core diameter than the TCF, light propagating through SMF1 will divide into two parts: the core mode with a major energy and the cladding modes with a minor energy, at the interface, i.e. interface-I, between SMF1 and the TCF and then are reflected at the cleaved right end of the TCF. The reflected core and cladding modes will interfere with each other, i.e. Michelson interference, in the core of SMF1. Since the reflected core mode has a much larger energy than the reflected cladding modes, low interference fringe visibility is observed in the reflection spectrum, as shown in Fig. 2(c). In case SMF2 is spliced with the right end of the TCF, the core mode reflected at the cleaved right end facet, i.e. interface-III, of SMF2 will propagate through SMF2 and then transfer partially into the cladding modes at the interface, i.e. interface-II, between the TCF and SMF2, which results in the decrease of the reflected core mode and the increase of the reflected cladding modes in the TCF. Consequently, the reflected core mode has a similar energy to the reflected cladding modes so that high interference fringe visibility was observed in the reflection spectrum, as shown in Fig. 2(e).

As shown in Fig. 1(b), optical distance difference between the reflected core and cladding modes can be given by

$$\Delta d = L_1 \Delta n_{TCF}^m + L_2 \Delta n_{SMF2}^m \quad (1)$$

where  $L_1$  and  $L_2$  is the length of the TCF and SMF2, respectively;  $\Delta n_{TCF}^m$  and  $\Delta n_{SMF2}^m$  are the effective RI difference between the core mode and the  $m$ th order cladding mode in the TCF and SMF2, respectively; so the interference intensity can be calculated by

$$I = I_1 + I_2 + 2\sqrt{I_1 I_2} \cos(\Delta\Phi) \quad (2)$$

where  $I_1$  and  $I_2$  are the intensity of the core and cladding modes, respectively;  $\lambda$  is the wavelength of the propagating light. According to phase matching condition as

$$\Delta\Phi = \frac{4\pi(L_1 \Delta n_{TCF}^m + L_2 \Delta n_{SMF2}^m)}{\lambda_m} = (2m + 1)\pi \quad (3)$$

So free spectral range (FSR) in the interference fringe can be calculated by

$$FSR = \frac{\lambda^2}{2(L_1 \Delta n_{TCF}^m + L_2 \Delta n_{SMF2}^m)}. \quad (4)$$

As shown in Eq. (4), the FSR depends strongly on the lengths, i.e.  $L_1$  and  $L_2$ , of the TCF and SMF2. So we can achieve a desired FSR by means of improving the length of TCF and SMF2, as described below.

Interference fringe visibility in the reflection spectrum depends strongly on the intensity of the reflected core and cladding modes, which are decided by the lengths of the TCF and SMF2, the core diameters of the TCF and the standard SMF, and the spliced joints. So it is easy for us to enhance interference fringe visibility by means of cleaving gradually SMF2 to improve its length, as shown in Fig. 3, which is a critical advantage of our proposed in-fiber MI structure. In case the lengths of the TCF and SMF2 were improved to be 1736 and 58  $\mu\text{m}$ , respectively, we achieved a desired interference fringe with a high visibility of up to 24 dB. In contrast, the observed fringe visibility of the RI interferometer sensor based on a rounded tip and core-off was only about 5 dB, as reported in ref. [12], in which repeated arc discharges have to done to reshape the fiber end into a rounded tip.

### 3. Index sensing application

We investigated the response of the MI sample to surrounding refractive index by means of immersing it into a series

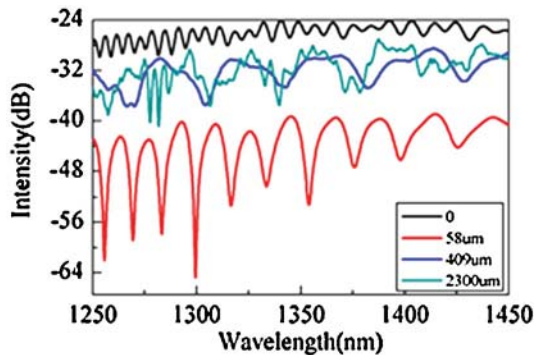


**Fig. 3.** Reflection spectra of the in-fiber Michelson interferometer while the length of SMF2 is improved to be 0, 58, 409 and 2300  $\mu\text{m}$ . Note that the zero length of SMF2 indicates that no SMF is spliced with the right end of the TCF.

of liquids, e.g. Refractive index matching liquid (Cargille Labs, <http://www.cargille.com>) with a RI from 1.300 to 1.700 at room temperature. Every time the MI sample was taken out from a liquid, it was carefully cleaned by use of alcohol to eliminate entirely the residual liquid on the fiber surface and then was immersed into another liquid.

As shown in Fig. 4(a), the intensity of the reflection spectrum decreased gradually while the surrounding refractive index was changed from 1.000 (air), 1.300 (liquid) to 1.460 (liquid). The reason for this is, that light reflected at the interface-III is gradually reduced with the increased surrounding refractive index,  $n_{\text{so}}$  from 1.0 to 1.460, according to Fresnel reflection,  $R = (n_{\text{si}} - n_{\text{so}})^2 / (n_{\text{si}} + n_{\text{so}})^2$

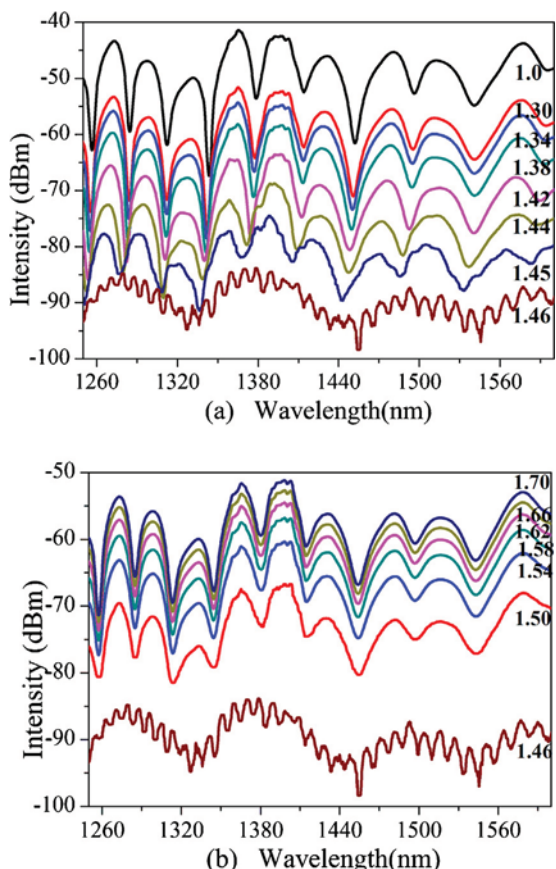


**Fig. 4.** Reflection spectrum evolution of the in-fiber MI sample immersed into a series of liquid with a refractive index (a) from 1.30 to 1.46, and (b) from 1.46 to 1.70.

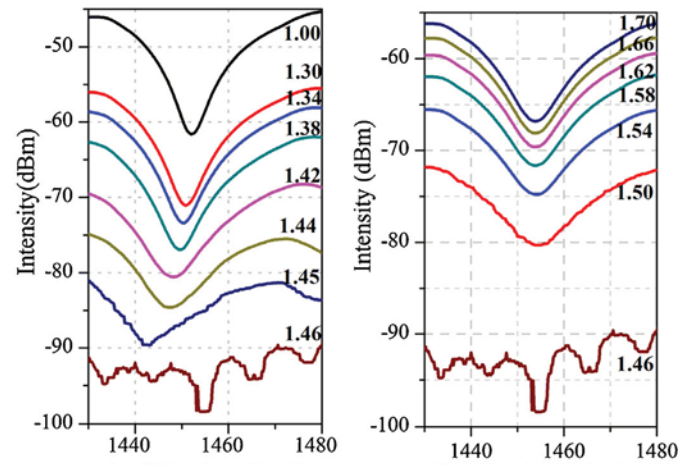


**Fig. 5.** Reflection spectrum evolution within the wavelength range from 1430 to 1480 nm while the surrounding RI changes (a) from 1.0 to 1.46 and (b) from 1.46 to 1.70; (c) The dip intensity of the interference fringe versus the surround RI; (d) The dip wavelength versus the surrounding RI.

where  $n_{\text{si}}$  and  $n_{\text{so}}$  are refractive index of silica and surround medium (air or liquid), respectively. Note that the RI of the fiber material, i.e. silica, is about 1.460. In contrast, as shown in Fig. 4(b), the intensity of the reflection spectrum increased gradually while the surrounding refractive index was changed from 1.460 to 1.700. The reason for this is, according to Fresnel reflection, that light reflected at the interface-III is enhanced gradually with the increased surrounding refractive index,  $n_{\text{so}}$ , from 1.460 to 1.700. It can be seen from Fig. 4 that, while the MI sample was immersed into a liquid with a similar refractive index (1.460) to silica index, interference fringes with a small FSR of about 10 nm was observed in the reflection spectrum, which results from the Fabry–Perot interference between the interface-II and the interface-III, rather than the Michelson interference, due to the reduce of light reflected at the interface-III.

Reflection spectra within the wavelength range from 1430 to 1480 nm in Fig. 4 are illustrated in Fig. 5(a) and (b) to analyze quantitatively the response of the in-fiber MI sample to the change of surrounding refractive index. As shown in Fig. 5(c), the dip intensity of the interference fringe decreases with the increased surrounding RI from 1.0 to 1.46 and increases with the increased surrounding RI from 1.46 to 1.70. Therefore, such an in-fiber MI could be used to develop a promising intensity-modulated RI sensor. The sensitivity of the MI-based RI sensor is calculated to be  $-208.24$  and  $125.44 \text{ dB/RIU}$  at the refractive index of 1.440 and 1.500, respectively, via polynomial fitting method.

As shown in Fig. 5(d), the dip wavelength of the interference fringe also decreases with the increased surrounding RI from 1.0 to 1.46, which the wavelength sensitivity of RI sensor is calculated to be  $-72.87 \text{ nm/RIU}$  at the RI of 1.44, and hardly changes with the increased surrounding RI from 1.46 to 1.70, but the intensity modulation, rather than the wavelength modulation, was used in our proposed MI-based refractive index sensor in order to solve the

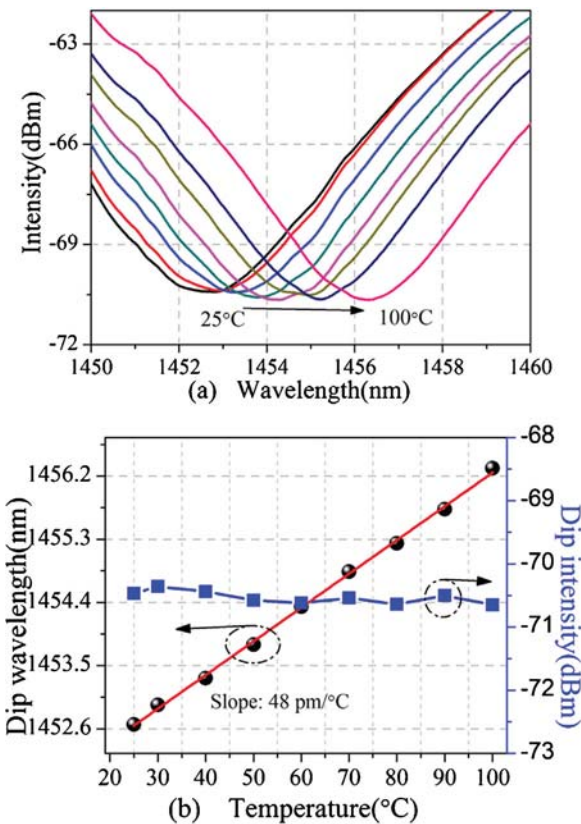


**Fig. 6.** Reflection spectrum evolution of the in-fiber MI sample (a) temperature rise from 25 to 100 °C with a step of 10 °C.(b) dip wavelength and corresponding dip intensity vary with temperature.

cross-sensitivity problem between temperature and surrounding refractive index, as described below.

#### 4. Temperature response

The cross sensitivity between surrounding refractive index and temperature has to be considered in the application of refractive index sensors. So we investigated the temperature response of the MI-based RI sensor by use of an oven with a temperature stability of  $\pm 0.2$  °C. While the temperature rose from room temperature, i.e. 25–100 °C, as shown in Fig. 6(a), the reflection spectrum of the MI-based sensor shifted toward a longer wavelength with a sensitivity of 0.048 nm/°C whereas the dip intensity of the interference fringe hardly changed. In other words, the dip intensity is insensitive to temperature. So our proposed intensity-modulated refractive index sensor based on the in-fiber MI is insensitive to temperature and thus solve the cross-sensitivity problem between temperature and surrounding refractive index.

#### 5. Conclusion

A compact in-fiber MI with a short size of less than 2 mm was created by splicing a section of thin core fiber between two standard SMFs. Interference fringes in the reflection spectrum have a high extinction ratio of up to 24 dB. Such an in-fiber MI could be used to develop a promising intensity-modulated refractive index sensor that exhibits an ultrahigh sensitivity of  $-208.24$  and  $125.44$  dB/RIU at the refractive index of 1.440 and 1.500, respectively. Moreover, the MI-based refractive index sensor solves the cross-sensitivity problem between temperature and surrounding refractive index

and could find potential applications in the fields of chemical and biomedical sensing, and environmental monitoring.

#### Acknowledgements

This work was supported by National Natural Science Foundation of China (grant nos. 11174064, 61308027, and 61377090), Science & Technology Innovation Commission of Shenzhen (grant nos. KQCX20120815161444632, and JCYJ20130329140017262), and Distinguished Professors Funding from Shenzhen University (grant nos. 810-000001) and Guangdong Province Pearl River Scholars (grant nos. 829-000001).

#### References

- [1] X. Fang, C.R. Liao, D.N. Wang, Femtosecond laser fabricated fiber Bragg grating in microfiber for refractive index sensing, *Opt. Lett.* 35 (7) (2010) 1007–1009.
- [2] Y.E. Fan, T. Zhu, L.L. Shi, Y.J. Rao, Highly sensitive refractive index sensor based on two cascaded special long-period fiber gratings with rotary refractive index modulation, *Opt. Lett.* 50 (23) (2011) 4604–4610.
- [3] D.W. Kim, Y. Zhang, K.L. Cooper, A. Wang, In-fiber reflection mode interferometer based on a long-period grating for external refractive-index measurement, *Appl. Opt.* 44 (26) (2005) 5368–5373.
- [4] Y. Fan, T. Zhu, L. Shi, Y. Rao, Highly sensitive refractive index sensor based on two cascaded special long-period fiber gratings with rotary refractive index modulation, *Appl. Opt.* 50 (23) (2011) 4604–4610.
- [5] S.S. Zhang, W. Zhang, P. Geng, S. Gao, Fiber Mach-Zehnder interferometer based on concatenated down- and up-tapers for refractive index sensing applications, *Opt. Commun.* 288 (2013) 47–51.
- [6] P. Bhatia, B.D. Gupta, Surface-plasmon-resonance-based fiber optic refractive index sensor: sensitivity enhancement, *Appl. Opt.* 50 (14) (2011) 2032–2036.
- [7] Y. Wang, D.N. Wang, C.R. Liao, T. Hu, J. Guo, H. Wei, Temperature-insensitive refractive index sensing by use of micro Fabry-Perot cavity based on simplified hollow-core photonic crystal fiber, *Opt. Lett.* 38 (3) (2013) 269–271.
- [8] C.R. Liao, T.Y. Hu, D.N. Wang, Optical fiber Fabry-Perot interferometer cavity fabricated by femtosecond laser micromachining and fusion splicing for refractive index sensing, *Opt. Express* 20 (20) (2012) 22813–22818.
- [9] A. Zhou, G. Li, Y. Zhang, Y. Wang, C. Guan, J. Yang, et al., Asymmetrical twin-core fiber based Michelson interferometer for refractive index sensing, *J. Lightwave Technol.* 29 (19) (2011) 2985–2991.
- [10] C.R. Liao, D.N. Wang, M. Wang, M.H. Yang, Fiber in-line Michelson interferometer tip sensor fabricated by femtosecond laser, *IEEE Photon. Technol. Lett.* 24 (22) (2012) 2060–2063.
- [11] Q. Rong, X. Qiao, Y. Du, D. Feng, R. Wang, Y. Ma, et al., In-fiber quasi-Michelson interferometer with a core-cladding-mode fiber end-face mirror, *Appl. Opt.* 52 (7) (2013) 1441–1447.
- [12] W.C. Wong, C.C. Chan, Y.F. Zhang, K.C. Leong, Miniature single-mode fiber refractive index interferometer sensor based on high order cladding mode and core-offset, *IEEE Photon. Technol. Lett.* 24 (5) (2012) 359–361.
- [13] Z.B. Tian, S.S.H. Yam, H.P. Loock, Refractive index sensor based on an abrupt taper Michelson interferometer in a single-mode fiber, *Opt. Lett.* 33 (10) (2008) 1105–1107.
- [14] D.Q. Yang, H.P. Tian, Y.F. Ji, Q.M. Quan, Design of simultaneous high-Q and high-sensitivity photonic crystal refractive index sensors, *J. Opt. Soc. Am. B: Opt. Phys.* 30 (8) (2013) 2027–2031.
- [15] Y. Wang, D. Richardson, G. Brambilla, X. Feng, M. Petrovich, M. Ding, et al., Intensity measurement bend sensors based on periodically tapered soft glass fibers, *Opt. Lett.* 36 (4) (2011) 558–560.
- [16] Y. Wang, D.N. Wang, W. Jin, CO<sub>2</sub> laser-grooved long period fiber grating temperature sensor system based on intensity modulation, *Appl. Opt.* 45 (31) (2006) 7966–7970.
- [17] Y. Wang, L. Xiao, D.N. Wang, W. Jin, Highly sensitive long-period fiber-grating strain sensor with low temperature sensitivity, *Opt. Lett.* 31 (23) (2006) 3414–3416.
- [18] Y.J. Rao, X.K. Zeng, Y. Zhu, Y.P. Wang, T. Zhu, Z.L. Ran, et al., Temperature-strain discrimination sensor using a WDM chirped in-fibre Bragg grating and an extrinsic Fabry-Perot, *Chin. Phys. Lett.* 18 (5) (2001) 643–645.
- [19] J. Grochowski, M. Mysliwiec, P. Mikulic, W.J. Bock, M. Smietana, Temperature cross-sensitivity for highly refractive index sensitive nanocoated long-period gratings, *Acta Phys. Polon. A* 124 (3) (2013) 421–424.
- [20] K.M. Zhou, L. Zhang, X.F. Chen, I. Bennion, Optic sensors of high refractive-index responsivity and low thermal cross sensitivity that use fiber Bragg gratings of >80 degrees tilted structures, *Opt. Lett.* 31 (9) (2006) 1193–1195.

#### Biographies

**Zhengyong Li** was born in Hubei Province, China in 1988. He received his bachelor degree from Huazhong University of Science and Technology Wenhua College in 2012. He is currently completing his master degree in the field of fiber optic sensors in Shenzhen University, China.

**Yiping Wang** is a Distinguished Professor and a Pearl River Scholar in the College of Optoelectronic Engineering, Shenzhen University, Shenzhen, China. He was born in Chongqing, China, in July 15, 1971. He received the B.S. degree in Precision Instrument Engineering from Xi'an Institute of Technology, Xi'an, China, in 1995, and the M.S. degree in Precision Instrument and Mechanism and the Ph.D. degree in Optical Engineering from Chongqing University, China, in 2000 and 2003, respectively, where he received the prestigious award of The National Excellent Doctoral Dissertations of China. In 2003, he joined the Department of Electronics Engineering, Shanghai Jiao Tong University, China, as a postdoctoral research fellow and an associate professor. In 2005, he joined the Department of Electrical Engineering, Hong Kong Polytechnic University, Hong Kong, as a postdoctoral research fellow and a research fellow. In 2007, he joined the Institute of Photonic Technology, Jena, Germany as a Humboldt research fellow. In 2009, he joined the Optoelectronics Research Centre, University of Southampton, U.K. as a Marie Curie Fellow. Since 2012, he has been with Shenzhen University as a Distinguished Professor and a Pearl River Scholar. His current research interests focus on optical fiber sensors, in-fiber gratings, photonic crystal fibers, and fluid-filling technologies. He has authored or coauthored 1 book, 9 patent applications, and more than 150 journal and conference papers with a SCI citation of more than 1200 times. Dr. Wang is a senior member of IEEE, the Optical Society of America, and the Chinese Optical Society.

**Changrui Liao** received the B.E. degree in optical information science and technology and the M.S. degree in physical electronics from Huazhong University of Science and Technology, China, in 2005 and 2007, and the Ph.D. degree from the Hong Kong Polytechnic University, Hong Kong, in 2012. Since 2012, he has been with the College of Optoelectronic Engineering, Shenzhen University as an assistant professor. His main research interests are femtosecond laser micromachining, optical fiber devices and sensors.

**Shen Liu** was born in Henan Province in China in 1986. He was awarded his master degree in Chongqing University of Posts and Telecommunications.

**Jiangtao Zhou** was born in Anhui province in China in 1990. He is currently completing his master degree in the field of fiber optic sensors in Shenzhen University, China.

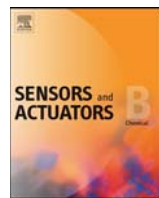
**Xiaoyong Zhong** was born in Guangdong Province in China in 1988. He received bachelor degree in Guangdong University of Technology. He is currently completing his master degree in the field of fiber optic sensors in Shenzhen University, China.

**Yingjie Liu** was born in Hubei Province, China in 1989. She is currently completing her master degree in the field of fiber optic sensors in Shenzhen University, China.

**Kaiming Yang** was born in Jiangxi Province in China in 1991. He is currently completing his master degree in the field of fiber optic sensors in Shenzhen University, China.

**Qiao Wang** was born in Hubei Province, China in 1991. He received his bachelor from Huazhong university of science and technology wenhua college in 2013. He is currently completing his master degree in the field of fiber optic sensors in Shenzhen University, China.

**Guolu Yin** received bachelor degree and Ph.D. from Department of Science in Beijing Jiaotong University in 2008 and in 2013, respectively. He joined in Shenzhen University, China, as a postdoctoral fellow.



## Intensity modulated refractive index sensor based on optical fiber Michelson interferometer

Jiangtao Zhou, Yiping Wang\*, Changrui Liao, Bing Sun, Jun He, Guolu Yin, Shen Liu, Zhengyong Li, Guanjun Wang, Xiaoyong Zhong, Jing Zhao

*Key Laboratory of Optoelectronic Devices and Systems of Ministry of Education and Guangdong Province, College of Optoelectronic Engineering, Shenzhen University, Shenzhen 518060, China*

### ARTICLE INFO

#### Article history:

Received 3 August 2014

Received in revised form 20 October 2014

Accepted 4 November 2014

Available online 11 November 2014

#### Keywords:

Optical fiber sensor

Reflective index sensor

Michelson interference

Fresnel reflection

Temperature insensitivity

### ABSTRACT

We demonstrated a refractive index (RI) sensor based on optical fiber Michelson interferometer (MI), which was fabricated by splicing a section of thin core fiber (TCF) to a standard single mode fiber with a core offset. Experimentally, such a MI-based RI sensor with a core offset of 8 μm and a TCF length of 3 mm exhibits a high resolution of  $4.9 \times 10^{-6}$  RIU and sensitivity of  $-202.46 \text{ dB/RIU}$ , which is two or three times higher than that of intensity-modulated RI sensors reported previously. In contrast, our MI-based RI sensor is insensitive to temperature, thus overcoming the cross-sensitivity problem between surrounding RI and temperature. Moreover, intensity modulation, rather than wavelength modulation, was used in the proposed MI-based RI sensor, and the sensor also has the advantages of compact size (8 mm), simple structure, easy fabrication, and good repeatability.

© 2014 Published by Elsevier B.V.

## 1. Introduction

Over the past decades, various refractive index (RI) sensors, e.g. Abbe refractometer, have been demonstrated for different applications. But traditional refractometers have the disadvantages of big size and weight. In recent years, optical fiber RI sensors were widely employed in the field of chemical and biochemical sensing applications because of their attractive characteristics, such as remote sensing, immunity to electromagnetic interference, corrosion resistance, small size, high sensitivity, and ultra-fast response [1]. A few types of optical fiber RI sensors have accordingly been demonstrated by means of employing fiber Bragg gratings (FBGs) [2], long period fiber gratings (LPFGs) [3–5], Mach-Zender interferometers (MZIs) [6], surface plasmon resonance (SPR) [7,8], Fabry-Perot interferometers (FPIs) [9,10], Michelson interferometers (MIs) [11–13], and photonic crystal fibers (PCFs) [14]. However, these approaches have their respective drawbacks. For example, LPFG and FBG-based sensors exhibited the cross-sensitivity between refractive index and temperature [15]. FPIs-based sensor exhibited a low sensitivity in the RI sensing applications [16]. PCFs required relatively expensive structures and complex fabrication process [14]. In addition, MI-based sensors usually utilize the

wavelength modulation, rather than intensity-modulation, for RI measurement, which requires complex and expensive wavelength de-modulation devices [12,13].

In this paper, we demonstrated a high-sensitive intensity-modulated refractive index sensor based on an in-fiber Michelson interferometer which was fabricated by means of splicing a section of thin core fiber (TCF) to a standard single-mode fiber (SMF) with a lateral offset. The lateral offset and the TCF length were optimized to enhance the fringe contrast of the MI. Several advantages are involved in the proposed sensor, such as a short size and a simple structure, a high sensitivity of  $-202.46 \text{ dB/RIU}$ , and insensitivity to temperature.

## 2. Sensor fabrication

As shown in Fig. 1(a), a broad band source (BBS) with a laser wavelength range from 1250 to 1650 nm, an optical spectrum analyzer (OSA) (ANDO AQ6317B) and an optical circulator were employed to monitor the reflection spectrum of the proposed MI-based sensor, which was fabricated as described below. Firstly, a section of TCF (Nufern UHNA-3) with core and cladding diameters of 4 and 125 μm, respectively, was spliced to a standard SMF, i.e. Lead-in SMF, with a 6 μm lateral offset between the two fiber cores by use of a commercial fusion splicer machine (Fujikura, FSM-100P+), in which there are two pairs of motors, i.e. the axial and vertical moving motors, with a movement accuracy of 0.01 and

\* Corresponding author. +86 755 26066281.

E-mail address: [ypwang@szu.edu.cn](mailto:ypwang@szu.edu.cn) (Y. Wang).

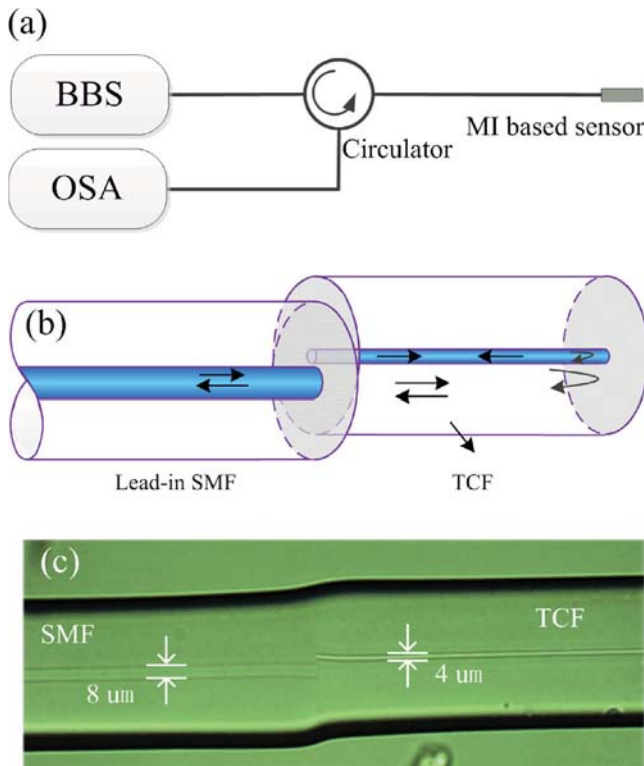


**Fig. 1.** (a) Schematic diagram of the proposed MI-based sensor system; (b) schematic diagram and (c) microscope image of the MI-based sensor.

0.1 μm, respectively. Then, another end of the TCF was cleaved with a length of 20 mm. Consequently, as shown in Fig. 2(a), a clear interference fringes pattern was observed in the reflection spectrum.

As shown in Fig. 1(b), light transmitting in the SMF is divided into two parts at the misalignment-spliced joint. A part of light is coupled into the core of the TCF as a core mode, and another part of light is coupled into the cladding of the TCF as cladding modes. The two part of light will be reflected at the cleaved ends of the PCF and then re-coupled into the core of the lead-in SMF at the

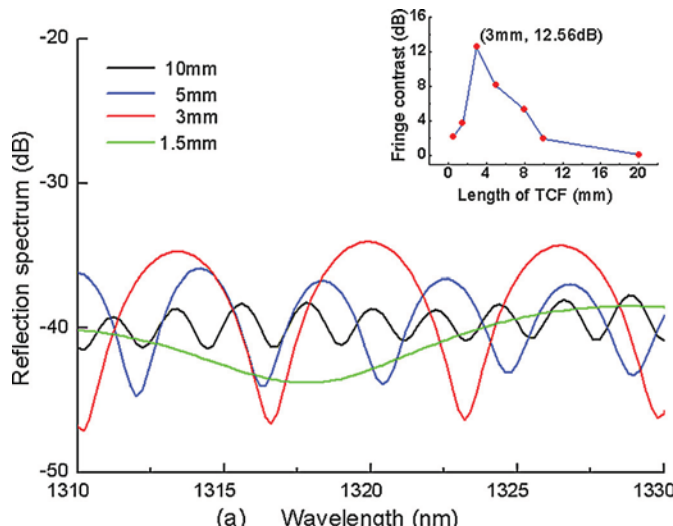


**Fig. 2.** (a) Reflection spectra of the four MI samples with a core offset of 6 μm and TCF lengths of 1.5, 3, 5, and 10 mm, respectively; the insert shows the fringe contrasts in the interference patterns of the seven MI samples as a function of the measured TCF length; (b) measured and calculated FSR of the interference fringes of the MI sensor samples with different TCF lengths.

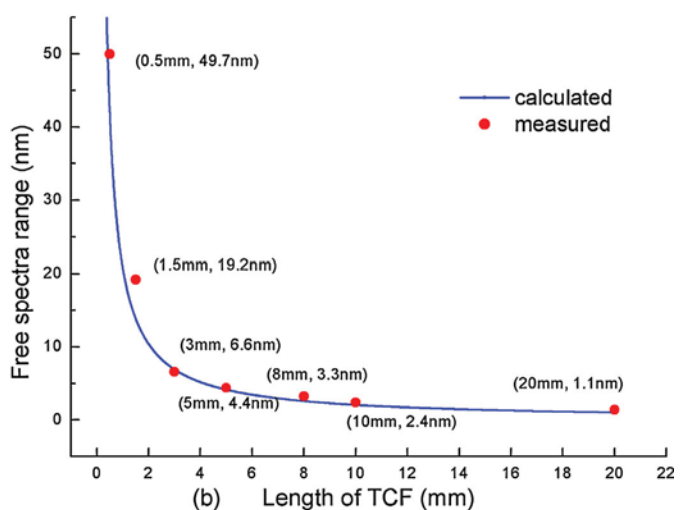
misalignment-spliced joint, resulting in Michelson interference in the core of the SMF. Thus, a MI-based sensor was achieved, and visible interference fringe pattern were observed in the reflection spectrum, as shown in Fig. 2(a). According to Michelson interference, the fringe contrast in the interference pattern depends strongly on the ratio of lights coupled into the core and cladding modes in the TCF and their transmission loss, so it is essential to improve the TCF length and the core offset for enhancing the interference fringe contrast.

Thus the TCF was repeatedly cleaved to gradually shorten the TCF to a desired length by employing a microscope-assisted cleaving technique, accordingly achieving seven MI samples with a core offset 6 μm and different TCF lengths of 20, 10, 8, 5, 3, 1.5 and 0.5 mm. Fig. 2(a) illustrates four of the seven MI interference patterns. Each MI sample with different TCF length exhibits distinct fringe contrast in the interference patterns, as shown in Fig. 2(a). And it can be found in the insert of Fig. 2(a) that the MI sample with a TCF length of 3 mm has the largest fringe contrast of 12.56 dB. Moreover, we calculated the free spectrum range (FSR) of the interference fringes by

$$\Delta\lambda_{\text{dip}}^m \approx \frac{\lambda^2}{2\Delta n_{\text{eff}}^m L} \quad (1)$$

$\Delta n_{\text{eff}}^m$  is the effective RI difference between the core and  $m$ th cladding modes in the TCF,  $L$  is the length of the TCF. As shown in Fig. 2(b), the measured FSR of the seven MI samples is 1.1, 2.4, 3.3, 4.4, 6.6, 19.2 and 49.7 nm, respectively, which shows a good agreement with the calculated value.

Furthermore, the core offset between the SMF and the TCF was improved to enhance the fringe contrast in the interference pattern by moving the X- and Y-directional motors in the splicer. Another six MI samples with a TCF length of 3 mm and different core offsets of 2, 4, 6, 8, 10, and 12 μm, respectively, were fabricated. Fig. 3 illustrates four of the six MI interference patterns. As shown in Fig. 3, each MI sample with a certain core offset exhibits distinct fringe contrast in the interference patterns due to the core-offset-induced change of the ratio of lights coupled into the core and cladding modes in the TCF. And it can be found in the insert of Fig. 3 that the MI sample with a core offset of 8 μm and a TCF length of 3 mm has the largest fringe contrast of 18.21 dB.



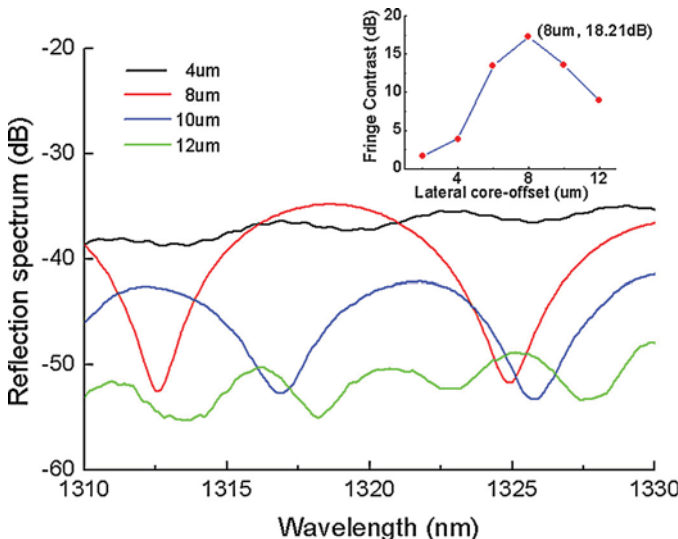


**Fig. 3.** Reflection spectra of the MI-based samples with a TCF length of 3 mm and core-offsets of 4, 8, 10, 12 μm, respectively; the insert shows the fringe contrast in the interference patterns of the six MI samples with different core offsets.

### 3. Application and discussion

Due to the fact that the interference pattern is mainly formed by the core and cladding modes, the intensity of the interference pattern can be calculated as [13,17]:

$$I = \left( I_{\text{core}} + \sum_m I_{\text{clad}}^m + \sum_m 2\sqrt{I_{\text{core}} \cdot I_{\text{clad}}^m} \cdot \cos \Phi^m \right) \cdot R \quad (2)$$

where  $I_{\text{core}}$  and  $I_{\text{clad}}^m$  are the light intensity of the core mode, and the  $m$ th cladding mode, respectively;  $\Phi^m$  is the phase delay between the core mode and the  $m$ th cladding mode.  $R$  is the reflectivity on the cleaved endface of the TCF and can be given by [18,19]:

$$R = \frac{(n_{\text{core}} - n)^2}{(n_{\text{core}} + n)^2} \quad (3)$$

where  $n_{\text{core}}$  and  $n$  are the RI of the fiber core and surrounding medium, respectively. According to Eqs. (2) and (3), the intensity of the interference pattern depends strongly on the surrounding RI.

Hence, our misalignment-spliced MI-based structure could be used to develop a promising RI sensor. Accordingly, another misalignment-spliced MI sample with optimized parameters, i.e. a core offset of 8 μm and a TCF length of 3 mm was fabricated to investigate its response to surrounding RI and temperature. As shown in Fig. 4, the interference pattern of the proposed MI-based sensor exhibits a large fringe contrast of up to 18.85 dB. The insertion loss of our MI-based RI sensor was measured to be about -34 dB, which is approximate to those (about -42 dB [20] and about -32 dB [21]) of other RI sensing devices based on Fresnel reflection [20] and multimode interference [21].

#### 3.1. Response to refractive index

The MI-based sensor illustrated in Fig. 4 was orderly immersed into a series of commercial refractive index matching liquids (Cargille Lab, <http://www.cargille.com>) with a RI from 1.30 to 1.43 with a step of 0.01 to investigate its response to surrounding RI. After each investigation, the MI-based sensor was dipped into alcohol for 5 min in order to remove the matching liquid adhered on the fiber surface. In order to avoid the disturbance of the liquid pressure, each RI measurement was performed at the same liquid

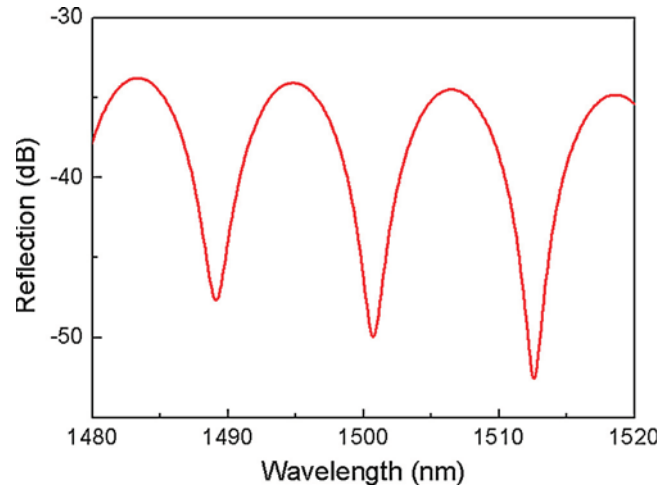


**Fig. 4.** Reflection spectrum of the proposed MI-based sensor with a core offset of 8 μm and a TCF length of 3 mm.

level. As shown in Fig. 5(a), while the surrounding RI increased, the reflection spectrum of the MI-based sensor shifted toward a shorter wavelength and the light intensity decreased gradually. As shown in Fig. 5(b), the changes of the fringe dip wavelength and intensity with surrounding RI show good agreements with the polynomial fitting curves.

As shown in Fig. 5(b), the RI sensitivity of the MI-based sensor was calculated to be -202.46 dB/RIU at the refractive index of 1.42 via polynomial fitting method, which is two or three times larger than those (27 dB/RIU [16], 94.58 dB/RIU [20], and -110 dB/RIU [21]) of the intensity-modulated RI sensors reported previously. Moreover, the intensity modulation, rather than the wavelength modulation [22], was used in our proposed MI-based RI sensor, which solves the cross-sensitivity problem between temperature and surrounding RI, as described below.

#### 3.2. Response to temperature

The proposed MI-based sensor was placed in a tube furnace with a temperature range from room temperature to 100 °C in order to investigate its temperature response. Temperature in the furnace rose gradually from 30 °C to 100 °C with a step of 10 °C and maintained about 30 min after each temperature heating. As shown in Fig. 6(a), while temperature rose, the dip wavelength of interference fringe shifted linearly toward a longer wavelength with a sensitivity of 42 pm/°C, in contrast, the dip intensity of interference fringe hardly changed. Temperature-induced 'red' shift of the dip wavelength could be explained below: since thermo-optic coefficient of the Ge-doped silica core is higher than that of the cladding consisting of fused silica, effective refractive index difference between the core and the cladding modes will increase with temperature rise [23,24]. As a result, the dip wavelength shifts toward a longer wavelength due to the temperature-induced change of effective index difference while surrounding temperature rises. As shown in Fig. 6(b), the dip intensity hardly changed while temperature rose, and the maximum temperature-induced intensity change is ±0.028 dB. Thus the temperature-induced RI measurement error is less than ±1.38 × 10<sup>-4</sup> without using temperature compensation, which is similar to that (±5 × 10<sup>-4</sup>) of the RI sensor reported in Ref. [25].

### 4. Discussion

As shown in Figs. 5(b) and 6(b), the dip intensity of interference fringes decreases with the increase of surrounding RI, whereas

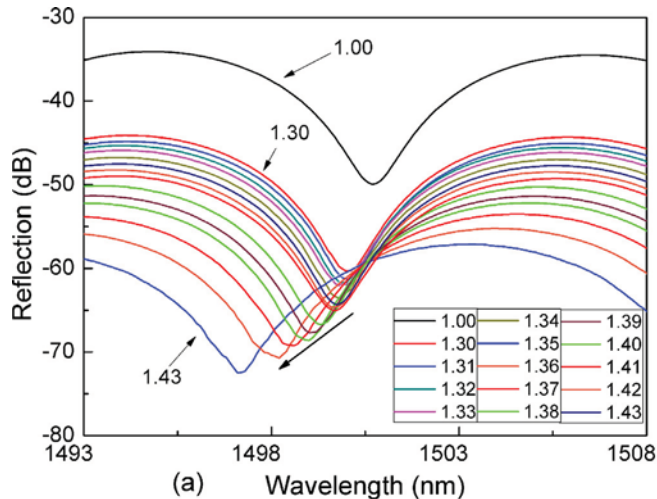


**Fig. 5.** (a) Reflection spectra evolution of the MI-based sensor with different surrounding RI from 1.30 to 1.43; (b) measured fringe dip intensity (upper) and wavelength (lower) versus surrounding RI and their polynomial fits.

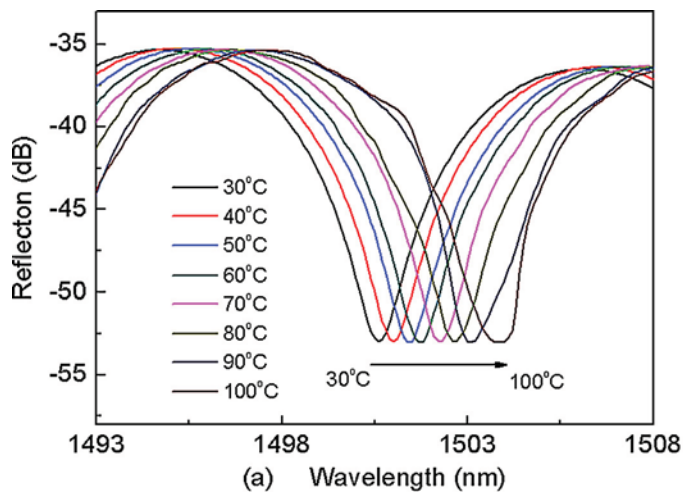
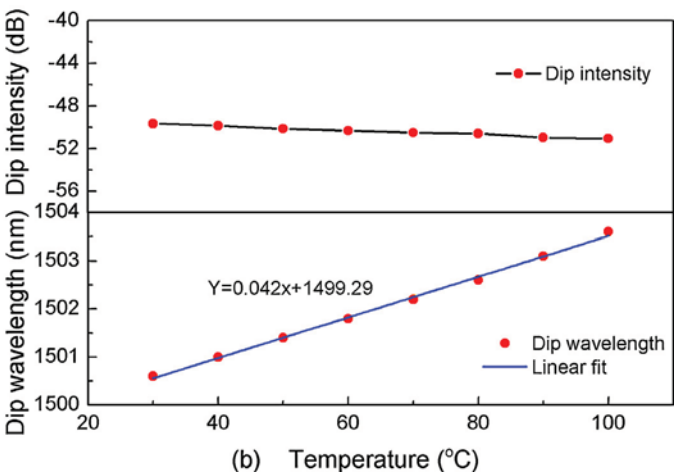
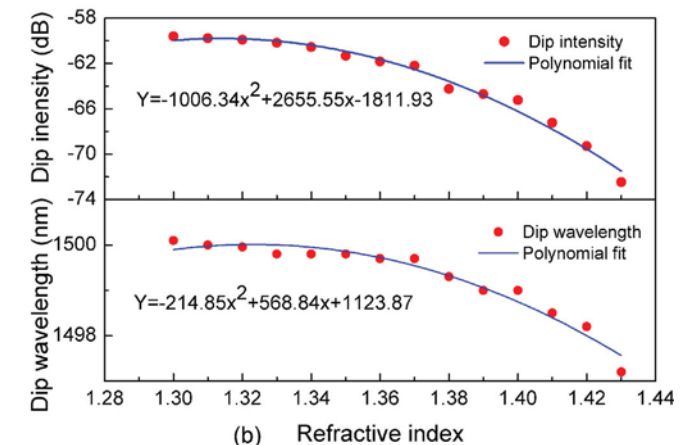


**Fig. 6.** (a) Reflection spectrum evolution of the MI-based sensor with different temperatures; (b) measured fringe dip intensity (upper) and wavelength (lower) versus temperature and their linear fits.

it is insensitive to temperature. Hence, the misalignment-spliced MI could be used to develop a promising intensity-modulated RI sensor with temperature insensitivity, which overcomes the cross-sensitivity between surrounding RI and temperature in the practical sensing applications. The proposed MI-based RI sensor exhibits a high sensitivity of  $-202.46 \text{ dB/RIU}$  at the refractive index of 1.42. The resolution of our proposed RI sensor depends on the resolution of the instrument employed to measure the intensity of the output light. Provided that an optical spectrum analyzer with a resolution of 0.001 dB is employed to measure the output power of our proposed RI sensor, a high RI resolution of  $4.9 \times 10^{-6} \text{ RIU}$  could be achieved, which is about one order higher than that ( $4.2 \times 10^{-5} \text{ RIU}$  [16] and  $3.8 \times 10^{-5} \text{ RIU}$  [21]) of the RI sensor reported in Refs. [16,21].

The reason why we choose the TCF (Nufern UHNA-3) is that it exhibits a high number aperture (NA) of 0.35, which lead to an ability of gathering more light into the core rather than the loss from the fiber cladding. Our experiments showed that this type of TCF cannot be replaced with a low NA fiber, e.g. SMF-28. To verify the repeatability of our fabrication process, additional several MI-based samples with the optimized parameters had been fabricated and a good repeatability of the interference spectra was achieved. Moreover, our MI-based sensor with improved parameters (8 μm



core offset and 3 mm TCF length) exhibits a larger fringe contrast of up to 18 dB than other MI-based devices [13,20].

## 5. Conclusion

A novel and compact fiber MI-based sensor was demonstrated by means of splicing a section of TCF to a standard SMF with a core offset. The core offset and the TCF length were improved to 8 μm and 3 mm, respectively, in order to achieve a large fringe contrast of up to 18 dB. Such a MI-based RI sensor based on intensity modulation exhibits a high sensitivity of at the  $-202.46 \text{ dB/RIU}$  at the refractive index of 1.42, which is two or three times higher than that of other intensity-modulated RI sensors reported previously. Moreover, the RI sensor is insensitive to temperature, thus overcoming the cross sensitivity problem between surrounding RI and temperature. Our MI-based RI sensor also exhibits the advantages of compact size (8 mm), simple structure, easy fabrication, and good repeatability. However, a complex and large spectrum analyzer has to be employed to measure the change of the dip intensity in our current experiments, which is disadvantageous to RI measurements. So in the practical sensing applications, a simple

demodulation device should be developed to measure the intensity at the dip wavelength.

## Acknowledgements

This work was supported by the National Science Foundation of China (grants no. 11174064, 61308027, and 61377090), the Science &Technology Innovation Commission of Shenzhen (grants no. KQCX20120815161444632, ZDSYS20140430164957664, and JCYJ20130329140017262), and the Distinguished Professors Funding from Shenzhen University and Guangdong Province Pearl River Scholars.

## References

- [1] N.S. Kapany, J.N. Pike, Fiber optics. Part IV. A photorefractometer, *J. Opt. Soc. Am.* 47 (1957) 1109–1114.
- [2] A. Iadicicco, S. Campopiano, A. Cutolo, M. Giordano, A. Cusano, Self temperature referenced refractive index sensor by non-uniform thinned fiber Bragg gratings, *Sens. Actuators B: Chem.* 120 (2006) 231–237.
- [3] Y. Tan, W. Ji, V. Mamidala, K. Chow, S. Tjin, Carbon-nanotube-deposited long period fiber grating for continuous refractive index sensor applications, *Sens. Actuators B: Chem.* 196 (2014) 260–264.
- [4] T. Zhu, Y.J. Rao, Q.J. Mo, Simultaneous measurement of refractive index and temperature using a single ultra-long-period fiber grating, *IEEE Photon. Technol. Lett.* 17 (2005) 2700–2702.
- [5] Y. Wang, L. Xiao, D.N. Wang, W. Jin, Highly sensitive long-period fiber-grating strain sensor with low temperature sensitivity, *Opt. Lett.* 31 (2006) 3414–3416.
- [6] R. Bernini, A. Cusano, Generalized Mach-Zehnder interferometers for sensing applications, *Sens. Actuators B: Chem.* 100 (2004) 72–74.
- [7] H. Liang, H. Miranto, N. Granqvist, J.W. Sadowski, T. Viitala, B. Wang, M. Yliperttilä, Surface plasmon resonance instrument as a refractometer for liquids and ultrathin films, *Sens. Actuators B: Chem.* 149 (2010) 212–220.
- [8] J.L. Qu, L.X. Liu, Y.H. Shao, H.B. Niu, B. Gao, Recent progress in multifocal multi-photon microscopy, *J. Innov. Opt. Health Sci.* 5 (3) (2012) 1250018–1250021.
- [9] Y. Wang, D. Wang, C. Liao, T. Hu, J. Guo, H. Wei, Temperature-insensitive refractive index sensing by use of micro Fabry-Pérot cavity based on simplified hollow-core photonic crystal fiber, *Opt. Lett.* 38 (2013) 269–271.
- [10] C. Liao, T. Hu, D. Wang, Optical fiber Fabry-Pérot interferometer cavity fabricated by femtosecond laser micromachining and fusion splicing for refractive index sensing, *Opt. Express* 20 (2012) 22813–22818.
- [11] Z. Li, Y. Wang, C. Liao, S. Liu, J. Zhou, X. Zhong, Y. Liu, K. Yang, Q. Wang, G. Yin, Temperature-insensitive refractive index sensor based on in-fiber Michelson interferometer, *Sens. Actuators B: Chem.* 199 (2014) 31–35.
- [12] Y. Wang, J. Chen, X. Li, X. Zhang, J. Hong, A. Ye, Simultaneous measurement of various optical parameters in a multilayer optical waveguide by a Michelson precision reflectometer, *Opt. Lett.* 30 (2005) 979–981.
- [13] Q. Rong, X. Qiao, Y. Du, D. Feng, R. Wang, Y. Ma, H. Sun, M. Hu, Z. Feng, In-fiber quasi-Michelson interferometer with core-cladding-mode fiber end-face mirror, *Appl. Opt.* 52 (2013) 1441–1447.
- [14] Y. Wang, X. Tan, W. Jin, D. Ying, Y.L. Hoo, S. Liu, Temperature-controlled transformation in fiber types of fluid-filled photonic crystal fibers and applications, *Opt. Lett.* 35 (2010) 88–99.
- [15] G. Yin, S. Lou, H. Zou, Refractive index sensor with asymmetrical fiber Mach-Zehnder interferometer based on concatenating single-mode abrupt taper and core-offset section, *Opt. Laser Technol.* 45 (2013) 294–300.
- [16] Z.L. Ran, Y.J. Rao, W.J. Liu, X. Liao, K.S. Chiang, Laser-micromachined Fabry-Pérot optical fiber tip sensor for high-resolution temperature-independent measurement of refractive index, *Opt. Express* 16 (2008) 2252–2263.
- [17] Z. Tian, S.S. Yam, H.-P. Loock, Refractive index sensor based on an abrupt taper Michelson interferometer in a single-mode fiber, *Opt. Lett.* 33 (2008) 1105–1107.
- [18] M.S. Meyer, G.L. Eesley, Optical fiber refractometer, *Rev. Sci. Instrum.* 58 (1987) 2047.
- [19] C.B. Kim, C.B. Su, Measurement of the refractive index of liquids at 1.3 and 1.5 micron using a fibre optic Fresnel ratio meter, *Meas. Sci. Technol.* 15 (2004) 1683.
- [20] H. Xue, H. Meng, W. Wang, R. Xiong, Q. Yao, B. Huang, Single-mode–multimode fiber structure based sensor for simultaneous measurement of refractive index and temperature, *IEEE Sens. J.* 13 (11) (2013) 4220–4223.
- [21] S. Silva, O. Frazão, J. Santos, F. Malcata, A reflective optical fiber refractometer based on multimode interference, *Sens. Actuators B: Chem.* 161 (2012) 88–92.
- [22] B.H. Lee, Y.H. Kim, K.S. Park, J.B. Eom, M.J. Kim, B.S. Rho, H.Y. Choi, Interferometric fiber optic sensors, *Sensors* 12 (2012) 2467–2486.
- [23] J. Zhou, C. Liao, Y. Wang, G. Yin, X. Zhong, K. Yang, B. Sun, G. Wang, Z. Li, Simultaneous measurement of strain and temperature by employing fiber Mach-Zehnder interferometer, *Opt. Express* 22 (2014) 1680–1686.
- [24] P. Lu, L. Men, K. Sooley, Q. Chen, Tapered fiber Mach-Zehnder interferometer for simultaneous measurement of refractive index and temperature, *Appl. Phys. Lett.* 94 (2009) 131110.
- [25] Y. Kim, S.J. Park, S. Jeon, S. Ju, C. Park, W. Han, B.H. Lee, Thermo-optic coefficient measurement of liquids based on simultaneous temperature and refractive index sensing capability of a two-mode fiber interferometric probe, *Opt. Express* 20 (2012) 23744–23754.

## Biographies

**Jiangtao Zhou** was born in Anhui province in China in 1990. He received his bachelor degree from Anhui University of Architecture in 2012. He is currently completing his master degree in the field of fiber optic sensors in Shenzhen University, China.

**Yiping Wang** is a Distinguished Professor and a Pearl River Scholar in the College of Optoelectronic Engineering, Shenzhen University, Shenzhen, China. He was born in Chongqing, China, in July 15, 1971. He received the B.S. degree in Precision Instrument Engineering from Xi'an Institute of Technology, Xi'an, China, in 1995, and the M.S. degree in Precision Instrument and Mechanism and the Ph.D. degree in Optical Engineering from Chongqing University, China, in 2000 and 2003, respectively, where he received the prestigious award of The National Excellent Doctoral Dissertations of China. In 2003, he joined the Department of Electronics Engineering, Shanghai Jiao Tong University, China, as a postdoctoral research fellow and an associate professor. In 2005, he joined the Department of Electrical Engineering, Hong Kong Polytechnic University, Hong Kong, as a postdoctoral research fellow and a research fellow. In 2007, he joined the Institute of Photonic Technology, Jena, Germany as a Humboldt research fellow. In 2009, he joined the Optoelectronics Research Centre, University of Southampton, UK, as a Marie Curie Fellow. Since 2012, he has been with Shenzhen University as a Distinguished Professor and a Pearl River Scholar. His current research interests focus on optical fiber sensors, in-fiber gratings, photonic crystal fibers, and fluid-filling technologies. He has authored or coauthored 1 book, 9 patent applications, and more than 150 journal and conference papers with a SCI citation of more than 1200 times. Dr. Wang is a senior member of IEEE, the Optical Society of America, and the Chinese Optical Society.

**Changrui Liao** received the B.E. degree in optical information science and technology and the M.S. degree in physical electronics from Huazhong University of Science and Technology, China, in 2005 and 2007, and the Ph.D. degree from the Hong Kong Polytechnic University, Hong Kong, in 2012. Since 2012, he has been with the College of Optoelectronic Engineering, Shenzhen University as an assistant professor. His main research interests are femtosecond laser micromachining, optical fiber devices and sensors.

**Bing Sun** received bachelor degree and Ph.D. from Department of Science in Jiangsu University in 2008 and in 2013, respectively. He joined in Shenzhen University, China, as a postdoctoral fellow.

**Jun He** received bachelor degree and Ph.D. from Wuhan University and Chinese Academy of Sciences in 2008 and in 2013, respectively. He joined in Shenzhen University, China, as a postdoctoral fellow.

**Guolu Yin** received bachelor degree and Ph.D. from Department of Science in Beijing Jiaotong University in 2008 and in 2013, respectively. He joined in Shenzhen University, China, as a postdoctoral fellow.

**Shen Liu** was born in Henan Province, China in 1984, and received bachelor degree from Chongqing University of Posts and Telecommunication in 2013. He is currently completing her doctoral degree in the field of fiber optic sensors in Shenzhen University, China.

**Zhengyong Li** was born in Hubei Province, China in 1988. He received his bachelor degree from Huazhong University of Science and Technology Wenhua College in 2012. He is currently completing his master degree in the field of fiber optic sensors in Shenzhen University, China.

**Guanjun Wang** received bachelor degree and Ph.D. from Beijing University of Aeronautics and Astronautics in 2008 and in 2013, respectively. He joined in Shenzhen University, China, as a postdoctoral fellow.

**Xiaoyong Zhong** was born in Guangdong Province in China in 1988. He received bachelor degree in Guangdong University of Technology. He is currently completing his master degree in the field of fiber optic sensors in Shenzhen University, China.

**Jing Zhao** was born in Hubei Province, China in 1983, and received bachelor degree from University of Electronic Science and Technology of China in 2004. She is currently completing her doctoral degree in the field of fiber optic sensors in Shenzhen University, China.

# Long Period Fiber Gratings Inscribed With an Improved Two-Dimensional Scanning Technique

Volume 6, Number 4, August 2014

Xiaoyong Zhong

Yiping Wang, Senior Member, IEEE

Changrui Liao

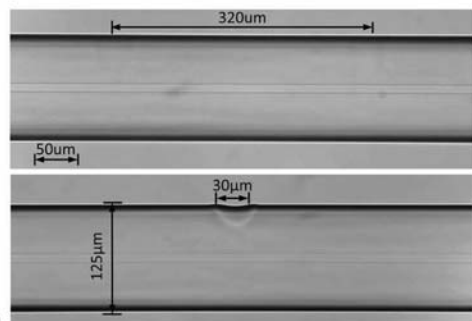
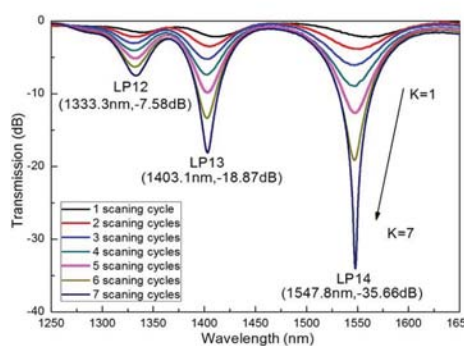
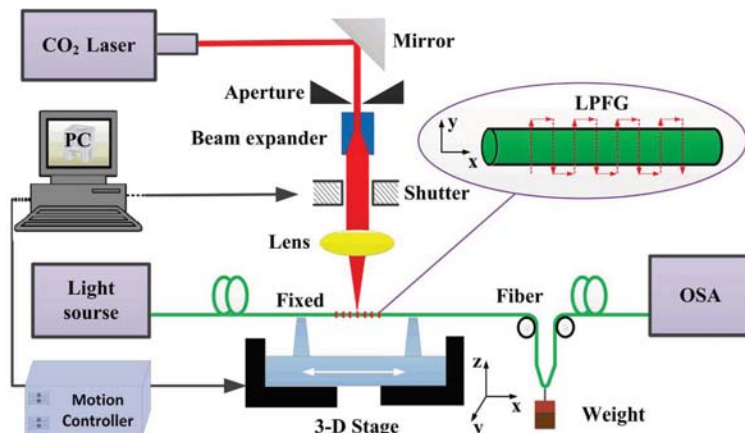
Guolu Yin

Jiangtao Zhou

Guanjun Wang

Bing Sun

Jian Tang



DOI: 10.1109/JPHOT.2014.2337875

1943-0655 © 2014 IEEE

# Long Period Fiber Gratings Inscribed With an Improved Two-Dimensional Scanning Technique

Xiaoyong Zhong, Yiping Wang, Senior Member, IEEE, Changrui Liao, Guolu Yin, Jiangtao Zhou, Guanjun Wang, Bing Sun, and Jian Tang

Key Laboratory of Optoelectronic Devices and Systems of the Ministry of Education and Guangdong Province, College of Optoelectronic Engineering, Shenzhen University, Shenzhen 518060, China

DOI: 10.1109/JPHOT.2014.2337875

1943-0655 © 2014 IEEE. Translations and content mining are permitted for academic research only.  
Personal use is also permitted, but republication/redistribution requires IEEE permission.  
See [http://www.ieee.org/publications\\_standards/publications/rights/index.html](http://www.ieee.org/publications_standards/publications/rights/index.html) for more information.

Manuscript received May 23, 2014; revised June 27, 2014; accepted July 1, 2014. Date of publication July 10, 2014; date of current version August 11, 2014. This work was supported in part by the National Science Foundation of China under Grants 61308027, 61377090, and 11174064; by the Science & Technology Innovation Commission of Shenzhen under Grants KQCX20120815161444632 and JCYJ20130329140017262; and by the Distinguished Professors Funding from Shenzhen University and Guangdong Province Pearl River Scholars. Corresponding author: Y. Wang (e-mail: ypwang@szu.edu.cn).

**Abstract:** We demonstrated a promising CO<sub>2</sub> laser irradiation system based on an improved 2-D scanning technique. Such a system could be used to inscribe high-quality long period fiber gratings (LPFGs) with good reproducibility of grating inscription, which attributes to the fact that our system includes a CO<sub>2</sub> laser with an excellent power stability of less than ±2% and a 3-D ultraprecision motorized translation stages with an excellent bidirectional repeatability value of 80 nm. Moreover, a control program with an easy-to-use operation interface was developed in our system so that a high-quality LPFG could be achieved as soon as grating parameters, such as grating pitch and number of grating periods, are entered, which has a widespread commercial value and prospects for development. Additionally, near mode fields of the CO<sub>2</sub>-laser-induced LPFG were observed and simulated to investigate mode coupling in the gratings.

**Index Terms:** Long period fiber gratings (LPFGs), optical fiber sensors, CO<sub>2</sub> laser 2-D scanning, fiber optics components.

## 1. Introduction

Long period fiber gratings (LPFGs) have been widely used in the field of optical fiber sensors, communications, and lasers. A few inscription methods, such as UV laser exposure [1], CO<sub>2</sub> laser irradiation [2]–[5], electric arc discharge [6], femtosecond laser exposure [7], [8], mechanical microbends [9], etched corrugations [10], [11], and ion beam implantation [12], [13], have been demonstrated to inscribe LPFGs in different types of optical fibers. Among these methods, the CO<sub>2</sub> laser irradiation method is particularly flexible and low cost, as it could be applied to inscribe LPFG in almost all type of fibers without using a phase mask [14], [15]. Since Davis *et al.* reported the first CO<sub>2</sub>-laser-induced LPFG in a conventional glass fiber in 1998 [16], various CO<sub>2</sub> laser irradiation techniques have been demonstrated and/or improved to inscribe LPFGs in different types of optical fibers such as SMFs [17], [18], PCFs [19], [20], and PBFs [21]. In 2003, Rao *et al.*, reported a typical CO<sub>2</sub> laser inscribing system in which an industrial 2-D optical scanner with a poor bi-directional repeatability was employed so that the precision of grating

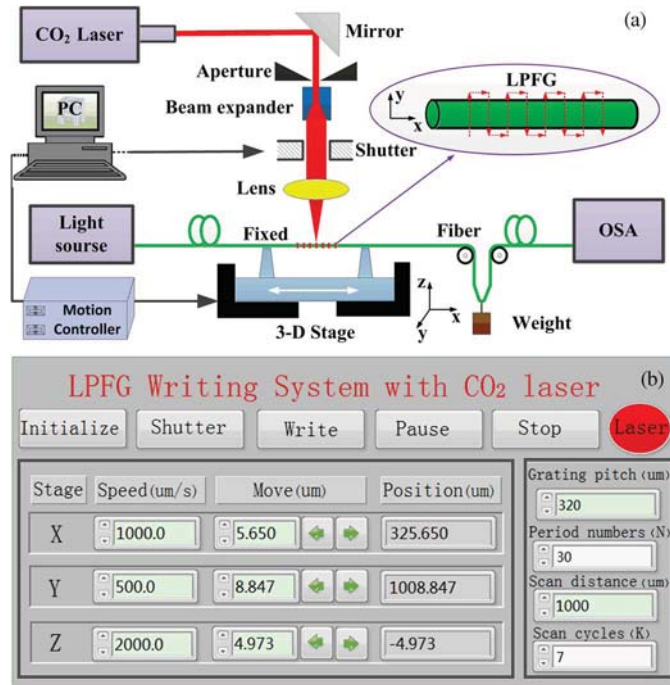


Fig. 1. (a) Schematic diagram of the LPFG inscribing system based on a 2-D scanning technique employing a CO<sub>2</sub> laser. (b) Easy-to-use operation interface of the control program. Z-dimension of the 3-D stage is used to focus the laser beam on the fiber, and X- and Y-dimensions are used to realize the 2-D scanning of the laser beam.

pitch was not good [22]. In addition, in the CO<sub>2</sub> laser irradiation systems reported, an industrial CO<sub>2</sub> laser with a maximum output power of 10 W usually was employed to inscribe LPFGs. However, such a CO<sub>2</sub> laser has a poor power stability of  $\pm 10\%$  so that the reproducibility of LPFGs is not good. In other words, the output power of the CO<sub>2</sub> laser employed has to be finely adjusted to achieve a high-quality LPFG during each grating inscription.

In this letter, we demonstrated a promising CO<sub>2</sub> laser irradiation system based on an improved 2-D scanning technique for inscribing high-quality LPFGs. Such a system employs a 3-D ultra-precision motorized translation stages with an excellent bi-directional repeatability of 80 nm, a CO<sub>2</sub> laser with an excellent power stability of less than  $\pm 2\%$ , and a control program with a easy-to-use operation interface to inscribe high-quality LPFGs. Moreover, near mode fields of the achieved LPFGs was observed to investigate their mode coupling.

## 2. LPFG Inscription Setup

A promising LPFG inscribing system based on an improved 2-D scanning technique was demonstrated by use of a focused CO<sub>2</sub> laser beam, as shown in Fig. 1(a). This system consisted of an industrial CO<sub>2</sub> laser with a maximum power of 10 W (SYNRAD 48-1) and a power stability of  $\pm 10\%$ , an electric shutter for turning on/off the laser beam, an infrared ZNSE PO/CX lens with a focused length of 63.5 mm, a four-times beam expander for decreasing the diameter of the focused laser spot, and a 3-D ultra-precision motorized stage (Newport XMS50, VP-25X and GTS30V) with a minimum incremental motion of 10 nm and a bi-directional repeatability of 80 nm. A closed loop control system was, for the first time, employed to improve the power stability of the CO<sub>2</sub> laser to  $\pm 2\%$ , which is a huge advantage of our LPFG inscribing system. Our experiment results showed that the power stability ( $\pm 2\%$ ) of the CO<sub>2</sub> laser improved effectively the stability and reproducibility of grating inscription. For example, the success rate of grating inscription is almost 100% in our current experiments. In contrast, the success rate was about

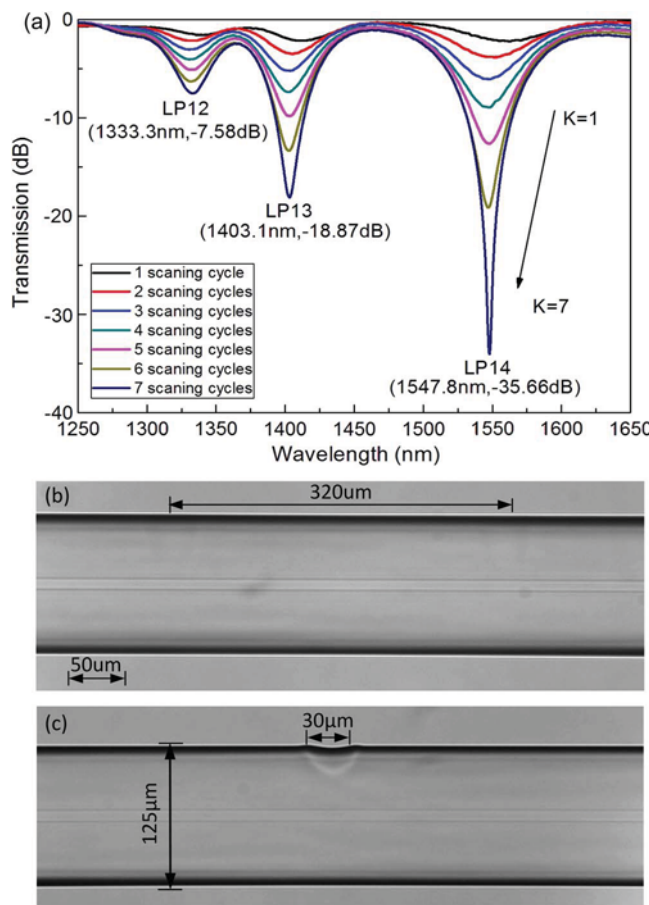


Fig. 2. (a) Transmission spectrum evolution of a CO<sub>2</sub>-laser-inscribed LPFG with 30 grating periods and a grating pitch of 320  $\mu\text{m}$  while the number of scanning cycles (K) increases from 1 to 7. (b) Microscope image of the CO<sub>2</sub>-laser-inscribed LPFG. (c) CO<sub>2</sub>-laser-ablated zone on the surface of the fiber.

30% in our previous experiments with a CO<sub>2</sub> laser with a power stability of  $\pm 10\%$  [22], [23]. A supercontinuum light source (NKT Photonics SuperK Compact) and an optical spectrum analyzer (YOKOGAWA AQ6370C) were employed to monitor the transmission spectrum of the CO<sub>2</sub>-laser-inscribed LPFG during grating inscription.

A control program with a easy-to-use operation interface was developed by use of LabVIEW software in order to control every devices in the system and to inscribe high-quality LPFGs. As soon as the grating parameters, such as grating pitch, number of grating periods, number of scanning cycles, are entered via the operation interface illustrated in Fig. 1(b) and the “Write” button is clicked, a high-quality LPFG could be achieved. Of course, the grating inscribing process could be paused or stopped at any time by means of clicking the “Pause” button or the “Stop” button. Hence, such an improved LPFG inscription system could potentially be integrated with a fiber drawing tower to inscribe continuously a large number of LPFGs during drawing a fiber, which has the widespread commercial value and the prospects for development.

Our LPFG inscription could be described as follow. First of all, one end of a standard single mode fiber (YOF Inc) is fixed on the 3-D motorized stage by use of a pair of fiber holders, and another end of the fiber is attached by a small weight to provide a constant pre-strain in the fiber, thus enhancing the efficiency of inscribing LPFGs [24], [25]. The CO<sub>2</sub> laser beam propagates through the beam expander and the lens and then is focused on the fiber by means of adjusting Z-dimension of the 3-D stage. We achieved the diameter of the focused spot by means of observing the CO<sub>2</sub>-laser-ablated zone on the surface of the fiber. As shown in Fig. 2(c), a

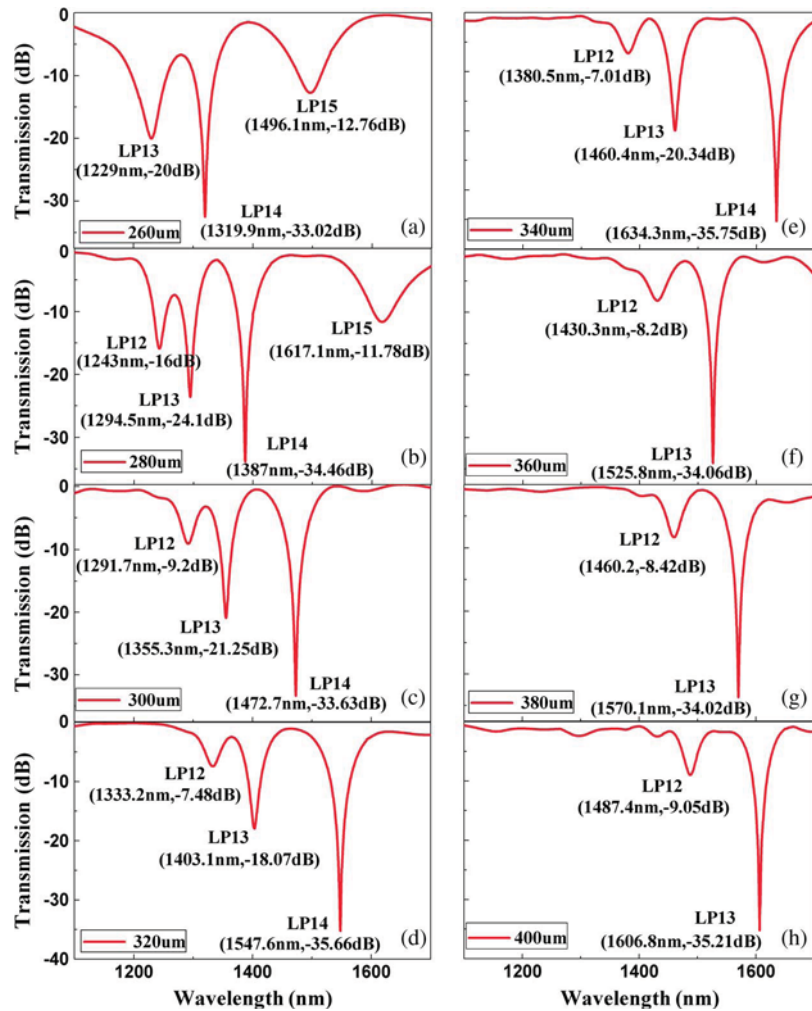


Fig. 3. Measured transmission spectrum of the CO<sub>2</sub>-laser-inscribed LPFGs with 30 grating periods and different grating pitches of (a) 260  $\mu\text{m}$ , (b) 280  $\mu\text{m}$ , (c) 300  $\mu\text{m}$ , (d) 320  $\mu\text{m}$ , (e) 340  $\mu\text{m}$ , (f) 360  $\mu\text{m}$ , (g) 380  $\mu\text{m}$ , and (h) 400  $\mu\text{m}$ .

groove was carved on one side of the optical fiber by repeated scanning of a focused CO<sub>2</sub> laser beam with a higher power of 5 W. The width of the groove was measured to be 30  $\mu\text{m}$ . So the diameter of the focused laser spot is about 30  $\mu\text{m}$ . To the best of knowledge, this is the smallest focused spot in the LPFG inscribing system employing a CO<sub>2</sub> laser so far [22]. Second, the motorized stage is moved by 1 mm with a speed of 0.5 mm/s along the "Y" direction, i.e., the vertical orientation of the fiber axis, in order that the focused CO<sub>2</sub> laser beam scans/irradiates cross the fiber. Therefore, the first period of LPFG is created. Thirdly, the motorized stage is shifted by a grating pitch, e.g., 320  $\mu\text{m}$ , along the "X" direction, i.e., the fiber axis, and then moved by 1 mm along the "-Y" direction in order that the focused CO<sub>2</sub> laser beam scans/irradiates cross the fiber again. Therefore, the second period of LPFG is created. This scanning and shifting processes are periodically carried out N times (N is the number of grating periods) until the last grating period is created. The process above may be repeated for K cycles from the first grating period to the last grating period until a desired LPFG is achieved.

### 3. Experiment Results

As shown in Fig. 2(a), with the increase of the number of scanning cycles, the resonant wavelength of the LPFG shifts toward the shorter wavelength, the resonant attenuation is increased,

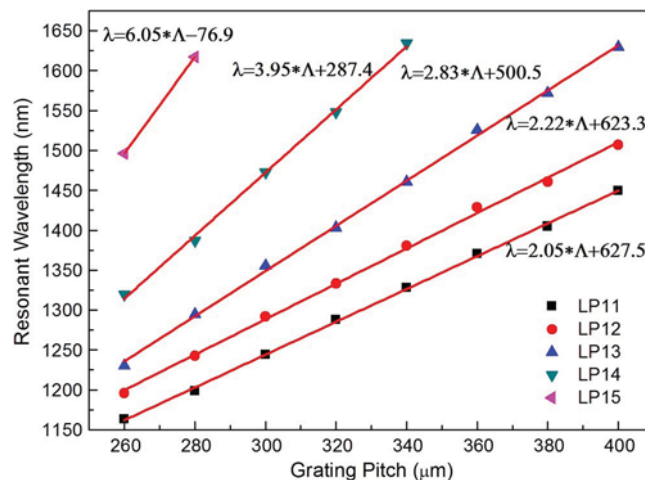


Fig. 4. The measured resonant wavelengths versus the grating pitches of the CO<sub>2</sub>-laser-inscribed LPFGs illustrated in Fig. 3.

and the 3 dB bandwidth of the resonant dip is decreased. One high-quality LPFG with a large dip attenuation of  $-35.66$  dB at the resonant wavelength of 1547.8 nm and a low insertion loss of less than 0.3 dB was achieved in a standard single mode fiber after only seven scanning cycles were done. As shown in Fig. 2(b), no obvious physics deformation was observed on the surface of the grating. This is due to the fact that, during the grating inscription, the CO<sub>2</sub> laser power was decreased to 0.5 W in order to avoid to induce physics deformation (i.e. grooves) on the surface of the fiber. So residual stress relaxation and glass densification are the possible mechanisms for refractive index modulation in our CO<sub>2</sub>-laser-induced LPFGs [2]. In contrast, physical deformation is the dominant mechanism for refractive index modulation in the asymmetric LPFGs with periodic grooves (i.e. physical deformation).

In our system, the CO<sub>2</sub> laser beam is immovable, and the employed fiber is periodically moved-shifted along the "X" and "Y" directions via the 2-D ultra-precision motorized stage with an excellent bi-directional repeatability of 80 nm and a minimum incremental motion of 10 nm. In contrast, in the system reported in reference [22], the fiber is fixed, and the CO<sub>2</sub> laser beam periodically scans the fiber via an industrial 2-D optical scanner with a poor bi-directional repeatability. Compared with our 2-D scanning technique, providing a common point-to-point technique is used to inscribe a LPFG, the CO<sub>2</sub> laser beam has to be aligned with and focused on the fiber core during each inscription of grating period, which is a very difficult work and is of disadvantage to the stability and repeatability of grating inscription.

To investigate the phase matching condition as function of a resonant wavelength, eight LPFGs with the same number of grating periods ( $N = 30$ ) and different pitches of 260, 280, ..., and 400  $\mu\text{m}$  were inscribed in the standard SMF by use of the improved CO<sub>2</sub> laser system above. As shown in Fig. 3, each LPFG has a large dip attenuation of more than  $-33$  dB at the resonant wavelength and a low insertion loss of less than 0.5 dB, as well as more than three attenuation dips for each LPFG are observed from 1100 to 1700 nm, indicating that the fundamental mode is coupled to different cladding modes. As shown in Fig. 4, the CO<sub>2</sub>-laser-inscribed LPFG with a longer grating pitch has a longer resonant wavelength corresponding to the same order cladding mode, which is the same as the phase matching condition of the UV-laser-inscribed LPFGs illustrated in Fig. 8 reported in reference [1]. Therefore, we can inscribe a high-quality LPFG with a desired resonant wavelength by mean of determining a suitable grating pitch from the curve illustrated in Fig. 4.

As shown in Fig. 5, another four LPFGs, i.e. LPFG<sub>1</sub>, LPFG<sub>2</sub>, LPFG<sub>3</sub>, LPFG<sub>4</sub>, with different grating pitch of 420, 380, 320, and 280  $\mu\text{m}$ , respectively, were inscribed in a standard SMF in order to investigate mode coupling in the CO<sub>2</sub>-laser-inscribed gratings. A single-wavelength light from

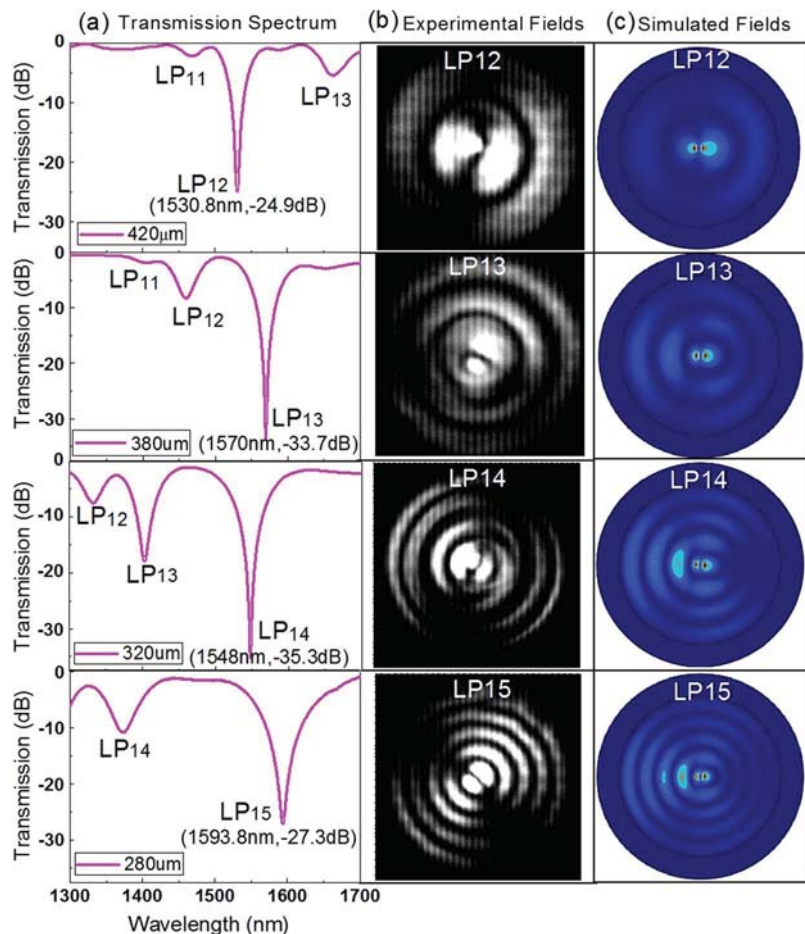


Fig. 5. (a) Transmission spectra, (b) experimental, and (c) simulated near field profiles of the CO<sub>2</sub>-laser-inscribed LPFGs at the resonant wavelength, i.e., LPFG<sub>1</sub> at 1530.8 nm, LPFG<sub>2</sub> at 1570.0 nm, LPFG<sub>3</sub> at 1548.2 nm, and LPFG<sub>4</sub> at 1593.8 nm.

a tunable laser with a wavelength range from 1510 to 1612 nm (EXFO FLS-2600B) was input into one end of each LPFG. Another end of the LPFG was cleaved at the last grating period to observe its near fields by use of an infrared camera (Model 7290A, Electro Physics Corp.) and a microscope (Leica DM2500 M). As shown in Fig. 5(b), asymmetrical mode field profile was observed at the resonant wavelength of each LPFG. That is, the fundamental mode of LPFG<sub>1</sub> at the resonant wavelength of 1530.8 nm, LPFG<sub>2</sub> at the resonant wavelength of 1570.0 nm, LPFG<sub>3</sub> at the resonant wavelength of 1548.2 nm, and LPFG<sub>4</sub> at the resonant wavelength of 1593.8 nm, was coupled into the circularly asymmetric cladding mode of LP<sub>12</sub>, LP<sub>13</sub>, LP<sub>14</sub>, and LP<sub>15</sub>, respectively.

Moreover, it is easily seen from Fig. 5(b) that the cladding mode energy on one side is obviously larger than that on another side, that is, the cladding mode in the CO<sub>2</sub>-laser-induced LPFG is asymmetrical within the cross section of the fiber cladding. This is due to the fact that, during the LPFG inscription, an circularly asymmetric refractive index modulation within the cross section of fiber is induced by the asymmetric residual stress relaxation resulting from the single side irradiation of CO<sub>2</sub> laser [26]–[28].

We simulated the cladding mode field in a LPFG written in a standard SMF by use of a mode solver (COMSOL version 3.5) based on the Finite Element Method (FEM). It has been found that, in case the CO<sub>2</sub> laser irradiation induces a low refractive index modulation in the LPFG, a linear, quadratic or exponential refractive-index profile assumed in the numerical simulations

results in a small quantitative difference, rather than a qualitative change, in the simulation results [26]. Thus we assumed a linear refractive index profile within the cross-section of the grating to simply the simulation of near field profiles of the CO<sub>2</sub>-laser-inscribed LPFGs. Assuming refractive index within the cross-section of the grating is linearly modulated with a relationship of  $n = n_0 + (1 - X/2R) \times \Delta n$  ( $n_0$  is the cladding refractive index before CO<sub>2</sub> laser irradiation;  $\Delta n$  is the amplitude of refractive index modulation after CO<sub>2</sub> laser irradiation;  $X$  is the distance of CO<sub>2</sub> laser irradiation and  $R$  is the fiber radius). For  $\Delta n = 0.5 \times 10^{-6}$ , the simulated near mode filed profile of the four LPFGs are illustrated in Fig. 5(c), which is similar to the experimental results shown in Fig. 5(b). Hence, the circularly asymmetric mode field profiles shown in Fig. 5 experimentally and theoretically verify that asymmetry refractive index modulation are induced within the cross section of the CO<sub>2</sub>-laser-induced LPFGs. However, nonuniform absorption of laser energy results in an asymmetrical refractive index profile within the cross-section of the grating, which is more complicated than a simple linear profile. As a result, the simulated near filed profiles are somehow different from the observed ones.

#### 4. Conclusion

A promising CO<sub>2</sub> laser irradiation system based on an improved 2-D scanning technique was demonstrated to inscribe high-quality LPFGs. Compared with other CO<sub>2</sub> laser inscribing systems, in our system the laser beam was fixed and the employed fiber was periodically moved along X-direction and shifted along Y-direction so that the focused laser beam periodically scans/irradiates the fiber. About 5 minutes were required to inscribe a high-quality LPFG with a large attenuation dip of  $-35.7$  dB, a bandwidth of 87.8 nm, and 30 grating periods in a standard single mode fiber by use of our current experimental system with an improved power stability of less than  $\pm 2\%$  and the 2-D scanning technique. In contrast, more time, e.g., about 30 minutes, have to be required to inscribe a LPFG with a small attenuation dip of about  $-25.1$  dB, and a bandwidth of 12.0 nm and 55 grating periods in the same type of optical fiber by use of our previous experimental system with a poor power stability of less than  $\pm 10\%$  [22], [23]. Circularly asymmetric mode field profiles indicates asymmetry mode coupling in the CO<sub>2</sub>-laser-induced LPFGs. Moreover, a control program with a easy-to-use operation interface was developed; therefore, our system has the widespread commercial value and the prospects for development.

---

#### References

- [1] A. M. Vengsarkar *et al.*, "Long-period fiber gratings as band-rejection filters," *J. Lightw. Technol.*, vol. 14, no. 1, pp. 58–65, Jan. 1996.
- [2] Y. Wang, "Review of long period fiber gratings written by CO<sub>2</sub> laser," *J. Appl. Phys.*, vol. 108, no. 8, pp. 081101-1–081101-18, Oct. 2010.
- [3] Y. P. Wang, Y. J. Rao, Z. L. Ran, T. Zhu, and X. K. Zeng, "Bend-insensitive long-period fiber grating sensors," *Opt. Lasers Eng.*, vol. 41, no. 1, pp. 233–239, Jan. 2004.
- [4] Y.-P. Wang, J.-P. Chen, and Y.-J. Rao, "Torsion characteristics of long-period fiber gratings induced by high-frequency CO<sub>2</sub> laser pulses," *J. Opt. Soc. Amer. B, Opt. Phys.*, vol. 22, no. 6, pp. 1167–1172, Jun. 2005.
- [5] Y. P. Wang, Y. J. Rao, Z. L. Ran, and T. Zhu, "Unique characteristics of long-period fibre gratings fabricated by high-frequency CO<sub>2</sub> laser pulses," *Acta Phys. Sin.*, vol. 52, no. 6, pp. 1432–1437, Jun. 2003.
- [6] S. G. Kosinski and A. M. Vengsarkar, "Splicer-based long-period fiber gratings," in *OFC Conf. Exhib. Tech. Dig.*, 1998, pp. 278–279.
- [7] Y. Kondo *et al.*, "Fabrication of long-period fiber gratings by focused irradiation of infrared femtosecond laser pulses," *Opt. Lett.*, vol. 24, no. 10, pp. 646–648, May 1999.
- [8] Y. J. Rao *et al.*, "Temperature-strain discrimination sensor using a WDM chirped in-fibre Bragg grating and an extrinsic Fabry-Perot," *Chin. Phys. Lett.*, vol. 18, no. 5, pp. 643–645, May 2001.
- [9] I. K. Hwang, S. H. Yun, and B. Y. Kim, "Long-period fiber gratings based on periodic microbends," *Opt. Lett.*, vol. 24, no. 18, pp. 1263–1265, Sep. 1999.
- [10] C. Y. Lin and L. A. Wang, "Loss-tunable long period fibre grating made from etched corrugation structure," *Electron. Lett.*, vol. 35, no. 21, pp. 1872–1873, Oct. 14, 1999.
- [11] J. Qu, L. Liu, Y. Shao, H. Niu, and B. Z. Gao, "Recent progress in multifocal multiphoton microscopy," *J. Innov. Opt. Health Sci.*, vol. 5, no. 3, pp. 626–627, Jul. 2012.
- [12] M. Fujimaki, Y. Nishihara, Y. Ohki, J. L. Brebner, and S. Roorda, "Ion-implantation-induced densification in silica-based glass for fabrication of optical fiber gratings," *J. Appl. Phys.*, vol. 88, no. 10, pp. 5534–5537, Nov. 2000.

- [13] X. Zhang *et al.*, "Long-wavelength, photostable, two-photon excitable BODIPY Fluorophores readily modifiable for molecular probes," *J. Organic Chem.*, vol. 78, no. 18, pp. 9153–9160, Sep. 2013.
- [14] T. Zhu, Y.-J. Rao, and Q.-J. Mo, "Simultaneous measurement of refractive index and temperature using a single ultralong-period fiber grating," *IEEE Photon. Technol. Lett.*, vol. 17, no. 12, pp. 2700–2702, Dec. 2005.
- [15] T. Zhu *et al.*, "Characterization of long-period fiber gratings written by CO<sub>2</sub> laser in twisted single-mode fibers," *IEEE J. Lightw. Technol.*, vol. 27, no. 21, pp. 4863–4869, Nov. 2009.
- [16] D. D. Davis *et al.*, "Long-period fibre grating fabrication with focused CO<sub>2</sub> laser pulses," *Electron. Lett.*, vol. 34, no. 3, pp. 302–303, Feb. 1998.
- [17] Y. J. Rao, Y. P. Wang, Z. L. Ran, T. Zhu, and B. M. Yu, "Characteristics of novel long-period fiber gratings written by focused high-frequency CO<sub>2</sub> laser pulses," in *Proc. SPIE*, 2001, pp. 327–333.
- [18] H. M. Chan, F. Alhassen, I. V. Tomov, and H. P. Lee, "Fabrication and mode identification of compact long-period gratings written by CO<sub>2</sub> laser," *IEEE Photon. Technol. Lett.*, vol. 20, no. 8, pp. 611–613, Apr. 2008.
- [19] Y. P. Wang, L. M. Xiao, D. N. Wang, and W. Jin, "Highly sensitive long-period fiber-grating strain sensor with low temperature sensitivity," *Opt. Lett.*, vol. 31, no. 23, pp. 3414–3416, Dec. 1, 2006.
- [20] Y. J. Rao, D. W. Duan, Y. E. Fan, T. Kai, and M. Xin, "High-temperature annealing behaviors of CO<sub>2</sub> laser pulse-induced long-period fiber grating in a photonic crystal fiber," *J. Lightw. Technol.*, vol. 28, no. 10, pp. 1530–1535, May 2010.
- [21] Y. P. Wang *et al.*, "Long period gratings in air-core photonic bandgap fibers," *Opt. Exp.*, vol. 16, no. 4, pp. 2784–2790, Feb. 2008.
- [22] Y. J. Rao, Y. P. Wang, Z. L. Ran, and T. Zhu, "Novel fiber-optic sensors based on long-period fiber gratings written by high-frequency CO<sub>2</sub> laser pulses," *J. Lightw. Technol.*, vol. 21, no. 5, pp. 1320–1327, May 2003.
- [23] Y. P. Wang, D. N. Wang, W. Jin, Y. J. Rao, and G. D. Peng, "Asymmetric long period fiber gratings fabricated by use of CO<sub>2</sub> laser to carve periodic grooves on the optical fiber," *Appl. Phys. Lett.*, vol. 89, no. 15, pp. 151105-1–151105-3, Oct. 2006.
- [24] Y. Liu and K. S. Chiang, "CO<sub>2</sub> laser writing of long-period fiber gratings in optical fibers under tension," *Opt. Lett.*, vol. 33, no. 17, pp. 1933–1935, Sep. 2008.
- [25] H. W. Lee and K. S. Chiang, "CO<sub>2</sub> laser writing of long-period fiber grating in photonic crystal fiber under tension," *Opt. Exp.*, vol. 17, no. 16, pp. 4533–4539, Mar. 2009.
- [26] R. Slavík, "Coupling to circularly asymmetric modes via long-period gratings made in a standard straight fiber," *Opt. Commun.*, vol. 275, no. 1, pp. 90–93, Jul. 2007.
- [27] Y. P. Wang, D. N. Wang, W. Jin, H. L. Ho, and H. Ju, "Mode field profile and polarization dependence of long period fiber gratings written by CO<sub>2</sub> laser," *Opt. Commun.*, vol. 281, no. 9, pp. 2522–2525, May 2008.
- [28] G. D. VanWiggeren *et al.*, "Axial rotation dependence of resonances in curved CO<sub>2</sub>-laser-induced long-period fibre gratings," *Electron. Lett.*, vol. 36, no. 16, pp. 1354–1355, Aug. 2000.

# Simultaneous Refractive Index and Temperature Measurement With LPFG and Liquid-Filled PCF

Guolu Yin, Yiping Wang, *Senior Member, IEEE*, Changrui Liao, Bing Sun, Yingjie Liu, Shen Liu, Qiao Wang, Kaiming Yang, Jian Tang, and Xiaoyong Zhong

**Abstract**—We proposed and demonstrated a novel scheme for simultaneous measurement of temperature and refractive index (RI) by cascading a liquid-filled photonic crystal fiber (PCF) to a long period fiber grating (LPFG) written in a single-mode fiber. The liquid-filled PCF showed a high-temperature sensitivity of  $1.695 \text{ nm}^{\circ}\text{C}$ , which is two orders of magnitude higher than that of the LPFG ( $0.0642 \text{ nm}^{\circ}\text{C}$ ). The LPFG exhibited a blue shift with the increased RI. In contrast, liquid-filled PCF showed a total immunity to the surrounding RI. So, the temperature was solely measured by the liquid-filled PCF, and the RI information was extracted from the total response of the LPFG with the temperature effect having been compensated by the liquid-filled PCF.

**Index Terms**—Optical fiber sensors, long period fiber grating, photonic crystal fiber.

## I. INTRODUCTION

REFRACTIVE index (RI) is an important physical parameter in many applications [1]–[5], such as water quality monitoring, solution concentration measuring, food quality controlling, etc. Since the RI of solution has a strong dependence on temperature, it is essential to measure simultaneously temperature and RI in practical applications. In order to meet such requirements, a few techniques based on long period fiber gratings (LPFGs) have been proposed by using a surface LPFG inscribed on a D-shaped photonic crystal fiber (PCF) [6], a two-section LPFG with an Ag-coated LPFG section and a bare LPFG section [7], a LPFG with ultra-long period of several millimeters [8], and a LPFG inscribed on a concatenated double-clad and single-clad fiber [9]. However, the complicated fabrication process of these specialty LPFGs restricts their practical applications. Alternative schemes are to

Manuscript received October 8, 2014; revised November 3, 2014; accepted November 21, 2014. Date of publication December 2, 2014; date of current version January 21, 2015. This work was supported in part by the China Post-Doctoral Science Foundation Funded Project under Grant 2014M552227, in part by the National Science Foundation of China under Grant 11174064, Grant 61308027, Grant 61377090, and Grant 61405128, in part by the Science and Technology Innovation Commission of Shenzhen under Grant JCYJ 20130329140017262 and Grant KQCX 20120815161444632, and in part by the Distinguished Professors Funding through Shenzhen University and Guangdong Province Pearl River Scholars.

The authors are with the Key Laboratory of Optoelectronic Devices and Systems, College of Optoelectronic Engineering, Ministry of Education, Shenzhen University, Shenzhen 518053, China (e-mail: glyn@szu.edu.cn; ypwang@szu.edu.cn; cliao@szu.edu.cn; pcf13@szu.edu.cn; 814423256@qq.com; liushen.szu@gmail.com; 894817530@qq.com; yangkaiming@email.szu.edu.cn; 286087958@qq.com; 2120190105@email.szu.edu.cn).

Color versions of one or more of the figures in this letter are available online at <http://ieeexplore.ieee.org>.

Digital Object Identifier 10.1109/LPT.2014.2375337

1041-1135 © 2014 IEEE. Personal use is permitted, but republication/redistribution requires IEEE permission.  
See [http://www.ieee.org/publications\\_standards/publications/rights/index.html](http://www.ieee.org/publications_standards/publications/rights/index.html) for more information.

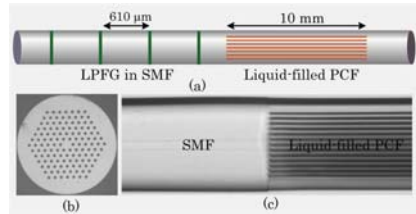


Fig. 1. (a) Schematic diagram of the cascaded fiber device consisting of a LPFG and a liquid-filled PCF, (b) cross section image of the PCF, (c) spliced section of the PCF with a SMF.

cascade another sensing element, e.g. fiber Bragg grating [10], Fabry-Perot interferometer [11], [12], S-taper Mach-Zehnder interferometer [13], PCF-based modal interferometer [14], multimode fiber-based modal interferometer [15], or a small core fiber-based modal interferometer [16], to a LPFG for temperature compensation. The difference of temperature sensitivity between the LPFG and these cascaded elements usually is relative small and almost on the same order of magnitude, which limits the accuracy of temperature compensation. Furthermore, the modal interferometers suffer from a low accuracy of the peak wavelength determination because the peak profiles result from the interference between the fundamental mode and uncertain cladding modes [17], [18].

In this letter, we proposed and demonstrated a novel temperature compensation scheme by cascading a liquid-filled PCF to a LPFG. The bandgap edge of the liquid-filled PCF was strongly influenced by temperature due to thermal-optic effect of the filled liquid, whereas it is almost independent of the surrounding RIs because the light is well bounded in the core region. Thus, the liquid-filled PCF was developed to compensate for the temperature effect in case a LPFG was used for RI sensing. Compared with the reported LPFG-based cascaded device [10]–[16], the proposed scheme has two main advantages. Firstly, the resonant dip of the LPFG and the bandgap edge of the liquid-filled PCF has a wavelength separation of 130 nm, which is large enough to avoid the optical crosstalk. Secondly, the temperature sensitivity of the liquid-filled PCF was two orders of magnitude higher than that of the LPFG. To the best of our knowledge, it is the maximum difference of the temperature sensitivities between two sensing elements in the LPFG-based structures. Such temperature difference improves the accuracy of temperature compensation.

## II. DEVICE FABRICATION

Our proposed sensor structure consists of a LPFG and a liquid-filled PCF, as shown in Fig. 1(a). The LPFG was

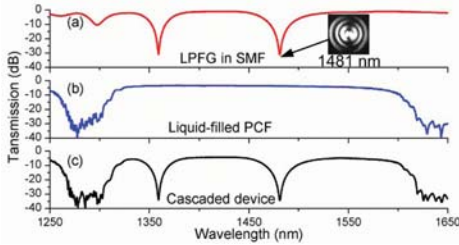


Fig. 2. Transmission spectra of (a) the LPFG, inset: the near mode field pattern of LP<sub>14</sub> cladding mode at 1481 nm, (b) the liquid-filled PCF, and (c) the cascaded LPFG and liquid-filled PCF device.

inscribed in a standard single mode fiber (SMF) (Yangtze Optical Fiber and Cable Co., Ltd.) by use of a commercial splicer machine (Fujikura, ARC master FSM-100P+) with our improved arc discharge technique [19], [20]. Firstly, the standard SMF with a short unjacketed section was positioned between the electrodes by means of the two fiber holders of the splicer. Secondly, arc discharge with a current of 13 mA and duration of 6 s was performed to induce refractive index modulation in the fiber. Thirdly, the fiber was moved by a grating pitch of 610  $\mu\text{m}$  via the SWEEP motor of the splicer. Afterwards, the second and third steps were repeated 28 times. Consequently, a LPFG without visible physical deformation was achieved.

A broadband amplified spontaneous emission (ASE) light source with a wavelength range from 1250 to 1650 nm and an optical spectrum analyzer (YOKOGAWA, AQ6370C) with a wavelength resolution of 0.02 nm were employed to measure the transmission spectra of our proposed devices. As shown in Fig. 2(a), four resonant dips are observed in the transmission spectrum of the LPFG. The resonant dip at 1481 nm has a maximum attenuation up to 30 dB. In order to determine the corresponding cladding mode of the resonant dip, another LPFG was inscribed with the same grating parameter. The inset in Fig. 2(a) illustrates the near mode field pattern at 1481 nm measured by use of a near-infrared camera. The intensity distribution indicates that the resonant dip at 1481 nm corresponds to the coupling from the fundamental mode to the LP<sub>14</sub> cladding mode.

Furthermore, large-mode-area pure silica PCF (ESM-12, NKT) with a core diameter of about 12  $\mu\text{m}$  was employed to fabricate a liquid-filled PCF sample. Air holes with a diameter of 3.3  $\mu\text{m}$  are arranged in a hexagonal pattern with a pitch of 7.4  $\mu\text{m}$ , as shown in Fig. 1(b). Firstly, a section of PCF with a length of 10 mm was prepared by cleaving two ends of the PCF. Secondly, one end of the PCF was immersed into liquid oil (refractive index matching liquid from Cargille Labs) with a RI of 1.698 at 589.3 nm at 25 °C and a thermo-optic coefficient of  $-4.79 \times 10^{-4}/^\circ\text{C}$ . After 5 minutes, the air holes of the 10 mm PCF were fully filled with well-known capillary action. Finally, two ends of the liquid-filled PCF were spliced with SMFs by using a commercial arc fusion splicer (Fujikura FSM-60S), as described below.

The major challenge of splicing the SMF and the liquid-filled PCF is maybe resulting in bubble in the splicing joint due to the gasification of the liquid material. In order

to solve this problem, we preliminarily removed the liquid material at the end of the liquid-filled PCF before splicing. The way of removing the liquid is to perform the cleaning arc discharge with a short duration of 50 ms for several times at the end of the liquid-filled PCF. On the one hand, the arc discharge can gasify the liquid, and on the other, the short duration is not enough to collapse the air hole of the PCF. After the pre-processing above, we spliced the liquid-filled PCF to a SMF by making a 30  $\mu\text{m}$  offset from the joint to the central axis of arc discharge in order to apply a smaller heat amount to the PCF than the SMF [21]. After several trials, the total insertion loss of two splicing joints is around 4 dB. Fig. 1(c) shows the microscope image of the spliced section, where the smooth splicing joint and non evident collapse of the holes indicate that the light in SMF is well coupled into the liquid-filled PCF.

Fig. 2(b) illustrates the transmission spectrum of the liquid-filled PCF. As shown in Fig. 2(b), one bandgap with an extinction ratio of 30 dB occurred in the wavelength range the transmission spectrum from 1250 to 1650 nm. Here, the liquid-filled PCF can be considered as a fiber where the pure silica core is surrounded by a finite array of high-index rods. Because the RI of the liquid rods (1.698 at 589.3 nm) is much larger than that of the silica (1.444 at 1550 nm), the effective RI of the cladding is higher than that of the core. As a result, the index-guided PCF was transferred into a bandgap-guided photonics bandgap fiber (PBF). Thus, the light guidance mechanism in the liquid-filled PCF can be described as photonic bandgap effects [22], [25]. In detail, the light is confined in the pure silica core thanks to the photonic bandgaps which are formed by the periodically arranged liquid rods.

After fabricating the LPFG and the liquid-filled PCF, separately, we constructed the cascaded device by splicing the LPFG and the liquid-filled PCF together. Fig. 2(c) illustrates the transmission spectrum of the cascaded LPFG and liquid-filled PCF device. Two resonant dips of the LPFG were embedded within the bandgap range of the liquid-filled PCF, while the other two resonant dips in the short wavelength direction were attenuated by the band-stop of the liquid-filled PCF. In this letter, we selected the resonant dip at 1481 nm and the right bandgap edge for dual parameter sensing.

The most common LPFG-based cascaded device for dual-parameter sensing is usually composed of a LPFG and an interferometer [11]–[16], which has to face a problem of distinguishing the resonant dip of the LPFG from the fringe pattern of the interferometer because the resonant dip and the fringe pattern are usually inextricably intertwined. Here, our proposed device overcomes this problem by providing a large separation between the resonant dip and the right bandgap edge. In fact, we have much freedom in adjusting the separation by designing the grating pitch of the LPFG and the RI of the filled liquid. According to the phase matching curve of the LPFG [24], the larger the grating pitch is, the longer wavelength the resonant dip locates. On the other hand, the bandgap shifts toward longer wavelength with an increased RI of the filled liquid [23], [25]. Based on the design concept above, we selected the grating pitch of 610  $\mu\text{m}$  and

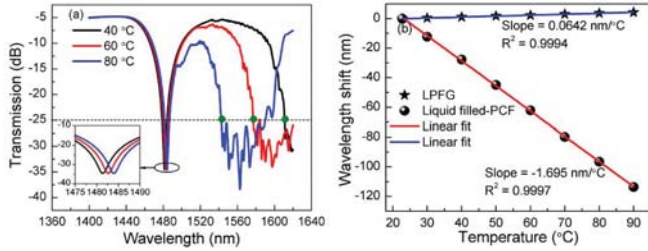


Fig. 3. (a) Transmission spectra of the proposed device at temperatures of 40, 60, and 80 °C, inset: enlarged resonant dip of the LPFG, (b) wavelength shift of the LPFG and the liquid-filled PCF at different temperature.

the liquid with RI of 1.698, which results in a 130 nm separation between the resonant dip and the right bandgap edge. Such a separation is large enough to distinguish the resonant dip from the bandgap edge and to avoid the optical crosstalk.

### III. REFRACTIVE INDEX AND TEMPERATURE RESPONSES

To characterize the temperature response of our proposed device, we employed a column oven (LCO 102, ECOM) with a temperature resolution of 0.1 °C to heat the device from room temperature to 90 °C with a step of 10 °C. At each step, the temperature was stabilized at the target values for 10 min, and then the transmission spectrum was recorded. As shown in Fig. 3(a), when temperature was raised, the resonant dip of the LPFG shifted toward a longer wavelength (“red shift”), while the bandgap of the liquid-filled PCF shifted toward a shorter wavelength (“blue shift”). Although the resonant band of LPFG and the bandgap edge of liquid-filled PCF partly overlapped with each other with the rise of temperature, the resonant dip and the banggap edge can still be clearly distinguished.

Fig. 3(b) illustrates the dependence of the wavelength shift on temperature for both the resonant dip of LPFG and the right bandgap edge of liquid-filled PCF. Here, we quantified the wavelength shift of the bandgap edge by tracing the wavelengths, corresponding to -25 dB, of the right bandgap edge at different temperature. Using a linear-regression analysis below

$$\Delta\lambda_{\text{PCF}}^T = 39.202 - 1.695 \times T$$

$$\Delta\lambda_{\text{LPFG}}^T = -1.489 + 0.0642 \times T \quad (1)$$

As shown in Fig. 3(b), the resonant dip of the LPFG has a low temperature sensitivity of 64.2 pm/°C. In contrast, the right bandgap edge of the liquid-filled PCF has a very high temperature sensitivity of 1.695 nm/°C, which is two orders of magnitude higher than that of the LPFG.

To characterize the RI performance, we employed a set of refractive index matching liquids (Cargille Labs) with a RI from 1.300 to 1.430 with an interval of 0.01. For each refractive index matching liquid, Cargille Labs gives three RIs at wavelengths of 589.3, 486.1, and 656.3 nm at 25 °C [26]. In order to improve the accuracy of the experimental results, we should calculate the RIs of the liquids at the resonant wavelength of 1481 nm and at the room temperature of 23 °C. Firstly, we applied Cauchy dispersion equation to obtain the RIs at the wavelength of 1481 nm [27]

$$n(\lambda) = C_1 + \frac{C_2}{\lambda^2} + \frac{C_3}{\lambda^4} \quad (2)$$

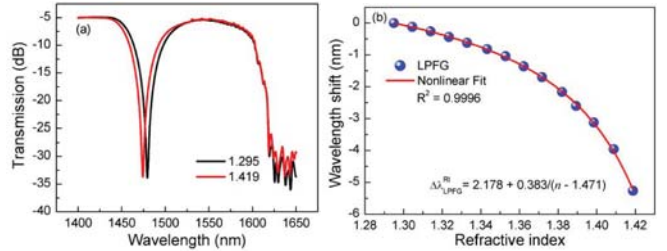


Fig. 4. (a) Transmission spectra of the proposed device immersed in the liquids with a RI of 1.295 and 1.419, (b) resonant wavelength shift of the LPFG at different surrounding RIs.

where the coefficients  $C_1$ ,  $C_2$  and  $C_3$  can be obtained by substituting the three RIs at wavelengths of 589.3, 486.1, and 656.3 nm to Eq. (2). Secondly, we calculated the RIs at 23 °C by considering the thermal coefficient of each liquid which is also given by Cargille Labs. After that, the labelled refractive indices 1.300 and 1.430 at 589.3 nm at 25 °C are calibrated to be 1.295 and 1.419 at 1481 nm at 23 °C, respectively.

The cascaded LPFG and liquid-filled PCF device was sequentially immersed into different refractive index matching liquids, and then its transmission spectrum was measured. After each measurement, a careful clean-and-dry process was done by using alcohol to remove residual liquid on the device surface until the transmission spectrum comes back to the original one in air. Fig. 4(a) illustrates the transmission spectra of the device at the RIs of 1.295 and 1.419. The resonant wavelength shift of the LPFG was plotted in Fig. 4(b). A nonlinear fitting of the experimental results is as follow.

$$\Delta\lambda_{\text{LPFG}}^{\text{RI}} = 2.178 + 0.383/(n - 1.471) \quad (3)$$

It is found from Fig. 4 that the resonant wavelength of the LPFG exhibits a “blue shift” with the increased RI. In contrast, as shown in Fig. 4(a), the bandgap edge of the liquid-filled PCF was not affected by the surrounding RIs. In other words, the liquid-filled PCF showed a total immunity to the surrounding RI. So the temperature could be solely measured from the spectrum response of the liquid-filled PCF. The surrounding RI could be achieved by means of measuring the resonant wavelength shift of the LPFG with temperature compensation, as described below.

After characterizing the temperature and RI responses of the LPFG and the liquid-filled PCF, separately, we demonstrated the cascaded LPFG and liquid-filled PCF sensor’s capability for simultaneous measurement of temperature and surrounding RI. Firstly, the sensor was inserted into a 40 mm-long glass capillary with an inner diameter of 300 μm. Secondly, one end of the capillary tube was immersed into refractive index matching liquid with a RI of 1.35 at 589.3 nm at 25 °C and a thermal coefficient of  $-3.39 \times 10^{-4}/\text{°C}$ , and then the capillary tube was fully filled by the liquid via capillary action. Thirdly, two ends of the capillary tube were sealed with AB glue. The sensor was then placed into the column oven employed in the previous temperature experiments. The transmission spectra of the sensor were recorded at different temperature of 23, 25, 30, 34, 37.9, 42.3, 48.5, 51.7, 58.4, 62.5, and 68.9 °C.

In data processing, first of all, the measured temperature values were calculated from the bandgap edge shift of

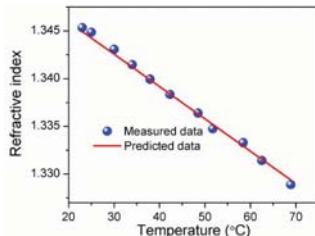


Fig. 5. Variation of the RI of a refractive index matching liquid with temperature.

the liquid-filled PCF by equation (1). According to the temperature sensitivity of the liquid-filled PCF illustrated in Fig. 3(b) and the OSA resolution of 0.02 nm, the theoretic temperature resolution of the proposed sensor is 0.01 °C. Therefore the measured temperature values agreed well with the setting values with a resolution of 0.1 °C. Due to ripples on the bandgap edge which was caused most probably by interference of the fundamental mode and the surface modes, a realistic temperature measurement resolution was estimate around 0.1 °C in the practical application.

After obtaining the measured temperature values, the temperature-induced wavelength shift of the LPFG was calculated by equation (1) and then subtracted from the total resonant wavelength shift of the LPFG, leaving a net wavelength shift resulting from the surrounding RI. Finally, the surrounding RIs were calculated from equation (3) and plotted in Fig. 5 by sphere symbols. Furthermore, the predicated RIs around the wavelength of 1480 nm at different temperatures were calculated by the Cauchy equation and the thermal coefficient of the liquid, and then depicted in Fig. 5 by a solid line. Compared with the measured and predicted RIs, the average error is  $\sim 3.03 \times 10^{-4}$ , and the standard deviation is  $\sim 2.01 \times 10^{-4}$ .

#### IV. CONCLUSION

In conclusion, a novel scheme was proposed and demonstrated for simultaneous measurement of temperature and RI by means of cascading a liquid-filled PCF to a LPFG. The dual-parameter sensing ability of the device originates from the sole temperature response of the liquid-filled PCF, which is used to compensate for the temperature contribution in the total spectral response of the LPFG, leaving a net effect resulting from the surrounding RI. The simultaneous measurement of temperature and surrounding RI was experimentally demonstrated and showed a good agreement with actual values.

#### REFERENCES

- [1] S. Singh, "Refractive index measurement and its applications," *Phys. Scripta*, vol. 65, no. 2, pp. 167–180, 2002.
- [2] L. Mosquera, D. Sáez-Rodríguez, J. L. Cruz, and M. V. Andrés, "In-fiber Fabry-Perot refractometer assisted by a long-period grating," *Opt. Lett.*, vol. 35, no. 4, pp. 613–615, Feb. 2010.
- [3] Y. Wang, "Review of long period fiber gratings written by CO<sub>2</sub> laser," *J. Appl. Phys.*, vol. 108, no. 8, pp. 081101-1–081101-18, Oct. 2010.
- [4] A. Pliss, L. L. Zhao, T. Y. Ohulchansky, J. L. Qu, and P. N. Prasad, "Fluorescence lifetime of fluorescent proteins as an intracellular environment probe sensing the cell cycle progression," *ACS Chem. Biol.*, vol. 7, no. 8, pp. 1385–1392, Aug. 2012.
- [5] Z. Li *et al.*, "Temperature-insensitive refractive index sensor based on in-fiber Michelson interferometer," *Sens. Actuators B, Chem.*, vol. 199, pp. 31–35, Aug. 2014.
- [6] H.-J. Kim, O.-J. Kwon, S. B. Lee, and Y.-G. Han, "Polarization-dependent refractometer for discrimination of temperature and ambient refractive index," *Opt. Lett.*, vol. 37, no. 11, pp. 1802–1804, Jul. 2012.
- [7] T. Allsop, R. Neal, D. Giannone, D. J. Webb, D. J. Mapps, and I. Bennion, "Sensing characteristics of a novel two-section long-period grating," *Appl. Opt.*, vol. 42, no. 19, pp. 3766–3771, Jul. 2003.
- [8] T. Zhu, Y.-J. Rao, and Q.-J. Mo, "Simultaneous measurement of refractive index and temperature using a single ultralong-period fiber grating," *IEEE Photon. Technol. Lett.*, vol. 17, no. 12, pp. 2700–2702, Dec. 2005.
- [9] Q. Han *et al.*, "Long-period grating inscribed on concatenated double-clad and single-clad fiber for simultaneous measurement of temperature and refractive index," *IEEE Photon. Technol. Lett.*, vol. 24, no. 13, pp. 1130–1132, Jul. 1, 2012.
- [10] X. Shu, B. A. L. Gwande, Y. Liu, L. Zhang, and I. Bennion, "Sampled fiber Bragg grating for simultaneous refractive-index and temperature measurement," *Opt. Lett.*, vol. 26, no. 11, pp. 774–776, Jun. 2001.
- [11] D. W. Kim, F. Shen, X. Chen, and A. Wang, "Simultaneous measurement of refractive index and temperature based on a reflection-mode long-period grating and an intrinsic Fabry-Perot interferometer sensor," *Opt. Lett.*, vol. 30, no. 22, pp. 3000–3002, Nov. 2005.
- [12] C.-L. Lee, W.-F. Liu, Z.-Y. Weng, and F.-C. Hu, "Hybrid AG-FFPI/RLPFG for simultaneously sensing refractive index and temperature," *IEEE Photon. Technol. Lett.*, vol. 23, no. 17, pp. 1231–1233, Sep. 1, 2011.
- [13] J. Li *et al.*, "Long-period fiber grating cascaded to an S fiber taper for simultaneous measurement of temperature and refractive index," *IEEE Photon. Technol. Lett.*, vol. 25, no. 9, pp. 888–891, May 1, 2013.
- [14] D. J. Juan Hu *et al.*, "Long period grating cascaded to photonic crystal fiber modal interferometer for simultaneous measurement of temperature and refractive index," *Opt. Lett.*, vol. 37, no. 12, pp. 2283–2285, Jun. 2012.
- [15] J. Huang, X. Lan, A. Kaur, H. Wang, L. Yuan, and H. Xiao, "Temperature compensated refractometer based on a cascaded SMS/LPFG fiber structure," *Sens. Actuators B, Chem.*, vol. 198, pp. 384–387, Jul. 2014.
- [16] Q. Wu *et al.*, "Enhanced refractive index sensor using a combination of a long period fiber grating and a small core singlemode fiber structure," *Meas. Sci. Technol.*, vol. 24, no. 9, p. 094002, 2013.
- [17] Y. Li, E. Harris, L. Chen, and X. Y. Bao, "Application of spectrum differential integration method in an-in-line fiber Mach-Zehnder refractive index sensor," *Opt. Exp.*, vol. 18, no. 8, pp. 8135–8143, Apr. 2010.
- [18] G. Yin, S. Lou, and H. Zou, "Refractive index sensor with asymmetrical fiber Mach-Zehnder interferometer based on concatenating single-mode abrupt taper and core-offset section," *Opt. Laser Technol.*, vol. 45, pp. 294–300, Feb. 2013.
- [19] G. Yin *et al.*, "Long period fiber gratings inscribed by periodically tapering a fiber," *IEEE Photon. Technol. Lett.*, vol. 26, no. 7, pp. 698–701, Apr. 1, 2014.
- [20] G. Yin *et al.*, "Improved arc discharge technique for inscribing compact long period fiber gratings," *Proc. SPIE*, vol. 9157, p. 91577X, Jun. 2014.
- [21] L. Xiao, M. S. Demokan, W. Jin, Y. Wang, and C.-L. Zhao, "Fusion splicing photonic crystal fibers and conventional single-mode fibers: Microhole collapse effect," *J. Lightw. Technol.*, vol. 25, no. 11, pp. 3563–3574, Jun. 1, 2007.
- [22] Y. Wang, X. Tan, W. Jin, D. Ying, Y. Hoo, and S. Liu, "Temperature-controlled transformation in fiber types of fluid-filled photonic crystal fibers and applications," *Opt. Lett.*, vol. 35, no. 1, pp. 88–90, Jan. 2010.
- [23] Y. Liu *et al.*, "Compact tunable multibandpass filters based on liquid-filled photonic crystal fibers," *Opt. Lett.*, vol. 39, no. 7, pp. 2148–2151, Apr. 2014.
- [24] A. M. Vengsarkar, P. J. Lemire, J. B. Judkins, V. Bhatia, T. Erdogan, and J. E. Sipe, "Long-period fiber gratings as band-rejection filters," *J. Lightw. Technol.*, vol. 14, no. 1, pp. 58–65, Jan. 1996.
- [25] B. T. Kuhlmeij, B. J. Eggleton, and D. K. C. Wu, "Fluid-filled solid-core photonic bandgap fibers," *J. Lightw. Technol.*, vol. 27, no. 11, pp. 1617–1630, Jun. 1, 2009.
- [26] Cargille Labs. (1924). *Introduction to Optical Liquids*. [Online]. Available: <http://www.cargille.com/opticalintro.shtml>
- [27] S. C. Su, F. D. Bloss, and M. Gunter, "Procedures and computer programs to refine the double variation method," *Amer. Mineralogist*, vol. 72, pp. 1011–1013, Oct. 1987.

# Intensity-Modulated Strain Sensor Based on Fiber In-Line Mach–Zehnder Interferometer

Jiangtao Zhou, Yiping Wang, *Senior Member, IEEE*, Changrui Liao, Guolu Yin, Xi Xu, Kaiming Yang, Xiaoyong Zhong, Qiao Wang, and Zhengyong Li

**Abstract**—We demonstrated a novel intensity-modulated strain sensor based on a fiber in-line Mach–Zehnder interferometer with a large fringe visibility of up to 17 dB, which was fabricated by splicing a section of thin core fiber between two sections of single mode fibers with one misalignment-spliced joint. Such a strain sensor exhibited an ultrahigh sensitivity of  $-0.023 \text{ dBm}/\mu\epsilon$  within a measurement range of  $500 \mu\epsilon$ , which is about one order of magnitude higher than that reported in references. Displacement and stress distributions at the misalignment spliced joint were simulated by use of finite element method. In addition, the proposed strain sensor has an advantage of compact size of  $\sim 10 \text{ mm}$ .

**Index Terms**—Elasto-optical effect, intensity-modulation, misalignment splicing, physical deformation, strain sensor, thin core fiber.

## I. INTRODUCTION

FIBER in-line Mach–Zehnder interferometer (MZI) sensors are having attracted great research interests and widely used in practical industrial engineering and military fields due to their unique advantages, such as compact size, low cost, high sensitivity, and immunity to electromagnetic interference [1]–[3]. So far, many types of fiber MZI configurations have been demonstrated via singlemode-multimode-singlemode (SMS) fiber structure [4], [5], fiber mode field mismatch fusion [6], [7], waist-deformed fiber taper [8], [9], long period fiber gratings (LPFGs) [10]–[13], in-fiber femtosecond laser micromachining [14], [15], microfiber-based structures [16], [17], and photonic crystal fibers (PCFs) [18], [19]. These configurations show good performance in the applications of sensing temperature, strain, curvature and surrounding refractive index.

Manuscript received October 22, 2013; revised December 10, 2013; accepted December 16, 2013. Date of publication December 20, 2013; date of current version February 11, 2014. This work was supported in part by the National Science Foundation of China under Grants 11174064, 61308027, and 61377090, in part by the Science and Technology Innovation Commission of Shenzhen under Grants KQCX20120815161444632 and JCYJ20130329140017262, and in part by the Distinguished Professors Funding from Shenzhen University and Guangdong Province Pearl River Scholars. (Corresponding author: Y. Wang.)

J. Zhou, Y. Wang, C. Liao, G. Yin, K. Yang, X. Zhong, Q. Wang, and Z. Li are with the Key Laboratory of Optoelectronic Devices and Systems of Ministry of Education and Guangdong Province, Shenzhen University, Shenzhen 518060, China (e-mail: ypwang@szu.edu.cn).

X. Xu is with the College of Civil Engineering, Shenzhen University, Shenzhen 518060, China.

Color versions of one or more of the figures in this letter are available online at <http://ieeexplore.ieee.org>.

Digital Object Identifier 10.1109/LPT.2013.2295826

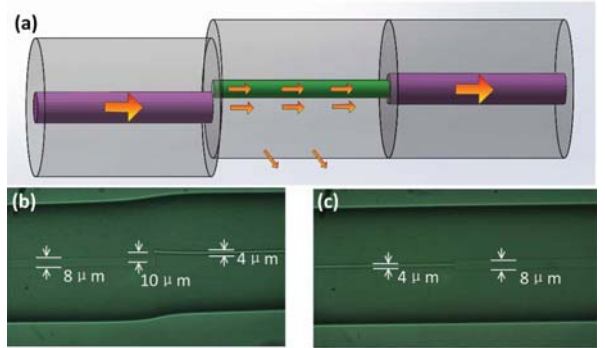


Fig. 1. (a) Fiber in-line MZI structure. Optical microscope images of (b) the lead-in spliced joint with a core offset and (c) the lead-out spliced joint without a core offset.

Unfortunately, wavelength modulation, rather than intensity modulation, were employed in almost of MZI-based sensors [20]–[22], which has to require expensive demodulation devices in practical sensing applications.

In this letter, we demonstrated a novel intensity-modulated strain sensor based on a fiber in-line MZI. This MZI was created by splicing a section of thin core fiber (TCF) between two sections of standard single mode fibers (SMFs) with one misaligned spliced joint. Such a strain sensor exhibited an ultrahigh sensitivity of  $-0.023 \text{ dBm}/\mu\epsilon$  within a measurement range of  $500 \mu\epsilon$ .

## II. PRINCIPLE

As shown in Fig. 1(a), a section of TCF is spliced between two sections of SMFs, i.e. so-called the lead-in SMF and the lead-out SMF. A core offset is created at the lead-in spliced joint. Resulting from the core offset, the light propagating from the lead-in SMF is divided into two parts: a fraction of light will propagate into the core of the TCF as a core mode, and majority of light propagate into the cladding of the TCF as a cladding mode. After propagating through the TCF, the two parts of light meet at the lead-out spliced joint and interfere each other in the core of the lead-out SMF [23]–[25], resulting in an interference. The visibility of fringe pattern can be given as [26]:

$$V = 2\alpha \left( \alpha^2 \frac{\gamma}{1-\gamma} + \frac{1-\gamma}{\gamma} \right)^{-1} \quad (1)$$

where  $\gamma$  is the ratio of light emitted into the core of the TCF at the lead-in spliced joint in which light is excited into the

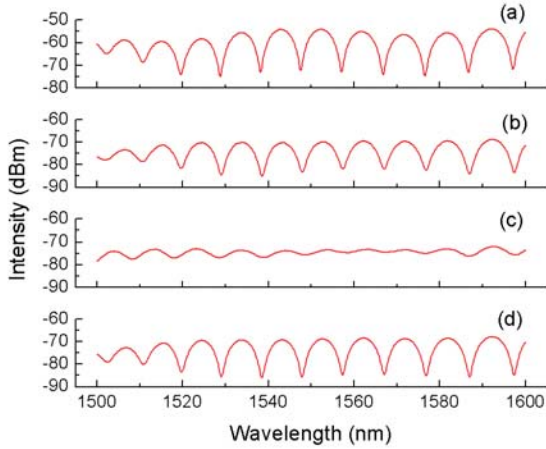


Fig. 2. Interference fringe patterns of the MZI (a) before and (b) after arc discharge was done, (c) after the lead-in spliced joint was removed from the fiber holders in the splicer, and (d) after the MZI was slightly stretched along the fiber axis.

core and cladding modes, and  $\alpha$  is the propagation loss of the cladding modes in the TCF and its unit is percentage. It can be easily found from Eq. 1 that the fringe visibility is critically determined by the splitting ratio of  $\gamma$ , which can be carefully adjusted by changing the core offset at the lead-in spliced joint. The strain-induced wavelength shift of fringe dips can be expressed as [7]:

$$\delta\lambda_{dip,\varepsilon} = \frac{2(\Delta n_{eff,\varepsilon} - \delta n_{eff,\varepsilon})(L + \delta L)}{2m + 1} - \frac{2\Delta n_{eff,\varepsilon} \cdot L}{2m + 1} \approx 2 \frac{\Delta n_{eff,\varepsilon} \cdot \delta L - \delta n_{eff,\varepsilon} \cdot L}{2m + 1} \quad (2)$$

where  $L$  is the length of the TCF,  $\Delta n_{eff,\varepsilon}$  is effective refractive index difference between the core mode and the cladding mode at the tensile strain of  $\varepsilon$ , the  $\delta n_{eff,\varepsilon}$  is the strain-induced change of  $\Delta n_{eff,\varepsilon}$ , the  $\delta L$  is the strain-induced change of the TCF length, and  $m$  is the order of the cladding mode.

### III. EXPERIMENTS AND DISCUSSION

#### A. Fabrication of the MZI

First of all, a section of TCF (Nufern UHNA-3) with a length of 8 mm was spliced with the lead-out SMF (Corning SMF-28) without any core offset by a commercial splicer (Fujikura FSM-60s), as illustrated in Fig. 2(c). That is, the lead-out spliced joint was achieved. Secondly, another end of the TCF and the lead-in SMF were fixed by the left and right fiber holders located in the splicer, respectively. Meanwhile, a broadband light source and an optical spectrum analyzer were connected with the lead in/out SMF, respectively, to monitor interference spectrum. Thirdly, the core offset between the lead-in SMF and the TCF was carefully adjusted via the hand mode of the splicer until the best fringe visibility (about 20 dB near the wavelength of 1550 nm) was observed, as shown in Fig. 2(a). Fourthly, arc discharge was done. Consequently, the lead-in spliced joint with a core offset of about 10  $\mu\text{m}$  was created, as illustrated in Fig. 1(b), where the core of

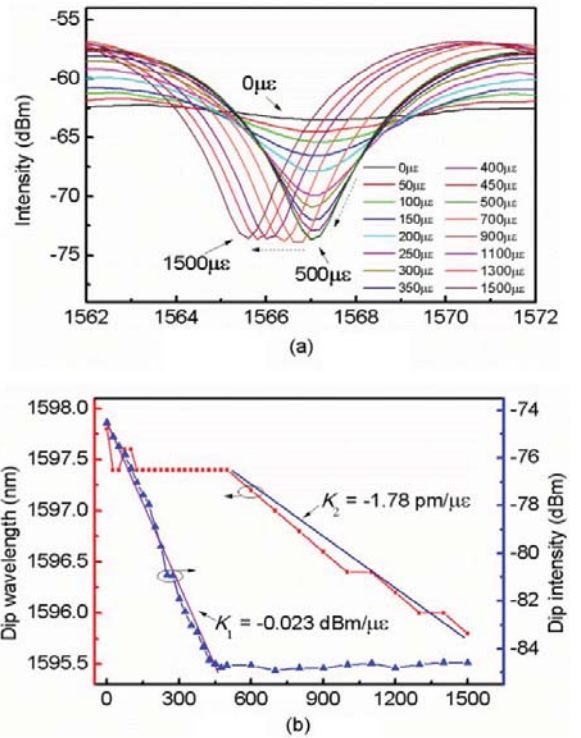


Fig. 3. (a) Interference fringes of the MZI with different tensile strains. (b) Dip wavelength and dip intensity versus tensile strain.

TCF was curved upward slightly, resulting from the splice-induced overlap between the ends of the lead-in SMF and the TCF.

Fig. 2(b) illustrates a fringe pattern observed after arc discharge was done, where the fringe visibility is about 17dB near the wavelength of 1550 nm. As soon as the lead-in spliced joint was removed from the fiber holders in the splicer, poor fringe visibility was observed, as shown in Fig. 2(c), due to the release of the fiber-holder-induced tensile stress in the lead-in spliced joint and the change of the splitting ratio,  $\gamma$ . Furthermore, it is interesting to note that good fringe visibility reappeared, as shown in Fig. 2(d), as soon as the MZI was slightly stretched along the fiber axis. Detailed reason of this unique phenomenon will be discussed in next paragraphs. Therefore, such an M-Z interferometer could be developed a promising strain sensor, as described below.

#### B. Response to Strain

To investigate the response of the MZI structure to tensile strain, the lead-in SMF of the structure was fixed, and the lead-out SMF was attached to a translation stage with a resolution of 10  $\mu\text{m}$ . Then the MZI was stretched along the fiber axis with a step of 10  $\mu\text{m}$  (namely a strain of 50.0  $\mu\text{e}$ ) by means of moving the translation stage to induce a tensile strain of up to 1500  $\mu\text{e}$ , where the length of the stretched fibers, including the lead-in and lead-out SMFs and the TCF, was 200 mm. Typical interference fringe patterns of the MZI with different tensile strains are illustrated in Fig. 3(a), where the tensile strain increases from 0 to 500  $\mu\text{e}$  with a step of 50  $\mu\text{e}$  and from 500 to 1500  $\mu\text{e}$  with a step of 200  $\mu\text{e}$ .

As shown in Fig. 3(a), the fringe visibility was enhanced with an increased tensile strain from 0 to  $500 \mu\epsilon$ , but the center wavelength of interference fringe hardly changed. In contrast, while the tensile strain was increased beyond  $500 \mu\epsilon$ , the fringe visibility hardly changed but the interference fringe exhibited a blue shift.

As shown in Fig. 3(b), the minimum intensity of interference fringe, i.e. dip intensity, linearly decreased with an ultrahigh sensitivity of  $K_1 = -0.023 \text{ dBm}/\mu\epsilon$  while the applied tensile strain was increased from 0 to  $500 \mu\epsilon$ , but the change of the center wavelength of interference fringe, i.e. dip wavelength, was negligible. To the best of our knowledge, this sensitivity is about one order of magnitude higher than that reported in references [27], [28], in which a highly birefringent photonic crystal fiber loop mirror was employed to achieve a strain sensor with a sensitivity of  $-0.0032 \text{ dB}/\mu\epsilon$ . While the tensile strain was increased beyond  $500 \mu\epsilon$ , the dip wavelength shifted toward a shorter wavelength with a sensitivity of  $K_2 = 1.78 \text{ pm}/\mu\epsilon$ . Providing an optical power meter with a resolution of 0.01 dB is employed to measure the output power of our MZI-based strain sensor, a high strain resolution of  $0.43 \mu\epsilon$  could be achieved during strain measurement, which is about one order higher than that (i.e.  $3.1 \mu\epsilon$ ) of the strain sensor reported in reference [27]. The above strain experiment of the MZI sample were done five times, and good repeatability was achieved owe to simple and compact MZI structure, strong strength of the lead-in spliced joint, and power stability of the broadband light source employed.

### C. Simulated Analysis

As shown in Fig. 4, we simulated stress and displacement distributions at the lead-in spliced joint with a core offset of  $10 \mu\text{m}$  via finite element method. Due to the limit of calculation speed, the simulated misalignment-spliced joint sample has a length of  $200 \mu\text{m}$ . We assume that each end of the misalignment-spliced joint sample are stretched by a displacement of  $20 \text{ pm}$ . That is, a tensile strain of  $200 \mu\epsilon$  occurs at the two ends of the spliced joint. The interface between the SMF and the TCF is assumed to be the origin point, as illustrated by white dash line in Fig. 4.

Although uniform stretch force is applied to the two ends of the misalignment-spliced joint to simulate stress and displacement distributions, as shown in Fig. 4(a) and (b), distinct color in each grids indicates that different areas of the joint suffer distinct/asymmetric stress and displacement due to the core offset. In other words, different displacements, namely asymmetric physics deformation, occur near the interface between the SMF and the TCF, as illustrated in Fig. 4(a). And different stress occur in each grids at the spliced joint, as illustrated in Fig. 4(b), which results in a change of refractive index profile at the spliced joint due to elasto-optical effect. Consequently, the change of refractive index profile and asymmetric physics deformation alter the ratio,  $\gamma$ , of light emitted into the core and the cladding of the TCF. As a result, the fringe visibility is effectively modulated, according to Eq. (1). Hence, the dip intensity of interference fringes was linearly decreased

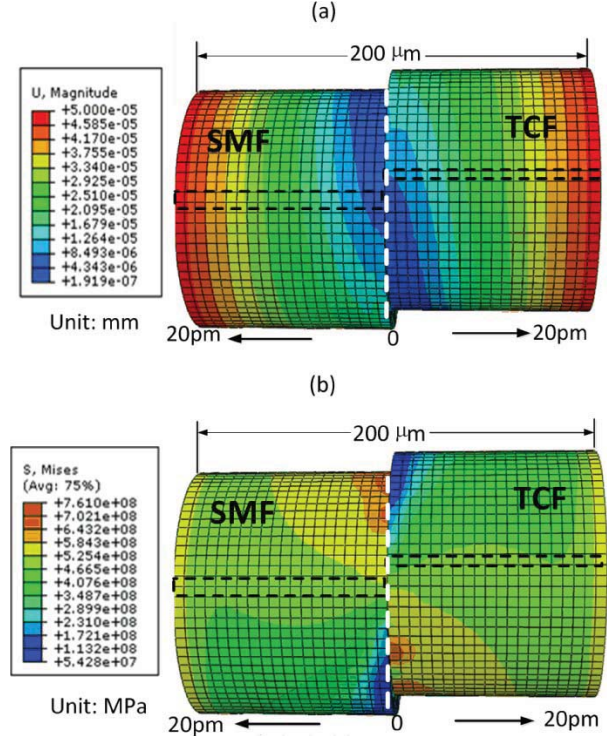


Fig. 4. Simulated (a) displacement and (b) stress distributions at the lead-in spliced joint with a core offset of  $10 \mu\text{m}$  under a tensile strain of  $200 \mu\epsilon$  via finite element method. Different color in each grid indicate the value of stress and displacement in the grid. White dash line denotes the origin interface between the two spliced fibers. Black dash line denotes the position of fiber cores.

with the increased tensile strain, as shown in Fig. 3(b). So the fiber in-line MZI can be used to develop a promising intensity-modulated strain sensor with a high sensitivity of  $-0.023 \text{ dBm}/\mu\epsilon$ . Meanwhile, according to Eq. 2, the dip wavelength of interference fringes maintain steadily because it does not depend on the splitting ratio of light.

Simulation results show that, providing the applied tensile strain is increased over a threshold of  $500 \mu\epsilon$ , such a strain hardly induces further physical deformation and refractive index change. In other words, a large tensile strain mainly results in an extension of the MZI cavity length, rather than of a change of the splitting ratio of light. As a result, the dip intensity is insensitive to the applied strain of more than  $500 \mu\epsilon$ , whereas the dip wavelength linearly shifted toward a shorter wavelength, as shown in Fig. 3(b). The reason of this phenomenon is that, according to Eq. 2, the increase of the MZI cavity length,  $\Delta n_{eff,\epsilon} \cdot \delta L$ , has a weaker impact on the dip wavelength than the decrease of effective refractive index difference,  $-\delta n_{eff,\epsilon} \cdot L$  [7], [9] so that the dip wavelength will ‘blue’ shift while the tensile strain increases over  $500 \mu\epsilon$ .

### IV. CONCLUSION

In conclusion, a novel fiber in-line MZI with a misalignment-spliced joint was demonstrated to develop a promising intensity-modulated strain sensor. Such a strain sensor exhibited an ultrahigh sensitivity of  $-0.023 \text{ dBm}/\mu\epsilon$  within a strain range of less than  $500 \mu\epsilon$ , which is about

one order of magnitude higher than the reported values. And a strain resolution of  $0.43 \mu\epsilon$  could be achieved. The fiber in-line MZI can also be used to measure a large tensile strain of more than  $500 \mu\epsilon$  by means of wavelength modulation with a high sensitivity of  $-1.78 \text{ pm}/\mu\epsilon$ . Furthermore, our MZI-based sensor presents the merits of compact size (only 10 mm), high sensitivities, good repeatability, and good mechanical reliability. Hence, it is expected to have a good practical application in strain measurement fields.

## REFERENCES

- [1] J. Dakin and B. Culshaw, *Optical Fiber Sensors: Principles and Components*. Norwood, MA, USA: Artech House, 1988.
- [2] K. T. V. Grattan and B. T. Meggitt, *Optical Fiber Sensor Technology*. London, U.K.: Chapman & Hall, 1995.
- [3] B. Lee, "Review of the present status of optical fiber sensors," *Opt. Fiber Technol.*, vol. 9, no. 2, pp. 57–79, 2003.
- [4] E. B. Li, X. L. Wang, and C. Zhang, "Fiber-optic temperature sensor based on interference of selective higher-order modes," *Appl. Phys. Lett.*, vol. 89, pp. 091119-1–091119-3 Aug. 2006.
- [5] A. B. Socorro, I. Del Villar, J. M. Corres, F. J. Arregui, and I. R. Matias, "Mode transition in complex refractive index coated single-mode-multimode-single-mode structure," *Opt. Express*, vol. 21, pp. 12668–12682, May 2013.
- [6] L. V. Nguyen, D. Hwang, S. Moon, D. S. Moon, and Y. Chung, "High temperature fiber sensor with high sensitivity based on core diameter mismatch," *Opt. Express*, vol. 16, pp. 11369–11375, Jul. 2008.
- [7] P. Lu and Q. Chen, "Asymmetrical fiber Mach-Zehnder interferometer for simultaneous measurement of axial strain and temperature," *IEEE Photon. J.*, vol. 2, no. 6, pp. 942–953, Dec. 2010.
- [8] G. L. Yin, S. Q. Lou, and H. Zou, "Refractive index sensor with asymmetrical fiber Mach-Zehnder interferometer based on concatenating single-mode abrupt taper and core-offset section," *Opt. Laser Technol.*, vol. 45, pp. 294–300, Feb. 2013.
- [9] P. Lu, L. Men, K. Sooley, and Q. Chen, "Tapered fiber Mach-Zehnder interferometer for simultaneous measurement of refractive index and temperature," *Appl. Phys. Lett.*, vol. 94, pp. 131110-1–131110-3, 2009.
- [10] Z. Wu, *et al.*, "In-line Mach-Zehnder interferometer composed of microtaper and long-period grating in all-solid photonic bandgap fiber," *Appl. Phys. Lett.*, vol. 101, pp. 141106-1–141106-4, Oct. 2012.
- [11] Y. P. Wang, Y. J. Rao, Z. L. Ran, T. Zhu, and X. K. Zeng, "Bend-insensitive long-period fiber grating sensors," *Opt. Lasers Eng.*, vol. 41, pp. 233–239, Jan. 2004.
- [12] Y. P. Wang, "Review of long period fiber gratings written by CO<sub>2</sub> laser," *J. Appl. Phys.*, vol. 108, pp. 081101-1–081101-18, Oct. 2010.
- [13] Y. J. Rao, Y. P. Wang, Z. L. Ran, T. Zhu, and B. Yu, "Characteristics of novel long-period fibre gratings written by focused high-frequency CO<sub>2</sub> laser pulses," *Proc. SPIE*, vol. 4581, pp. 327–333, Nov. 2001.
- [14] L. Zhao, L. Jiang, S. Wang, H. Xiao, Y. Lu, and H.-L. Tsai, "A high-quality Mach-Zehnder interferometer fiber sensor by femtosecond laser one-step processing," *Sensors*, vol. 11, pp. 54–61, Jan. 2011.
- [15] C. R. Liao, Y. Wang, D. N. Wang, and M. W. Yang, "Fiber in-line Mach-Zehnder interferometer embedded in FBG for simultaneous refractive index and temperature measurement," *IEEE Photon. Technol. Lett.*, vol. 22, no. 22, pp. 1686–1688, Nov. 15, 2010.
- [16] X. Xing, Y. Wang, and B. Li, "Nanofibers drawing and nanodevices assembly in poly(trimethylene terephthalate)," *Opt. Express*, vol. 16, no. 14, pp. 10815–10822, 2008.
- [17] Y. H. Li and L. M. Tong, "Mach-Zehnder interferometers assembled with optical microfibers or nanofibers," *Opt. Lett.*, vol. 33, no. 4, pp. 303–305, 2008.
- [18] R. Jha, J. Villatoro, G. Badenes, and V. Pruneri, "Refractometry based on a photonic crystal fiber interferometer," *Opt. Lett.*, vol. 34, pp. 617–619, Mar. 2009.
- [19] W. Zhou, W. C. Wong, C. C. Chan, L.-Y. Shao, and X. Dong, "Highly sensitive fiber loop ringdown strain sensor using photonic crystal fiber interferometer," *Appl. Opt.*, vol. 50, pp. 3087–3092, Jul. 2011.
- [20] J. Zheng, *et al.*, "Temperature and index insensitive strain sensor based on a photonic crystal fiber in line Mach-Zehnder interferometer," *Opt. Commun.*, vol. 297, pp. 7–11, Jun. 2013.
- [21] C. Shen, *et al.*, "Temperature-insensitive strain sensor using a fiber loop mirror based on low-birefringence polarization-maintaining fibers," *Opt. Commun.*, vol. 287, pp. 31–34, Jan. 2013.
- [22] L. V. Nguyen and Y. Chung, "All-optical signal gating using ytterbium-doped fiber and a pair of thermally expanded core fibers," *Appl. Phys. Lett.*, vol. 95, pp. 161111-1–161111-3, Oct. 2009.
- [23] B. Dong, D.-P. Zhou, and L. Wei, "Temperature insensitive all-fiber compact polarization-maintaining photonic crystal fiber based interferometer and its applications in fiber sensors," *J. Lightw. Technol.*, vol. 28, no. 7, pp. 1011–1015, Apr. 1, 2010.
- [24] Y. P. Wang, J. P. Chen, X. W. Li, J. X. Hong, and X. H. Zhang, "Measuring electro-optic coefficients of poled polymers using fiber-optic Mach-Zehnder interferometer," *Appl. Phys. Lett.*, vol. 85, no. 21, pp. 5102–5103, 2004.
- [25] Y. J. Rao, X. K. Zeng, and Y. Zhu, "Temperature-strain discrimination sensor using a WDM chirped in-fibre Bragg grating and an extrinsic Fabry-Pérot," *Chin. Phys. Lett.*, vol. 18, pp. 643–645, May 2001.
- [26] C. R. Liao, D. N. Wang, M. Wang, and M. Yang, "Fiber in-line Michelson interferometer tip sensor fabricated by femtosecond laser," *IEEE Photon. Technol. Lett.*, vol. 24, no. 22, pp. 2060–2063, Nov. 15, 2012.
- [27] W. Qian, C.-L. Zhao, X. Dong, and W. Jin, "Intensity measurement based temperature-independent strain sensor using a highly birefringent photonic crystal fiber loop mirror," *Opt. Commun.*, vol. 283, no. 24, pp. 5250–5254, 2010.
- [28] M. S. Yoon, S. Park, and Y. G. Han, "Simultaneous measurement of strain and temperature by using a micro-tapered fiber grating," *J. Lightw. Technol.*, vol. 30, no. 8, pp. 1156–1160, Apr. 15, 2012.

# Long Period Fiber Gratings Inscribed by Periodically Tapering a Fiber

Guolu Yin, Yiping Wang, *Senior Member, IEEE*, Changrui Liao, Jiangtao Zhou, Xiaoyong Zhong, Guanjun Wang, Bing Sun, and Jun He

**Abstract**—A promising technique for inscribing long period fiber gratings (LPFGs) was demonstrated by only using a commercial splicer. The commercial splicer was developed secondarily to build up a new program for periodically tapering a single mode fiber. High-quality LPFGs with a low insertion loss of  $\sim 1$  dB and a large resonant attenuation of more than  $-30$  dB were achieved. The achieved periodic tapers exhibited an excellent reproducibility with a small error of less than  $\pm 0.3 \mu\text{m}$ . To the best of our knowledge, it is the minimum reproducibility error of tapers achieved by arc discharge technique so far. Near mode fields of three LPFG samples with different pitches were observed to investigate the mode coupling in the taper-inscribed LPFGs. In addition, the resonant wavelengths of our taper-inscribed LPFGs exhibited a blue shift first and then red shift with an increased number of grating periods, resulting from residual stress relaxation together with physical deformation.

**Index Terms**—Long period fiber gratings, periodic tapers, optical fiber sensors, optical fiber devices.

## I. INTRODUCTION

LONG period fiber gratings (LPFGs) have been increasingly used in a wide variety of fields including optical fiber sensors, gain-flattening filters, wavelength rejection filters, and tunable filters [1]–[5]. At first, LPFGs are inscribed by exposure of photosensitive fiber to UV radiation [4]. After that, several non-UV methods have been demonstrated to inscribe LPFGs on both photosensitive fibers and non-photosensitive fibers, such as the CO<sub>2</sub> radiation [5], [6], femtosecond laser radiation [7], ion-beam irradiation [8], periodic microbends [9], [10], and periodically tapering with heating source [11], [12]. Moreover, electric arc discharge has drawn wide attention in recent years because arc discharge technique is much simpler and does not need expensive laser equipment [13]–[17]. In the published setups, however, the electrodes and the translation stage are usually separated each other so that the alignment and stability of the system are the first

Manuscript received December 24, 2013; accepted January 22, 2014. Date of publication January 28, 2014; date of current version March 11, 2014. This work was supported in part by the National Natural Science Foundation of China under Grants 11174064, 61308027, and 61377090, in part by the Science and Technology Innovation Commission of Shenzhen under Grants KQCX20120815161444632 and JCYJ20130329140017262, and in part by the Distinguished Professors Funding through Shenzhen University and Guangdong Province Pearl River Scholars.

The authors are with the Key Laboratory of Optoelectronic Devices and Systems of Ministry of Education and Guangdong Province, Shenzhen University, Shenzhen 518060, China (e-mail: ypwang@szu.edu.cn).

Color versions of one or more of the figures in this letter are available online at <http://ieeexplore.ieee.org>.

Digital Object Identifier 10.1109/LPT.2014.2302901

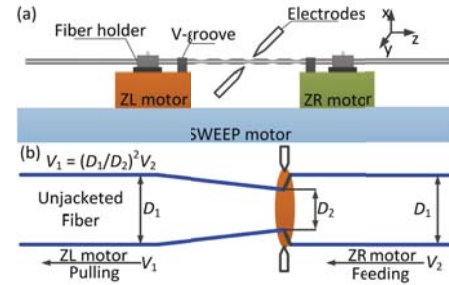


Fig. 1. Schematic diagrams for (a) inscribing a LPFG with periodic tapers by employing a commercial splicer machine and (b) inscribing desired taper.

challenge [18]. In addition, a mass has to be attached to one end of the employed fiber in order to keep the fiber under a constant axial tension. Such a mass seriously influences fabrication efficiency, resonant dip and insertion loss of the achieved LPFGs [19]. As well known, arc discharge often leads to tapering of the fiber. Unfortunately, the shape profile of the taper is seriously influenced by electric current, arc duration and the weight of the mass [20], resulting in a poor reproducibility of the tapers and a large repeatability error of up to  $5 \mu\text{m}$  [21].

In this letter, a promising technique was demonstrated to inscribe high-quality LPFGs by periodically tapering a standard single mode fiber (SMF) with a commercial fusion splicer. The taper profile was finely controlled by two motors with a precision of  $0.01 \mu\text{m}$ , exhibiting an excellent repeatability with a small error of less than  $\pm 0.3 \mu\text{m}$ . Moreover, transmission spectra and near mode fields of the inscribed LPFGs with periodic tapers were investigated, followed by discussion on the evolution of resonance dips.

## II. FABRICATION TECHNIQUE

In our experiment, as shown in Fig. 1, a commercial splicer machine (Fujikura, ARC master FSM-100P+) was employed to inscribe LPFGs by means of periodically tapering an optical fiber. Compared with traditional fusion splicers, besides ZL and ZR motors, this machine has a SWEEP motor which can move the fiber fixed by the left and right fiber holders along the fiber axis with a maximum moving range of  $+/-18 \text{ mm}$  and a precision of  $0.01 \mu\text{m}$ . This is due to the fact that the two fiber holders are placed on a translation stage that can be driven by the SWEEP motor. The FSM-100P+ commercial splicer is originally designed to splice various types of special fibers [22], such as photonic crystal fibers,

polarization maintaining fiber, and large diameter fibers up to 1200 micron cladding diameter. But the FSM-100P+ does not have a ready program for tapering periodically an optical fiber. In other words, the standard functions of the FSM-100P+ splicer does not include the inscription of LPFGs. Here, we carried out, for the first time, the second development of the splicer by means of building up a new program for tapering periodically a fiber to inscribe a high-quality LPFG. Such a program can be saved in the program store of the splicer and be transplanted to any FSM-100 series splicers for LPFGs inscription. Furthermore, the program is performed easily by pushing only one button, like standard fusion program.

Our designed program includes three main steps. The first and second steps are to inscribe the down-taper section and up-taper section, respectively. Here, arc current and arc duration are manually selected to approximately 11 mA and  $\sim 4$  s, respectively. When arc discharge is down, the two ends of the fiber are synchronously stretched by the left and right fiber holders those were driven by the ZL and ZR motors, respectively. As a result, a taper is created at the discharged section of the fiber. Thirdly, the fiber is moved by a grating pitch, e.g. 650  $\mu\text{m}$ , along its axis via the SWEEP motor in order to create another taper at a new location of the fiber.

The detail LPFG inscription can be carried out by the designed program as follows. When a standard SMF (Yangtze Optical Fiber and Cable Co., Ltd.) with a short unjacketed section was fixed by the left and right fiber holders, the designed program was performed repeatedly for a number of times until a desired LPFG transmission spectrum was observed. Consequently, a LPFG with periodic tapers was inscribed on the employed fiber.

In order to understand our designed program, we give the fabrication principle of the taper as shown in Fig. 1(b). When arc discharge is done to form a heat zone, the unjacketed fiber is fed from the right side of the heat zone by using the ZR motor with a constant speed  $V_2$  (typically 0.04  $\mu\text{m}/\text{ms}$ ) and pulled from left side of the heat zone by using the ZL motor with a variable speed  $V_1$ . The feeding and the pulling directions are the same. But the feeding and pulling speeds are different, which control the tapering ratio. According to material conservation, the glass fed into the heat zone should be equal to the glass pulled out from the heat zone. Hence, the pulling speed is determined by the equation  $V_1 = (D_1/D_2)^2 V_2$ , where  $D_1$  and  $D_2$  are the cladding diameter of SMF and the local diameter of the taper, respectively. As a result, a desired taper is created by means of controlling the feeding speed of ZR motor and the pulling speed of the ZL motor as discussed above.

Summarizing the fabrication technique above, our proposed technique employs only a commercial splicer, i.e. FSM-100P+, and no other devices are required to inscribed LPFGs. In contrast, the traditional arc discharge techniques for inscribing LPFGs not only employ a commercial splicer but also require an additional translation stage, a mass and a computer that is used to control the translation stage [18], [21]. In traditional techniques, the fiber is clamped by the holder fixed on the top of the translation stage, instead of the holders of the splicer. Therefore, the alignment and stability are the

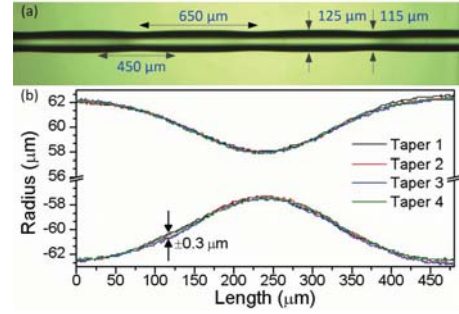


Fig. 2. (a) Image of the LPFG inscribed by periodically tapering a SMF, (b) shape profiles of four tapers.

first challenge due to the separation between the electrodes and the translation stage [18]. Furthermore, in the traditional techniques, tapers are created by the drawing force of the mass that attached to one end of the fiber. Consequently, the shape profile of the taper is seriously influenced by electric current, arc duration and the weight of the mass [20]. Compared with traditional technique, our proposed technique is conducted to build up a portable program in the commercial splicer. This technique avoids the alignment problem and the influence of the mass and has a few advantages of compactness, integration, stability, flexibility, simplify operation and high precision. Therefore, our proposed technique could be used to inscribe high-quality LPFGs with a good reproduction of tapers.

### III. EXPERIMENTAL RESULTS AND DISCUSSION

Fig. 2(a) illustrates microscope image of the LPFG inscribed by periodically tapering the SMF. The measured grating pitch of the LPFG is about 650  $\mu\text{m}$ . Each taper has a waist diameter of about 115  $\mu\text{m}$  and a length of about 450  $\mu\text{m}$ . To evaluate the reproducibility of the tapers, we randomly chose four tapers in the LPFG and measured their shape profiles by use of a digital graph processing technique [23], as illustrated in Fig. 2(b). It can be found from Fig. 2(b) that the radius error at any axis position of each taper profile, i.e. the reproducibility error of tapers, is less than  $\pm 0.3 \mu\text{m}$ , which is one order of magnitude smaller than the reproducibility error (i.e. 5  $\mu\text{m}$ ) of the taper produced by attaching a mass to the fiber end [21]. To the best of our knowledge, it is the minimum reproducibility error of the tapers achieved by arc discharge technique so far [21], [22], [24]. Such an excellent reproducibility attributes to our designed program, which can synchronously control the arc discharge and translation devices with a high precision. Firstly, electrodes, V-grooves and translation stages are integrated in the splicer, avoiding the alignment problem between each other. Wind protector of the splicer can provide a relatively stable environmental during tapering the fiber. Secondly, a pre-alignment between V-grooves ensures that the fiber remains in the same position relative to the electrodes. The last but most important, the shape profile of the taper is finely controlled by the translation stages with a precision of 0.01  $\mu\text{m}$  in the Z direction.

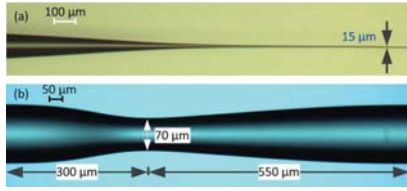


Fig. 3. Microscope images of the created tapers with (a) a symmetric shape profile (small waist diameter of  $15\ \mu\text{m}$ ) and (b) an asymmetric shape profile (large waist diameter of  $70\ \mu\text{m}$ ).

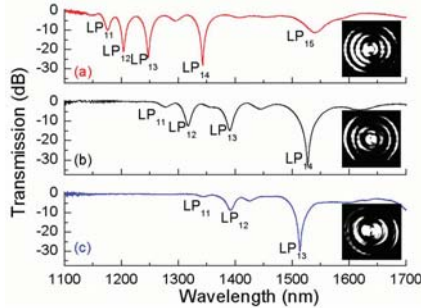


Fig. 4. Transmission spectra of three taper-inscribed LPFGs (a) LPFG<sub>1</sub> with a pitch of  $550\ \mu\text{m}$ , (b) LPFG<sub>2</sub> with a pitch  $650\ \mu\text{m}$ , and (c) LPFG<sub>3</sub> with a pitch of  $730\ \mu\text{m}$ . Insets: near mode fields corresponding to the three LPFGs' resonant wavelength of 1538.32, 1525.06 and 1513.43 nm, respectively.

Moreover, we can control the tapering process of fiber to achieve a desired taper by means of modifying our designed program. According to the fabrication principle of the taper as discussion in the last section, we can modify the designed program to control the feeding speed of ZR motor and the pulling speed of the ZL motor. Therefore, we can create tapers with desired diameter and shape profile. In order to evaluate this capability, we created two desired taper samples. The first sample has a symmetric shape profile with a down-taper transition length of 2 mm, a uniform waist length of 1 mm and an up-taper transition length of 2 mm. The local diameter of the taper can be gradually reduced to  $15\ \mu\text{m}$  in the waist region. Due to the field range limitation of our microscope, the microscope image of only a section of taper is illustrated in Fig. 3(a). The second sample, as shown in Fig. 3(b), has a down-taper transition length of 300  $\mu\text{m}$ , an up-taper transition length of 550  $\mu\text{m}$  and a waist diameter of  $70\ \mu\text{m}$ , exhibiting an asymmetric shape profile along the fiber axis. In a word, such flexible and high-precision tapering process can achieve various kinds of tapers which would find wide applications in mode filtering [24], laser beam shaping [25] and optical fiber sensing [26].

We inscribed three LPFG samples, i.e. LPFG<sub>1</sub>, LPFG<sub>2</sub>, and LPFG<sub>3</sub>, with different grating pitches of 550, 650, and 730  $\mu\text{m}$ , respectively, in order to investigate mode coupling in the taper-inscribed gratings. A supercontinuum light source (NKT Photonics, Superk Compact) and an optical spectral analyzer (YOKOGAWA, AQ6370C) were employed to monitor the transmission spectrum of the inscribed LPFG during grating inscription. As shown in Fig. 4, within the wavelength range from 1100 to 1700 nm, five, four and three resonant dips were observed in the transmission spectrum of LPFG<sub>1</sub>, LPFG<sub>2</sub> and LPFG<sub>3</sub>, respectively. And each LPFG has a

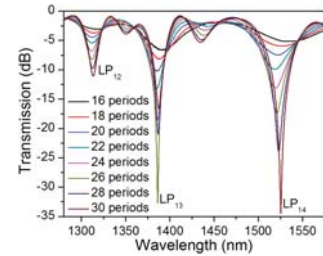


Fig. 5. Transmission spectrum evolution of LPFG<sub>2</sub> with a pitch of  $650\ \mu\text{m}$  while the number of grating period increases from 16 to 30.

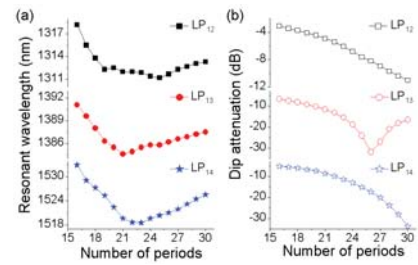


Fig. 6. Evolutions of (a) resonant wavelength and (b) the corresponding dip attenuations at each resonant dip, i.e. LP<sub>12</sub>, LP<sub>13</sub>, and LP<sub>14</sub>, of LPFG<sub>2</sub> while the number of grating periods increases from 16 to 30.

strong coupling attenuation of up to  $-30\ \text{dB}$  at the resonant wavelength and a low insertion loss of about 1 dB.

A tunable laser (EXFO, FLS-2600B) with a tunable wavelength range from 1510 to 1610 nm was connected to one end of a LPFG sample as a single wavelength light source. Another end of the LPFG sample with periodic tapers was cleaved at the last grating period, i.e. taper, to observe near mode field by use of a near-infrared camera. Inserts in Fig. 4 illustrate the observed near mode fields at the longer resonant wavelength, i.e. 1538.32, 1525.06, and 1513.43 nm, of LPFG<sub>1</sub>, LPFG<sub>2</sub>, and LPFG<sub>3</sub>, respectively. Intensity distribution of near mode field pattern illustrated in Fig. 4 indicts that the observed resonant dips of LPFG<sub>1</sub>, LPFG<sub>2</sub>, and LPFG<sub>3</sub> correspond to the coupling from the fundamental mode to the LP<sub>15</sub>, LP<sub>14</sub>, and LP<sub>13</sub> cladding modes, respectively. Thus, the cladding modes corresponding to other resonant dips of each LPFG sample are determined sequentially, as shown in Fig. 4.

Transmission spectrum evolution of LPFG<sub>2</sub> with an increased number of grating periods, i.e. tapers, is illustrated in Fig. 5, in which transmission spectra of LPFG<sub>2</sub> with more than 16 tapers are illustrated because dip attenuation in the grating spectrum is too small to be measured before the 16<sup>th</sup> taper is created. Evolutions of resonant wavelength and the corresponding dip attenuation at each resonant dip, i.e. LP<sub>12</sub>, LP<sub>13</sub>, and LP<sub>14</sub>, with the increased number of grating periods are illustrated in Fig. 6. It is interesting to be found from Figs. 5 and 6(b) that dip attenuations corresponding to the LP<sub>12</sub> and LP<sub>14</sub> cladding modes gradually grow with the increased number of grating periods whereas the value corresponding to the LP<sub>13</sub> cladding mode grows first and then reduces after the 26<sup>th</sup> taper is created due to the over-coupling from the LP<sub>13</sub> cladding mode to the fundamental mode.

As shown in Figs. 5 and 6(a), resonant wavelengths of LPFG<sub>2</sub> exhibit a blue shift first and then a red shift with

an increased number of grating periods. It is the reason for this that refractive index modulation mechanisms in the taper-inscribed LPFGs include two facts: residual stress relaxation and physical deformation. Residual stress in the arc-discharge area of the fiber core is relaxed due to the fast local heating-cooling process, which results in a decrease of effective refractive index in the fiber core [5], [27]. According to phase matching condition [4], the decrease in effective refractive index of the fundamental mode results in a blue shift of resonant wavelength. Therefore, the resonant wavelength shifts toward the shorter wavelength with the increased number of grating periods, as shown in Fig. 6(a). On the other hand, as shown in Fig. 2, the fiber diameter decrease at the taper region is up to  $\sim 8\%$ . Therefore, the physical-deformation-induced perturbation in effective refractive index of the fiber has to be considered. In case a large number of tapers are created, the equivalent fiber diameter in the whole grating region could be considered to be decreased due to the cumulative effect of the local diameter decrease at each taper region, which results in an increase in effective index difference between the fundamental mode and the cladding modes, as reported in Fig. 3(b) in reference [28]. Therefore, the resonant wavelength shifts towards the longer wavelength, rather than the short wavelength, after the number of the created tapers increase to a certain value [4]. For example, as shown in Fig. 6(a), the resonant wavelength corresponding to the LP<sub>14</sub> cladding mode shifts towards the longer wavelength after the 23<sup>rd</sup> taper is created.

#### IV. CONCLUSION

In conclusion, an improvement technique was demonstrated to inscribe high-quality LPFGs with periodic tapers by use of only a commercial splicer. No other devices are required to inscribe a LPFG with a dip attenuation of up to  $-30$  dB and a low insertion loss of about 1 dB. Such a technique has a few advantages of compactness, integration, stability, flexibility, simplify operation and high precision. The shape profile of the periodic tapers was finely controlled by two motors with a high precision of  $0.01 \mu\text{m}$ , avoiding the influence of the attached mass in the traditional method. The periodic tapers exhibited an excellent reproducibility with a small error of less than  $\pm 0.3 \mu\text{m}$ . Refractive index modulation mechanisms in the taper-inscribed LPFGs include two facts: residual stress relaxation and physical deformation.

#### REFERENCES

- [1] V. Bhatia, "Applications of long-period gratings to single and multi-parameter sensing," *Opt. Express*, vol. 4, no. 11, pp. 457–466, May 1999.
- [2] C. E. Chryssou, "Gain-equalizing filters for wavelength division multiplexing optical communication systems: A comparison of notch and long-period grating filters for integrated optoelectronics," *Opt. Commun.*, vol. 184, nos. 5–6, pp. 375–384, Oct. 2000.
- [3] Y. J. Rao, Y. P. Wang, Z. L. Ran, and T. Zhu, "Novel fiber-optic sensors based on long-period fiber gratings written by high-frequency CO<sub>2</sub> laser pulses," *J. Lightw. Technol.*, vol. 21, no. 5, pp. 1320–1327, May 2003.
- [4] A. M. Vengsarkar, P. J. Lemaire, J. B. Judkins, V. Bhatia, T. Erdogan, and J. E. Sipe, "Long-period fiber gratings as band-rejection filters," *J. Lightw. Technol.*, vol. 14, no. 1, pp. 58–65, Jan. 1996.
- [5] Y. P. Wang, "Review of long period fiber gratings written by CO<sub>2</sub> laser," *J. Appl. Phys.*, vol. 108, no. 8, pp. 081101-1–081101-18, Oct. 2010.
- [6] D. D. Davis, T. K. Gaylord, E. N. Glytsis, S. G. Kosinski, S. C. Mettler, and A. M. Vengsarkar, "Long-period fibre grating fabrication with focused CO<sub>2</sub> laser pulses," *Electron. Lett.*, vol. 34, no. 3, pp. 302–303, Feb. 1998.
- [7] Y. Kondo, K. Nouchi, T. Mitsuyu, M. Watanabe, P. G. Kazansky, and K. Hirao, "Fabrication of long-period fiber gratings by focused irradiation of infrared femtosecond laser pulses," *Opt. Lett.*, vol. 24, no. 10, pp. 646–648, May 1999.
- [8] M. L. von Bibra, A. Roberts, and J. Canning, "Fabrication of long-period fiber gratings by use of focused ion-beam irradiation," *Opt. Lett.*, vol. 26, no. 11, pp. 765–767, Jun. 2001.
- [9] I. K. Hwang, S. H. Yun, and B. Y. Kim, "Long-period fiber gratings based on periodic microbends," *Opt. Lett.*, vol. 24, no. 18, pp. 1263–1265, Sep. 1999.
- [10] H. Sakata and K. Yamahata, "Magnetic-force-induced long-period fiber gratings," *Opt. Lett.*, vol. 37, no. 7, pp. 1250–1252, Apr. 2012.
- [11] L. Y. Shao, J. Zhao, X. Dong, H. Y. Tam, C. Lu, and S. He, "Long-period grating fabricated by periodically tapering standard single-mode fiber," *Appl. Opt.*, vol. 47, no. 10, pp. 1549–1552, May 2008.
- [12] M. S. Yoon, S. Park, and Y. G. Han, "Simultaneous measurement of strain and temperature by using a micro-tapered fiber grating," *J. Lightw. Technol.*, vol. 30, no. 8, pp. 1156–1160, Apr. 15, 2012.
- [13] G. Rego, O. Okhotnikov, E. Dianov, and V. Sulimov, "High-temperature stability of long-period fiber gratings produced using an electric arc," *J. Lightw. Technol.*, vol. 19, no. 10, pp. 1574–1579, Oct. 2001.
- [14] H. Georges and M. Abdelrafik, "Electric-arc-induced gratings in non-hydrogenated fibres: Fabrication and high-temperature characterizations," *J. Opt. A, Pure Appl. Opt.*, vol. 4, no. 2, pp. 194–198, Mar. 2002.
- [15] K. Morishita and Y. Miyake, "Fabrication and resonance wavelengths of long-period gratings written in a pure-silica photonic crystal fiber by the glass structure change," *J. Lightw. Technol.*, vol. 22, no. 2, pp. 625–630, Feb. 2004.
- [16] M. Smitiana, W. J. Bock, P. Mikulic, and J. Chen, "Increasing sensitivity of arc-induced long-period gratings—Pushing the fabrication technique toward its limits," *Meas. Sci. Technol.*, vol. 22, no. 1, pp. 015201-1–015201-6, Jan. 2011.
- [17] A. Iadicicco, S. Campopiano, and A. Cusano, "Long-period gratings in hollow core fibers by pressure-assisted arc discharge technique," *IEEE Photon. Technol. Lett.*, vol. 23, no. 21, pp. 1567–1569, Nov. 1, 2011.
- [18] G. Rego, "Arc-induced long-period fibre gratings: Fabrication and their applications in optical communications and sensing," Ph.D. dissertation, Dept. Electr. Comput. Eng., Porto Univ., Porto, Portugal, 2006.
- [19] G. Rego, P. V. S. Marques, J. L. Santos, and H. M. Salgado, "Arc-induced long-period gratings," *Fiber Integr. Opt.*, vol. 24, nos. 3–4, pp. 245–259, May 2005.
- [20] M. Kim, D. Lee, B. I. Hong, and H. Chung, "Performance characteristics of long-period fiber-gratings made from periodic tapers induced by electric-arc discharge," *J. Korean Phys. Soc.*, vol. 40, no. 2, pp. 369–373, Feb. 2002.
- [21] W. J. Bock, C. Jiahua, P. Mikulic, and T. Eftimov, "A novel fiber-optic tapered long-period grating sensor for pressure monitoring," *IEEE Trans. Instrum. Meas.*, vol. 56, no. 4, pp. 1176–1180, Aug. 2007.
- [22] (2012). *ArcMaster FSM-100M+ and 100P+* [Online]. Available: <http://www.fujikura.co.uk/products/fusion-splicers-and-accessories/fusion-splicers-specialty/arcmaster-fsm-100mplus-and-100pplus/>
- [23] L. W. Wang, S. Q. Lou, W. G. Chen, and H. L. Li, "A novel method of rapidly modeling optical properties of actual photonic crystal fibres," *Chin. Phys. B*, vol. 19, no. 8, pp. 084209-1–084209-7, Aug. 2010.
- [24] Y. Jung, G. Brambilla, and D. J. Richardson, "Broadband single-mode operation of standard optical fibers by using a sub-wavelength optical wire filter," *Opt. Express*, vol. 16, no. 19, pp. 14661–14667, Sep. 2008.
- [25] T. Z. Tian, M. Nix, and S. S. H. Yam, "Laser beam shaping using a single-mode fiber abrupt taper," *Opt. Lett.*, vol. 34, no. 3, pp. 229–231, Feb. 2009.
- [26] T. Z. Tian, S. S. H. Yam, and H.-P. Loock, "Refractive index sensor based on an abrupt taper Michelson interferometer in a single-mode fiber," *Opt. Lett.*, vol. 33, no. 10, pp. 1105–1107, May 2008.
- [27] F. Abrishamian, N. Dragomir, and K. Morishita, "Refractive index profile changes caused by arc discharge in long-period fiber gratings fabricated by a point-by-point method," *Appl. Opt.*, vol. 51, no. 34, pp. 8271–8276, Dec. 2012.
- [28] M. S. Yoon, H. J. Kim, S. J. Kim, and Y. G. Han, "Influence of the waist diameters on transmission characteristics and strain sensitivity of microtapered long-period fiber gratings," *Opt. Lett.*, vol. 38, no. 15, pp. 2669–2672, Aug. 2013.



## Compact device employed a hybrid plasmonic waveguide for polarization-selective splitting

Bing Sun <sup>a</sup>, Yiping Wang <sup>a,\*</sup>, Yingjie Liu <sup>a</sup>, Shen Liu <sup>a</sup>, Changrui Liao <sup>a</sup>, Ming-Yang Chen <sup>b</sup>

<sup>a</sup> Key Laboratory of Optoelectronic Devices and Systems of Ministry of Education and Guangdong Province, College of Optoelectronic Engineering, Shenzhen University, Shenzhen 518060, China

<sup>b</sup> Department of Optical Engineering, School of Mechanical Engineering, Jiangsu University, Zhenjiang 212013, Jiangsu Province, China



### ARTICLE INFO

#### Article history:

Received 1 July 2014

Received in revised form

3 August 2014

Accepted 6 August 2014

Available online 20 August 2014

#### Keywords:

Coupler

Optical waveguide devices

Optical polarization

Plasmonic

### ABSTRACT

We proposed an ultra compact polarization beam splitter (PBS) with a short coupling length of 2.82 μm consisting of a horizontally slotted waveguide (HSWG) and a hybrid plasmonic waveguide (HPWG). Only the TM-polarized mode can be supported in the HPWG, and the effective index, corresponding to the TM-polarized mode, in the HPWG is similar to that in the HSWG within a wide wavelength range. Consequently, the TM-polarized mode in the HSWG could be coupled into that in the HPWG. As a result, the TE- and TM-polarized modes are split. Such a PBS exhibits a high extinction ratio of up to –20 dB within an ultra wide wavelength range of 130 nm. Moreover, fabrication tolerances of the PBS are investigated.

© 2014 Elsevier B.V. All rights reserved.

### 1. Introduction

Silicon-on-insulator (SOI) technology has attracted lots of interests as a platform for guiding and manipulating optical signals in photonic integrated circuits. However, SOI waveguides involve highly polarization-dependent guiding owing to the high index difference between silicon and air/silica. As a result, the implementations of polarization beam splitters (PBSs) are essential in the applications of SOI waveguides. Although various configurations, such as multimode interference structures [1–3], Mach-Zehnder interferometers [4–6], photonic crystal structures [7,8], have been demonstrated to split polarization modes, one would prefer to implement PBSs based on directional couplers [9–22] due to their simplicity and easy design. For instance, Dai et al. [14] demonstrated an ultrashort polarization splitter with a strip-nanowire and a vertically slotted waveguide, which took advantage of the completely phase-matching condition for the TM polarization, while significantly suppressed the coupling for the TE polarization. Zhang, et al. presented a compact and efficient PBS using horizontally slotted waveguides with extinction ratio across C+L broadband [15]. Recently, a directional coupler, consisting of a vertically slotted waveguide and a channel waveguide, has been developed to realize polarization splitting with high extinction ratio of 20 dB for through port [16].

In recent years, plasmonic waveguides [23] have attracted intensive research interest due to their excellent ability to break the diffraction limit. Among them, hybrid plasmonic waveguides (HPWGs) are emerging because of their unique advantages of both long propagation length and strong confinement, and, in particular, large birefringence [24–28]. Recently, we demonstrated an on-chip PBS based on directional coupling system consisting of a horizontally slotted waveguide (HSWG) and a HPWG [18], in which only one polarization state was index-matched, whereas the index difference was very high for another polarization so that the effective coupling between the two polarization modes was prevented. Almost at the same time, Gao et al. [19] presented an ultracompact PBS consisting of a HPWG and a strip dielectric waveguide, which showed an extinction ratio of over 14.7 dB for the TE-polarized mode within the whole C band. In addition, Lou et al. [20] demonstrated a compact PBS based on a dielectric-hybrid plasmonic-dielectric coupler. In the meanwhile, Chee et al. [21] designed a similar device by use of Cu as the metal cap and demonstrated an ultrashort integrated polarization splitter with a bandwidth of more than 70 nm and an extinction ratio of less than 15 dB. An asymmetrical coupling system consisting of a hybrid plasmonic waveguide and a silicon nanowire has been proposed by Guan et al. [22].

In this paper, we present a promising PBS based on a directional coupling system consisting of a HSWG and a HPWG. Such a PBS is optimally designed to satisfy the phase-matching condition for TM-polarized modes of the two waveguides, while the TE-polarized mode cannot be supported in the HPWG. In the

\* Corresponding author.

E-mail address: [ypwang@szu.edu.cn](mailto:ypwang@szu.edu.cn) (Y. Wang).

proposed PBS, the two index-curves of the TM-polarized modes in the HSWG and the HPWG have a very small index difference so that strong coupling occurs within a wide wavelength range. In contrast, the effective coupling for the TE-polarized mode is prevented due to the fact that only TM-polarized guided mode can be supported in the HPWG. Consequently, our PBS could be used to split the TM- and TE-polarized modes with a high extinction ratio within an ultra wide wavelength range.

## 2. Numerical simulation

As shown in Fig. 1, we designed a PBS consisting of a HSWG with a width of  $w$  and a HPWG with a width of  $w_h$ . The HSWG is composed of a silica spacer with a thickness of  $h_{slot}$  and two silicon layers with a thickness of  $h_s$ . The HPWG is composed of a metal layer, a silica spacer, and a silicon layer with a thickness of  $h_m$ ,  $h_d$ , and  $h$ , respectively. The gap distance between the two waveguides is defined as  $d$ . The substrate of the PBS is assumed to be silica with a refractive index of 1.4500. Refractive index of silicon ( $n_{silicon}$ ) is 3.4764. Gold is chose to be the metal layer of the HPWG and its permittivity can be given by [29].

$$\epsilon_{Au}(\lambda) = \epsilon_{\infty} - \frac{1}{\lambda_p^2(1-\lambda^2+i/\lambda_p\lambda)} + \sum_{j=1,2} \frac{A_j}{\lambda_j} \left[ \frac{e^{i\phi_j}}{(1/\lambda_j-1/\lambda+i/\lambda_j)} + \frac{e^{-i\phi_j}}{(1/\lambda_j+1/\lambda-i/\lambda_j)} \right] \quad (1)$$

where the first and second terms are the contribution from the Drude model, and the third and fourth terms are the contribution from the interband transitions. The parameters in Eq. (1) are listed in Table 1. The default operation wavelength is 1550 nm.

Fig. 2 illustrates the calculated effective refractive indices ( $N_{eff}$ ) and propagation distances of the TM-polarized mode in the HPWG as a function of the HPWG width of  $w_h$ , where the propagation distance of the TM- and TE-polarized modes is defined as a distance over which the guided power drops to 1/e of its initial magnitude. As shown in Fig. 2(a) and (b), the effective index and the propagation length of the TE-polarized mode decreases and increases, respectively, with the decrease of  $w_h$ . It can be seen from that the TE-polarized mode is gradually coupled into the silica substrate with the decreases of  $w_h$  (Fig. 2(e)), while the TE-polarized mode is confined in the HPWG (Fig. 2(f)). Simulation results show that the TE-polarized mode is completely leaked into the silica substrate while  $w_h$  is less than 240 nm. In other words, the TE-polarized mode cut off in the HPWG with a width of less than 240 nm. On the other hand, as shown in Fig. 2(c) and (d), both the effective index and the propagation length of the TM-polarized mode decrease with the decrease of  $w_h$ . We also calculated the effective refractive indices and the propagation lengths of

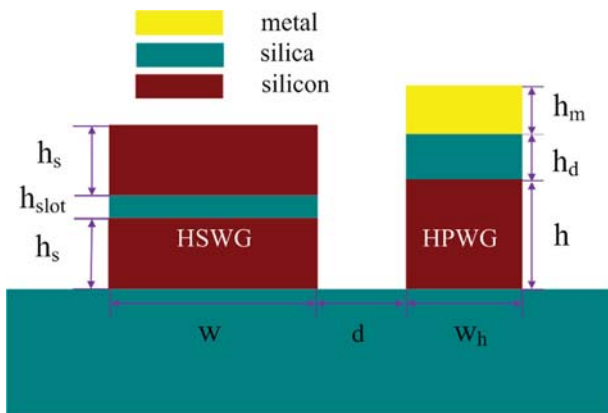


**Fig. 1.** Schematic diagram of the cross section of a proposed PBS consisting of a HSWG and a HPWG.

the TM- and TE-polarized modes in the HPWG with different silica spacer thicknesses,  $h_d$ , of 60, 80, and 100 nm in order to find an optimal silica spacer thickness of 80 nm, as described below.

As shown in Fig. 3(a), the refractive index differences between the TM- and TE-polarized modes in the HSWG with a silicon layer thickness of 150 nm and a silica layer thickness ( $h_s$ ) of 30, 45, and 50 nm are 0.568608, 0.592991 and 0.596920, respectively, at the wavelength of 1550 nm. As shown in Fig. 3(b), in case the silicon layer thickness is 200 nm, the refractive index differences above are decreased by 0.384813, 0.444664 and 0.459149, respectively. As a result, smaller silicon layer thickness and larger silica layer thickness are best except larger silica layer thickness may lead to higher order guided-modes.

Based on the above analysis, we improve the parameters of the desired PBS to be  $w=450$  nm,  $w_h=200$  nm,  $h_m=100$  nm,  $h_d=80$  nm,  $h_{slot}=36.5$  nm,  $h=250$  nm,  $h_s=150$  nm, and  $d=100$  nm. The parameters above will be used in all simulations below. We calculated the effective indices of the fundamental modes in a HSWG and a HPWG with the parameters above, as shown in Fig. 4. Obviously, only the TM-polarized mode can be supported in the HPWG. It can be easily found from Fig. 4 that the index difference between the TM-polarized modes of the two waveguides is very small in an ultra wide wavelength range from 1.45 μm to 1.65 μm. Therefore, the TM-polarized modes in the HSWG and the HPWG are index-matched in the wide wavelength range. On the other hand, the evanescent coupling of the TE-polarized light is entirely suppressed due to the cutoff of the TE-polarized mode in the HPWG.

The reason for choosing a HSWG, rather than a single silicon waveguide (SWG) could be described as follow. As shown in Fig. 5, although the HSWG and the SWG have the same index-matching point with the HPWG, each waveguide exhibits different index curves. And effective index difference of the TM-polarized modes between the SWG and the HPWG is quite larger than that between the HSWG and the HPWG. As a result, the coupling efficiency of the TM-polarized mode from the HSWG to the HPWG is much higher than that from the SWG to the HPWG [30]. So a HSWG, rather than a SWG, is integrated in our PBS.

Operation principle of our PBS could also be explained in terms of the supermode theory for the TM-polarized modes. In case each core of a coupler is a single-mode-guided waveguide, such a coupler structure can support two modes, including one odd mode and one even mode, and the coupling length,  $L$ , can be calculated by:

$$L_c^{TM} = \frac{\lambda}{2(n_e^{TM} - n_o^{TM})} \quad (2)$$

where  $n_e^{TM}$  and  $n_o^{TM}$  are the effective indices of the even and odd supermodes, respectively. Electric field distributions of the guided modes in the PBS with a gap distance of 100 nm were simulated by finite element method. As shown in Figs. 6(a) and (b), antisymmetric

**Table 1**  
Parameters used in Eq. (1) for gold.

Parameter (units)	Data of Johnson and Christy
$\epsilon_{\infty}$	1.54
$\lambda_p$ (nm)	143
$\gamma_p$ (nm)	14500
$A_1$	1.27
$\phi_1$ (rad)	$-\pi/4$
$\lambda_1$ (nm)	470
$\gamma_1$ (nm)	1900
$A_2$	1.4
$\phi_2$ (rad)	$-\pi/4$
$\lambda_2$ (nm)	325
$\gamma_2$ (nm)	1060

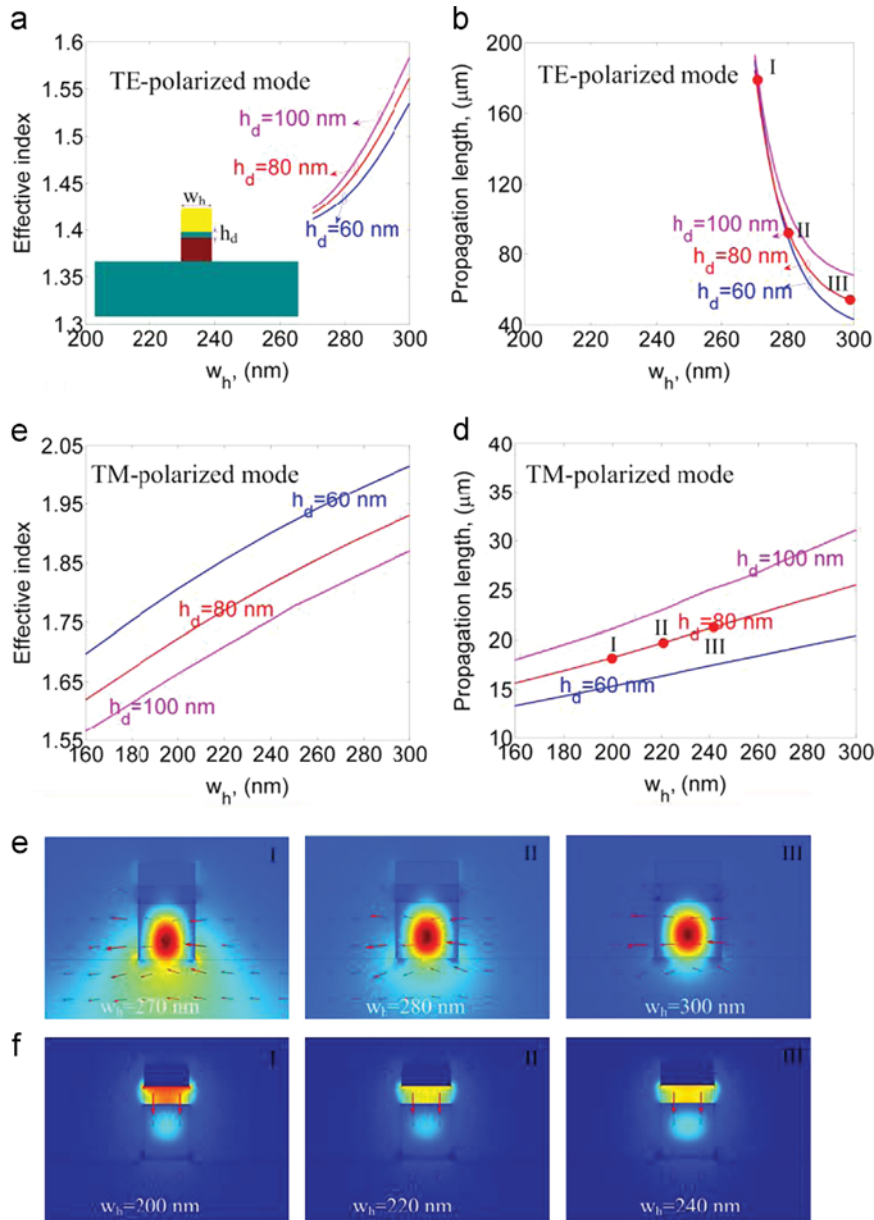


**Fig. 2.** (a) and (b) effective refractive index ( $N_{\text{eff}}$ ), and (c) and (d) propagation distance of the TM- and TE-polarized modes, respectively, as a function of the width,  $w_h$ , in the HPWG with different silica spacer thicknesses,  $h_d$ , of 60, 80, and 100 nm. Other parameters are  $h_m=100$  nm,  $h=250$  nm. Operation wavelength is 1550 nm. Fig. 2(e) and (f) illustrate mode filed profiles corresponding to different width,  $w_h$  in the case of  $h_d=80$  nm.

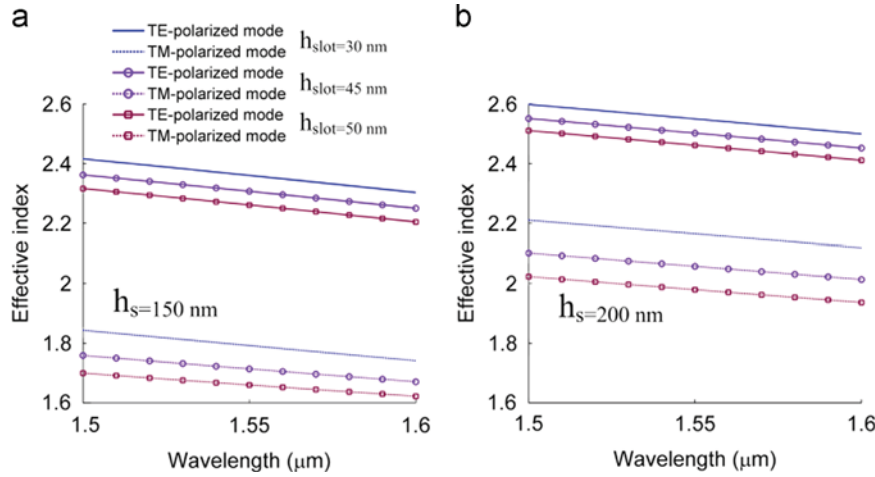
and symmetric TM-polarized supermodes can be simultaneously supported in the PBS. As shown in Fig. 6(c), whereas, only the TE-polarized supermode can be supported in the HPWG.

Fig. 7 illustrates the energy of the TM- and TE-polarized modes at the output end of the HSWG when light is launched at the input end of the HSWG. It can be found from the blue curve illustrated in Fig. 7 that the normalized optical intensity of the TM-polarized mode is periodically modulated in the HSWG. In case light transmits to a length of  $2.82 \mu\text{m}$ , the optical intensity is decreased to zero. That is, the TM- and TE-polarized modes can be completely separated. Such a length is the so-called coupling length of the TM-polarized modes. Although the metal employed will result in a transmission loss, the loss is very small in the PBS because such a device has a very short length of  $2.82 \mu\text{m}$ . Our simulation shows the metal-induced losses of the TE- and TM-polarized modes, are only 0.08 and 0.17 dB, respectively.

Extinction ratios of the TM- and TE-polarized modes, i.e.  $ER_{TM}$  and  $ER_{TE}$ , are defined as the energy ratio between the undesired

and the desired polarized mode at the output end of the HPWG and the HSWG, respectively. As shown in Fig. 8,  $ER_{TM}$  and  $ER_{TE}$  at the output end of the HPWG and the HSWG are up to  $-41$  dB and  $-33$  dB at the wavelength of 1550 nm, respectively. Moreover,  $ER_{TM}$  at the output end of the HPWG is more than  $-20$  dB within the wavelength range from 1490 to 1620 nm,  $ER_{TE}$  at the output end of the HSWG is more than  $-25$  dB at each wavelength. Therefore, the extinction ratios of both the TM- and TE-polarized modes are more than  $-20$  dB over an ultra-wide wavelength range of 130 nm.

The HPWG and the HSWG have different transmission loss. For example, the complex refractive indices of the even and odd supermodes are calculated as  $1.601073+0.004801i$  and  $1.875172+0.00256i$  at  $\lambda=1.55 \mu\text{m}$ , respectively. As a result, the propagation lengths are calculated via  $L_m=1/[2\text{Im}(\beta)]$  as  $25.6 \mu\text{m}$  and  $48.1 \mu\text{m}$ , respectively. Accordingly, the TM-polarized mode remained in the HPWG only undergo a litter transmission loss owing to the small size ( $2.82 \mu\text{m}$ ). Moreover, the transmission



**Fig. 3.** Effective index ( $N_{eff}$ ), corresponding to the TM- and TE-polarized modes, as a function of wavelength in the HSWG with a silicon layer thickness ( $h_s$ ) of (a) 150 nm and (b) 200 nm and different silica layer thickness ( $h_{slot}$ ) of 30, 45, 50 nm.

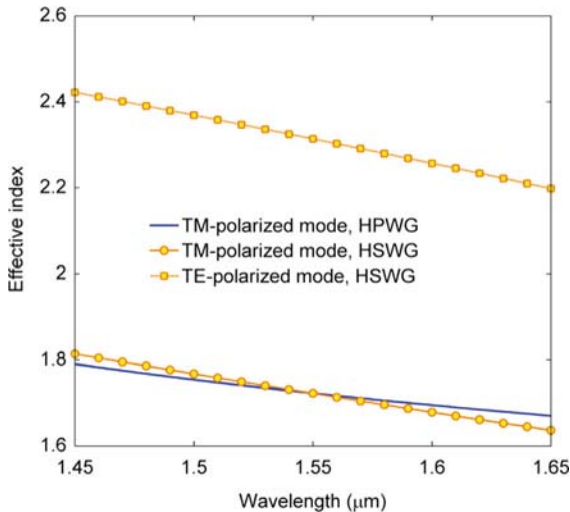


**Fig. 4.** Effective indices versus wavelength in the HSWG and the HPWG with improved parameters.

losses of the TE-polarized mode is nearly zero, and that of the TM-polarized mode is less than 0.5 dB within a wide wavelength from 1450 nm to 1650 nm, as shown in Fig. 8.

As well-known, the properties of an optical waveguide strongly depend on the device dimension and size. We calculated the extinction ratios of the TM- and TE-polarized modes at the wavelength of 1550 nm while the silica layer thickness of the HPWG ( $h_d$ ), the silicon layer thickness of the HSWG ( $h_s$ ), the width of the HSWG ( $w$ ) are changed by  $\Delta h_d$ ,  $\Delta h_s$ , and  $\Delta w$ , respectively. As shown in Fig. 9, a good extinction ratio (more than  $-20$  dB) of the TM-polarized mode can be achieved while the PBS has a size change of  $-25 \text{ nm} < \Delta h_d < 35 \text{ nm}$ ,  $-22 \text{ nm} < \Delta h_s < 30 \text{ nm}$ , or  $-21 \text{ nm} < \Delta w < 16 \text{ nm}$ . Therefore, our PBS has an excellent size tolerance.

We will couple light to/from our proposed PBS by means of the same method reported in Ref. [21]. The light can be coupled to/from a hybrid plasmonic waveguide to a standard single-mode fiber through grating couplers with an insert loss of 2.8 dB and 6.0 dB for TE and TM modes, respectively, as described in Ref. [21] in which the waveguide employed is similar to our PBS. The grating couplers are used not only for high-efficiency fiber-chip

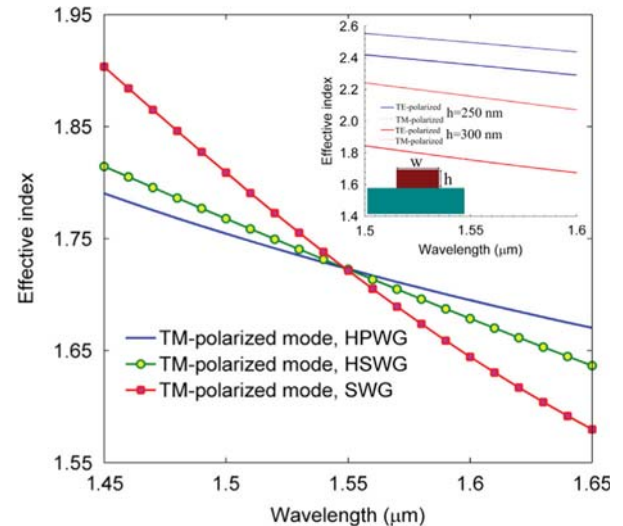


**Fig. 5.** Effective refractive indices,  $N_{eff}$ , versus wavelength in a SWG, a HSWG, and a HPWG. Inset shows  $N_{eff}$  of a SWG with a width of 450 nm versus wavelength.

coupling but also for the high extinction-ratio polarizer. Also it can be minimized through the improved coupling efficiency. Further investigation on the package for our PBS will done in the future.

In our previous publication [18], we presented a compact polarization beam splitter consisting of a horizontally slotted waveguide and a hybrid plasmonic waveguide. Such a splitter has a large difference between the effective indices of the TE-polarized modes in the two waveguides, while the effective index difference of the TM-polarized modes is quite small in a wide wavelength range. However, a coupling of the TE-polarized modes always happens between the two waveguides due to a litter weak phase matching so that the polarization splitter has a narrow bandwidth. Compared with the device reported in Ref. [18], we currently present an improved PBS configuration in which only the TM-polarized mode can be supported in the hybrid plasmonic waveguide. So the coupling of the TE-polarized modes cannot exist in the proposed PS. Furthermore, the effective index curves of the TM-polarized modes in the HSWG and the HPWG are improved to be very closely each other to achieve a phase-matching condition in a wide wavelength range. Consequently, the PBS has an

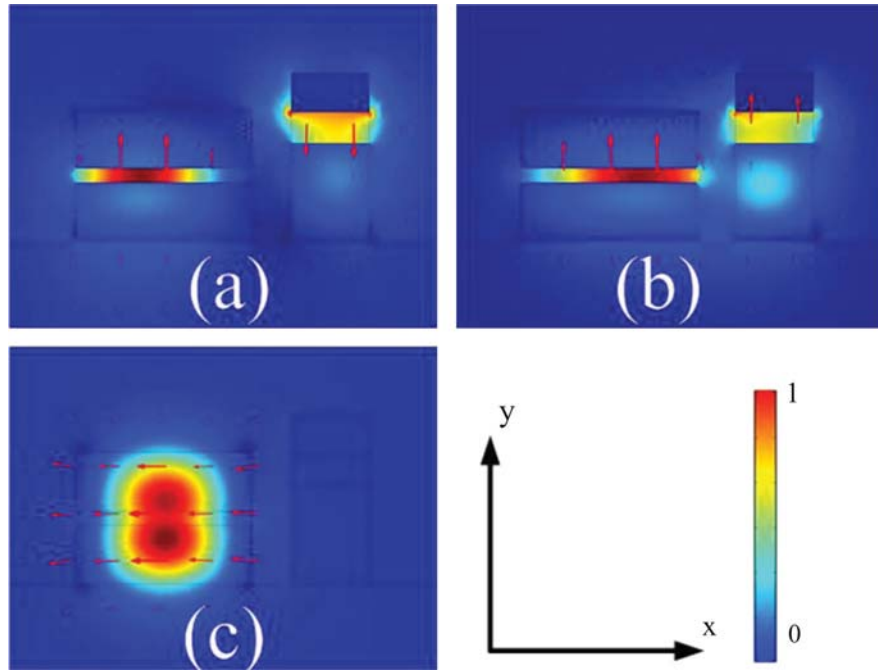


**Fig. 6.** Electric field profiles of (a) antisymmetric and (b) symmetric TM-polarized supermodes and (c) TE-polarized supermode at 1550 nm in the PBS.

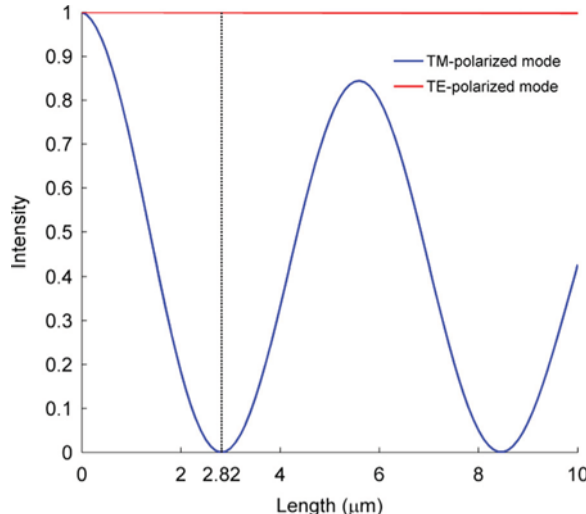


**Fig. 7.** The normalized optical intensities of the TM- and TE-polarized modes at the output end of the HSWG in case light is launched at the input end of the HSWG.

extinction ratio of more than  $-20$  dB within an ultrawide bandwidth of 130 nm. Moreover, the proposed PBS is an ultracompact device with a short coupling length of  $2.82 \mu\text{m}$ .

### 3. Discussion

#### 3.1. The effect of bending waveguides

We have designed an output waveguide (a sharply bent HSWG) at the end of the coupling region to stop coupling light back. The bending radius ( $R$ ) depends on the waveguide design and its bending loss. The length of the coupling region usually needed to be reduced to compensate the extra coupling in the beginning section of the bending region. The performance of our PBS was

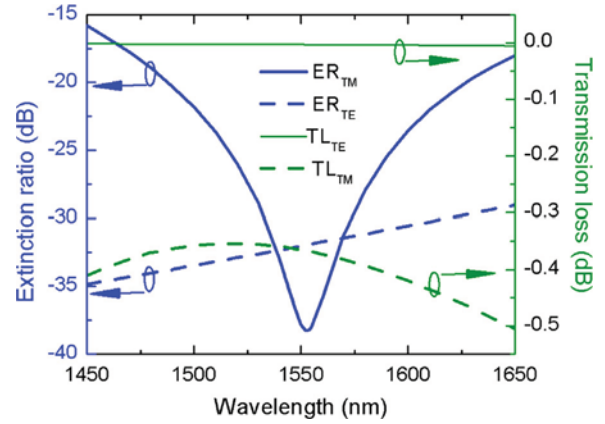


**Fig. 8.** Extinction ratios and transmission loss of the TM- and TE-polarized modes versus wavelength at the output end of the HPWG and the HSWG, respectively.

investigated by means of three dimensional finite-difference-time-domain (3D-FDTD) simulation [31]. The computational region is uniformly meshed in each direction and surrounded by the Perfectly Matched Layer boundary conditions. Figs. 10(a) and (b) show the simulated light propagation in the designed PBS with  $R=1.3 \mu\text{m}$  and  $L_c=2.6 \mu\text{m}$  for TE-polarized and TM-polarized modes at the wavelength of 1550 nm, respectively. The grid sizes are chosen as  $\Delta x=15 \text{ nm}$ ,  $\Delta y=8 \text{ nm}$ , and  $\Delta z=20 \text{ nm}$ . It can be seen from Fig. 10 that the TM-polarized light couples efficiently from the HSWG to the HPWG, while the TE-polarized light fully transmits in the HSWG.

#### 3.2. Device fabrication

The designed splitter was fabricated together with other photonic and plasmonic devices on SOI wafers with top-Si and buried oxide. The reference [21] schematically described some key steps of fabrication flow. Providing these layer thicknesses are the

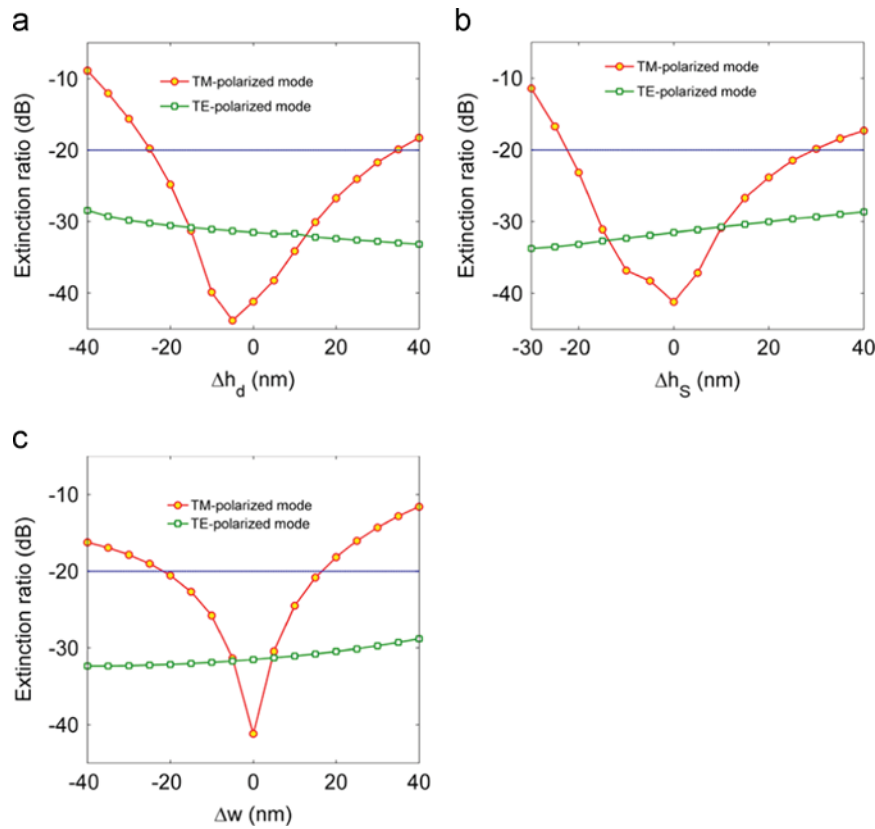


Fig. 9. Size tolerance of the designed device with variations (a)  $\Delta h_d$ , (b)  $\Delta h_s$ , and (c)  $\Delta w$ .

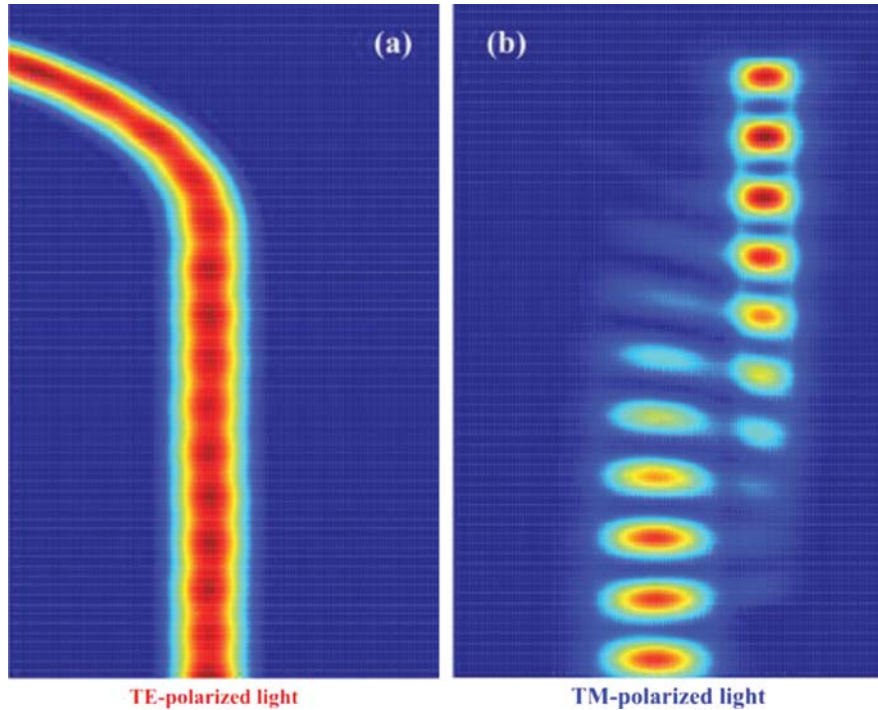


Fig. 10. FDTD propagation field profiles of the (a) TE- and (b) TM-polarized modes.

same, the device can be fabricated with less difficulty. But only the widths of the HSWG and the HPWG could be changed/improved so that such a device is with less flexibility and cannot realize the desired functions. Hence, our device has two different lower silicon ( $h$ ,  $h_s$ ) and silica layers ( $h_{slot}$ ,  $h_d$ ). However, we can further optimize the structure and make it be compatible.

#### 4. Conclusion

We designed an ultracompact silicon-based PBS consisting of a horizontally slotted waveguide and a hybrid plasmonic waveguide. By the optimized procedure, the TM-polarized states of the HSWG and HPWG are index-matched in a wide wavelength range. On the

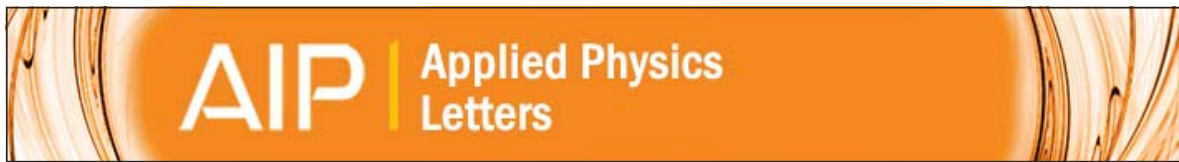
other hand, the evanescent coupling is significantly suppressed due to the fact that the TE-polarized state cannot be supported in the HPWG. In particular, our improved PBS has a very short coupling length of 2.82 μm and the extinction ratios of both the TM- and TE-polarized modes are more than –20 dB over a wide wavelength range of 130 nm.

## Acknowledgments

This work was supported by the National Science Foundation of China (Grant no. 11174064, Grant no. 61377090, and Grant no. 61308027), the Science & Technology Innovation Commission of Shenzhen (Grant no. KQCX 20120815161 444632, and Grant no. JCYJ20130329140017262), and the Distinguished Professors Funding from Shenzhen University and Guangdong Province Pearl River Scholars.

## References

- [1] J.M. Hong, H.H. Ryu, S.R. Park, J.W. Jeong, S.G. Lee, E.-H. Lee, et al., Photon. Technol. Lett. IEEE 15 (2003) 72.
- [2] A. Katigbak, J.F. Strother, J. Lin, Opt. Eng. 48 (2009) 080503.
- [3] B.-K. Yang, S.-Y. Shin, D. Zhang, Photon. Technol. Lett. IEEE 21 (2009) 432.
- [4] T. Liang, H. Tsang, Photon. Technol. Lett. IEEE 17 (2005) 393.
- [5] L. Augustin, R. Hanfouq, J. van der Tol, W. de Laat, M. Smit, Photon. Technol. Lett. IEEE 19 (2007) 1286.
- [6] D. Dai, Z. Wang, J. Peters, J. Bowers, Photon. Technol. Lett. IEEE (2011) 1.
- [7] Y. Shi, D. Dai, S. He, Photon. Technol. Lett. IEEE 19 (2007) 825.
- [8] X. Ao, L. Liu, L. Wosinski, S. He, Appl. Phys. Lett. 89 (2006) 171115.
- [9] I. Kiyat, A. Aydinli, N. Dagli, Photon. Technol. Lett. IEEE 17 (2005) 100.
- [10] X. Tu, S.S.N. Ang, A.B. Chew, J. Teng, T. Mei, Photon. Technol. Lett. IEEE 22 (2010) 1324.
- [11] Y. Yue, L. Zhang, J.Y. Yang, R.G. Beausoleil, A.E. Willner, Opt. Lett. 35 (2010) 1364.
- [12] K. Saitoh, M. Koshiba, Opt. Express 17 (2009) 19225.
- [13] S. Lin, J. Hu, K.B. Crozier, Appl. Phys. Lett. 98 (2011) 151101.
- [14] D. Dai, Z. Wang, J.E. Bowers, Opt. Lett. 36 (2011) 2590.
- [15] H. Zhang, Y. Huang, S. Das, C. Li, M. Yu, P.G.-Q. Lo, et al., Opt. Express 21 (2013) 3363.
- [16] J. Wang, J. Xiao, X. Sun, J. Opt. 15 (2013) 035501.
- [17] Q. Li, Y. Song, G. Zhou, Y. Su, M. Qiu, Opt. Lett. 35 (2010) 3153.
- [18] B. Sun, M.-Y. Chen, Y.-K. Zhang, J. Zhou, Appl. Phys. B 113 (2013) 179.
- [19] L. Gao, F. Hu, X. Wang, L. Tang, Z. Zhou, Appl. Phys. B 113 (2013) 199.
- [20] F. Lou, D. Dai, L. Wosinski, Opt. Lett. 37 (2012) 3372.
- [21] J. Chee, S. Zhu, G. Lo, Opt. Express 20 (2012) 25345.
- [22] X. Guan, H. Wu, Y. Shi, L. Wosinski, D. Dai, Opt. Lett. 38 (2013) 3005.
- [23] D.K. Gramotnev, S.I. Bozhevolnyi, Nat. Photon. 4 (2010) 83.
- [24] R.F. Oulton, V.J. Sorger, D. Genov, D. Pile, X. Zhang, Nat. Photon. 2 (2008) 496.
- [25] D. Dai, S. He, Opt. Express 17 (2009) 16646.
- [26] M. Wu, Z. Han, V. Van, Opt. Express 18 (2010) 11728.
- [27] L. Gao, L. Tang, F. Hu, R. Guo, X. Wang, Z. Zhou, Opt. Express 20 (2012) 11487.
- [28] M.Z. Alam, J.S. Aitchison, M. Mojahedi, IEEE J. Sel. Top. Quantum Electron. 19 (2013) 4602008.
- [29] P.G. Etchegoin, E.C.L. Ru, M. Meyer, J. Chem. Phys. 125 (2006) 164705.
- [30] B. Sun, M.-Y. Chen, Y.-K. Zhang, J.-C. Yang, J.-Q. Yao, H.-X. Cui, Opt. Express 19 (2011) 4091.
- [31] G. Seniutinas, L. Rosa, G. Gervinskas, E. Brasselet, S. Juodkazis, Beilstein J. Nanotechnol. 4 (2013) 534.



## Highly birefringent suspended-core photonic microcells for refractive-index sensing

Chao Wang, Wa Jin, Changrui Liao, Jun Ma, Wei Jin, Fan Yang, Hoi Lut Ho, and Yiping Wang

Citation: *Applied Physics Letters* **105**, 061105 (2014); doi: 10.1063/1.4892962

View online: <http://dx.doi.org/10.1063/1.4892962>

View Table of Contents: <http://scitation.aip.org/content/aip/journal/apl/105/6?ver=pdfcov>

Published by the AIP Publishing

---

### Articles you may be interested in

**Behavior of a hollow core photonic crystal fiber under high radial pressure for downhole application**  
Appl. Phys. Lett. **104**, 071910 (2014); 10.1063/1.4866334

**Microfluidic refractive-index sensors based on small-hole microstructured optical fiber Bragg gratings**  
Appl. Phys. Lett. **98**, 221109 (2011); 10.1063/1.3597623

**Birefringent solid-core photonic bandgap fibers assisted by interstitial air holes**  
Appl. Phys. Lett. **94**, 131102 (2009); 10.1063/1.3104856

**Quantitative broadband chemical sensing in air-suspended solid-core fibers**  
J. Appl. Phys. **103**, 103108 (2008); 10.1063/1.2924408

**Extruded single-mode high-index-core one-dimensional microstructured optical fiber with high index-contrast for highly nonlinear optical devices**  
Appl. Phys. Lett. **87**, 081110 (2005); 10.1063/1.2034094

---

An advertisement for Asylum Research Cypher™ AFMs. The top half features a stylized film strip with a purple and yellow textured surface. The text reads: "Not all AFMs are created equal", "Asylum Research Cypher™ AFMs", and "There's no other AFM like Cypher". The bottom half has a blue background with the website "www.AsylumResearch.com/NoOtherAFMLikeIt" and the Oxford Instruments logo, which includes the text "OXFORD INSTRUMENTS" and "The Business of Science".

# Highly birefringent suspended-core photonic microcells for refractive-index sensing

Chao Wang,<sup>1,2</sup> Wa Jin,<sup>1</sup> Changrui Liao,<sup>3</sup> Jun Ma,<sup>1</sup> Wei Jin,<sup>1,a)</sup> Fan Yang,<sup>1</sup> Hoi Lut Ho,<sup>1</sup> and Yiping Wang<sup>3</sup>

<sup>1</sup>Department of Electrical Engineering, The Hong Kong Polytechnic University, Hong Kong, China

<sup>2</sup>The Hong Kong Polytechnic University Shenzhen Research Institute, Shenzhen 518057, China

<sup>3</sup>Key Laboratory of Optoelectronic Devices and Systems of Ministry of Education/Guangdong Province, Shenzhen University, Shenzhen 518060, China

(Received 18 June 2014; accepted 1 August 2014; published online 12 August 2014)

An in-line photonic microcell with a highly birefringent suspended microfiber core is fabricated by locally heating and pressurizing selected air-holes of an endless single mode photonic crystal fiber. The microfiber core has rhombus-like cross-sectional geometry and could achieve a high birefringence of up to  $10^{-2}$ . The microfiber core is fixed at the center of the microcell by thin struts attached to an outer jacket tube, which protects and isolates the microfiber from environmental contaminations. Highly sensitive and robust refractive index sensors based on such microcells are experimentally demonstrated. © 2014 AIP Publishing LLC. [<http://dx.doi.org/10.1063/1.4892962>]

Optical microfibers with two-fold geometric symmetry have attracted considerable interests recently. These microfibers possess the properties of conventional circular-shaped microfiber such as strong evanescent field, tight optical confinement, small size and light weight,<sup>1</sup> and at the same time exhibit high birefringence, which would enable useful applications such as highly sensitive refractive-index (RI) sensors,<sup>2,3</sup> optical wavelength filters,<sup>3,4</sup> birefringent fiber coil resonator,<sup>5</sup> and polarization converters.<sup>6</sup>

The birefringence of a microfiber is affected by the geometric aspect ratio, the size of microfiber, and the RI contrast between the core and cladding. For a microfiber with air-cladding, the birefringence gets higher with larger aspect ratio and approaches a maximum value when the cross-sectional dimension is about the wavelength-scale.<sup>7</sup> So far, highly birefringent (Hi-Bi) microfibers have been fabricated by tapering non-cylindrical fibers such as rectangular fiber<sup>7,8</sup> and D-fiber<sup>9</sup> or by etching cylindrical fibers with traveling micro-droplets of hydrofluoric acid.<sup>10</sup>

In this Letter, we report Hi-Bi microfiber with a rhombus-like cross-sectional shape. As illustrated in Fig. 1, the microfiber is housed inside a photonic microcell made by locally inflating selected air-holes<sup>11</sup> of a photonic crystal fiber (PCF). The two ends of the microfiber are automatically and adiabatically connected PCF pigtails from which the microcell is fabricated. The expanded holes are sufficiently large to prevent leakage of the evanescent field, while the jacket tube protects the microfiber from external contaminations and makes the device much more robust as compared with a bare air-clad microfiber. The air-region between the jacket and the microfiber provides a contamination-free platform for light-matter interaction through the evanescent field of an optical mode propagating in the suspended micro fiber core.

The fabrication of the photonic microcell follows a three-step process: At first, four air-holes at one end of the

PCF, as illustrated in Fig. 2(a), are selectively opened by use of a femtosecond laser-assisted selective opening technique.<sup>12</sup> The other end of the PCF is spliced to a single mode fiber (SMF) to seal all the air-holes at this end. Second, high pressure gas is applied to the four selected air-columns of the PCF via the openings. Gas pressures in other air-columns remain at atmospheric pressure. Finally, the pressurized air-columns are locally inflated via a heating/tapering process.<sup>11</sup> During this process, the pressurized columns expand while other columns collapse gradually and eventually the central core is isolated from other part of the fiber by a large air region, with extremely thin struts which support the core.

The micrographs of a typical microcell at the suspended core region and the transition region are given in Figs. 2(b) and 2(c), respectively. The rhombus-like core (microfiber) is supported by four struts connected to the outer jacket tube and the thicknesses of the struts are thinner than 300 nm. The microfiber geometry is formed as the result of asymmetric stretching of the struts that have different thicknesses and has a high aspect ratio of  $\sim 2$ , exhibiting high birefringence. To minimize the loss occurring in transition, the struts with sub-wavelength width should be formed before the unpressurized air-holes are completely collapsed. This is done by controlling the gas pressure so that the expansion rate of selected air-holes is much faster than the collapsing rate of the remaining air-holes. However, if the applied pressure is

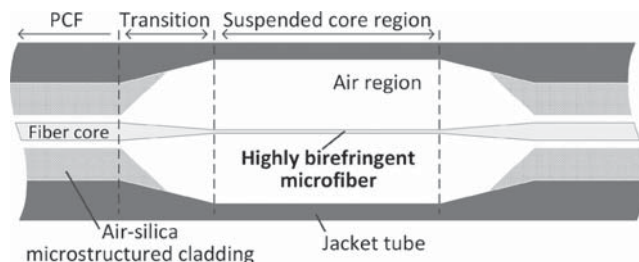
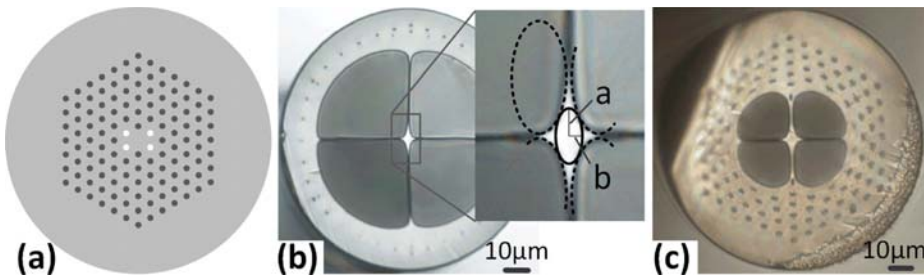


FIG. 1. Schematic of a photonic microcell with a suspended highly birefringent microfiber core.

<sup>a)</sup>Email: eewjin@polyu.edu.hk



too high, controlling of the expansion would become difficult, especially when the wall-thickness of the jacket tube becomes thin and high gas pressure would blow up the microcell very quickly. In our experiments, gas pressures in the range from 6 to 9 bars were used, and the insertion loss of the microcell in the wavelength range from 1250 to 1650 nm is  $\sim 0.2$  dB.

The cross-sectional shape of the microfiber core may be modeled approximately by an ellipse with a long to short axis ratio of  $a/b = 2$ , as indicated in the inset of Fig. 2(b). The four curved sides of the microfiber are parts of four identical ellipses with long/short axis ratio of 2, and the minimum horizontal and vertical separations between ellipses, which correspond to the thicknesses of the struts, are set to be one-twentieth of the short and long axes, respectively. Based on this model, we numerically calculated the phase birefringence  $B(\lambda) = |n_x(\lambda) - n_y(\lambda)|$  by use of the COMSOL software. Here,  $n_x$  and  $n_y$  represent, respectively, the effective RI of the two polarization states of the fundamental HE<sub>11</sub> mode. The calculated results are shown in Fig. 3.

In air, the Hi-Bi microfiber exhibits a theoretical maximal birefringence  $B_{\max}$  of  $\sim 3.5 \times 10^{-2}$  when the normalized core radius  $r_N = r_{eq}/\lambda$  is around 0.257, where  $\lambda$  is the operation wavelength and the equivalent radius  $r_{eq}$  is defined as  $(a-b)^{1/2}$ . At  $\lambda = 1550$  nm, the largest birefringence  $B_{\max}$  would be obtained when the radius  $r_{eq}$  is  $\sim 400$  nm. The birefringence decreases with increasing ambient RI around the microfiber, as shown in Fig. 3(a). The peak birefringence  $B_{\max}$  and the corresponding normalized core radius ( $r_N$ ) as functions of  $n_{amb}$  are shown in Fig. 3(b). Based on the results in Fig. 3(a), the group birefringence  $G$  was calculated by using  $G = B - \lambda \cdot (dB/d\lambda)$  and shown in Fig. 3(c). The maximum theoretical group birefringence  $G_{\max}$  reaches  $\sim 8.2 \times 10^{-2}$  at  $r_N \approx 0.19$  for  $n_{amb} = 1$ .

The group birefringence of the Hi-Bi microfiber was measured by use of a Sagnac loop interferometer (SLI) illustrated in Fig. 4(a). The loop coupler is a 3-dB coupler and multiple side-holes were drilled on the outer-jacket of the microcell for liquid and gas filling. A polarization controller (PC) was used in the loop to maximize the fringe contrast. Fig. 4(b) shows the measured transmission spectra of a photonic microcell with a rhombus-like microfiber core when the cell is filled with air and a RI liquid with  $n = 1.3$ . The length and the radius of the microfiber are, respectively,  $L \approx 1$  cm and  $r_{eq} \approx 1.6 \mu\text{m}$ . Interference fringes were observed and the fringe spacing is related to the group birefringence ( $G$ ) and length ( $L$ ) of the microfiber by  $\Delta\lambda \approx |\lambda^2/G \cdot L|^{1/3}$ .

At the wavelength of  $\sim 1550$  nm,  $G$  value of the microfiber in air was determined to be  $\sim 4.8 \times 10^{-3}$  and  $\sim 1.5 \times 10^{-3}$  when the microcell is filled with the RI liquid. These results are in agreement with the simulation results in Fig. 3(c).

By monitoring the wavelength at one of the fringe dips as shown in Fig. 4(b), the Hi-Bi microfiber microcell may be used as a sensor to measure the RI of the surrounding material. The sensitivity ( $S$ ) may be expressed as  $S = d\lambda / dn_{amb} = (\lambda/G) \cdot (dB/dn_{amb})$ .<sup>2</sup> Due to the existence of  $G=0$  point (refer to Fig. 3(c)), the sensitivity around the sign reversing point could be significantly increased. The black and blue lines in Fig. 4(c) are, respectively, the calculated sensitivity and fringe space around the wavelength of 1550 nm as functions of microfiber radius ( $r_{eq}$ ) and ambient RI ( $n_{amb}$ ). The fringe space is defined as the wavelength separation between adjacent attenuation dips. For a larger  $n_{amb}$  value, the higher sensitivity region becomes broader and shifts toward larger  $r_{eq}$  values. This would allow high sensitivity RI sensors with relatively larger and practical sized

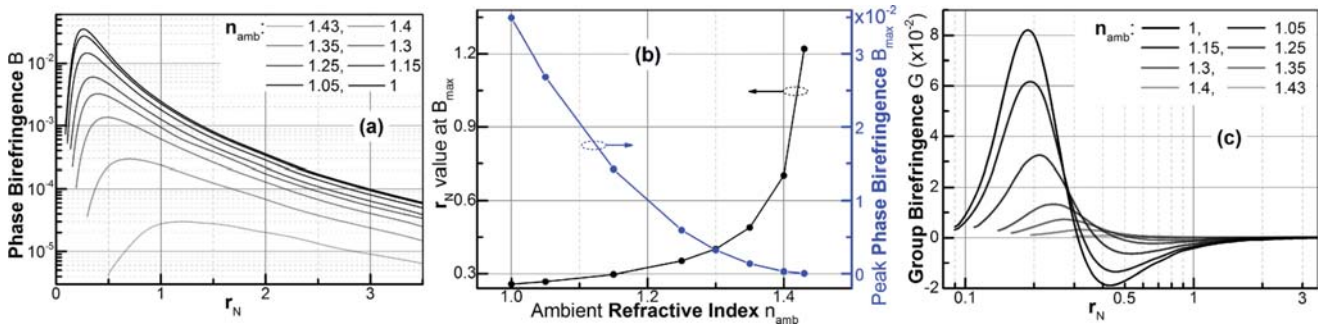


FIG. 3. (a) Calculated phase birefringence of the highly birefringent microfiber as a function of normalized core radius  $r_N$  (defined as  $(a-b)^{1/2}/\lambda$ ), for different ambient refractive index ( $n_{amb}$ ). (b) Shift of birefringence peak with ambient refractive index. (c) Calculated group birefringence as a function of normalized core radius.

FIG. 2. (a) Schematic of photonic crystal fiber endface with four air-holes (labeled as white circles) opened for pressurization while all other air-holes are sealed. Cross-sectional micrographs of a photonic microcell with a highly birefringent (Hi-Bi) microfiber core at (b) the suspended core region and (c) the transition region. Inset of (b): model of Hi-Bi microfiber used for theoretical calculation.

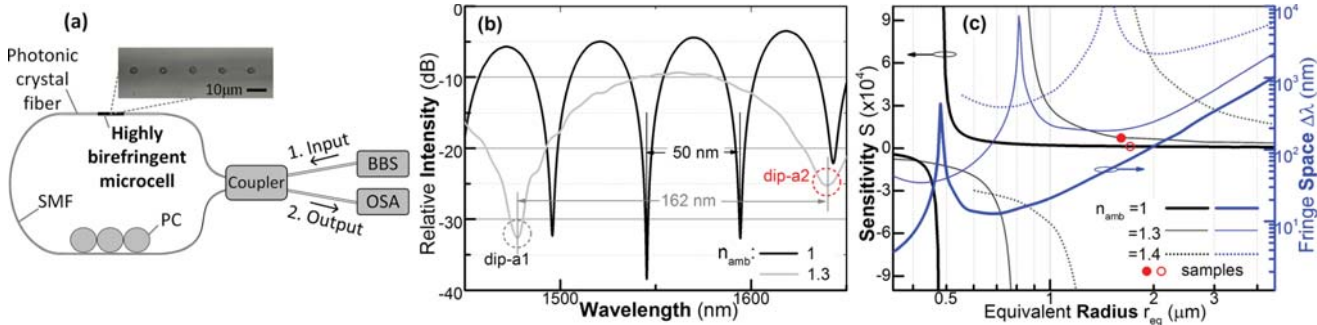


FIG. 4. (a) Experimental setup of the Sagnac loop interferometer. Inset: micrograph of the through-holes on the jacket tube of the highly birefringent (Hi-Bi) microcell. SMF: single mode fiber; PC: polarization controller; BBS: broad band source; and OSA: optical spectrum analyzer. (b) Measured transmission spectra of a Hi-Bi microfiber with ambient refractive index  $n_{\text{amb}} = 1$  (black) and 1.3 (gray). (c) Calculated refractive index sensitivity (black) and fringe space (blue) around the wavelength of 1550 nm with different  $n_{\text{amb}}$ . Red dots represent samples made in experiments for refractive index sensing.

microfibers. However, the fringe space ( $\Delta\lambda$ ) also increases with ambient RI and hence would require a longer length of microfiber to ensure at least one fringe dip is located in the operating wavelength range of the source.

The innate chambers around the Hi-Bi microfiber provide a compact and isolated space for confining small volume of sample materials and for exploiting light-matter interaction via evanescent field of the microfiber. The filling and emptying of the chambers can be achieved by the micro-channels fabricated on the jacket tube. The inset of Fig. 4(a) shows the micro-channels fabricated on the microcell by use of a femtosecond infrared laser micromachining system. As examples of potential applications, the Hi-Bi microcell which is RI-sensitive was tested for temperature and gas pressure measurement by use of the SLI set up shown in Fig. 4(a).

Temperature measurements were carried out with a liquid-filled Hi-Bi microcell with its spectra shown in Fig. 4(b). The RI liquid used was made by R. P. Cargille Lab., Inc., and has a RI of  $n = 1.3$  at room temperature and a thermo-optic coefficient  $d\eta/dT = -3.34 \times 10^{-4}/^\circ\text{C}$ . The liquid-filled sample was placed in a column oven (ECOMLCO-102) and tested from 25 to 95 °C. The wavelengths of the dips change linearly as shown in Fig. 5(a) and the dip-a2, which was always present within the wavelength range from 1450 to 1650 nm, exhibited a high temperature sensitivity of  $\sim 3 \text{ nm}/^{\circ}\text{C}$ , corresponding to a RI sensitivity of  $\sim 9.1 \times 10^3 \text{ nm/RIU}$ . This RI sensitivity is shown as the red dot in Fig. 4(c) and agrees well with the theoretical prediction.

Measurement of gas pressure was carried out with a similar Hi-Bi microcell. The fringe spectrum of this microcell was also measured with the SLI and shown in the inset of Fig. 5(b). Eight through-holes with diameter of 3–5 μm are drilled on the microcell's jacket tube and on each strut to equalize gas pressure inside and outside the microcell. Then, the microcell was sealed inside a gas chamber made of a glass tube with bore size of  $\sim 600 \mu\text{m}$ , which was connected to a high pressure nitrogen gas cylinder via a T-tube. Pressurizing the gas within the gas chamber changes the RI of the gas<sup>14</sup> and results in a change in the birefringence of the microfiber. The responses of the dip wavelengths to pressure from 1 bar to 9 bars are shown in Fig. 5(b). The pressure sensitivity of the microcell is  $\sim 300 \text{ pm/bars}$ , corresponding to a RI sensitivity of  $\sim 1.5 \times 10^3 \text{ nm/RIU}$ . The RI sensitivity is also shown in Fig. 4(c) as the un-filled circle and agrees with the theoretical prediction. It would be possible to improve the RI sensitivity by further optimizing the dimensions of the Hi-Bi microfiber to make it closer to the maximum sensitivity point.

It should be pointed out that the Hi-Bi microcell is composed of pure silica which has a low thermo-optic coefficient<sup>15</sup> and the effect of temperature-induced silica RI change would have very little effect on the measurement results in Fig. 5. To verify this, we tested the temperature response of a microcell sample without material filling. The microcell was first annealed at 1000 °C for 5 h and then tested from 25 to 1000 °C. As shown in Fig. 5(c), the dip wavelength responded linearly to temperature with a very low temperature sensitivity of 3.5 pm/°C.

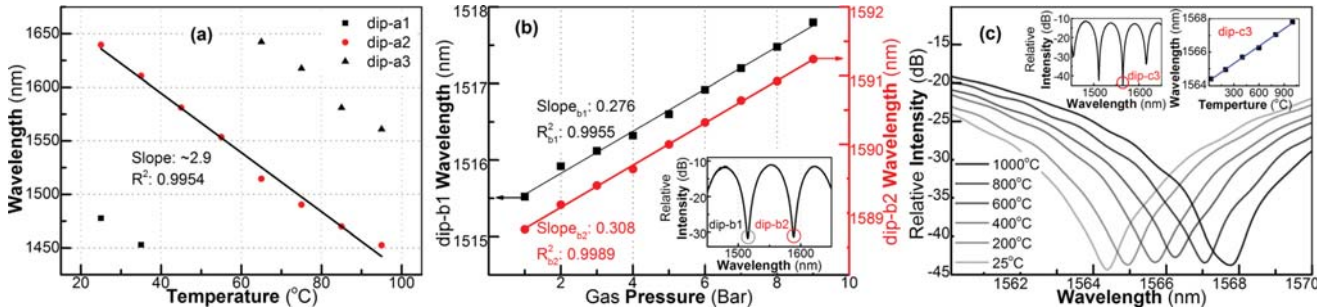


FIG. 5. (a) Measured temperature response of a highly birefringent (Hi-Bi) microcell filled with a refractive index liquid of  $n = 1.3$ . (b) Measured gas pressure response of a Hi-Bi microcell filled with nitrogen gas. (c) Measured temperature response of a Hi-Bi microcell without material filling (up to 1000 °C).

As compared with traditional prism-based RI sensors, optical-fiber RI sensors offer the advantages of compactness, remote detection capability, and operation in harsh environment. Different optical fiber sensors such as fiber gratings,<sup>16,17</sup> in-fiber cavity,<sup>18</sup> multimode interferometer,<sup>19</sup> and four-wave mixing<sup>20</sup> have been reported; the Hi-Bi microfiber-based sensors have demonstrated competitively high RI sensitivity ( $\sim 10^4 \text{ nm/RIU}$ ) with additional advantage of low temperature cross-sensitivity ( $\sim 10^{-7} \text{ RIU/}^\circ\text{C}$ ). However, the bare microfiber-based devices are vulnerable to contamination<sup>21</sup> and not easy to handle. The current microcell technology provides a way for embedding a Hi-Bi microfiber within an enclosed compartment and overcomes the problems associated with the use of optical microfibers. Furthermore, the tiny in-fiber cavity surrounding the microfiber provides a good platform for strong light-matter interaction in a reduced space-scale, which would be useful for nanoliter-volume spectroscopy<sup>22</sup> and bio-chemistry sensing.<sup>23</sup>

In conclusion, a Hi-Bi rhombus-like-shaped microfiber was fabricated and examined theoretically and experimentally. The microfiber is embedded inside a jacket tube to form a photonic microcell and adiabatically connects to PCF pigtailed at both ends. The birefringence of such microfiber could reach up to the order of  $10^{-2}$  and exhibits high sensitivity to ambient RI and low sensitivity to temperature. Such photonic microcells are compact and robust, have low loss, and are ideal platforms for sensors and functionalized in-fiber devices. Based on such microcells, RI, temperature, and gas pressure sensors are experimentally demonstrated, and the RI sensitivity is  $\sim 10^4 \text{ nm/RIU}$  around  $n = 1.3$ .

This work was supported by the Natural Science Fundament of China (Grant No. 61290313) and the Hong Kong Polytechnic University (Grant No. G-YK62).

- <sup>1</sup>L. Tong, F. Zi, X. Guo, and J. Lou, *Opt. Commun.* **285**(23), 4641 (2012).
- <sup>2</sup>J. Li, L.-P. Sun, S. Gao, Z. Quan, Y.-L. Chang, Y. Ran, L. Jin, and B.-O. Guan, *Opt. Lett.* **36**(18), 3593 (2011).
- <sup>3</sup>W. Jin, C. Wang, H. Xuan, and W. Jin, *Opt. Lett.* **38**(21), 4227 (2013).
- <sup>4</sup>W. Jin, H. Xuan, and W. Jin, *Opt. Lett.* **39**(12), 3363 (2014).
- <sup>5</sup>T. Lee, N. G. R. Broderick, and G. Brambilla, *Opt. Commun.* **284**(7), 1837 (2011).
- <sup>6</sup>H. Xuan, J. Ma, W. Jin, and W. Jin, *Opt. Express* **22**(3), 3648 (2014).
- <sup>7</sup>H. F. Xuan, J. Ju, and W. Jin, *Opt. Express* **18**(4), 3828 (2010).
- <sup>8</sup>Y. Jung, G. Brambilla, K. Oh, and D. J. Richardson, *Opt. Lett.* **35**(3), 378 (2010).
- <sup>9</sup>F. Beltrán-Mejía, J. H. Osório, C. R. Biazoli, and C. M. B. Cordeiro, *J. Lightwave Technol.* **31**(16), 2756 (2013).
- <sup>10</sup>J. C. Mikkelsen and J. K. S. Poon, *Opt. Lett.* **37**(13), 2601 (2012).
- <sup>11</sup>C. Wang, W. Jin, J. Ma, Y. Wang, H. Lut Ho, and X. Shi, *Opt. Lett.* **38**(11), 1881 (2013).
- <sup>12</sup>J. Ju, H. Feng Xuan, W. Jin, S. Liu, and H. Lut Ho, *Opt. Lett.* **35**(23), 3886 (2010).
- <sup>13</sup>M. Antkowiak, R. Kotynski, T. Nasilowski, P. Lesiak, J. Wojcik, W. Urbanczyk, F. Berghmans, and H. Thienpont, *J. Opt. A: Pure Appl. Opt.* **7**(12), 763 (2005).
- <sup>14</sup>E. R. Peck and B. N. Khanna, *J. Opt. Soc. Am.* **56**(8), 1059 (1966).
- <sup>15</sup>M. J. Weber, *Handbook of Optical Materials* (CRC Press LLC, 2002).
- <sup>16</sup>W. Liang, Y. Huang, Y. Xu, R. K. Lee, and A. Yariv, *Appl. Phys. Lett.* **86**(15), 151122 (2005).
- <sup>17</sup>L. Rindorf and O. Bang, *Opt. Lett.* **33**(6), 563 (2008).
- <sup>18</sup>C. R. Liao, T. Y. Hu, and D. N. Wang, *Opt. Express* **20**(20), 22813 (2012).
- <sup>19</sup>C. Li, S.-J. Qiu, Y. Chen, F. Xu, and Y.-Q. Lu, *IEEE Photonics Technol. Lett.* **24**(19), 1771 (2012).
- <sup>20</sup>M. H. Frosz, A. Stefani, and O. Bang, *Opt. Express* **19**(11), 10471 (2011).
- <sup>21</sup>M. Fujiwara, K. Toubaru, and S. Takeuchi, *Opt. Express* **19**(9), 8596 (2011).
- <sup>22</sup>Y. Cao, W. Jin, L. Hoi Ho, and Z. Liu, *Opt. Lett.* **37**(2), 214 (2012).
- <sup>23</sup>S. Heng, M.-C. Nguyen, R. Kostecki, T. M. Monro, and A. D. Abell, *RSC Adv.* **3**, 8308 (2013).

# Polarization-locked vector solitons in a mode-locked fiber laser using polarization-sensitive few-layer graphene deposited D-shaped fiber saturable absorber

Tao Chen,<sup>1,2,3</sup> Changrui Liao,<sup>2,4</sup> D. N. Wang,<sup>1,2,5,\*</sup> and Yiping Wang<sup>4</sup>

<sup>1</sup>College of Optical and Electronic Technology, China Jiliang University, Hangzhou, China

<sup>2</sup>Department of Electrical Engineering, The Hong Kong Polytechnic University, Hong Kong, China

<sup>3</sup>School of Physics and Technology, University of Jinan, Jinan, Shandong 250022, China

<sup>4</sup>College of Optoelectronic Engineering, Shenzhen University, Shenzhen, Guangdong 518060, China

<sup>5</sup>School of Electrical, Electronic and Information Engineering, Hubei Polytechnic University, Huangshi, China

\*Corresponding author: eednwang@polyu.edu.hk

Received December 19, 2013; revised March 21, 2014; accepted April 13, 2014;  
posted April 25, 2014 (Doc. ID 203351); published May 27, 2014

We have experimentally demonstrated polarization-locked vector soliton generation in a passively mode-locked erbium-doped fiber laser by using a few-layer graphene deposited D-shaped fiber to act as a saturable absorber (SA). Due to the long light/graphene interaction length and the asymmetric structure, the SA used in this work has large polarization-dependent loss, and as a result, the stationary polarization-locked vector solitons can be generated, being different from the scalar solitons produced by the nonlinear polarization rotation technique. The formation mechanism of such solitons is studied and it is found that they are elliptically polarized solitons. © 2014 Optical Society of America

OCIS codes: (140.3510) Lasers, fiber; (140.4050) Mode-locked lasers; (140.7090) Ultrafast lasers; (320.5550) Pulses.

<http://dx.doi.org/10.1364/JOSAB.31.001377>

## 1. INTRODUCTION

Graphene is a material with point bandgap structure owing to its two-dimensional honeycomb crystal lattice, and it has many remarkable optoelectronic properties such as ultra-wideband absorption [1], controllable interband transition [2], and nonlinear saturable absorption [3]. Recently, many graphene-based devices have been demonstrated including photodetectors [4], broadband polarizers [5], optical modulators [6,7], and ultrafast pulsed lasers [8,9]. These devices mainly employ the optical absorption characteristic of graphene. For the incident light normal to the monolayer graphene layer, the constant absorption coefficient is ~2.3%. Considering the 0.33 nm thickness of monolayer graphene, the absorption is remarkably high. In this case, however, the interaction length between the optical field and the graphene is limited to the thickness of graphene. In order to achieve longer light/graphene interaction length, the graphene can be integrated on the surface of the waveguide or attached on a special fiber, and the interaction length is adjustable. In such graphene/waveguide or fiber structures, the evanescent field of the propagating light interacts with the graphene covering on their surface. Such a technique has been implemented to realize the silicon-on-insulator waveguide-integrated double-layer graphene electroabsorption modulator [6], broadband graphene-based fiber polarizer [5], nonlinear modes in graphene dielectric waveguide [10], and graphene-based microfiber saturable absorber (SA) [11].

As a novel SA, graphene exhibits outstanding optical properties, such as ultrafast recovery time and ultrabroad operation bandwidth [1]. The graphene-based SA is superior to the semiconductor saturable absorber mirror (SESAM) and single-wall carbon nanotubes (SWCNTs) as it does not require bandgap design and diameter control to improve its performance [12], which leads to intensive investigation on it in the development of passively mode-locked fiber lasers [13–21]. In general, graphene or graphene composites are prepared by mechanical exfoliation of graphene from bulk graphite [22,23], self-assembled graphene membrane [24], graphene-polyvinyl alcohol composite [12,25], few-layered graphene oxide solution [26], graphene nanoparticles from bulk graphite [27], chemical vapor deposition (CVD) synthetic multilayer graphene on Ni film with SiO<sub>2</sub>/Si substrate [28–30], and CVD synthetic monolayer graphene on polycrystalline Cu substrate [31,32].

To activate the interaction of the evanescent field of optical fiber with graphene, the SAs have been fabricated by covering the surface of the microfiber [11], tapered fiber [33], and side-polished D-shaped fiber [34] with graphene. When compared with microfiber and tapered fiber, the D-shaped fiber is slightly robust and can be easily and tightly attached with saturable absorption material. The SWCNTs-deposited D-shaped fiber for passively mode-locked fiber lasers has been reported [35,36]. More recently, the mode-locked fiber lasers based on graphene oxide-deposited D-shaped fiber SA had

been demonstrated for producing femtosecond pulses [37,38]. Owing to the asymmetric structure of the D-shaped fiber, the graphene-based SA has a high polarization-dependent loss (PDL), which leads to the polarization-sensitive saturable absorption.

The generation of solitons from passively mode-locked fiber lasers with net negative cavity dispersion is due to the natural balance between the cavity dispersion and the Kerr effect in optical fiber. Since both the gain and the loss exist, the solitons produced are essentially the dissipative solitons, whose dynamics is governed by the complex Ginzburg-Landau equation. The nonlinear coupling between the two polarization modes in the fiber laser results in vector solitons. The formation of vector solitons is influenced by the fiber birefringence, nonlinear Kerr effect, cavity gain, cavity loss, and cavity dispersion. A crucial condition for the vector soliton formation is that there are no polarization discrimination components used in the fiber laser cavity [28]. The strong polarization discrimination component could cause the nonlinear polarization rotation mode locking and would fix the polarization of light in the cavity to form scalar solitons. Adopting the polarization-insensitive graphene-based SA, the dissipative vector soliton operation [39], polarization rotation vector soliton operation [28], and the vector multisoliton operation [40] have been investigated experimentally. By the use of polarization-sensitive D-shaped fiber graphene oxide SA, the passively mode-locked fiber laser with different operation schemes, such as stable Q-switching, continuous-wave (CW) mode-locking and Q-switched mode-locking, have been investigated by simply tuning the polarization states in the laser cavity [37,38]. However, the soliton features of the lasers with polarization-sensitive SA are still unknown. In order to investigate the soliton features with strong polarization-sensitive SA, here we employ a few-layer graphene deposited D-shaped fiber SA with large PDL.

In this paper, the polarization-dependent SA of a few-layer graphene deposited D-shaped fiber is used to implement the passive mode-locking in an erbium-doped fiber (EDF) laser. The polarization-dependent absorption is measured experimentally and explained theoretically. It can be observed from experimental results that stable polarization-locked vector solitons could be obtained in the fiber lasers with high PDL, and the solitons are elliptically polarized solitons.

## 2. FABRICATION AND CHARACTERIZATION OF GRAPHENE-BASED SATURABLE ABSORBER

In order to obtain a large PDL, we use a D-shaped fiber covered with few-layer graphene. The side-polished D-shaped fiber is prepared by burnishing the single-mode fiber (SMF) with a grinding wheel, while using electrode discharge to improve its smoothness. The microscope image of the D-shaped fiber surface is shown in the upper part of Fig. 1(a), obtained by use of a Nikon Eclipse 80i microscope with 40 $\times$  objective lens. The central cross section and the mode field are shown in the lower part of Fig. 1(a). The mode field is measured by use of a micronviewer (Model 7290A, Electrophysics) together with a microscope (IM7B, Atto Instruments). It can be clearly seen from Fig. 1(a) that the surface touches the fiber core, and the part of the mode field is exposed to air. The central region thickness of the D-shaped fiber is estimated

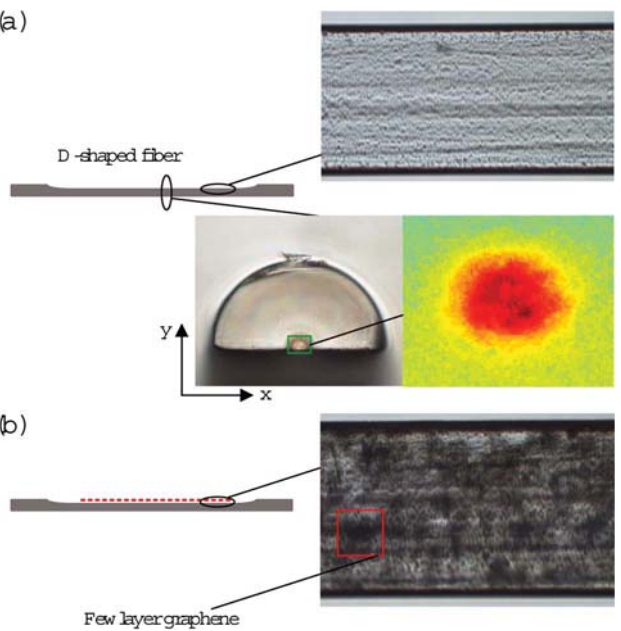


Fig. 1. (a) The upper photo is the surface of the D-shaped fiber, and the lower pictures are the cross section and mode field. (b) Microscope image of the surface with few-layer graphene.

to be  $\sim 64 \mu\text{m}$  from the cross section. The total length of the D-shaped fiber is  $\sim 2 \text{ cm}$ , and the length of the central region is about  $1 \text{ cm}$ , which increases the interaction between the evanescent field and graphene. Its minimum insertion loss and PDL are measured to be  $\sim 13$  and  $\sim 0.6 \text{ dB}$  at the wavelength of  $1550 \text{ nm}$ , respectively. Figure 1(b) illustrates the surface of the D-shaped fiber covered with few-layer graphene. The few-layer graphene film is directly synthesized by use of the CVD method on Ni substrate (Graphene Supermarket). The graphene/Ni/Si layer is soaked with  $0.05 \text{ mg/ml} \text{ FeCl}_3$  solution to remove the Ni layer, and the large-area few-layer graphene film is then thoroughly transferred into the de-ionized water to soak and rinse several times. The length of the graphene is  $\sim 10 \text{ mm}$ . After cleaning the polished surface of the D-shaped fiber with 99.5% propyl alcohol, the fiber is immersed slowly beneath the graphene/water interface. Followed by a gentle scooping of the graphene sheet onto the fiber, the SA is finished and the graphene can interact with the evanescent field.

The graphene or graphene oxide-deposited D-shaped fibers have nonnegligible PDL due to the asymmetry structure of the fiber [5,37], which can be measured by using a tunable CW light source in the telecommunication band ( $1500$ – $1600 \text{ nm}$ ) together with a polarizer, and the experimental setup is schematically shown in Fig. 2(a). By adjusting the polarization controller (PC), the polarization direction of the incident light can be adjusted, and the output maximum corresponds to TE light [x-axis polarization in Fig. 1(a)] while the output minimum corresponds to TM light (y-axis polarization). With  $0 \text{ dBm}$  CW output power, the measured PDL values are shown in Fig. 2(b). It can be noticed that the PDL is irregular as a function of wavelength and has the values of  $\sim 20 \text{ dB}$  and  $\sim 2.5 \text{ dB}$  at  $1550$  and  $1600 \text{ nm}$ , respectively. The irregularity may originate from the mode field change with the wavelength as the D-shaped fiber is polished into the fiber core with a depth of  $\sim 2 \mu\text{m}$ . In order to verify the measured results, we analyze the PDL with a photonic all-parameter analyzer (81910A, Agilent), and the analyzed data are shown in Fig. 2(b). It is

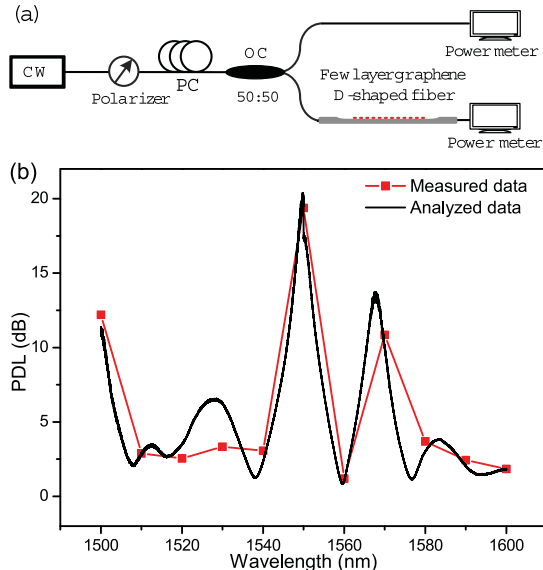


Fig. 2. (a) Measurement system for PDL of the graphene-based SA. (b) The measured PDL as a function of wavelength.

found that the results obtained in the measurement are consistent with those obtained from the parameter analyzer.

The PDL of the D-shaped fiber with graphene is much higher than that without graphene. For further insight, we consider the thin layer graphene is a perturbative absorption for the light field of the D-shaped fiber without graphene. For the unperturbed situation, according to waveguide theory the boundary conditions for the TE and TM modes are expressed by [41]

$$\hat{n} \times (\mathbf{E}_2 - \mathbf{E}_1) = 0 \text{ (TE)}, \quad (1)$$

$$\hat{n} \cdot (\mathbf{D}_2 - \mathbf{D}_1) = 0 \text{ (TM)}, \quad (2)$$

where  $\hat{n}$  is along the y-axis,  $\mathbf{E}_2$ ,  $\mathbf{D}_2$  are the fields on the air side of the interface,  $\mathbf{E}_1$ ,  $\mathbf{D}_1$  are the corresponding fields on the fiber side of the interface. So the electric field is continuous for the TE mode, and the electric displacement field is continuous for the TM mode. Since  $\mathbf{D}_{1,2} = \epsilon_{1,2}\mathbf{E}_{1,2}$  (where  $\epsilon_{1,2}$  are dielectric constants for fiber or air), the electric field on the air side of the interface for the TM mode is larger than that for the TE mode, thus the TM mode suffers higher absorption loss when the D-shaped fiber is covered with graphene.

Figure 3(a) schematically shows the experimental configuration for measurement of polarization-dependent absorption of the graphene-based SA. A femtosecond fiber laser (central wavelength 1552.19 nm, pulse width of ~2 ps, and repetition rate of 20 MHz, PriTel FFL-700) is amplified by an erbium-doped fiber amplifier (EDFA, Amonics). After passing through a polarizer, the polarized light controlled by an adjacent PC, is injected into graphene-based SA via an attenuator (ATT) and a 10:90 optical coupler (OC) [42]. Within the output power range of the pulsed fiber laser, the polarization-dependent absorption of graphene-based SA is measured and the results obtained are shown in Fig. 3(b). When the average output power is raised from 0.3 to 11 mW, the transmission increases by ~2% for the TE mode and ~1.3% for the TM mode.

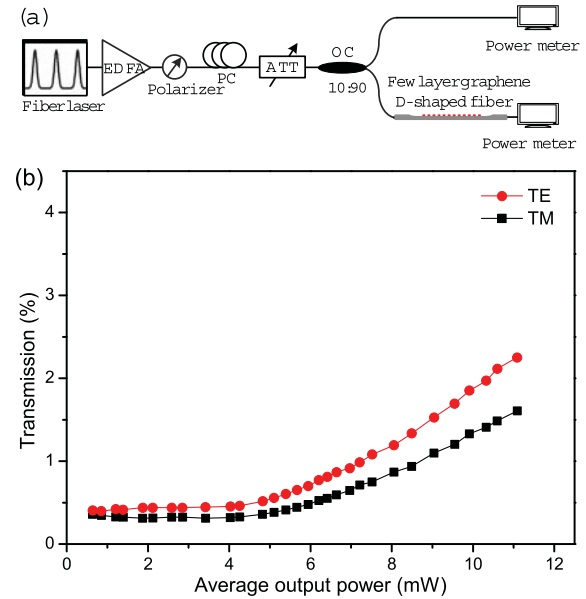


Fig. 3. (a) Schematic experimental setup for the measurement of polarization-dependent absorption of the graphene-based SA. (b) The measured nonlinear absorption of the graphene-based SA for TE mode and TM mode.

### 3. EXPERIMENTAL SETUP

The passively mode-locked EDF laser with a ring cavity configuration is presented in Fig. 4. A 1.6 m high concentration EDF (OFS EDF-80) is used as the gain medium, pumped by a 1480 nm high power laser diode (Anritsu AF4B150FA75L) through a 1480/1550 nm wavelength division multiplexer (WDM) coupler. An intracavity PC is used to optimize the mode-locking operation while a polarization-independent isolator maintains the unidirectional laser pulse propagation. The graphene-based SA is inserted in the cavity between the PC and OC. A section of SMF with 10 m in length is inserted into the cavity to adjust the total cavity dispersions. The PDLs of the OC, WDM, and optical isolator are less than 0.1 dB. The mode-locked pulses can be directed out by use of a 90:10 coupler connecting with another polarization-independent isolator. The group velocity dispersion (GVD) plays an important role in maintaining the mode-locked fiber laser stability. The GVD of the EDF used in the system is -46.25 ps/nm/km

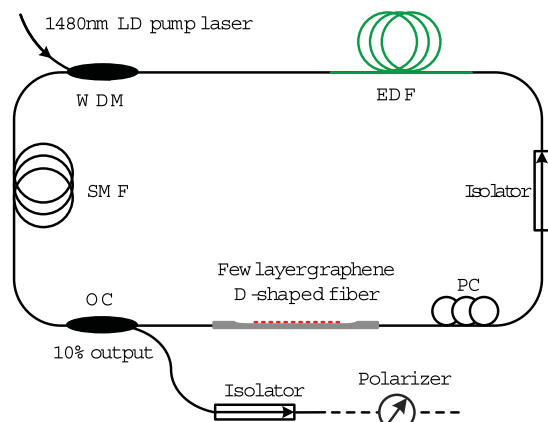


Fig. 4. Experimental setup of the few-layer graphene deposited D-shaped fiber mode-locked laser.

and that of the SMF is 18 ps/nm/km, at the wavelength of 1560 nm. The total laser cavity length is  $\sim 21$  m, thus the round-trip dispersion of the whole cavity is  $\sim -0.32$  ps $^2$ , which ensures that the cavity has net anomalous GVD.

#### 4. RESULTS AND DISCUSSION

First, the pump power is fixed at 230 mW, and the polarizer is not connected to the output port of the fiber laser. The laser optical spectrum is obtained by use of an optical spectrum analyzer (ANDO AQ6319) with 0.01 nm resolution. The fiber laser is easily tuned to operate in the CW state, and the corresponding optical spectrum is shown in Fig. 5(a). There are two peaks in the spectrum, the left one centered at  $\sim 1532$  nm is the peak of the gain spectrum of the EDF. In CW operation the spontaneous gain is not completely suppressed because of the large loss of the graphene-based SA. By slightly tuning the PC, the fiber laser can operate in a stable mode-locking state, and its optical spectrum is also shown in Fig. 5(a), where it can be found that the spontaneous gain is further suppressed. The central wavelength is 1553 nm, and the FWHM bandwidth value is  $\sim 5$  nm. The Kelly sidebands, resulting from the intra-cavity periodical perturbation, clearly appear with discrete and well-defined peaks in the optical spectrum. The pulse intensity profile is monitored by a second-harmonic generation autocorrelator (FEMTOCHROME FR-103XL, resolution

$<5$  fs) and recorded by an oscilloscope (Tektronix, TPS 2024). Figure 5(b) demonstrates the recorded AC trace of the laser pulses, and the pulse width of 1.3 ps can be observed for a sech $^2$  curve fit. Considering its decorrelation factor of 0.648, the actual pulse width is  $\sim 842$  fs. The time-bandwidth product of the pulses is 0.518, indicating that the soliton pulses are chirped. The chirp may originate from the net dispersion in the laser cavity [43].

The pulse train is measured by use of a high-speed photodetector (Newfocus 1414, 25 GHz), which is connected to the same oscilloscope. The pulse train of the laser output shown in Fig. 6(a) has a period of 107.9 ns, which matches well with the cavity round-trip time and verifies that the laser is mode locked. To study the operation stability, we have measured the radio frequency (RF) spectrum of the passively mode-locked fiber laser by the high-speed photodetector together with a real-time spectrum analyzer (Tektronix RSA 3303A, 3 GHz). The fundamental peak is located at the repetition rate of 9.248 MHz, as shown in Fig. 6(b), with a signal-to-noise ratio (SNR) of 70 dB. The inset of Fig. 6(b) shows the higher order of harmonic RF spectrum up to 200 MHz, in which the high SNR can also be observed, indicating the good mode-locking stability. The average output power is  $\sim 8.93$  dBm, with pulse energy of  $\sim 0.845$  nJ.

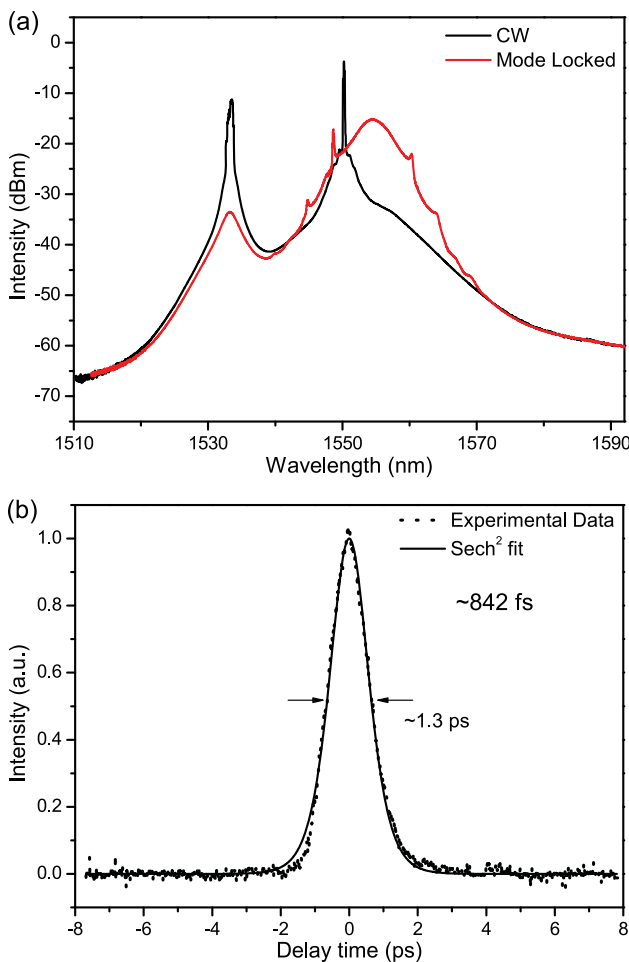


Fig. 5. (a) Output optical spectra for CW and passively mode-locked fiber lasers. (b) Mode-locked pulse shape (experimental data) with Sech $^2$  fit.

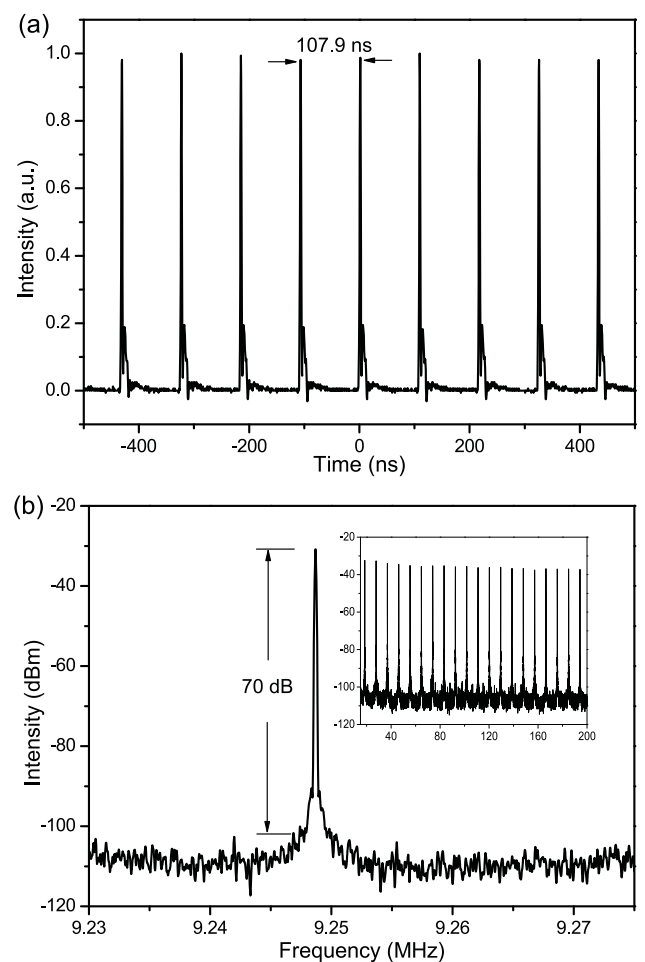


Fig. 6. (a) Typical laser output pulse trains. (b) RF spectrum measured around the fundamental repetition rate, and the inset is the RF spectrum with high-order harmonic of the repetition rate.

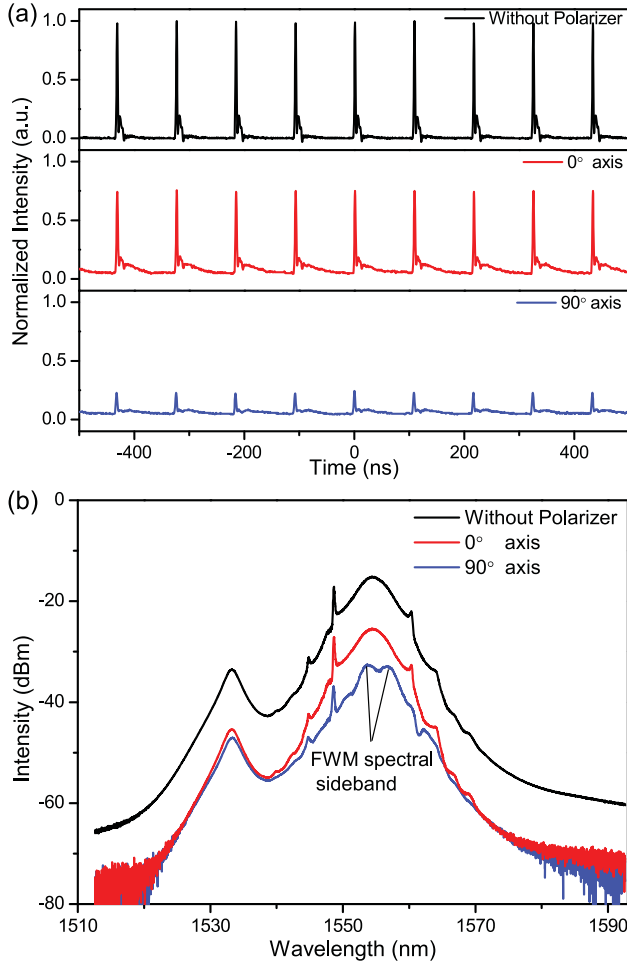


Fig. 7. (a) Pulse trains of the polarization-locked vector soliton. (b) Optical spectrums of the polarization-locked vector soliton.

To experimentally resolve the two orthogonal polarization components of the solitons, a polarizer is connected to the output port of the fiber laser, as shown in Fig. 4. By tuning the polarizer, the polarization angle is set at  $0^\circ$  when the output power is the maximum, thus the other orthogonal polarization direction is  $90^\circ$ . Figure 7 shows the state of the polarization-locked soliton operation of the laser. After the polarizer, the two orthogonal polarization pulse traces show uniform pulse trains, as demonstrated in Fig. 7(a). That is, all vector solitons in the cavity keep the same pulse intensity after each cavity trip. Furthermore, all vector solitons have exactly same polarization and the polarization features keep unchanged inside or outside of the cavity. In addition, it is found that the intensity for the  $90^\circ$  polarization becomes the minimum, much lower than the intensity of the  $0^\circ$  polarization, and the intensity ratio obtained is  $\sim 0.321$ . This indicates that the solitons are elliptical polarization due to the high PDL. Figure 7(b) shows the optical spectrums of the pulses along two orthogonal polarization directions and the total pulse without polarizer. The soliton spectrum along the  $0^\circ$  and  $90^\circ$  polarization directions have different spectral profiles and sidebands, indicating that the solitons are vector solitons.

The formation of vector solitons is determined by the combination of the nonlinear polarization evolution of two polarization components and the mode locking by a SA [44,45]. Based on the coupled complex Ginzburg-Landau equations

for the two polarization components, the polarization-locked vector solitons have been theoretically studied, and elliptically polarized solitons may be generated for certain laser operation parameters [46]. With the high PDL graphene-based SA, the absorption for the TE mode is much lower than that of the TM mode. Therefore, the intracavity pulse energy of the TE mode is much higher than that of the TM mode for a fixed pump power. The coherence energy exchange occurs among the two orthogonal polarization components through the four-wave mixing (FWM) process [47], and the FWM spectral sidebands could form on the polarization resolved spectrum of the vector solitons, as shown in Fig. 7(b). Since the FWM process is the internal process of the vector soliton and the  $0^\circ$  polarization component intensity is high enough, no FWM spectral sidebands appear on the total and  $0^\circ$  polarization soliton spectrums. It is noted that the FWM sidebands are strong on the weak  $90^\circ$  polarization soliton spectrum. These experimental results suggest that the  $90^\circ$  polarization soliton may be created by FWM and cavity birefringence-induced cross-phase modulation [48]. In addition, no polarization rotation vector solitons are observed by slightly tuning the intracavity PC [49,50]; it proves that it is difficult to transfer energy from the  $90^\circ$  polarization soliton to the  $0^\circ$  polarization one, since the loss of the  $90^\circ$  polarization component is much larger than that of the  $0^\circ$  polarization component.

## 5. CONCLUSION

In conclusion, we have experimentally investigated the polarization-locked vector soliton operation of a mode-locked laser with a few-layer graphene deposited D-shaped fiber. It demonstrated that the resonant energy transfer between two orthogonal polarization components induces the elliptical polarization vector solitons with the large PDL of graphene-based SA. As the SA is highly polarization sensitive, our work may provide a new insight for the dynamics of vector solitons.

## ACKNOWLEDGMENTS

The authors are pleased to acknowledge support from the Hong Kong Polytechnic University research grants 4-ZZE6 and G-YM19.

## REFERENCES

1. F. Bonaccorso, Z. Sun, T. Hasan, and A. Ferrari, "Graphene photonics and optoelectronics," *Nat. Photonics* **4**, 611–622 (2010).
2. F. Wang, Y. Zhang, C. Tian, C. Girit, A. Zettl, M. Crommie, and Y. R. Shen, "Gate-variable optical transitions in graphene," *Science* **320**, 206–209 (2008).
3. Q. Bao, H. Zhang, Y. Wang, Z. Ni, Y. Yan, Z. X. Shen, K. P. Loh, and D. Y. Tang, "Atomic-layer graphene as a saturable absorber for ultrafast pulsed lasers," *Adv. Funct. Mater.* **19**, 3077–3083 (2009).
4. T. Mueller, F. Xia, and P. Avouris, "Graphene photodetectors for high-speed optical communications," *Nat. Photonics* **4**, 297–301 (2010).
5. Q. Bao, H. Zhang, B. Wang, Z. Ni, C. H. Y. Lim, Y. Wang, D. Y. Tang, and K. P. Loh, "Broadband graphene polarizer," *Nat. Photonics* **5**, 411–415 (2011).
6. M. Liu, X. Yin, and X. Zhang, "Double-layer graphene optical modulator," *Nano Lett.* **12**, 1482–1485 (2012).
7. C. Xu, Y. Jin, L. Yang, J. Yang, and X. Jiang, "Characteristics of electro-refractive modulating based on graphene-oxide-silicon waveguide," *Opt. Express* **20**, 22398–22405 (2012).
8. Z. Sun, T. Hasan, F. Torrisi, D. Popa, G. Privitera, F. Wang, F. Bonaccorso, D. M. Basko, and A. C. Ferrari, "Graphene mode-locked ultrafast laser," *ACS Nano* **4**, 803–810 (2010).

9. Z. Sun, D. Popa, T. Hasan, F. Torrisi, F. Wang, E. J. Kelleher, J. C. Travers, V. Nicolosi, and A. C. Ferrari, "A stable, wideband tunable, near transform-limited, graphene-mode-locked, ultrafast laser," *Nano Res.* **3**, 653–660 (2010).
10. A. Auditore, C. De Angelis, A. Locatelli, S. Boscolo, M. Midrio, M. Romagnoli, A. D. Capobianco, and G. Nalessio, "Graphene sustained nonlinear modes in dielectric waveguides," *Opt. Lett.* **38**, 631–633 (2013).
11. X. He, Z. B. Liu, D. N. Wang, M. Yang, C. Liao, and X. Zhao, "Passively mode-locked fiber laser based on reduced graphene oxide on microfiber for ultra-wide-band doublet pulse generation," *J. Lightwave Technol.* **30**, 984–989 (2012).
12. D. Popa, Z. Sun, F. Torrisi, T. Hasan, F. Wang, and A. Ferrari, "Sub 200 fs pulse generation from a graphene mode-locked fiber laser," *Appl. Phys. Lett.* **97**, 203106 (2010).
13. H. Zhang, Q. Bao, D. Tang, L. Zhao, and K. Loh, "Large energy soliton erbium-doped fiber laser with a graphene-polymer composite mode locker," *Appl. Phys. Lett.* **95**, 141103 (2009).
14. H. Zhang, D. Tang, R. Knize, L. Zhao, Q. Bao, and K. P. Loh, "Graphene mode locked, wavelength-tunable, dissipative soliton fiber laser," *Appl. Phys. Lett.* **96**, 111112 (2010).
15. H. Zhang, D. Tang, L. Zhao, Q. Bao, K. Loh, B. Lin, and S. Tjin, "Compact graphene mode-locked wavelength-tunable erbium-doped fiber lasers: from all anomalous dispersion to all normal dispersion," *Laser Phys. Lett.* **7**, 591–596 (2010).
16. J. Sotor, G. Sobon, K. Krzempek, and K. M. Abramski, "Fundamental and harmonic mode-locking in erbium-doped fiber laser based on graphene saturable absorber," *Opt. Commun.* **285**, 3174–3178 (2012).
17. P. L. Huang, S. C. Lin, C. Y. Yeh, H. H. Kuo, S. H. Huang, G. R. Lin, L. J. Li, C. Y. Su, and W. H. Cheng, "Stable mode-locked fiber laser based on CVD fabricated graphene saturable absorber," *Opt. Express* **20**, 2460–2465 (2012).
18. J. Xu, S. Wu, J. Liu, Q. Wang, Q. H. Yang, and P. Wang, "Nanosecond-pulsed erbium-doped fiber lasers with graphene saturable absorber," *Opt. Commun.* **285**, 4466–4469 (2012).
19. W. Cao, H. Wang, A. Luo, Z. Luo, and W. Xu, "Graphene-based, 50 nm wide-band tunable passively Q-switched fiber laser," *Laser Phys. Lett.* **9**, 54–58 (2012).
20. B. Fu, L. Gui, W. Zhang, X. Xiao, H. Zhu, and C. Yang, "Passive harmonic mode locking in erbium-doped fiber laser with graphene saturable absorber," *Opt. Commun.* **286**, 304–308 (2013).
21. Q. Sheng, M. Feng, W. Xin, T. Han, Y. Liu, Z. Liu, and J. Tian, "Actively manipulation of operation states in passively pulsed fiber lasers by using graphene saturable absorber on microfiber," *Opt. Express* **21**, 14859–14866 (2013).
22. Y. M. Chang, H. Kim, J. H. Lee, and Y. W. Song, "Multilayered graphene efficiently formed by mechanical exfoliation for nonlinear saturable absorbers in fiber mode-locked lasers," *Appl. Phys. Lett.* **97**, 211102 (2010).
23. J. Sotor, G. Sobon, and K. M. Abramski, "Scalar soliton generation in all-polarization-maintaining, graphene mode-locked fiber laser," *Opt. Lett.* **37**, 2166–2168 (2012).
24. L. Gui, W. Zhang, X. Li, X. Xiao, H. Zhu, K. Wang, D. Wu, and C. Yang, "Self-assembled graphene membrane as an ultrafast mode-locker in an erbium fiber laser," *IEEE Photon. Technol. Lett.* **23**, 1790–1792 (2011).
25. S. Y. Choi, D. K. Cho, Y. W. Song, K. Oh, K. Kim, F. Rotermund, and D. I. Yeom, "Graphene-filled hollow optical fiber saturable absorber for efficient soliton fiber laser mode-locking," *Opt. Express* **20**, 5652–5657 (2012).
26. Z. B. Liu, X. He, and D. N. Wang, "Passively mode-locked fiber laser based on a hollow-core photonic crystal fiber filled with few-layered graphene oxide solution," *Opt. Lett.* **36**, 3024–3026 (2011).
27. Y. H. Lin, C. Y. Yang, J. H. Liou, C. P. Yu, and G. R. Lin, "Using graphene nano-particle embedded in photonic crystal fiber for evanescent wave mode-locking of fiber laser," *Opt. Express* **21**, 16763–16776 (2013).
28. Y. F. Song, H. Zhang, D. Y. Tang, and D. Y. Shen, "Polarization rotation vector solitons in a graphene mode-locked fiber laser," *Opt. Express* **20**, 27283–27289 (2012).
29. G. Sobon, J. Sotor, and K. M. Abramski, "Passive harmonic mode-locking in Er-doped fiber laser based on graphene saturable absorber with repetition rates scalable to 2.22 GHz," *Appl. Phys. Lett.* **100**, 161109 (2012).
30. J. Du, S. Zhang, H. Li, Y. Meng, X. Li, and Y. Hao, "L-band passively harmonic mode-locked fiber laser based on a graphene saturable absorber," *Laser Phys. Lett.* **9**, 896 (2012).
31. Q. Bao, H. Zhang, Z. Ni, Y. Wang, L. Polavarapu, Z. Shen, Q. H. Xu, D. Tang, and K. P. Loh, "Monolayer graphene as a saturable absorber in a mode-locked laser," *Nano Res.* **4**, 297–307 (2011).
32. X. He, Z. Liu, and D. N. Wang, "Wavelength-tunable, passively mode-locked fiber laser based on graphene and chirped fiber Bragg grating," *Opt. Lett.* **37**, 2394–2396 (2012).
33. J. Wang, Z. Luo, M. Zhou, C. Ye, H. Fu, Z. Cai, H. Cheng, H. Xu, and W. Qi, "Evanescent-light deposition of graphene onto tapered fibers for passive Q-switch and mode-locker," *IEEE Photon. J.* **4**, 1295–1305 (2012).
34. Y. W. Song, S. Y. Jang, W. S. Han, and M. K. Bae, "Graphene mode-lockers for fiber lasers functioned with evanescent field interaction," *Appl. Phys. Lett.* **96**, 051122 (2010).
35. Y. W. Song, S. Yamashita, C. S. Goh, and S. Y. Set, "Carbon nanotube mode lockers with enhanced nonlinearity via evanescent field interaction in D-shaped fibers," *Opt. Lett.* **32**, 148–150 (2007).
36. S. Wang, Y. Pan, R. Gao, X. Zhu, X. Su, and S. Qu, "Mode-locked double-clad fiber laser with a carbon nanotubes saturable absorber," *Acta Phys. Sin.* **62**, 024209 (2013).
37. M. Jung, J. Koo, J. Park, Y. W. Song, Y. M. Jhon, K. Lee, S. Lee, and J. H. Lee, "Mode-locked pulse generation from an all-fiberized, Tm-Ho-codoped fiber laser incorporating a graphene oxide-deposited side-polished fiber," *Opt. Express* **21**, 20062–20072 (2013).
38. J. Lee, J. Koo, P. Debnath, Y. Song, and J. Lee, "A Q-switched, mode-locked fiber laser using a graphene oxide-based polarization sensitive saturable absorber," *Laser Phys. Lett.* **10**, 035103 (2013).
39. H. Zhang, D. Tang, L. Zhao, Q. Bao, and K. P. Loh, "Vector dissipative solitons in graphene mode locked fiber lasers," *Opt. Commun.* **283**, 3334–3338 (2010).
40. Y. F. Song, L. Li, H. Zhang, D. Y. Shen, D. Y. Tang, and K. P. Loh, "Vector multi-soliton operation and interaction in a graphene mode-locked fiber laser," *Opt. Express* **21**, 10010–10018 (2013).
41. G. W. Hanson, "Quasi-transverse electromagnetic modes supported by a graphene parallel-plate waveguide," *J. Appl. Phys.* **104**, 084314 (2008).
42. T. Hasan, Z. Sun, F. Wang, F. Bonaccorso, P. H. Tan, A. G. Rozhin, and A. C. Ferrari, "Nanotube–polymer composites for ultrafast photonics," *Adv. Mater.* **21**, 3874–3899 (2009).
43. K. Kashiwagi and S. Yamashita, "Deposition of carbon nanotubes around microfiber via evanescent light," *Opt. Express* **17**, 18364–18370 (2009).
44. S. Smirnov, S. Kobtsev, S. Kukarin, and S. Turitsyn, "Mode-locked fibre lasers with high-energy pulses," in *Laser Systems for Applications* (InTech, 2011).
45. W. H. Renninger and F. W. Wise, "Dissipative soliton fiber lasers," in *Fiber Lasers* (Wiley, 2012), pp. 97–133.
46. J. Soto-Crespo, N. Akhmediev, B. Collings, S. Cundiff, K. Bergman, and W. Knox, "Polarization-locked temporal vector solitons in a fiber laser: theory," *J. Opt. Soc. Am. B* **17**, 366–372 (2000).
47. H. Zhang, D. Tang, L. Zhao, and N. Xiang, "Coherent energy exchange between components of a vector soliton in fiber lasers," *Opt. Express* **16**, 12618–12623 (2008).
48. H. Zhang, D. Tang, L. Zhao, and H. Tam, "Induced solitons formed by cross-polarization coupling in a birefringent cavity fiber laser," *Opt. Lett.* **33**, 2317–2319 (2008).
49. L. Zhao, D. Tang, H. Zhang, and X. Wu, "Polarization rotation locking of vector solitons in a fiber ring laser," *Opt. Express* **16**, 10053–10058 (2008).
50. L. Zhao, D. Tang, X. Wu, H. Zhang, and H. Tam, "Coexistence of polarization-locked and polarization-rotating vector solitons in a fiber laser with SESAM," *Opt. Lett.* **34**, 3059–3061 (2009).

# Passively mode-locked fiber laser by using monolayer chemical vapor deposition of graphene on D-shaped fiber

Tao Chen,<sup>1,3</sup> Changrui Liao,<sup>1,4</sup> D. N. Wang,<sup>1,2,\*</sup> and Yiping Wang<sup>4</sup>

<sup>1</sup>Department of Electrical Engineering, The Hong Kong Polytechnic University, Hong Kong, China

<sup>2</sup>School of Electrical, Electronic and Information Engineering, Hubei Polytechnic University, Huangshi, China

<sup>3</sup>School of Physics and Technology, University of Jinan, Jinan, Shandong 250022, China

<sup>4</sup>College of Optoelectronic Engineering, Shenzhen University, Shenzhen, Guangdong 518060, China

\*Corresponding author: eednwang@polyu.edu.hk

Received 19 December 2013; revised 6 March 2014; accepted 27 March 2014;  
posted 28 March 2014 (Doc. ID 203443); published 24 April 2014

We demonstrate a monolayer graphene saturable absorber (SA) based on D-shaped fiber for operation of the mode-locked fiber laser. The monolayer graphene is grown by chemical vapor deposition (CVD) on Cu substrate and transferred onto the polymer, and then covered with D-shaped fiber, which allows light-graphene interaction via the evanescent field of the fiber. Due to the side-coupled interaction, the length of graphene is long enough to avoid optical power-induced thermal damage. Using such a graphene-based SA, stable mode-locked solitons with 4.5 nm spectral bandwidth and 713 fs pulselwidth at the 1563 nm wavelength have been obtained under 280 mW pump power. The influence of total cavity dispersion on the optical spectrum and pulse is also investigated by adding different lengths of single-mode fiber in the laser cavity. © 2014 Optical Society of America

*OCIS codes:* (140.4050) Mode-locked lasers; (140.7090) Ultrafast lasers; (320.5550) Pulses.  
<http://dx.doi.org/10.1364/AO.53.002828>

## 1. Introduction

Graphene exhibits outstanding optical properties, such as ultrafast recovery time, broad operation bandwidth, and nonlinear optical response [1]. Recently, graphene has attracted huge interest in the development of passively mode-locked fiber lasers owing to its excellently saturable absorption feature [2–15]. To fabricate the graphene-based saturable absorber (SA), several methods have been developed. The first one is transferring the atomic-layer graphene onto a fiber ferrule to form a SA, and the graphene materials can be obtained from chemical vapor deposition (CVD) synthetical graphene on SiO<sub>2</sub>/Si substrates with Ni films [16–18], mechanical

exfoliation of graphene from bulk graphite [19,20], self-assembled graphene membrane [21], graphene-PVA (polyvinyl alcohol) composite [22], etc. The second method is filling the hollow-core photonic crystal with few-layered graphene oxide solution [23], filling the hollow optical fiber with graphene/PVA composite [24], and syphoning the graphene nanoparticles into a multicore photonic crystal fiber (PCF) [25]. The third technique is employing the evanescent field interaction of the propagating light with the graphene covered on the surface of side-polished D-shaped fiber [26], microfiber [27], and tapered fiber [28]. In such a scheme, the interaction length of the light beam with graphene is adjustable, which can essentially overcome the difficulty of optical power-induced thermal damage. When compared with the microfiber and tapered fiber, the D-shaped

---

1559-128X/14/132828-05\$15.00/0  
© 2014 Optical Society of America

fiber can be tightly attached by graphene film, and is robust and convenient for packaging. Very recently, mode-locked fiber lasers based on the graphene oxide-deposited D-shaped fiber were demonstrated for producing femtosecond pulses [29,30].

Up to now, multilayer graphene as well as graphene composites have been widely used as the SAs in passively mode-locked fiber lasers. Although monolayer graphene has relatively low excitation intensity of saturable absorption and, hence, can act as a more effective SA for mode-locking fiber lasers [31], the transfer and manufacture of monolayer graphene is rather difficult because of its thin thickness. To develop a simple method for preparation, the polymer-supported monolayer graphene film becomes an attractive approach. In our previous work, polymer-supported monolayer graphene, covered on the microfiber, has been fabricated and used as a SA for wavelength-tunable and passively mode-locked pulse generation [32].

In this paper, the D-shaped fiber covered by polymer-supported monolayer graphene film is used as the SA. Such a structure enables strong light-graphene interaction along the fiber length, and as a result, mode-locked femtosecond laser pulses of ~713 fs with repetition rate of 11.53 MHz can be obtained under 280 mW pump power.

## 2. Fabrication and Polarization Characterization of Saturable Absorber

The side-polished fiber device for preparing D-shaped fiber is shown in Fig. 1(a). Here, the single-mode fiber (SMF) is burnished by the grinding wheel, and then is burned using the electrode discharge to improve the smoothness. The resulting fiber is viewed by using a Nikon Eclipse 80i microscope with 20 $\times$  objective lens. From the side view of the right picture, the fiber core is near the edge and the thickness is ~72  $\mu$ m. The vertical view of the right picture

is the photo of the polished surface. The total D-shaped fiber is 2 cm in length, and its minimum insertion loss and polarization-dependent loss (PDL) are measured to be 1.3 and 0.5 dB at the wavelength of 1560 nm, respectively. Figure 1(b) illustrates the schematic structure of the graphene-based SA. The monolayer graphene film is directly synthesized by the CVD method on polycrystalline Cu substrate. The polymer clad resin (EFiRON, PC-373, refractive index of 1.376) is uniformly adhered to the graphene film on a Cu substrate without an air bubble in it, and is then cured by ultraviolet (UV) light. After 24 h, the polymer/graphene/Cu layers are soaked with 0.05 mg/ml FeCl<sub>3</sub> solution to remove the Cu layer. Then the ferric icon is washed away from polymer/graphene layers using distilled water. The length of the graphene is ~10 mm. Finally, after cleaning the polished surface of the D-shaped fiber with 99.5% propyl alcohol, the polymer-supported monolayer graphene film is transferred onto the flat surface of the D-shaped fiber for interaction with the evanescent field. Such a structure is used as the graphene-based SA in our fiber laser system. In addition, it should be noted that the thickness of D-shaped fiber should be between 67  $\mu$ m (on top of fiber core) and 77  $\mu$ m, in order to obtain a low loss and strong evanescent field simultaneously. Considering the interaction length of ~10 mm of graphene, the 72  $\mu$ m thickness of D-shaped fiber is appropriate for our structure.

## 3. Experimental Setup

The experimental setup of the proposed graphene-based passively mode-locked erbium-doped fiber (EDF) laser with a ring cavity configuration is presented in Fig. 2. A 1.3 m high-concentration EDF (OFS EDF-80) is used as the gain medium, pumped by a 1480 nm high-power laser diode (LD, Anritsu AF4B150FA75L) via a 1480/1550 nm wavelength division multiplexer (WDM) coupler. A polarization-independent isolator is used to force the unidirectional operation of the ring, and an intracavity PC is

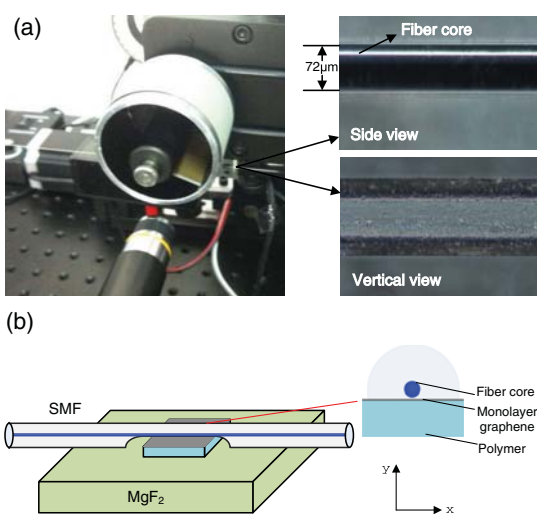


Fig. 1. (a) D-shaped fiber preparation through side-polished fiber device; the right pictures are the side and vertical views of the end product. (b) Schematic structure of the graphene-based SA; the right schematic diagram is the cross section.

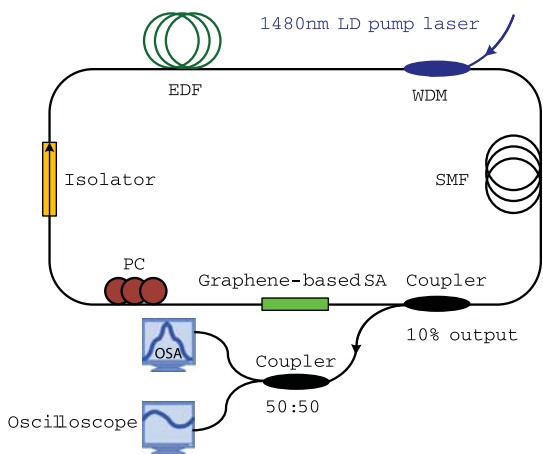


Fig. 2. Experimental setup of the graphene mode-locking fiber laser.

used to adjust the linear cavity birefringence. The graphene-based SA is inserted in the cavity between the PC and the optical coupler. The SMF is added in the cavity to change the total cavity dispersions. The PDLs of the 90:10 fiber coupler, WDM, and optical isolator are less than 0.1 dB. The generated mode-locked pulses are directed out by the optical coupler, and then pass through a 3 dB coupler. The pulses are simultaneously monitored by an optical spectrum analyzer (ANDO AQ 6319) with 0.01 nm resolution and a high-speed photodetector (New-focus 1414, 25 GHz) connected to an oscilloscope (Tektronix, TPS 2024). The radio frequency (RF) spectrum of the passively mode-locked laser output is measured by use of the same photodetector connected to a real-time spectrum analyzer (Tektronix RSA 3303A, 3 GHz). The pulse profile is measured by a second harmonic generation (SHG) autocorrelator (FEMTOCHROME FR-103XL, resolution <5 fs) and recorded by the Tektronix oscilloscope.

#### 4. Results and Discussion

Group velocity dispersion (GVD) plays an important role in maintaining the mode-locked fiber laser stability. The GVD of the EDF and the SMF used in the system is  $-46.25 \text{ ps/nm/km}$  and  $18 \text{ ps/nm/km}$  at the wavelength of  $1560 \text{ nm}$ , respectively. We first add 5 m SMF in the laser cavity, and the total laser cavity length is  $\sim 14.3 \text{ m}$ . By ignoring the dispersion of the short D-shaped fiber, the round-trip dispersion of the whole cavity is  $\sim -0.222 \text{ ps}^2$ . The continuous-wave (CW) operation pump threshold of the laser is  $\sim 40 \text{ mW}$ . Owing to the asymmetry of D-shaped fiber—it is well known that graphene or graphene oxide-deposited D-shaped fibers exhibit non-negligible PDL [29,33]—the intracavity pulse loss is changed for different pulse polarization states in graphene-based SA [15]. Increasing the pump power to  $80 \text{ mW}$  and slightly tuning the PC, the fiber laser can operate in states such as CW, stable Q-switching, Q-switched mode-locking, and CW mode-locking [30]. Here, we mainly investigate the laser in the steadily mode-locked state. Once the laser is in mode-locking, the operation can be maintained for a long time. During the operation, the pump power may be increased to  $300 \text{ mW}$ , until multipulse generation is observed. Under  $280 \text{ mW}$  pump power, the pulse train of the output solitons is shown in Fig. 3(a). The laser pulse train has a period of  $86.7 \text{ ns}$ , which matches well with the cavity round-trip time and indicates that the laser is in the passive mode-locked regime. Figure 3(b) shows the optical spectrum of the output. The central wavelength is  $1563 \text{ nm}$ , and the full width at half-maximum (FWHM) bandwidth is  $4.5 \text{ nm}$ . The Kelly sidebands, resulting from the intracavity periodical perturbation, clearly appear with discrete and well-defined peaks in the optical spectrum. For chirp-free soliton pulses, the  $m$ th order of the Kelly sideband position relative to the center wavelength is given by [29]

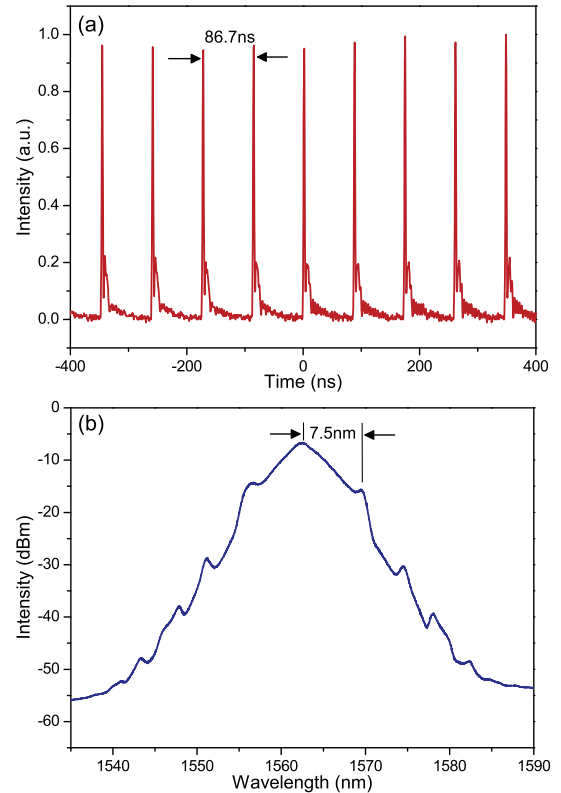


Fig. 3. Under  $280 \text{ mW}$  EDF pump power, (a) oscilloscope trace of pulse train and (b) optical spectrum of output pulse of mode-locked fiber laser.

$$\Delta\lambda = \frac{2 \ln(1 + \sqrt{2})\lambda^2}{2\pi c\tau} \sqrt{\frac{4m\pi}{|L\beta_2|} \left(\frac{\tau}{2\ln(1 + \sqrt{2})}\right)^2 - 1}, \quad (1)$$

where  $\lambda$  is the center wavelength,  $\tau$  is the temporal FWHM value of the pulses,  $L$  is the cavity length,  $\beta_2$  is the cavity dispersion parameter, and the total cavity dispersion  $|L\beta_2|$  is  $\sim 0.222 \text{ ps}^2$ . The  $\Delta\lambda$  for the first-order Kelly sideband is  $7.5 \text{ nm}$  in Fig. 3(b), and the transform-limited  $\tau$  is calculated to be  $\sim 0.4 \text{ ps}$  by using Eq. (1).

Figure 4(a) depicts the recorded AC trace of the laser pulses. The FWHM value of the pulses is  $\sim 1.1 \text{ ps}$ . Assuming a Sech<sup>2</sup> pulse profile, its decorrelation factor is 0.648, and the actual pulselwidth is  $\sim 713 \text{ fs}$ . This measured  $\tau$  is different from the theoretical value ( $\sim 0.4 \text{ ps}$ ), and the time-bandwidth product of the pulses is 0.395, indicating that the soliton pulses are small chirped. The measured RF results are shown in Fig. 4(b). The fundamental peak is located at the repetition rate of  $11.53 \text{ MHz}$ , with a signal-to-noise ratio (SNR) of  $60 \text{ dB}$ . It is found that there is a pedestal around the peak; it may result from the influence of vibration or thermal variations on the length of the fiber oscillator. Such a pedestal could be removed by using temperature and vibration control, or the phase-locking technique. The average output power is  $\sim 10.5 \text{ dBm}$ , with pulse energy  $\sim 1 \text{ nJ}$ . The inset of Fig. 4(b) reveals the higher

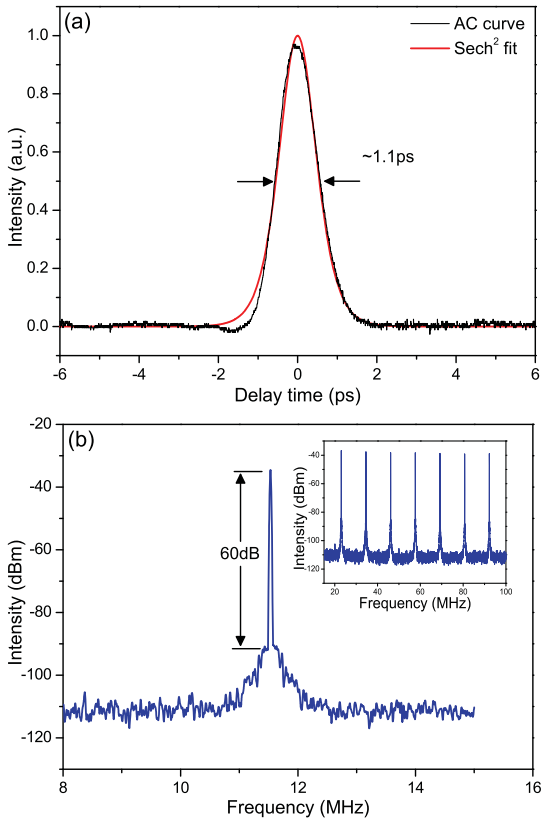


Fig. 4. (a) Autocorrelation traces of the solitons. (b) Fundamental RF spectrum of mode-locked laser; the inset is the RF spectrum of the high-order harmonic pulse.

order of the harmonic RF spectrum, in which a high SNR can also be observed. This indicates the good stability and high reliability of our system.

In order to investigate the dependence of pulses and net cavity dispersion, the length of SMF is varied while other equipment is unchanged. When the net cavity dispersion is small, the polarization controller needs to be fine tuned to start the mode locking. Figure 5 shows the optical spectra of our pulses with different SMF lengths, and the obvious sideband and narrow FWHM are obtained with larger dispersion. Table 1 summarizes the relationship

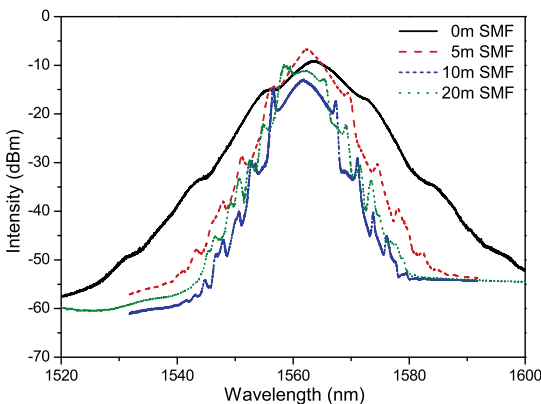


Fig. 5. Optical spectra of output pulse of mode-locked fiber laser with different lengths of added SMF under 280 mW EDF pump power.

Table 1. Optical Parameters of Mode-Locked Fiber Laser When Adding Different Lengths of SMF

Cavity Length (m)	Total Dispersion ( $\text{ps}^2$ )	Frequency (MHz)	FWHM (nm)	Pulsewidth (ps)
9.3	-0.107	16.47	7.8	0.668
14.3	-0.222	11.53	4.5	0.713
19.3	-0.336	8.74	4.2	0.809
29.3	-0.560	6.66	—	1.119

between the total cavity dispersion and the laser characteristics including four groups of data. When the total dispersion is varied from 0.107 to 0.560  $\text{ps}^2$ , the pulsewidth of the generated pulses is between 0.668 and 1.119 ps at a repetition rate of 16.47–6.66 MHz.

## 5. Conclusion

In conclusion, a femtosecond passively mode-locked fiber laser based on D-shaped fiber and monolayer graphene has been demonstrated. The method of transferring polymer-supported monolayer graphene film onto the flat surface of the D-shaped fiber is simple and effective. By varying the length of SMF, the total dispersion can be changed from 0.107 to 0.560  $\text{ps}^2$ . The corresponding pulsewidths of 0.668–1.119 ps were obtained at a repetition rate of 16.47–6.66 MHz. The easy fabrication and good stability of our system will facilitate potential applications of monolayer graphene in ultrafast photonics.

The authors are pleased to acknowledge support from the Hong Kong Polytechnic University research grants 4-ZZE6 and G-YM19.

## References

1. F. Bonaccorso, Z. Sun, T. Hasan, and A. Ferrari, "Graphene photonics and optoelectronics," *Nat. Photonics* **4**, 611–622 (2010).
2. Q. Bao, H. Zhang, Y. Wang, Z. Ni, Y. Yan, Z. X. Shen, K. P. Loh, and D. Y. Tang, "Atomic-layer graphene as a saturable absorber for ultrafast pulsed lasers," *Adv. Funct. Mater.* **19**, 3077–3083 (2009).
3. H. Zhang, Q. Bao, D. Tang, L. Zhao, and K. Loh, "Large energy soliton erbium-doped fiber laser with a graphene-polymer composite mode locker," *Appl. Phys. Lett.* **95**, 141103 (2009).
4. Z. Sun, T. Hasan, F. Torrisi, D. Popa, G. Privitera, F. Wang, F. Bonaccorso, D. M. Basko, and A. C. Ferrari, "Graphene mode-locked ultrafast laser," *ACS Nano* **4**, 803–810 (2010).
5. H. Zhang, D. Tang, R. Knize, L. Zhao, Q. Bao, and K. P. Loh, "Graphene mode locked, wavelength-tunable, dissipative soliton fiber laser," *Appl. Phys. Lett.* **96**, 111112 (2010).
6. Z. Sun, D. Popa, T. Hasan, F. Torrisi, F. Wang, E. J. Kelleher, J. C. Travers, V. Nicolosi, and A. C. Ferrari, "A stable, wide-band tunable, near transform-limited, graphene-mode-locked, ultrafast laser," *Nano Res.* **3**, 653–660 (2010).
7. H. Zhang, D. Tang, L. Zhao, Q. Bao, K. Loh, B. Lin, and S. Tjin, "Compact graphene mode-locked wavelength-tunable erbium-doped fiber lasers: from all anomalous dispersion to all normal dispersion," *Laser Phys. Lett.* **7**, 591–596 (2010).
8. H. Zhang, D. Tang, L. Zhao, Q. Bao, and K. P. Loh, "Vector dissipative solitons in graphene mode locked fiber lasers," *Opt. Commun.* **283**, 3334–3338 (2010).
9. J. Sotor, G. Sobon, K. Krzempek, and K. M. Abramski, "Fundamental and harmonic mode-locking in erbium-doped fiber laser based on graphene saturable absorber," *Opt. Commun.* **285**, 3174–3178 (2012).

10. P. L. Huang, S. C. Lin, C. Y. Yeh, H. H. Kuo, S. H. Huang, G. R. Lin, L. J. Li, C. Y. Su, and W. H. Cheng, "Stable mode-locked fiber laser based on CVD fabricated graphene saturable absorber," *Opt. Express* **20**, 2460–2465 (2012).
11. J. Xu, S. Wu, J. Liu, Q. Wang, Q. H. Yang, and P. Wang, "Nanosecond-pulsed erbium-doped fiber lasers with graphene saturable absorber," *Opt. Commun.* **285**, 4466–4469 (2012).
12. W. Cao, H. Wang, A. Luo, Z. Luo, and W. Xu, "Graphene-based, 50 nm wide-band tunable passively Q-switched fiber laser," *Laser Phys. Lett.* **9**, 54–58 (2012).
13. B. Fu, L. Gui, W. Zhang, X. Xiao, H. Zhu, and C. Yang, "Passive harmonic mode locking in erbium-doped fiber laser with graphene saturable absorber," *Opt. Commun.* **286**, 304–308 (2013).
14. Y. F. Song, L. Li, H. Zhang, D. Y. Shen, D. Y. Tang, and K. P. Loh, "Vector multi-soliton operation and interaction in a graphene mode-locked fiber laser," *Opt. Express* **21**, 10010–10018 (2013).
15. Q. Sheng, M. Feng, W. Xin, T. Han, Y. Liu, Z. Liu, and J. Tian, "Actively manipulation of operation states in passively pulsed fiber lasers by using graphene saturable absorber on microfiber," *Opt. Express* **21**, 14859–14866 (2013).
16. Y. F. Song, H. Zhang, D. Y. Tang, and D. Y. Shen, "Polarization rotation vector solitons in a graphene mode-locked fiber laser," *Opt. Express* **20**, 27283–27289 (2012).
17. G. Sobon, J. Sotor, and K. M. Abramski, "Passive harmonic mode-locking in Er-doped fiber laser based on graphene saturable absorber with repetition rates scalable to 2.22 GHz," *Appl. Phys. Lett.* **100**, 161109 (2012).
18. J. Du, S. Zhang, H. Li, Y. Meng, X. Li, and Y. Hao, "L-band passively harmonic mode-locked fiber laser based on a graphene saturable absorber," *Laser Phys. Lett.* **9**, 896–900 (2012).
19. Y. M. Chang, H. Kim, J. H. Lee, and Y. W. Song, "Multilayered graphene efficiently formed by mechanical exfoliation for nonlinear saturable absorbers in fiber mode-locked lasers," *Appl. Phys. Lett.* **97**, 211102 (2010).
20. J. Sotor, G. Sobon, and K. M. Abramski, "Scalar soliton generation in all-polarization-maintaining, graphene mode-locked fiber laser," *Opt. Lett.* **37**, 2166–2168 (2012).
21. L. Gui, W. Zhang, X. Li, X. Xiao, H. Zhu, K. Wang, D. Wu, and C. Yang, "Self-assembled graphene membrane as an ultrafast mode-locker in an erbium fiber laser," *IEEE Photon. Technol. Lett.* **23**, 1790–1792 (2011).
22. D. Popa, Z. Sun, F. Torrisi, T. Hasan, F. Wang, and A. Ferrari, "Sub 200 fs pulse generation from a graphene mode-locked fiber laser," *Appl. Phys. Lett.* **97**, 203106 (2010).
23. Z. B. Liu, X. He, and D. N. Wang, "Passively mode-locked fiber laser based on a hollow-core photonic crystal fiber filled with few-layered graphene oxide solution," *Opt. Lett.* **36**, 3024–3026 (2011).
24. S. Y. Choi, D. K. Cho, Y.-W. Song, K. Oh, K. Kim, F. Rotermund, and D. I. Yeom, "Graphene-filled hollow optical fiber saturable absorber for efficient soliton fiber laser mode-locking," *Opt. Express* **20**, 5652–5657 (2012).
25. Y. H. Lin, C. Y. Yang, J. H. Liou, C. P. Yu, and G. R. Lin, "Using graphene nano-particle embedded in photonic crystal fiber for evanescent wave mode-locking of fiber laser," *Opt. Express* **21**, 16763–16776 (2013).
26. Y. W. Song, S. Y. Jang, W. S. Han, and M. K. Bae, "Graphene mode-lockers for fiber lasers functioned with evanescent field interaction," *Appl. Phys. Lett.* **96**, 051122 (2010).
27. X. He, Z. B. Liu, D. N. Wang, M. Yang, C. Liao, and X. Zhao, "Passively mode-locked fiber laser based on reduced graphene oxide on microfiber for ultra-wide-band doublet pulse generation," *J. Lightwave Technol.* **30**, 984–989 (2012).
28. J. Wang, Z. Luo, M. Zhou, C. Ye, H. Fu, Z. Cai, H. Cheng, H. Xu, and W. Qi, "Evanescent-light deposition of graphene onto tapered fibers for passive Q-switch and mode-locker," *IEEE Photon. J.* **4**, 1295–1305 (2012).
29. M. Jung, J. Koo, J. Park, Y.-W. Song, Y. M. Jhon, K. Lee, S. Lee, and J. H. Lee, "Mode-locked pulse generation from an all-fiberized, Tm-Ho-codoped fiber laser incorporating a graphene oxide-deposited side-polished fiber," *Opt. Express* **21**, 20062–20072 (2013).
30. J. Lee, J. Koo, P. Debnath, Y. Song, and J. Lee, "A Q-switched, mode-locked fiber laser using a graphene oxide-based polarization sensitive saturable absorber," *Laser Phys. Lett.* **10**, 035103 (2013).
31. Q. Bao, H. Zhang, Z. Ni, Y. Wang, L. Polavarapu, Z. Shen, Q. H. Xu, D. Tang, and K. P. Loh, "Monolayer graphene as a saturable absorber in a mode-locked laser," *Nano Res.* **4**, 297–307 (2011).
32. X. He, Z. Liu, and D. N. Wang, "Wavelength-tunable, passively mode-locked fiber laser based on graphene and chirped fiber Bragg grating," *Opt. Lett.* **37**, 2394–2396 (2012).
33. Q. Bao, H. Zhang, B. Wang, Z. Ni, C. H. Y. X. Lim, Y. Wang, D. Y. Tang, and K. P. Loh, "Broadband graphene polarizer," *Nat. Photonics* **5**, 411–415 (2011).

# Side-opened suspended core fiber-based surface Plasmon resonance sensor

Guanjun Wang, Chao Wang, Shen Liu, Jing Zhao, Changrui Liao, Xizhen Xu, Haijian Liang, guolu Yin, Yiping Wang

**Abstract**—An integrated surface Plasmon resonance (SPR) based on an Au film-coated, side-opened suspended core fiber is proposed and simulated to develop a highly sensitive, real-time refractive index sensor. The inner surface of the side-opened hole is supposed to be uniformly deposited with a thin Au-film for realizing the surface Plasmon resonance operation. Such a sensor not only ensures a fast response time, but also brings up a designing flexibility for SPR bio-sensing applications. Two potential sensing mechanisms, i.e. monitoring the transmission loss spectrum peak shift, and measuring the transmission power change at a fixed wavelength, are utilized and analyzed to achieve a better sensitivity. Moreover, our calculation results show that this novel sensor could cover a wide index detection range with an optimized resolution of up to 2.3e-5 RIU.

**Index Terms**—Surface Plasmon resonance sensor, Suspended core fiber, Side-opened

## I. INTRODUCTION

The demand of fast responsive, high sensitive, integrated and label-free bio-chemical sensing is of vast importance in many areas, such as cancer biomarker detection [1]. Many types of integrated biosensors and their sensing characteristics have been proposed and analyzed during the past years [1-13], especially fiber sensors. Fiber-based surface Plasmon resonance (SPR) sensors are widely used for bio-chemical sensing due to its characteristic of high sensitivity to refractive index change in the surface plasmon state [8]. While miniaturization and integration of the SPR systems could also

be realized by utilizing the optical fiber configuration [9, 10, 11, 12, 13, 14, 15, 16]. Other advantages of the optical fiber-based SPR sensors include the possibility of label-free biochemical detection, simplified design, and the feasibility of the remote or distributive detection. Besides, the surface Plasmon resonance enhanced surface intensity can also contribute to the Raman scattering and the fluorescence excitation applications [17, 18].

For the optical fiber-based SPR sensors, the angle of the incident light is generally fixed. Broadband optical source or single wavelength laser are always utilized for the spectrum demodulation or intensity demodulation setups. When the resonance coupling occurs between the fundamental mode and the surface Plasmon mode, a sharp peak could be appeared in the transmission loss spectrum and used for calculating the refractive index of the target. SPR sensor based on many kinds of fibers, such as single mode fiber (SMF) [9], multimode fiber (MMF) [7] and conventional photonic crystal fiber (PCF) [11, 12, 13, 14, 15, 16] structures, have been demonstrated. But, it seems that the abovementioned structures exhibit some drawbacks. For examples, SPR sensors based on SMF and MMF always suffer from a less sensitivity and a low surface intensity due to the insufficient sharp transmission loss peak [9, 10]. PCF-based SPR sensors require a long response time due to the slow fluid filling speed. While tapered fiber based SPR sensor is fragile in handling [19].

To decrease the response time, side hole [20] and side polished [21, 22] designs were applied in building fiber SPR sensor. It seems that such designs could enhance both the response time and the sensitivity properties of sensors. However, there is still a large space for improvement. In this article, a novel high sensitive, fast responsive fiber SPR sensor design based on the side-opened suspended core fiber is proposed and analyzed. The struts' surface facing the opening hole is supposed to be uniformly deposited with an Au-film for realizing the surface plasmon resonance. Thus the low efficient, time-consuming metal film deposition process from fluids passing along the length of the holes of conventional side-closed suspended core fiber is avoided. Since the thickness and length of Au thin film could be controlled conveniently via the side opening in fiber, the single hole-coated fiber configuration provide a designing flexibility for the SPR sensing applications. In addition, this side opening configuration could ensure a fast response characteristic of less than 9s, which was provided in our previous reports [23, 24]. The fast response characteristic could be applied in real-time fluid detection, especially when the target is in the dynamic environments. By special designing the fiber structure, a SPR sensor with a wide detecting range and a maximum sensitivity of 2.3e-5 RIU is achieved in simulation, which is in the same level with the sensitivity of side-closed

Manuscript received June 13, 2014; revised Nov 30, 2014; accepted Dec. 14, 2014. Date of publication X X, XXXX; date of current version Dec. 14, 2014. This work was supported by National Natural Science Foundation of China (grant nos. 61405127, 61425007, 11174064, 61377090, and 61308027), China Postdoctoral Science Foundation (2014M562202), Shanxi Province Science Foundation for Youths(2014021023-1), Science Foundation of North University of China, Science & Technology Innovation Commission of Shenzhen/Nanshan (grants No.s KQCX20120815161444632, JCYJ20130329140017262, ZDSYS20140430164957664, KC2014ZDZJ0008A), and Pearl River Scholar Fellowships.

Guanjun Wang , Chao Wang, Jing Zhao, Changrui Liao, Shen Liu, xizhen Xu, Haijian Liang, Yiping Wang are with the Key Laboratory of Optoelectronic Devices and Systems of Ministry of Education and Guangdong Province, College of Optoelectronic Engineering, Shenzhen University(email: wangguanjun@163.com, travis.won@qq.com, 406434774@qq.com, Zhaojing090824@163.com, cliao@szu.edu.cn, 1518472969@qq.com, guoluoyin@gmail.com, ypwang@szu.edu.cn)

Guanjun Wang is also with the Shanxi Provincial Research Center for Opto-electronic Information and Instrument Engineering Technology, North University of China, taiyuan, 030051, China (e-mail: wangguanjun@163.com). The corresponding author is Yiping Wang (ypwang@szu.edu.cn)

suspended core fiber (1e-4RIU) [14]. The relationship of transmission loss spectrum characteristics, the thickness of Au film and the refractive index of target is also analyzed. Calculation results show that there is a close dependence among these parameters.

## II. GEOMETRY OF THE PROPOSED FIBER SPR SENSOR

Geometry of the proposed side-opened suspended core fiber-based SPR sensor is given in Fig.1. To accelerate the fluid filling and access the fiber core, side hole can be opened on the silica-based suspended core fiber by use of FIB [22] or selective etching [23] or femtosecond laser techniques[2]. In this paper, the opening hole of the suspended core fiber is assumed to be filled with a liquid target of refractive index  $n$ . For the purpose of ensuring a strong mode confinement and a fundamental mode transmission, the fiber struts are supposed to be a high index Ge-doped SiO<sub>2</sub> layer sandwiched between two layers consist of lower index pure SiO<sub>2</sub>. The suspended core is formed of the three struts at their intersection region at the center position of fiber. To stimulate the surface plasmon resonance, the inner surface of the opening hole could be uniformly deposited with the Au-film by SAVAC sputter [20] or chemical deposition method [19]. Here, the lateral length of Au film deposited section and the overall transmission loss of the proposed fiber SPR sensor could be controlled flexibly according to the actual demand. For reducing the calculation time, only the upper surface of the suspended core and the adjacent strut region is supposed to be Au film deposited. As has been proved in reference [14], this assumption doesn't influence the accuracy of the calculation results. The radius of the Ge-doped core and the thickness of the struts of Ge-doped SiO<sub>2</sub> and SiO<sub>2</sub> are denoted as  $R$ ,  $t_{Ge}$  and  $t_{SiO_2}$  respectively.

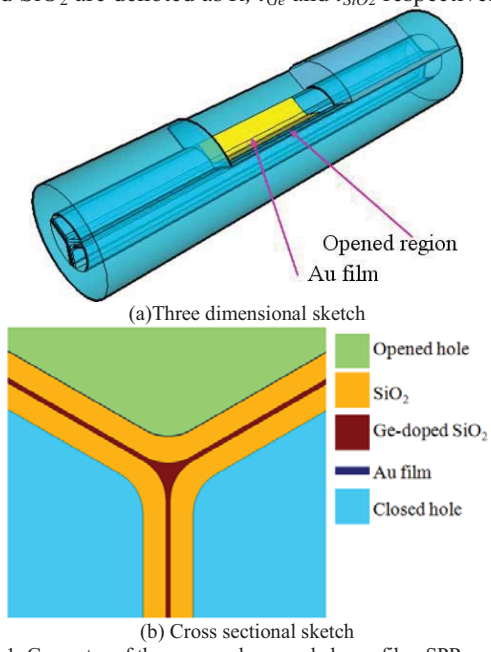


Fig.1. Geometry of the proposed suspended core fiber SPR sensor

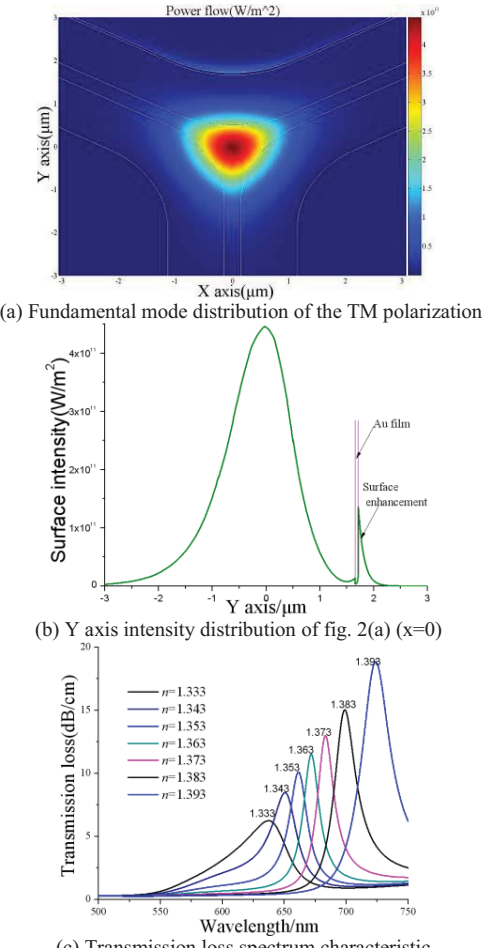


Fig.2. Characteristics of the proposed suspended core fiber-based SPR sensor ( $R_{core}=1200\text{nm}$ ,  $t_{Au}=50\text{nm}$ ,  $n=1.333\sim1.393$ ,  $\lambda=500\sim750\text{nm}$ ,  $t_{Ge}=300\text{nm}$ ,  $t_{SiO_2}=100\text{nm}$ ) (a) Fundamental mode distributions,  $\lambda=645\text{nm}$  (b)X axis intensity distribution of the fundamental mode ( $y=0$ ,  $\lambda=645\text{nm}$ ) (c) Transmission loss spectrum characteristic of the fundamental mode

The dielectric constant of the Au film here is got from the Drude model [23] and the refractive indices of SiO<sub>2</sub> and Ge-doped SiO<sub>2</sub> are got from the Sellmeier function [24]. The finite element method based software COMSOL multiphysics [14] and the perfectly matched layers boundary are utilized in simulation to find the complex effective mode index  $n_{eff}$  of the fiber modes over a wide wavelength range.  $n_{eff} = \text{Re}(n_{eff}) + i * \text{Im}(n_{eff})$ ,  $\text{Re}(n_{eff}) = \beta\lambda/2\pi$  and  $\text{Im}(n_{eff}) = \alpha\lambda/2\pi$ . Here  $\alpha$  means the transmission loss constant,  $\beta$  represents the propagation constant [11] and  $\lambda$  is the operating wavelength. The real part of  $n_{eff}$  reflects the propagation constant and the imaginary part of  $n_{eff}$  is proportional to the transmission loss. As the SPR effect is mainly related with the TM polarization, only the fundamental mode characteristic of the TM polarization is analyzed in this paper. Fig.2 (a,b) shows the mode distribution characteristic of the side-opened suspended core fiber with a layer of Au film ( $R_{core}=1200\text{nm}$ ,  $t_{Au}=50\text{nm}$ ,  $n=1.333$ ,  $\lambda=645\text{nm}$ ,  $t_{Ge}=300\text{nm}$ ,  $t_{SiO_2}=100\text{nm}$ ,  $\Delta=(t_{Ge}-t_{SiO_2})/t_{SiO_2}=1\%$ ). The inner surface of the side-opened hole is coated with Au film with thickness of  $t_{Au}$ . In fig.2, an enhanced and exponential damped field distribution appears at the outside surface of Au film, which is a characteristic of surface Plasmon excitation [14].

When the fiber fundamental mode energy is coupled into the Au film deposition region, the surface Plasmon mode could be excited. Tracking the transmission loss spectrum of the fundamental mode as a function of the operating wavelength, the transmission loss peak corresponding to the surface Plasmon resonance could be observed. Figure 2(c) shows the transmission spectrum characteristics, in which a sharp transmission loss peak appears within the operating waveband of 500nm~750nm. Monitoring the transmission loss spectrum characteristic, the refractive index of target could be calculated.

### III. ANALYSIS OF THE FIBER SPR SENSITIVITY

#### 3.1 Transmission loss spectrum characteristics

As the transmission loss spectrum characteristics of the fundamental mode is related with the thickness of Au film, fiber parameters and the refractive index of the target, those relations are analyzed firstly. Fig.3 (a-e) depicts the relation of transmission loss and the refractive index of target as a function of the wavelength and the thickness of Au film. It seems that a red-shift of peak wavelength and an increase of peak transmission loss appear with the increase of refractive index. While a red-shift of peak wavelength also occurs with the increase of the thickness of Au film. Therefore tracking the peak wavelength shift or the transmission loss at the fixed wavelength could distinguish the refractive index of the target. Depicting those relations could contribute to designing proper fiber SPR sensors for different demands.

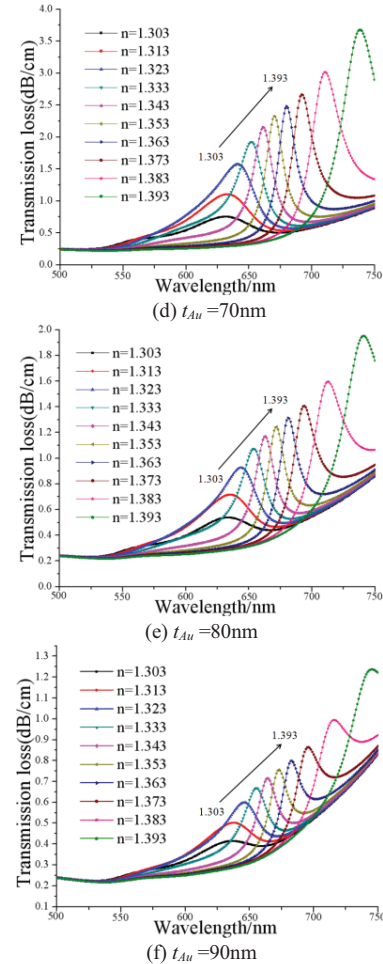
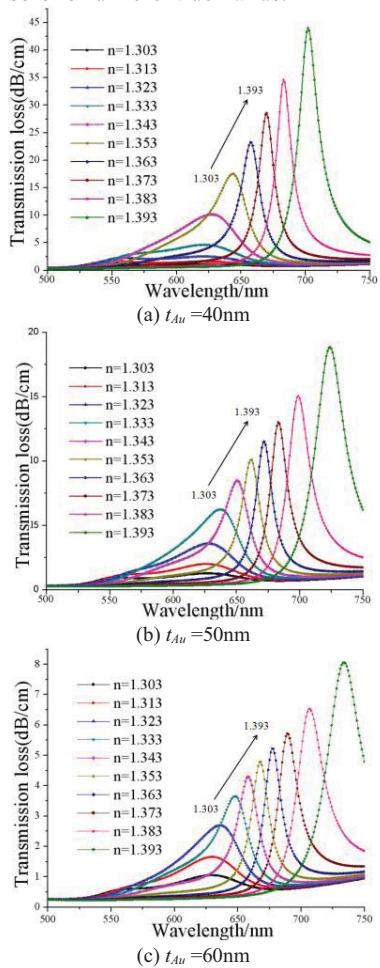
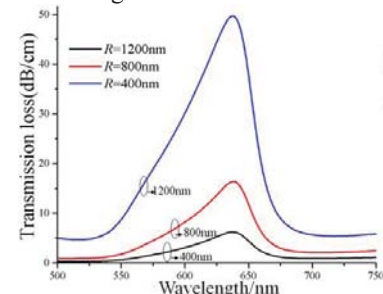
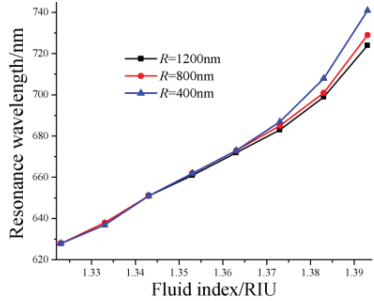


Fig.3 The relation of Transmission loss and fluid index Vs. different film thickness ( $R=1200\text{nm}$ ,  $t_{Ge}=300\text{nm}$ ,  $t_{SiO_2}=1000\text{nm}$ ,  $\lambda=500\text{--}750\text{nm}$ )  
 $n=1.303\text{--}1.393$  (a)  $t_{Au}=40\text{nm}$  (b)  $t_{Au}=50\text{nm}$  (c)  $t_{Au}=60\text{nm}$  (d)  $t_{Au}=70\text{nm}$  (e)  $t_{Au}=80\text{nm}$  (f)  $t_{Au}=90\text{nm}$

Fig.4(a) depicts the relation of the transmission loss and the fiber dimension. It seems that when the core radius  $R$  decreases from 1200nm to 400nm, the transmission loss increases. Fig. 4(b) shows that the fiber core size has little effect on the peak resonance wavelength when the filled fluid index is around 1.303~1.363. While the loss peak are separated when the filled fluid index becomes higher.



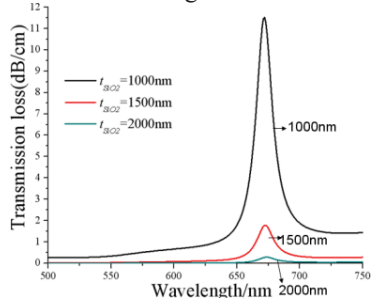
(a) Transmission loss vs. the core radius  $R$  ( $t_{Ge}=300\text{nm}$ ,  $t_{Au}=50\text{nm}$ )



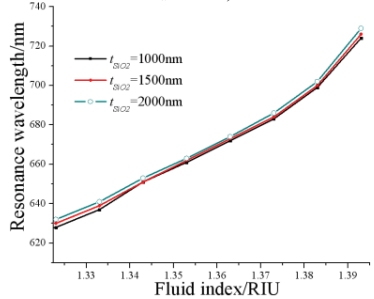
(b) Peak resonance wavelength vs. core radius  $R$  ( $t_{Ge} = 300\text{nm}$   $t_{Au} = 50\text{nm}$ )

Fig.4 Relation of transmission loss vs. the fiber parameter  $R$

Fig.5 (a) and fig.5 (b) shows the relation of the transmission loss and the struts' thickness. It seems that the change of strut's thickness has little effect on the resonance wavelength characteristic. As a thicker strut could ensure the fundamental mode transmission operation easily, a strut's thickness  $t_{SiO_2}$  of 1000nm is used in the following discussions.



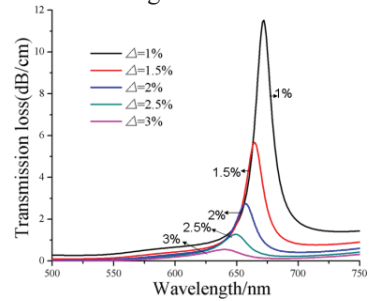
(a) Transmission loss vs. the thickness of the struts  $SiO_2$  ( $t_{Ge} = 300\text{nm}$   $t_{Au} = 50\text{nm}$ )



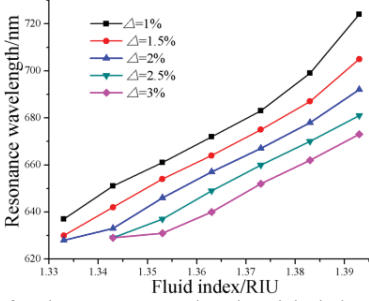
(b) Relation of peak resonance wavelength and the thickness of the struts  $SiO_2$  ( $t_{Ge} = 300\text{nm}$   $t_{Au} = 50\text{nm}$ )

Fig.5 Relation of transmission loss and the fiber parameter  $t_{SiO_2}$

Fig.6(a) reveals the relationship of transmission loss and index contrast  $\Delta$ . It looks that the peak wavelength of the transmission loss has little effect on the index contrast  $\Delta$  of Ge-doped  $SiO_2$  and pure  $SiO_2$ . Our results are consistent with the results of ref [12]. Considering all these factors, 1200nm, 1000nm, 300nm and 1% are taken for  $R$ ,  $t_{SiO_2}$ ,  $t_{Ge}$ ,  $\Delta$  respectively in the following simulation.



(a) Relation of transmission loss vs. the index contrast  $\Delta$  ( $t_{Ge} = 300\text{nm}$   $t_{Au} = 50\text{nm}$ )



(b) Relation of peak resonance wavelength and the index contrast  $\Delta$  ( $t_{Ge} = 300\text{nm}$   $t_{Au} = 50\text{nm}$ )

Fig.6 Relation of transmission loss and the index contrast  $\Delta$

To analyze the specific sensing characteristics of the proposed fiber SPR sensor, two sensing mechanisms based on monitoring the transmission loss spectrum peak shift and the transmission power change at the fixed wavelength are suggested and analyzed in the following sections.

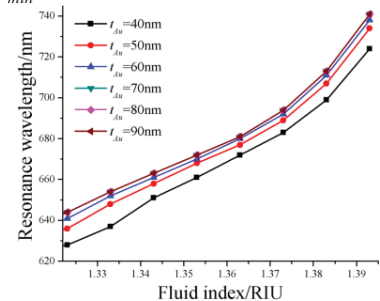
### 3.2 Sensing characteristics based on monitoring the peak shift of transmission loss spectrum

In this section, a quantitative sensitivity characteristics based on monitoring the transmission loss spectrum peak shift is analyzed according to the sensitivity function [14]

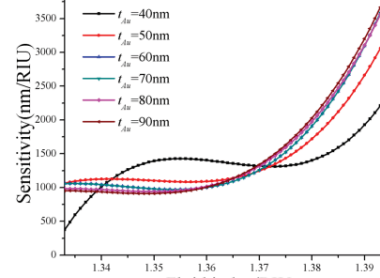
$$S = \frac{\Delta\lambda_{peak}}{\Delta n_a} \quad (1)$$

$$\gamma = \frac{\Delta\lambda_{min}}{S} \quad (2)$$

Here,  $S$  represents the sensitivity,  $\gamma$  means the sensing resolution,  $\Delta n_a$  (equals to 0.01) denotes the change of refractive index,  $\Delta\lambda_{min}$  represents the peak wavelength resolution,  $\Delta\lambda_{peak}$  is the shift of resonance wavelength. Here the peak wavelength resolution  $\Delta\lambda_{min}$  is assumed to be 0.1nm.



(a) Resonance wavelength shift vs. film thickness and refractive index



(b) Sensitivity characteristic of the SPR sensor (fitted result)

Fig.7 Sensitivity characteristics of the SPR sensor based on monitoring the transmission loss spectrum peak shift

Fig.7 (a) shows the fitted results of the resonance wavelength shift characteristics. We notice that some experimental reports claim that the sensitivity is related with the thin film thickness [6-13]. But we find that there is no much difference in resonance wavelength shift versus refractive index curve for

different thicknesses of film thickness in Fig.7 (a) as far as slopes are concerned. For quantitative analysis, Fig.7 (b) analyze the SPR sensitivity (fitted results) versus different fluid refractive indices. It means that the specific sensitivity characteristic has a little relation with the film thickness. A better sensitivity  $S$  of 3500 nm/RIU appears when the refractive index among 1.35~1.36 RIU. Here, the thickness of Au film is assumed to be 50nm. While the specific sensing resolution reported depends on the peak-wavelength resolution. Supposing the peak-wavelength resolution  $\Delta\lambda_{min}$  is 0.1nm, the corresponding sensitivity resolution could reach up to 2.3e-5 RIU. It is in the same level with that of the hole-closed suspended core fiber-based SPR sensor [14]. The resolution parameter is referred to the reference [11]. The data of 0.1nm originates from the sensing resolution of fiber spectrometer. It should be noted that the relation of sensitivity and film thickness is not obvious in current simulation condition. Further study on the relationship would be conducted by introducing more possible impact factors in modeling is in progress.

### 3.3 Sensing characteristics based on monitoring the transmission power at the fixed wavelength

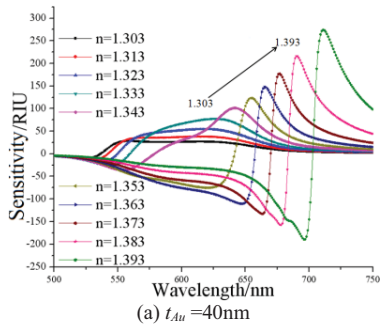
Here, another sensing mechanism based on monitoring the transmission power at the fixed wavelength is analyzed and compared. For this sensing mechanism, two sensitivity parameters ( $S$  and  $\gamma$ ) [15] are introduced for analysis.

$$S = (\Delta\alpha/\Delta n_a)/\alpha_{na} \quad (3)$$

$$\gamma = \Delta_p/S \quad (4)$$

Here,  $S$  denotes the sensitivity.  $\alpha_{na}$  represents the transmission loss, the refractive index of target is set as  $n_a$ ,  $\gamma$  means the sensing resolution. 1% change ( $\Delta_p$ ) of transmission power is assumed to be reliably measured. The difference of  $n_a$  equals to 0.001.

Fig.8 (a-f) shows the sensitivity characteristic of fiber SPR sensors with different Au film based on the second measurement method. It seems the specific sensitivity resolution is related with the specific operating wavelength and the thickness of Au film. With the increase of Au film thickness, the refractive index range of better sensitivity moves to a higher index region. Besides, the sensitivity resolution reaches its best when the operating wavelength is close to the resonance wavelength. It also appears the sensing resolution is straightly related with the refractive index of the target. With the increase of fluid index, the maximal sensitivity also increases too. The maximal sensitivity of 161/RIU appears when  $t_{Au}$  equals to 40nm and  $n$  equals to 1.363. The corresponding sensitivity resolution could reach up to 3.65e-5 RIU (supposing  $\Delta_p$  equals to 1%).



(a)  $t_{Au} = 40$  nm

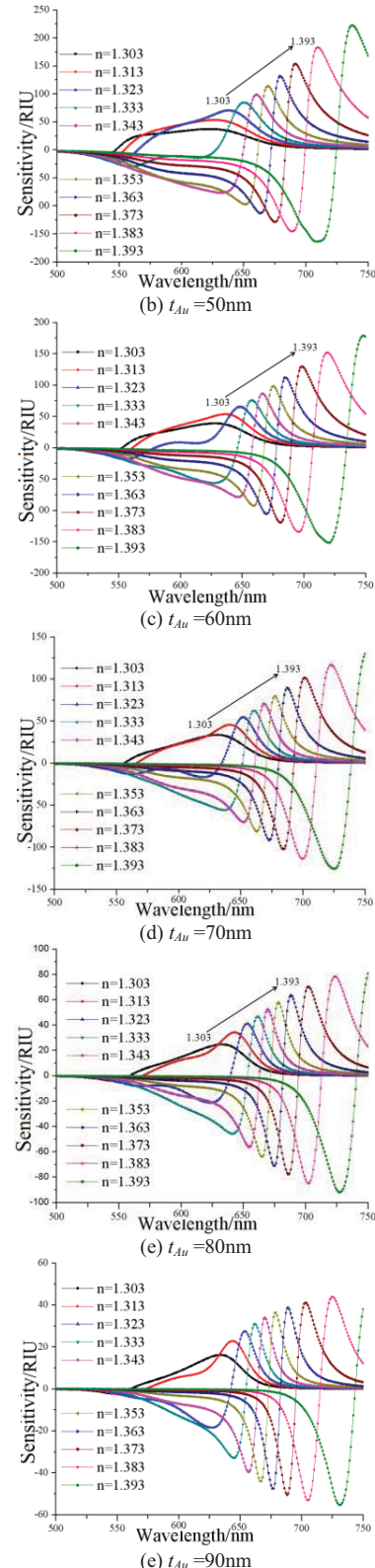


Fig.8 Sensitivity based on monitoring the transmission power at a fixed wavelength( $R=1200$ nm,  $t_{Ge}=300$ nm,  $t_{SiO_2}=1000$ nm,  $\Delta=1\%$ ) (a)  $t_{Au}=40$ nm (b)  $t_{Au}=50$ nm (c)  $t_{Au}=60$ nm (d)  $t_{Au}=70$ nm (e)  $t_{Au}=80$ nm (e)  $t_{Au}=90$ nm

By comparing the aforementioned two sensing mechanisms, we find that the maximal resolutions of both methods are in the same order of magnitude. However it seems the transmission loss spectrum peak shift sensing mechanism owns the

characteristics of wide sensing region. In addition, the detected refractive index range of maximal resolution based on the transmission loss spectrum peak shift sensing mechanism near 1.33 RIU (the index of water), which seems more useful for fluid detection. Furthermore, transmission loss spectrum peak shift sensing mechanism is also irrespective to the transmission power fluctuation. So, the SPR sensing mechanism based on transmission loss spectrum may exhibit more advantages in practical applications.

#### IV. CONCLUSIONS

Finally, a new side-opened suspended core fiber surface Plasmon resonance sensor with a single-hole Au-deposited film configuration is proposed and analyzed. The presented design has the following advantages: First, the removed side cladding facilitates the fabrication of the SPR sensor structure and speeds up the response. Second, the metallic film contributes to enhance the resonance status for SPR sensing. By suitably designing, a wide detected range with high optical sensitivity of 2.3e-5 RIU is achieved in simulation. The sensitivity value is close to that of the other reported counterpart without side opening.

#### References

- [1] J. Homola, "Present and future of surface plasmon resonance biosensors", *Anal Bioanal Chem*, vol.377, no.3, pp.528-539 ,Oct., 2003
- [2] A. J. C. Tubb, F. P. Payne, R. B. Millington, C. R. Lowe, "Single-mode optical fibre surface plasma wave chemical sensor", *Sensors and Actuators B: Chemical*, Vol.41, Issues 1–3, pp.71–79, June, 1997
- [3] A. Trouillet, C. Ronot-Trioli, C. Veillas, H. Gagnaire, "Chemical sensing by surface plasmon resonance in a multimode optical fibre", *Pure Appl Opt*, 5, 227,1996
- [4] A. Hassani and M. Skorobogatiy, "Design of the microstructured optical fiber-based surface plasmon resonance sensors with enhanced microfluidics", *Opt. Express*, vol. 14, no. 24, pp.11616-11621.Nov., 2006
- [5] Wang, Yiping,Tan, Xiaoling, Jin, Wei, et.al, "Temperature-controlled transformation in fiber types of fluid-filled photonic crystal fibers and applications", *OPTICS LETTERS*, vol. 35,no.1 pp.88-90, 2010
- [6] Wang, YP; Chen, JP; Rao, YJ , "Torsion characteristics of long-period fiber gratings induced by high-frequency CO<sub>2</sub> laser pulses" , *JOURNAL OF THE OPTICAL SOCIETY OF AMERICA B-OPTICAL PHYSICS*,vol.22,no.6,pp 1167-1172, 2005
- [7] Chao Wang, Wa Jin, Changrui Liao, Jun Ma, Wei Jin, Fan Yang, Hoi Lut Ho, Yiping Wang, "Highly birefringent suspended-core photonic microcells for refractive-index sensing", *Applied Physics Letters*,vol. 105,no.6, pp.0611051-0611054, Aug. 2014.
- [8] A. Hassani, M. Skorobogatiy, Design criteria for the microstructured optical fiber-based surface plasmon resonance sensors, *J. Opt. Soc. Am. B*,vol.24,no.6,pp.1423-1429, 2007.
- [9] Bertrand Gauvreau, Alireza Hassani, Majid Fassi Fehri, Andrei Kabashin, and Maksim Skorobogatiy, "Photonic bandgap fiber-based Surface Plasmon Resonance sensors", *Optics Express*, Vol. 15, Issue 18, pp. 11413-11426, 2007
- [10] Markus Hautakorpi, Maija Mattinen, and Hanne Ludvigsen, "Surface-plasmon-resonance sensor based on three-hole microstructured optical fiber", *Optics Express*, Vol. 16, Issue 12, pp. 8427-8432, 2008,
- [11] Chunying Guan, Yang Wang, Libo Yuan, "Multi-hole Optical Fiber Surface Plasmon Resonance Sensor", *Journal of Physics: Conference Series*, vol.276, no.012057, pp.1-6, 2011
- [12] C. Perrotton, N. Javahiry, M. Slaman, B. Dam, And P. Meyrueis, "Fiber optic Surface Plasmon Resonance sensor based on wavelength modulation for hydrogen sensing", *OPTICS EXPRESS*, vol. 19, no. S6, pp. A1175-A1183, Nov., 2011
- [13] Claire Gu, Chao Shi, He Yan, "Recent Advance in Fiber SERS Sensors", *Photonic Fiber and Crystal Devices: Advances in Materials and Innovations in Device Applications II*, Proc. of SPIE Vol. 7056, 70560H , 2008
- [14] S. Smolka, M. Barth, and O. Benson, "Selectively coated photonic crystal fiber for highly sensitive fluorescence detection," *Applied Physics Letters*, vol. 90, no. 11, Article ID 111101, 2007.
- [15] Lin HY, Huang CH, Cheng GL, Chen NK, Chui HC, "Tapered optical fiber sensor based on localized surface plasmon resonance", *Opt Express*. vol.20, no. 19, pp.21693-21701. Sep., 2012
- [16] Anna Wang, Andrew Docherty, Boris T. Kuhlmeier, Felicity M. Cox, Maryanne C. J. Large, "Side-hole fiber sensor based on surface plasmon resonance," *Optics Letters*, Vol. 34, Issue 24, pp. 3890-3892 (2009)
- [17] LUO Yun-han, CHEN Xiao-long, XU Meng-yun, GE Jia, ZHANG Yi-long, HE Yong-hong, TANG Jie-yuan, YU Jian-hui, ZHANG Jun, CHEN Zhe, CHEN Xing-dan, "Spectra Modulated Surface Plasmon Resonance Sensor Based on Side Polished Multi-Mode Optical Fiber", *SPECTROSCOPY AND SPECTRAL ANALYSIS*, vol.34,no.03,pp.577-581, 2014
- [18] Lin HY1, Tsai WH, Tsao YC, Sheu BC, "Side-polished multimode fiber biosensor based on surface plasmon resonance with halogen light". *Appl Opt*. vol.46,no.5,pp800-806, Feb., 2007
- [19] Guanjun Wang, Jiansheng Liu, Yi Yang,Zheng Zheng, Jing Xiao, Ruichao Li, "Gas Raman sensing with multi-opened-up suspended core fibre". *Applied Optics*, vol.50, no.31, pp.6026-6032, May, 2011
- [20] Guanjun Wang, Jiansheng Liu, Yi Yang,Zheng Zheng, Jing Xiao, "A fluidic sensor based on the side-opened and suspended dual-core fiber", *Applied Optics*, vol.51, no.15, pp.3096-3103, May.2012
- [21] Cristiano M B Cordeiro, Christiano J S de Matos, Eliane M dos Santos, Alexandre Bozolan, Jackson S K Ong, Tiloni Facincani, Giancarlo Chesini, Alfredo R Vaz, Carlos H Brito Cruz, "Towards practical liquid and gas sensing with photonic crystal fibres: side access to the fibre microstructure and single-mode liquid-core fibre", *Meas. Sci. Technol*. Vol.18, no.10, pp.3075-3081,Feb., 2007
- [22] Zhu W, Shi T, Tang Z, Gong B, Liao G, Tully J, "Dynamic selective etching: a facile route to parabolic optical fiber nano-probe". *Opt Express*. vol.21, no.6, pp.6919-6927, Mar., 2013
- [23] P. B. Johnson and R. W. Christy, "Optical constants of the noble metals", *Phys. Rev. B* 6(12), 4370–4379 (1972).
- [24] Weber M J, "Hand Book of Optical Materials", CRC Press LLC,2003



**Guanjun Wang** received the B.S.degree in electronic science and technology and M.S. degree in physical electronics from Zhengzhou University, Henan, China in2005 and 2008, and the Ph.D. degree in optical engineering from Beihang University, Beijing, China, in 2012.

After the graduation, he attended the North University of China as a lecturer.

He is currently a postdoctoral researcher at the institute of Optoelectronic Devices and Systems of Ministry of Education and Guangdong Province, College of Optoelectronic Engineering, Shenzhen University  
His research interests include fiber biochemical sensors and fiber grating.



**Yiping Wang** (M'04–SM'06) received the B.S. degree in Precision Instrument Engineering from Xi'an Institute of Technology, Xi'an, China, in 1995, and the M.S. degree in Precision Instrument and Mechanism and the Ph.D. degree in Optical Engineering from Chongqing University, China, in 2000 and 2003, respectively, where he received the prestigious award of The National Excellent Doctoral Dissertations of China.

In 2003, he joined the Department of Electronics Engineering, Shanghai Jiao Tong University, China, as a postdoctoral research fellow and an associate professor. In 2005, he joined the Department of Electrical Engineering, Hong Kong Polytechnic University, Hong Kong, as a postdoctoral research fellow and a research fellow. In 2007, he joined the Institute of Photonic Technology, Jena, Germany as a Humboldt research fellow. In 2009, he joined the Optoelectronics Research Centre, University of Southampton, U.K. as a Marie Curie Fellow. Since 2012, he has been with Shenzhen University as a Distinguished Professor and a Pearl River Scholar. His current research interests focus on optical fiber sensors, in-fiber gratings, photonic crystal fibers, and fluid-filling technologies. He has authored or coauthored 1 book, 9 patent applications, and more than 150 journal and conference papers with a SCI citation of more than 1200 times.

Dr. Wang is currently a senior member of IEEE, the Optical Society of America, and the Chinese Optical Society.

# Long Period Fiber Gratings Written in Photonic Crystal Fibers by Use of CO<sub>2</sub> Laser

Yiping WANG\*, Changrui LIAO, Xiaoyong ZHONG, Jiangtao ZHOU, Yingjie LIU,  
Zhengyong LI, Guanjun WANG, and Kaiming YANG

*Key Laboratory of Optoelectronic Devices and Systems of Ministry of Education/Guangdong Province, Shenzhen University, Shenzhen, 518060, China*

\*Corresponding author: Yiping WANG      E-mail: ypwang@szu.edu.cn

**Abstract:** Photonic crystal fibers are usually divided into two different types of fibers: solid-core photonic crystal fibers (PCFs) and air-core photonic bandgaps fibers (PBFs). We presented the fabrication methods and applications of long period fiber gratings (LPFGs) written in these two types of photonic crystal fibers by use of a CO<sub>2</sub> laser. A stain sensor with a high sensitivity was demonstrated by use of an LPFG written in solid-core PCFs. An in-fiber polarizer based on an LPFG was fabricated by use of a focused CO<sub>2</sub> laser beam to notch periodically on a PCF. A novel LPFG was written in an air-core PBF by use of a CO<sub>2</sub> laser to collapse periodically air holes in the fiber cladding.

**Keywords:** Long period fiber gratings, fiber Bragg gratings, photonic crystal fibers, photonic bandgap fibers, CO<sub>2</sub> lasers

---

Citation: Yiping WANG, Changrui LIAO, Xiaoyong ZHONG, Jiangtao ZHOU, Yingjie LIU, Zhengyong LI, *et al.*, "Long Period Fiber Gratings Written in Photonic Crystal Fibers by Use of CO<sub>2</sub> Laser," *Photonic Sensors*, DOI: 10.1007/s13320-013-0120-9.

---

## 1. Introduction

Optical fiber gratings already play a vital role in the field of the optical communications and sensors. There are two types of in-fiber gratings: fiber Bragg gratings (FBGs) with periodicities of the order of the optical wavelength [1, 2] and long period fiber gratings (LPFGs) with periodicities of several hundred wavelengths [3–7]. Various fabrication methods, such as UV laser exposure [3], CO<sub>2</sub> laser irradiation [4, 8–11], electric arc discharge [12], femtosecond laser exposure [13], mechanical microbend [14], and etched corrugation [15], have been demonstrated to write LPFGs in different types of optical fibers. Compared with the ultraviolet (UV)

laser exposure technique, the CO<sub>2</sub> laser irradiation technique is much more flexible and low cost because no photosensitivity and any other pretreated processes are required to write a grating in the glass fibers [4, 8–10]. Moreover, the CO<sub>2</sub> laser irradiation process can be controlled to generate complicated grating profiles via the well-known point-to-point technique without any expensive masks. This technique could be, hence, used to write LPFGs in almost all types of fibers including pure-silica photonic crystal fibers (PCFs). We reviewed the recent development of the CO<sub>2</sub>-laser-induced LPFGs.

Over the past decade, photonic crystal fibers have attracted a great deal of interest due to their

unique microstructures and optical properties [16]. Photonic crystal fibers are usually divided into two different types of fibers: solid-core photonic crystal fibers (PCFs) and air-core photonic bandgaps fibers (PBFs). This paper reviews the fabrication methods and applications of LPFGs written in both solid-core PCFs and air-core PBFs by use of a CO<sub>2</sub> laser.

## 2. CO<sub>2</sub> laser irradiation techniques for writing LPFGs

Since Davis *et al.* reported the first CO<sub>2</sub>-laser-induced LPFG in a conventional glass fiber in 1998 [8, 17], various CO<sub>2</sub> laser irradiation techniques have been demonstrated and improved to write high-quality LPFGs in different types of optical fibers, such as conventional glass fibers, PCFs, and PBFs, and to achieve unique grating properties. This section reviews the development of the CO<sub>2</sub> laser irradiation techniques for writing LPFGs in conventional glass fibers, solid-core PCFs, and air-core PBFs.

Typically, in most of LPFG fabrication setups employing a CO<sub>2</sub> laser [8, 17–19], as shown in Fig. 1, the fiber is periodically moved along its axis direction via a computer-controlled translation stage, and the CO<sub>2</sub> laser beam irradiates periodically the fiber through a shutter controlled by a same computer. A light source and an optical spectrum analyzer are employed to monitor the evolution of the grating spectrum during the laser irradiation. This is a typical point-to-point technique for writing a grating in an optical fiber. Such an LPFG fabrication system usually requires an exactly controlling of both the shutter and the translation stage to achieve a good simultaneousness of the laser irradiation and the fiber movement. Additionally, the vibration of the employed fiber, resulting from the periodic movement of the fiber, could occur during the irradiation of the CO<sub>2</sub> laser beam, which is a disadvantage to the stability and repeatability of the grating fabrication.

Rao *et al.* demonstrated, for the first time, a

novel grating fabrication system based on 2-dimentional scanning of the CO<sub>2</sub> laser beam [9, 10], as shown in Fig. 2. One end of the employed fiber was fixed, and the other end was attached to a small weight to provide a constant prestrain in the fiber, thus enhancing the efficiency of the grating fabrication. The focused high-frequency CO<sub>2</sub> laser pulses scanned periodically across the employed fiber along the X direction and then shifted a grating pitch along the Y direction, i.e. the fiber axis, to create the next grating period by means of 2-dimensional optical scanners under the computer control. Compared with the typical point-to-point fabrication system shown in Fig. 1, no exactly simultaneous controlling was required in such a system because the employed fiber was not periodically moved along the fiber axis. Such a system could write high-quality LPFGs with a near-zero insertion loss.

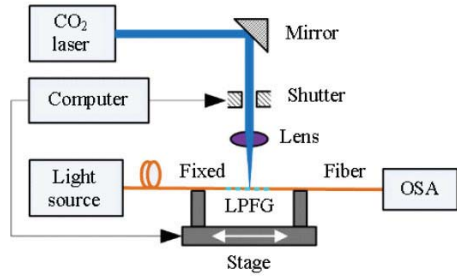


Fig. 1 Schematic diagram of a normal LPFG fabrication system based on the typical point-to-point technique employing a CO<sub>2</sub> laser.

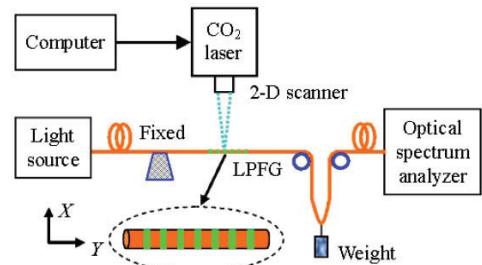


Fig. 2 Schematic diagram of an LPFG fabrication system based on 2-dimentional scanning of focused high-frequency CO<sub>2</sub> laser pulses [9].

The authors recently developed an improved LPFG fabrication system based on the point-to-point

technique employing a CO<sub>2</sub> laser, as shown in Fig. 3, combining with the advantages of the two fabrication systems illustrated in Figs. 1 and 2. A CO<sub>2</sub> laser beam was, through a shutter and a mirror, focused on the fiber by a cylindrical lens with a focus length of 254 mm. Both the mirror and the lens were mounted on a linear air-bearing motor stage (ABL 1500 from Aerotech). A Labview program has been developed to control simultaneously the operation of both the linear motor stage and the shutter so that the fiber was exposed once as soon as the focused laser beam was shifted by a grating pitch via the mirror. In other words, the fiber was not periodically moved in this system, which overcame the disadvantage of the fiber vibration, resulting from the periodic movement of the fiber, in the normal point-to-point grating fabrication setup shown in Fig. 1. A desired LPFG can be achieved as soon as the required fabrication parameters, such as the grating pitch, number of grating periods, exposure time per period, and number of exposure cycles, are input via an operation interface illustrated in Fig. 3(b). Such an improved fabrication

system could potentially be integrated with a fiber drawing tower to write continuously a large number of LPFGs during drawing a fiber.

CO<sub>2</sub> laser irradiation may cause unexpected physical deformation, resulting from laser heating, of fiber structures during LPFG fabrication. Such a physical deformation is usually avoided to decrease the insertion loss of the written LPFGs during early grating fabrications with a CO<sub>2</sub> laser [8, 9, 17]. Wang *et al.* reported a novel technique for writing an asymmetric LPFG by means of carving periodic grooves on the surface of an optical fiber with a focused CO<sub>2</sub> laser beam [20], as shown in Fig. 4. Physical deformation, i.e. periodic grooves, in such an asymmetric LPFG, did not cause a large insertion loss because these grooves were totally confined within the outer cladding and had no influence on the light transmission in the fiber core. Moreover, such grooves enhanced the efficiency of the grating fabrication and introduced unique optical properties, e.g. extremely high strain sensitivity, into the gratings [20, 21]. Further investigations discovered that the insertion loss of LPFGs was mainly due to the nonperiodicity and the disorder of refractive index modulations in the gratings.

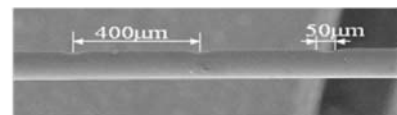


Fig. 4 Photograph of an asymmetric LPFG with periodic grooves [20].

### 3. To write LPFGs in solid-core PCFs

Over the past decade, PCFs have attracted a great deal of interest due to their unique microstructures and optical properties [16, 22]. Since Eggleton *et al.* reported the first grating in a photosensitive PCF with a Ge-doped core in 1999 [23], a large number of gratings have been written in different types of PCFs with or without photosensitivity by the use of various fabrication techniques such as UV laser exposure [24], CO<sub>2</sub> laser irradiation [18, 25–27], electric-arc discharge

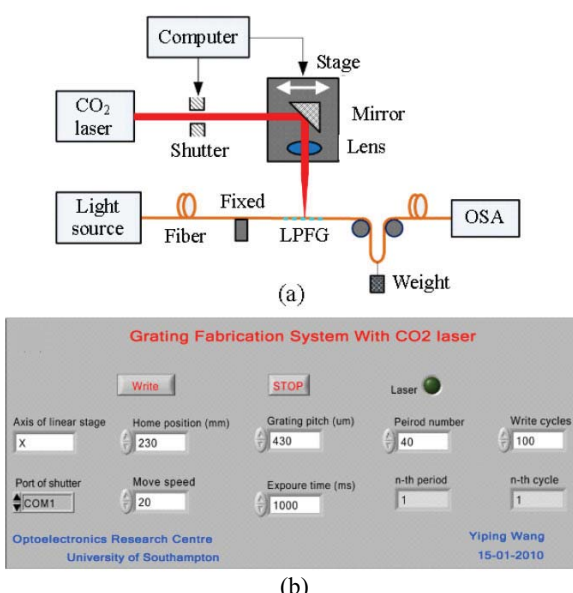


Fig. 3 LPFG fabrication system with a CO<sub>2</sub> laser: (a) the schematic diagram of an improved LPFG fabrication system employing a CO<sub>2</sub> laser and (b) the operation interface of the fabrication system.

[28], femtosecond laser exposure [29, 30], and two-photon absorption [31]. UV laser exposure is a common technique for writing an FBG/LPFG in a Ge-doped PCF with a photosensitivity [23, 32, 33]. In contrast, CO<sub>2</sub> laser irradiation can be used to write high-quality LPFGs with a near-zero insertion loss in different types of optical fibers without photosensitivity, including solid-core PCFs and air-core PBFs [18, 25–27].

As shown in Fig. 5, an asymmetrical LPFG with periodic grooves was written in a pure-silica large-mode-area PCF by the use of a focused CO<sub>2</sub> laser beam [26, 27]. The repeated scanning of the focused CO<sub>2</sub> laser beam created a local high temperature in the fiber, which led to the collapse of air holes and the gasification of SiO<sub>2</sub> on the fiber surface. Consequently, periodic grooves with a depth of about 15 μm and a width of about 50 μm were created on the fiber, as shown in Fig. 5(b). Such grooves, especially the collapse of air holes, induced periodic refractive index modulations along the fiber axis due to the well-known photoelastic effect, thus creating an LPFG in the PCF. This asymmetrical LPFG has unique optical properties, e.g. high strain sensitivity, low temperature sensitivity and high polarization dependence [26, 27].

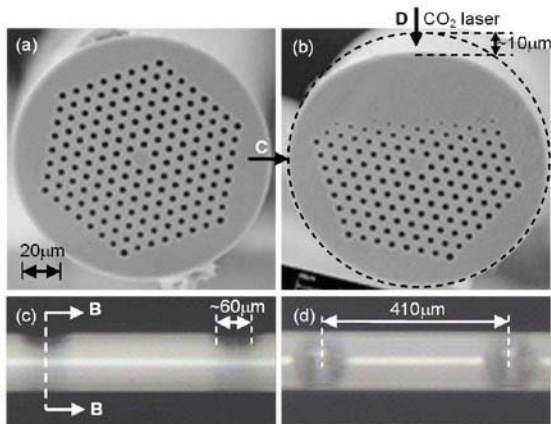


Fig. 5 Asymmetrical LPFG with periodic grooves in a pure-silica PCF [26].

A highly compact LPFG with only 8 periods and a short total length of 2.8 mm was written in a pure-silica large-mode-area PCF by the common

point-by-point technique employing a CO<sub>2</sub> laser [18], in which clear physical deformation was also observed. In contrast, another LPFG without geometrical deformation and fiber elongation was written in an endless single-mode PCF by periodic stress relaxation resulting from CO<sub>2</sub> laser irradiation [34]. Moreover, an LPFG pair has been successfully created in a pure-silica PCF with a CO<sub>2</sub> laser to develop a stain sensor. A novel coupled local-mode theory could be used to model and analyze this type of PCF-based LPFGs with the periodic collapse of air holes [35]. Such a theory is based on calculating the variations of local-mode profiles and propagation constants over the perturbed regions and on solving the coupled local-mode equations to obtain a quantitative description of the intermodal energy exchange.

#### 4. To write LPFGs in air-core PBFs

As discussed above, a large number of gratings have been demonstrated in different types of PCFs by the use of various fabrication techniques. All of these gratings, however, were written in index-guiding PCFs, instead of bandgap-guiding fibers. Recently, PBF-based gratings were also written in a new kind of bandgap-guiding fibers such as fluid-filled PBFs [36–40] and all-solid PBFs [41]. However, PBF-based gratings have not been reported in air-core PBFs until recent success in writing a high-quality LPFG in an air-core PBF [42].

Since almost 100% of the light propagates in the air holes of an air-core PBF and not in the glass, PBF-based gratings offer a number of unique features including: high dispersion, low nonlinearity, reduced environmental sensitivity, unusual mode coupling, and new possibilities for long-distance light-matter interactions (by incorporating additional materials into the air-holes). The bandgap-based grating in air-core PBFs, therefore, represents an important platform technology with manifest applications in areas such as communications, fiber lasers and sensing. Periodic index modulations are

usually required to realize mode coupling in in-fiber gratings. Although this presents no difficulties in conventional glass fibers [8, 9], solid-core PCFs [23, 26], and solid-core PBFs [37], it is very difficult, even impossible, to directly induce index modulations in an air-core PBF due to the air core structure, thereby seriously obstructing the development of PBF-based gratings over the past decade.

As shown in Fig. 6, we reported what is believed to be the first example of gratings written in an air-core PBF by the use of a focused CO<sub>2</sub> laser beam to periodically deform/perturb air holes along the fiber axis in 2008 [42, 43]. This reveals that it is experimentally possible to write a grating in an air-core PBF. Both the excellent stability of the CO<sub>2</sub> laser power and the good repeatability of optical scanning are very critical to writing a high-quality grating in an air-core PBF. An experimental setup being similar to that in Fig. 2 was used to write an LPFG in an air-core PBF (Crystal-Fiber's HC-1500-02). Compared with the fabrication parameters for writing a grating in a solid-core PCF [26, 27], a lower average laser power of about 0.2 W and shorter total time of laser irradiation were used to write an LPFG in an air-core PBF [42]. The focused CO<sub>2</sub> beam scanned periodically the PBF with a line speed of scanning of 2.9 mm/s, causing the ablation of glass on the fiber surface and the partial or complete collapse of air holes in the cladding due to the CO<sub>2</sub>-laser-induced local high temperature, as shown in Fig. 6. The outer rings of air holes in the cladding, facing to the CO<sub>2</sub> laser irradiation, were largely deformed; however, little or no deformation was observed in the innermost ring of air-holes and in the air core. As a result, periodic index modulations were achieved along the fiber axis due to the photoelastic effect, thus creating a novel LPFG in the air-core PBF. For the LPFG written in air-core PBF, periodic perturbations of the waveguide (geometric) structure could be the dominant factor that causes resonant mode coupling, although the stress-relaxation-induced index

variation may also contribute a little.

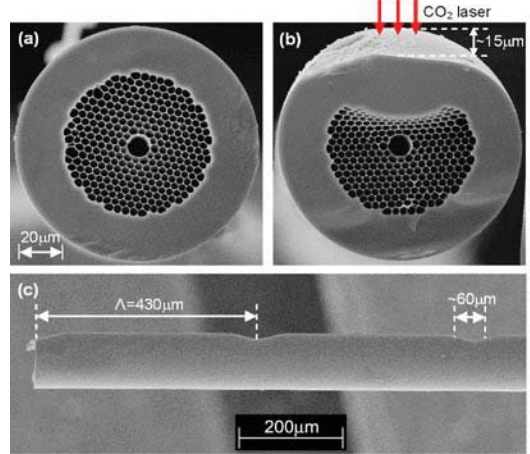


Fig. 6 Cross-section image of an air-core PBF (a) before and (b) after CO<sub>2</sub> laser irradiating, (c) side image of an LPFG written in the air-core PBF, where about two periods of the LPFG are illustrated [42].

Normal LPFGs written in the index-guiding fibers have a positive relationship between the resonant wavelength and grating pitch. In contrast, the LPFGs written in the bandgap-guiding air-core PBF have the distinct phase matching condition as a function of the wavelength. As shown in Fig. 7, the resonant wavelengths of the LPFGs written in an air-core PBF decrease with an increase in the grating

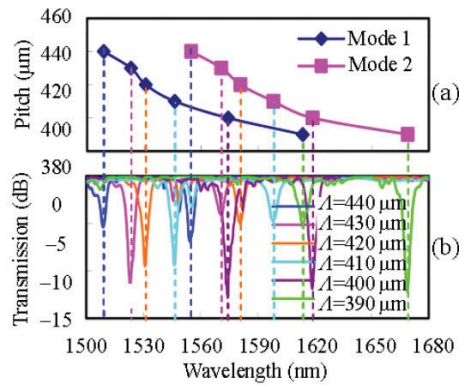


Fig. 7 Transmission spectra of LPFGs written in air-core PBFs: (a) the relationship between the pitch of each LPFG and the corresponding resonant wavelength, and (b) transmission spectra of six LPFGs with different grating pitches, where two attenuation dips for each LPFG are observed from 1500 nm to 1680 nm, indicating that the fundamental mode is coupled to two different higher order modes [42].

pitch, which is opposite to the LPFGs written in the index-guiding fibers [43]. Moreover, this PBF-based LPFG has unique optical properties such as very large polarization dependent loss (PDL), large strain sensitivity, and very small sensitivity or insensitivity to the temperature, bend and external refractive index, as shown in Fig. 4 in [42]. Further investigations are being done to well understand resonant mode coupling and unique optical properties in the gratings written in air-core PBFs.

Moreover, three years later, A. Iadicicco *et al.* reported on another fabrication method of LPFGs in hollow-core air-silica PBFs by using the pressure assisted electrode arc discharge (EAD) technique [44], as shown in Fig. 8. The EAD procedure combining with pressure actuation inside fiber holes enables the modification of the hole size and shape in both core and cladding regions avoiding the collapse of holes and thus acts as a useful tool to impress effective refractive index modulation leading to low loss gratings. Periodically repeated EAD treatments permit the fabrication of LPFG-based devices in hollow core optical fibers enabling new functionalities hitherto not possible. Here, the experimental demonstration of the LPFG prototype with different characteristics exhibiting attenuation bands with the depth up to 12 dB is reported.

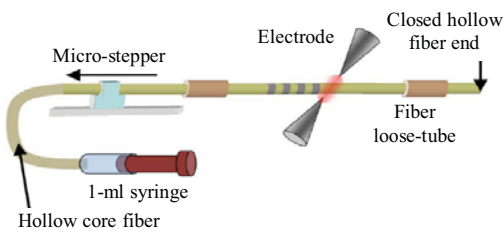


Fig. 8 Schematic diagram of LPFG fabrication employing a hollow-core PBF by using the pressure assisted EAD technique [44].

## 5. Applications of gratings writing in PCFs

### 5.1 Strain sensors

The CO<sub>2</sub>-laser-induced LPFGs with physical

deformation exhibit unique optical properties while a tensile strain is applied, thus being excellent strain sensing elements. As shown in Fig. 9, periodic microbends will be induced while a CO<sub>2</sub>-laser-induced LPFG with asymmetric grooves is stretched [20, 21, 27]. Such stretch-induced microbends effectively enhance refractive index modulation in the gratings. As a result, such an LPFG had an extremely high strain sensitivity of  $-102.89 \text{ nm}/\mu\epsilon$  [20, 21], which was two orders of magnitude higher than that of other CO<sub>2</sub>-laser-induced LPFGs without physics deformation in the same type of fibers [9].

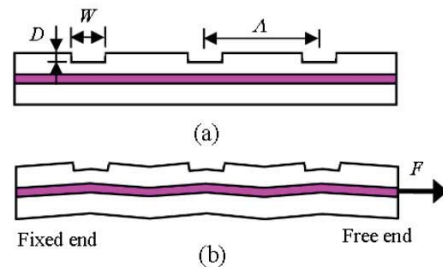


Fig. 9 Schematic diagram of the CO<sub>2</sub>-laser-carved LPFG with asymmetric grooves (a) before and (b) after a stretching force is applied to the grating [20].

An LPFG strain sensor with a high strain sensitivity of  $-7.6 \text{ pm}/\mu\epsilon$  and a very low temperature sensitivity of  $3.91 \text{ pm}/^\circ\text{C}$  has been developed by the use of the focused CO<sub>2</sub> laser beam to carve periodic grooves on the large mode area PCF [27]. Such a strain sensor could effectively reduce the cross-sensitivity between the strain and temperature, and the temperature-induced strain error obtained was only  $0.5 \mu\epsilon/^\circ\text{C}$  without temperature compensation. Another strain sensor based on a CO<sub>2</sub>-laser-induced LPFG pair in a PCF exhibited a high strain sensitivity of about  $-3 \text{ pm}/\mu\epsilon$  and a low temperature sensitivity of about  $4.6 \text{ pm}/^\circ\text{C}$  [45]. Theoretical analysis reveals that a simple, low-cost LPG sensor with approximately zero temperature sensitivity but large strain sensitivity could be realized by selecting an appropriate grating period [46].

### 5.2 Polarizers

Compared with bulk waveguide polarizers,

in-fiber polarizers are desirable devices in all-fiber communication systems because of their low insertion loss and compatibility with the optical fiber. The CO<sub>2</sub>-laser-induced LPFGs have clear polarization dependence due to their asymmetric refractive index profile, resulting from single-side laser irradiation, within the cross-section of the gratings [20, 21], thus being a potential in-fiber polarizing device. Moreover, the polarization dependence of the CO<sub>2</sub>-laser-induced LPFG with periodic grooves can be greatly enhanced by applying a tensile strain [21] or increasing temperature[47]. So a promising in-fiber polarizer based on an LPFG was developed by the use of a focused CO<sub>2</sub> laser beam to collapse or perturb periodically air holes in a pure-silica PCF, as shown in Fig. 10 [26]. In practical operation, a stretch strain was applied to the LPFG-based polarizer to enhance the polarization dependence of the grating. As a result, the maximum PDL and the maximum polarization extinction ratio of the LPFG were increased to 27.27 dB and 22.83 dB, respectively, as shown in Fig. 8. Such an LPFG-based polarizer thus exhibited a high polarization extinction ratio of more than 20 dB over a wide wavelength range of about 11 nm near the communication wavelength of 1550 nm [26]. Moreover, this polarizer had a very low temperature sensitivity of 3.9 pm/°C, which overcame the disadvantages of the temperature sensitivity in other in-fiber polarizers created in conventional glass fibers.

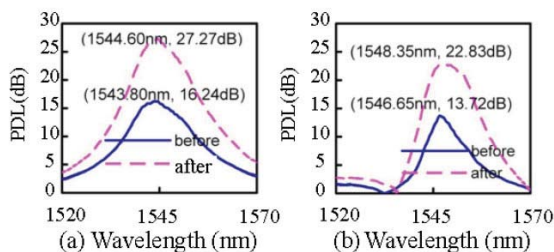


Fig. 10 Polarization dependence, (a) PDL and (b) polarization extinction ratio (PER), of the LPFG-based polarizer before (dashed curve) and after (solid curve) a stretch strain of 500  $\mu\text{e}$  is applied [26].

## 6. Conclusions

LPFGs could be written in different photonic crystal fibers, including solid-core PCFs and air-core PBGs by use of a focused laser beam. Compared with the UV laser exposure technique, the CO<sub>2</sub> laser irradiation technique is much more flexible and low cost because no photosensitivity and any other pretreated processes are required to induce a grating in the glass fibers. Moreover, the CO<sub>2</sub> laser irradiation process can be controlled to generate complicated grating profiles via the well-known point-to-point technique without any expensive masks. In-fiber gratings written in PCFs have found promising sensing and communication applications.

## Acknowledgment

This work was supported by the Distinguished Professors Funding from Shenzhen University, the National Science Foundation of China (Grant 11174064), and the Science & Technology Innovation Commission of Shenzhen (Grant KQCX20120815161444632).

**Open Access** This article is distributed under the terms of the Creative Commons Attribution License which permits any use, distribution, and reproduction in any medium, provided the original author(s) and source are credited.

## References

- [1] Y. J. Rao, "In-fibre Bragg grating sensors," *Measurement Science & Technology*, vol. 8, no. 4, pp. 355–375, 1997.
- [2] C. R. Liao and D. N. Wang, "Review of femtosecond laser fabricated fiber Bragg gratings for high temperature sensing," *Photonic Sensors*, vol. 3, no. 2, pp. 97–101, 2013.
- [3] A. M. Vengsarkar, P. J. Lemaire, J. B. Judkins, V. Bhatia, T. Erdogan, and J. E. Sipe, "Long-period fiber gratings as band-rejection filters," *Journal of Lightwave Technology*, vol. 14, no. 1, pp. 58–65, 1996.
- [4] Y. Wang, "Review of long period fiber gratings

- written by CO<sub>2</sub> laser," *Journal of Applied Physics*, vol. 108, no. 8, pp. 081101-1–081101-18, 2010.
- [5] Y. Gu and K. Chiang, "Effects of average index variation in apodized long-period fiber gratings," *Photonic Sensors*, vol. 3, no. 2, pp. 102–111, 2013.
- [6] J. Ju and W. Jin, "Long period gratings in photonic crystal fibers," *Photonic Sensors*, vol. 2, no. 1, pp. 65–70, 2012.
- [7] J. Canning, N. Groothoff, K. Cook, M. Stevenson, J. Holdsworth, M. Lancry, *et al.*, "Grating writing in structured optical fibers," *Photonic Sensors*, vol. 1, no. 3, pp. 199–203, 2011.
- [8] D. D. Davis, T. K. Gaylord, E. N. Glytsis, S. G. Kosinski, S. C. Mettler, and A. M. Vengsarkar, "Long-period fibre grating fabrication with focused CO<sub>2</sub> laser pulses," *Electronics Letters*, vol. 34, no. 3, pp. 302–303, 1998.
- [9] Y. J. Rao, Y. P. Wang, Z. L. Ran, and T. Zhu, "Novel fiber-optic sensors based on long-period fiber gratings written by high-frequency CO<sub>2</sub> laser pulses," *Journal of Lightwave Technology*, vol. 21, no. 5, pp. 1320–1327, 2003.
- [10] Y. J. Rao, T. Zhu, Z. L. Ran, Y. P. Wang, J. Jiang, and A. Z. Hu, "Novel long-period fiber gratings written by high-frequency CO<sub>2</sub> laser pulses and applications in optical fiber communication," *Optics Communications*, vol. 229, no. 1–6, pp. 209–221, 2004.
- [11] Y. P. Wang, Y. J. Rao, Z. L. Ran, T. Zhu, and X. K. Zeng, "Bend-insensitive long-period fiber grating sensors," *Optics and Lasers in Engineering*, vol. 41, no. 1, pp. 233–239, 2004.
- [12] I. K. Hwang, S. H. Yun, and B. Y. Kim, "Long-period fiber gratings based on periodic microbends," *Optics Letters*, vol. 24, no. 18, pp. 1263–1265, 1999.
- [13] Y. Kondo, K. Nouchi, T. Mitsuyu, M. Watanabe, P. G. Kazansky, and K. Hirao, "Fabrication of long-period fiber gratings by focused irradiation of infrared femtosecond laser pulses," *Optics Letters*, vol. 24, no. 10, pp. 646–648, 1999.
- [14] S. Savin, M. J. F. Digonnet, G. S. Kino, and H. J. Shaw, "Tunable mechanically induced long-period fiber gratings," *Optics Letters*, vol. 25, no. 10, pp. 710–712, 2000.
- [15] C. Y. Lin, G. W. Chern, and L. A. Wang, "Periodical corrugated structure for forming sampled fiber Bragg grating and long-period fiber grating with tunable coupling strength," *Journal of Lightwave Technology*, vol. 19, no. 9, pp. 1212–1220, 2001.
- [16] J. C. Knight, T. A. Birks, P. S. Russell, and D. M. Atkin, "All-silica single-mode optical fiber with photonic crystal cladding," *Optics Letters*, vol. 21, no. 19, pp. 1547–1549, 1996.
- [17] D. D. Davis, T. K. Gaylord, E. N. Glytsis, and S. C. Mettler, "CO<sub>2</sub> laser-induced long-period fibre gratings: spectral characteristics, cladding modes and polarisation independence," *Electronics Letters*, vol. 34, no. 14, pp. 1416–1417, 1998.
- [18] Y. Zhu, P. Shum, J. H. Chong, M. K. Rao, and C. Lu, "Deep-notch, ultracompact long-period grating in a large-mode-area photonic crystal fiber," *Optics Letters*, vol. 28, no. 24, pp. 2467–2469, 2003.
- [19] M. I. Braiwish, B. L. Bachim, and T. K. Gaylord, "Prototype CO<sub>2</sub> laser-induced long-period fiber grating variable optical attenuators and optical tunable filters," *Applied Optics*, vol. 43, no. 9, pp. 1789–1793, 2004.
- [20] Y. P. Wang, D. N. Wang, W. Jin, Y. J. Rao, and G. D. Peng, "Asymmetric long period fiber gratings fabricated by use of CO<sub>2</sub> laser to carve periodic grooves on the optical fiber," *Applied Physics Letters*, vol. 89, no. 15, pp. 151105-1–151105-3, 2006.
- [21] Y. P. Wang, W. Jin, and D. N. Wang, "Strain characteristics of CO<sub>2</sub>-laser-carved long period fiber gratings," *IEEE Journal of Quantum Electronics*, vol. 43, no. 2, pp. 101–108, 2007.
- [22] C. M. Smith, N. Venkataraman, M. T. Gallagher, D. Muller, J. A. West, N. F. Borrelli, *et al.*, "Low-loss hollow-core silica/air photonic bandgap fibre," *Nature*, vol. 424, no. 6949, pp. 657–659, 2003.
- [23] B. J. Eggleton, P. S. Westbrook, R. S. Windeler, S. Spalter, and T. A. Strasser, "Grating resonances in air-silica microstructured optical fibers," *Optics Letters*, vol. 24, no. 21, pp. 1460–1462, 1999.
- [24] B. J. Eggleton, P. S. Westbrook, C. A. White, C. Kerbage, R. S. Windeler, and G. L. Burdge, "Cladding-mode-resonances in air-silica microstructure optical fibers," *Journal of Lightwave Technology*, vol. 18, no. 8, pp. 1084–1100, 2000.
- [25] G. Kakarantzas, T. A. Birks, and P. S. Russell, "Structural long-period gratings in photonic crystal fibers," *Optics Letters*, vol. 27, no. 12, pp. 1013–1015, 2002.
- [26] Y. Wang, L. Xiao, D. N. Wang, and W. Jin, "In-fiber polarizer based on a long-period fiber grating written on photonic crystal fiber," *Optics Letters*, vol. 32, no. 9, pp. 1035–1037, 2007.
- [27] Y. P. Wang, L. M. Xiao, D. N. Wang, and W. Jin, "Highly sensitive long-period fiber-grating strain sensor with low temperature sensitivity," *Optics Letters*, vol. 31, no. 23, pp. 3414–3416, 2006.
- [28] G. Humbert, A. Malki, S. Fevrier, P. Roy, and D. Pagnoux, "Electric arc-induced long-period gratings in Ge-free air-silica microstructure fibres," *Electronics Letters*, vol. 39, no. 4, pp. 349–350, 2003.
- [29] L. B. Fu, G. D. Marshall, J. A. Bolger, P. Steinurzel, E. C. Magi, M. J. Withford, *et al.*, "Femtosecond laser writing Bragg gratings in pure silica photonic crystal fibres," *Electronics Letters*, vol. 41, no. 11, pp. 638–640, 2005.
- [30] S. J. Mihailov, D. Grobnić, D. Huimin, C. W.

- Smelser, and B. Jes, "Femtosecond IR laser fabrication of Bragg gratings in photonic crystal fibers and tapers," *IEEE Photonics Technology Letters*, vol. 18, no. 17, pp. 1837–1839, 2006.
- [31] N. Groothoff, J. Canning, E. Buckley, K. Lyttikainen, and J. Zagari, "Bragg gratings in air-silica structured fibers," *Optics Letters*, vol. 28, no. 4, pp. 233–235, 2003.
- [32] Y. Wang, H. Bartelt, M. Becker, S. Brueckner, J. Bergmann, J. Kobelke, *et al.*, "Fiber Bragg grating inscription in pure-silica and Ge-doped photonic crystal fibers," *Applied Optics*, vol. 48, no. 11, pp. 1963–1968, 2009.
- [33] Y. Wang, H. Bartelt, W. Ecke, R. Willsch, J. Kobelke, M. Kautz, *et al.*, "Sensing properties of fiber Bragg gratings in small-core Ge-doped photonic crystal fibers," *Optics Communications*, vol. 282, no. 6, pp. 1129–1134, 2009.
- [34] Y. Zhu, P. Shum, H. W. Bay, M. Yan, X. Yu, J. Hu, *et al.*, "Strain-insensitive and high-temperature long-period gratings inscribed in photonic crystal fiber," *Optics Letters*, vol. 30, no. 4, pp. 367–369, 2005.
- [35] L. Jin, W. Jin, J. Ju, and Y. Wang, "Coupled local-mode theory for strongly modulated long period gratings," *Journal of Lightwave Technology*, vol. 28, no. 12, pp. 1745–1751, 2010.
- [36] Y. Wang, W. Jin, L. Jin, X. Tan, H. Bartelt, W. Ecke, *et al.*, "Optical switch based on a fluid-filled photonic crystal fiber Bragg grating," *Optics Letters*, vol. 34, no. 23, pp. 3683–3685, 2009.
- [37] T. B. Iredale, P. Steinurzel, and B. J. Eggleton, "Electric-arc-induced long-period gratings in fluid-filled photonic bandgap fibre," *Electronics Letters*, vol. 42, no. 13, pp. 739–740, 2006.
- [38] Y. Wang, X. Tan, W. Jin, S. Liu, D. Ying, and Y. L. Hoo, "Improved bending property of half-filled photonic crystal fiber," *Optics Express*, vol. 18, no. 12, pp. 12197–12202, 2010.
- [39] Y. Wang, X. Tan, W. Jin, D. Ying, Y. L. Hoo, and S. Liu, "Temperature-controlled transformation in fiber types of fluid-filled photonic crystal fibers and applications," *Optics Letters*, vol. 35, no. 1, pp. 88–90, 2010.
- [40] Y. Wang, S. Liu, X. Tan, and W. Jin, "Selective-fluid-filling technique of microstructured optical fibers," *Journal of Lightwave Technology*, vol. 28, no. 22, pp. 3193–3196, 2010.
- [41] L. Jin, Z. Wang, Q. Fang, B. Liu, Y. Liu, G. Kai, *et al.*, "Bragg grating resonances in all-solid bandgap fibers," *Optics Letters*, vol. 32, no. 18, pp. 2717–2719, 2007.
- [42] Y. Wang, W. Jin, J. Ju, H. Xuan, H. L. Ho, L. Xiao, *et al.*, "Long period gratings in air-core photonic bandgap fibers," *Optics Express*, vol. 16, no. 4, pp. 2784–2790, 2008.
- [43] L. Jin, W. Jin, J. Ju, and Y. Wang, "Investigation of long-period grating resonances in hollow-core photonic bandgap fibers," *Journal of Lightwave Technology*, vol. 29, no. 11, pp. 1708–1714, 2011.
- [44] A. Iadicicco, S. Campopiano, and A. Cusano, "Long-period gratings in hollow core fibers by pressure-assisted arc discharge technique," *IEEE Photonics Technology Letters*, vol. 23, no. 21, pp. 1567–1569, 2011.
- [45] W. Shin, Y. L. Lee, T. J. Eom, B. A. Yu, and Y. C. Noh, "Temperature insensitive strain sensor based on long period fiber grating pair in photonic crystal fibers," in *14th OptoElectronics and Communications Conference (OECC 2009)*, Hong Kong, July 13–17, 2009, pp. 1–2, 2009.
- [46] C. L. Zhao, L. Xiao, J. Ju, M. S. Demokan, and W. Jin, "Strain and temperature characteristics of a long-period grating written in a photonic crystal fiber and its application as a temperature-insensitive strain sensor," *Journal of Lightwave Technology*, vol. 26, no. 1–4, pp. 220–227, 2008.
- [47] Y. Wang, W. Jin, and D. N. Wang, "Unique temperature sensing characteristics of CO<sub>2</sub>-laser-notched long-period fiber gratings," *Optics and Lasers in Engineering*, vol. 47, no. 10, pp. 1044–1048, 2009.